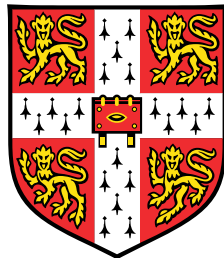


Numerical Analysis of Flux Reconstruction



Will Trojak

Supervisors:

Prof. P. G. Tucker and Prof. R. S. Cant

Department of Engineering
University of Cambridge

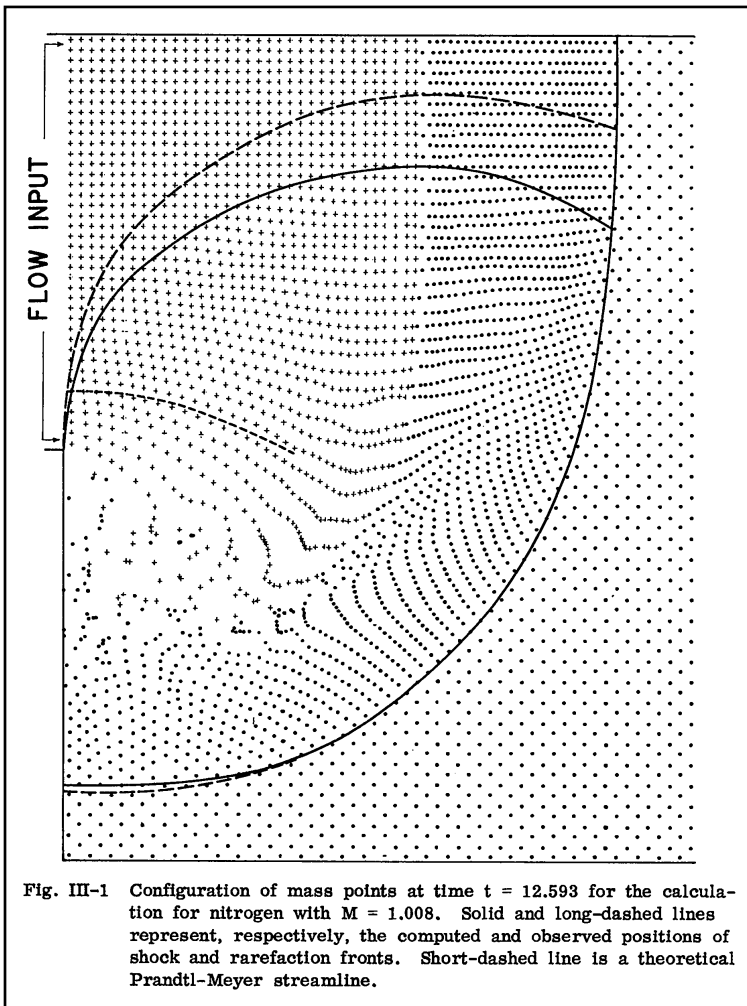
This dissertation is submitted for the degree of

Doctor of Philosophy

Peterhouse

February 2019

Numerical Analysis of Flux Reconstruction



Harlow's particle-in-cell method used to simulate shocks in supersonic flow, Harlow 1959. One of the earliest 2D inviscid flow calculations performed on a computer.

Will Trojak

Numerical Analysis of Flux Reconstruction
A Ph.D Thesis



Will Trojak  
Department of Engineering
Trumpington Street
CB2 1PZ
wt247@cam.ac.uk

Mathematics Subject Classification (2010): 46Exx, 65Jxx, 65Mxx, 65Nxx, 65Yxx, 65Zxx

Typeset using Krishna Kumar thesis class, modified by Will Trojak

© February 2019 Will Trojak

This work is licensed under the Creative Commons Attribution-NonCommercial-NoDerivatives 4.0 International (CC BY-NC-ND 4.0) License. 

Declaration

I hereby declare that except where specific reference is made to the work of others, the contents of this dissertation are original and have not been submitted in whole or in part for consideration for any other degree or qualification in this, or any other university. This dissertation is my own work and contains nothing which is the outcome of work done in collaboration with others, except as specified in the text and Acknowledgements. This dissertation contains fewer than 65,000 words including appendices, bibliography, footnotes, tables and equations and has fewer than 150 figures.

Will Trojak
February 2019

Acknowledgements

I would firstly like to thank Dr Rob Watson for initially sparking my interest in CFD and his continued help and support throughout my Masters and PhD. Even after his move to Queen's University Belfast he was more than willing to offer help when I needed it. I would also like to thank Prof. Paul Tucker, throughout my PhD, Paul has had his own battles but has continued to give as much assistance as he was able to, which was always greatly appreciated. Paul was also willing to frequently indulge my curiosity, principally by allowing me to undertake a PhD for which I am very grateful. Finally, I would like to thank the assistance of Prof. Stewart Cant who was ready and willing to provide his opinion on a range of subjects, and this made our discussions thoroughly enjoyable. I would like to dedicate this thesis to Damaris, because if listening to me talk about CFD wasn't enough, now she gets to read about it too.

Abstract

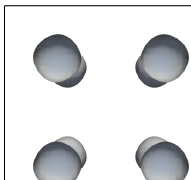
Stuff and things.

Contents

List of Contributions	xvii
List of Figures	xix
Nomenclature	xxv
1 Introduction	1
1.1 Motivation for High-Order Methods	1
1.2 Motivation For The Current Study	2
1.3 Literature Review	4
1.3.1 Development of High-Order Methods	4
Finite Difference	4
Finite Volume	6
Element Based	8
1.3.2 Computational Considerations	8
1.3.3 Flux Reconstruction	9
1.3.4 PDEs Characteristic of Industry	10
Advection Equations	10
Diffusion Equations	11
1.3.5 Correction Functions	12
2 Flux Reconstruction Methodology	15
2.1 Preliminaries	15
2.2 One-Dimensional Approach for First-Order PDEs	16
2.3 Two-Dimensional Approach for Second-Order PDEs	19
3 Implementation Aliasing	23
3.1 Introduction	23
3.2 Discrete Polynomial Aliasing	25
3.3 Primitive and Conserved Variables	29

3.3.1	Euler's Equation	29
	Conserved Variable Computation	29
	Inviscid Flux Computation	30
3.3.2	Navier-Stoke's Equation	31
3.4	Isentropic Convecting Vortex	34
3.5	Taylor-Green Vortex	36
3.6	Conclusions	43
4	Flux Reconstruction for First-Order PDEs on Stretched Grids	45
4.1	Introduction	45
4.2	Analytical Techniques	45
4.2.1	One-Dimensional von Neumann Analysis	46
4.2.2	Two-Dimensional von Neumann Analysis	50
4.3	Analytical Findings	55
4.3.1	One-Dimension	55
	Spatial Characteristics	55
	Coupled Spatial-Temporal Characteristics	56
4.3.2	Two-Dimensions	61
	Preliminaries	61
	Effect of Grid Expansion on Dispersion and Dissipation	62
	Effect of Grid Aspect Ratio on CFL Limit	68
	Effect of Grid Expansion on CFL Limit	69
	Effect of Grid Expansion of Fully Discrete Dispersion and Dissipation	71
	Effect of Correction Functions with Grid Expansion	73
4.4	Numerical Experiments	75
4.4.1	One-Dimensional Linear Advection Equation on Stretched Grids	75
4.4.2	Two-Dimensional Eulers Equation with Randomised Grids . .	78
4.4.3	Three-Dimensional Navier-Stokes Equations with Randomised Grids	82
4.5	Conclusions	88
5	Novel Correction Functions	89
5.1	Introduction	89
5.2	Stability Definition	90
5.2.1	Preliminaries	90
5.2.2	Sobolev Norm	91
5.2.3	Weighted Sobolev Norm	91

5.2.4	Generalised Sobolev Norm	94
5.2.5	Lebesgue Norm	94
5.3	Finding Stable Correction Functions	95
5.3.1	Original Stable Flux Reconstruction	95
5.3.2	Generalised Jacobi Stable Flux Reconstruction	95
	Spectral Difference Schemes	98
5.3.3	Generalised Sobolev Stable Flux Reconstruction	100
	GSFR for $p = 2$	102
	GSFR for $p = 3$	103
	GSFR for $p = 4$	103
5.3.4	Generalised Lebesgue Stable Flux Reconstruction	106
5.4	Analytical Findings	108
5.4.1	Generalised Jacobi Results	112
5.4.2	Generalised Sobolev Results	116
5.4.3	Generalised Lebesgue Results	119
5.5	Numerical Experiments	123
5.5.1	Linear Problems - GSFR	123
5.5.2	Isentropic Convecting Vortex - GSFR	126
5.5.3	Taylor-Green Vortex	128
	GJFR Results	129
	GLSFR Results	132
5.6	Conclusions	133
5.6.1	Generalised Jacobi	133
5.6.2	Generalised Sobolev	134
5.6.3	Generalised Lebesgue	135
6	Conclusions and Future Work	137
6.1	Conclusions	137
6.2	Future Work	137
References		139
Appendix A	Introductory Theory of Orthogonal Polynomials	149
A.1	Legendre Polynomials	151
A.2	Jacobi Polynomials	153
Appendix B	Extended Range of Energy Stable Flux Reconstruction Correction Functions	155

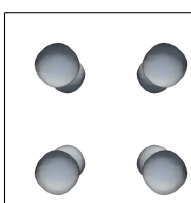


Appendix C Correction Fuinction Pseudo Code	157
C.1 Generalised Sobolev Stable FR	157
C.2 Generalised Lebesgue Stable FR	158

List of Contributions

Journal Papers

1. W. Trojak, R. Watson, and P.G. Tucker. High Order Flux Reconstruction on Stretched and Warped Meshes. *AIAA Journal*, Vol. 57, No. 1 (2019), pp. 341-351.
DOI: 10.2514/1.J056341.
2. W. Trojak. Generalised Sobolev Stable Flux Reconstruction. *Journal of Computational Physics*, Submitted May 2018.
ArXiv: 1804.04714
3. W. Trojak. Generalised Lebesgue Stable Flux Reconstruction. *Journal of Computational Physics*, Submitted June 2018.
ArXiv: 1805.12481
4. W. Trojak, R. Watson, A. Scillitoe, and P.G. Tucker. Effect of Mesh Quality on Flux Reconstruction in Multi-Dimensions. *Journal of Scientific Computing*. First review received December 2018, submitted January 2019.
ArXiv: 1809.05189
5. W. Trojak, and F.D. Witherden. A New Family of Weighed One-Parameter Flux Reconstruction Schemes. *Computer Methods in Applied Mechanics and Engineering*, Submitted September 2018.
ArXiv: 1809.07846
6. W. Trojak, A. Scillitoe, and R. Watson. All Equalities are Equal, but Some are More Equal Than Others: The Effect of Implementation Aliasing on the Numerical Solution of Conservation Equations. *Computers and Fluids*, Submitted January 2019.
ArXiv: 1901.08884



Conference Papers

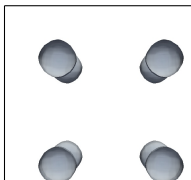
1. W. Trojak, R. Watson, and P.G. Tucker. High Order Flux Reconstruction on Stretched and Warped Meshes, Paper AIAA-2017-0521, *55th AIAA Aerospace Sciences Meeting*, Grapevine Texas, Jan 2017.
2. W. Trojak, R. Watson, and P.G. Tucker. Temporal Stabilisation of Flux Reconstruction on Linear Problems, Paper AIAA-2018-4263, *Fluid Dynamics Conference, AIAA AVIATION Forum*, Atlanta Georgia, June 2018.
3. R. Watson, W. Trojak, and P.G. Tucker. A Simple Flux Reconstruction Approach to Solving a Poisson Equation to Find Wall Distances for Turbulence Modelling, Paper AIAA-2018-4261, *Fluid Dynamics Conference, AIAA AVIATION Forum*, Atlanta Georgia, June 2018.
4. J. Tyacke, R. Watson, W. Trojak, and P.G. Tucker. High Fidelity Turbomachinery Simulation. *12th International ERCOFTAC Symposium on Engineering Turbulence Modelling and Measurements*, Montpellier France, Sept 2018.

Oral Presentations

1. W. Trojak, R. Watson, and P.G. Tucker. High Order Flux Reconstruction on Stretched and Warped Meshes, Paper AIAA-2017-0521, *55th AIAA Aerospace Sciences Meeting*, Grapevine Texas, Jan 2017.
2. W. Trojak, R. Watson, and P.G. Tucker. Temporal Stabilisation of Flux Reconstruction on Linear Problems, Paper AIAA-2018-4263, *Fluid Dynamics Conference, AIAA AVIATION Forum*, Atlanta Georgia, Jun 2018.

List of Figures

0	Harlow's particle-in-cell method used to simulate shocks in supersonic flow, Harlow 1959. One of the earliest 2D inviscid flow calculations performed on a computer.	iv
1.1	An example stencil of a Compact FD scheme, showing the interconnection between node and how this can be leveraged to give a far wider stencil.	6
1.2	Schematic of cell vertex finite volume grid, with dual generated via connecting centroids.	6
1.3	Examples of high frequency oscillation caused by discretisation approaches	7
2.1	Point layout in $\hat{\Omega}$ for $p = 4$ and example of flux correction.	19
3.1	Variation of error in ICV density with time for FR, $p = 4$, using methods A, B and D on $16 \times 16 \times 2$ and $20 \times 20 \times 2$ element grids.	35
3.2	Variation in total kinetic energy of the ICV, FR $p = 4$, for two grid resolutions. using methods A, B, and D.	36
3.3	Enstrophy of the Taylor-Green Vortex with $R_e = 1600$, $p = 4$ and 80^3 degrees of freedom for storage methods A-D.	38
3.4	Enstrophy of the Taylor-Green Vortex with $R_e = 1600$, $p = 3$ and 80^3 degrees of freedom.	39
3.5	Enstrophy of the Taylor-Green Vortex with $R_e = 3000$, $p = 4$ and 80^3 degrees of freedom.	40
3.6	Enstrophy of the Taylor-Green Vortex with $R_e = 400$, $p = 4$ and 40^3 degrees of freedom.	41
3.7	Taylor-Green Vortex Enstrophy $R_e = 1600$, $p = 4$ and 80^3 DoF for different variable storage precisions.	42
4.1	Example mesh slice from low pressure turbine calculation	46
4.2	Schematic showing transformation caused by numerical scheme with incoming and outgoing wave	50



4.3	52
4.4	Analytical filter kernel against Nyquist normalised wavenumber, for various orders of upwinded FR with Huynh, g_2 , correction functions	55
4.5	Dispersion relations for FR, with Huynh, g_2 , correction functions, on various geometrically stretched meshes.	57
4.6	Dissipation relations for FR, with Huynh, g_2 , correction functions, on various geometrically stretched meshes	58
4.7	Points Per Wavelength (PPW) for error < 1% against expansion rate, γ , for various spatial orders of upwinded FR with Huynh, g_2 , correction functions.	58
4.8	Effect of time step on spectral radius of upwinded FR update equation	60
4.9	Effect of time step and time scheme on spectral radius of upwinded FR update equation	60
4.10	Primary mode dispersion for 2D upwinded FR, with Huynh g_2 corrections, at various orders. Normalised wavenumber as radial distance (markers at $\pi/4$ intervals), and element angle of incidence as azimuthal distance.	63
4.11	Primary mode dissipation for 2D upwinded FR, with Huynh g_2 corrections, at various orders. Normalised wavenumber as radial distance (markers at $\pi/4$ intervals), and element angle of incidence as azimuthal distance.	64
4.12	Two dimensional upwinded FR, $p = 3$ with Huynh g_2 corrections, for different grid expansion factors. Normalised wavenumber as radial distance (markers at $\pi/4$ intervals), and element angle of incidence as azimuthal distance. The solid black line on the dissipation plots is the contour of zero dissipation.	65
4.13	Two dimensional upwinded FR, $p = 3$, with Huynh g_2 corrections at selected incident angles.	66
4.14	Two dimensional upwinded FR, $p = 3$ with NDG corrections, for different grid expansion factors. Normalised wavenumber as radial distance (markers at $\pi/4$ intervals), and element angle of incidence as azimuthal distance. The solid black line on the dissipation plots is the contour of zero dissipation.	67
4.15	Effect of varying: the relative size an element in x and y ; the angle of incidence; and CFL in 2D for upwinded FR. The method of temporal integration used here was RK44. (.....) $\Delta_y/\Delta_x = \tan\theta$	68
4.16	CFL limit for 2D linear advection with FR ($p = 4$) using Huynh correction function, showing variation with θ and γ_x for some set values of γ_y . Time integration is RK44.	70

4.17 Dispersion and dissipation of upwinded FR, $p = 3$, with Huynh g_2 corrections and explicit RK44 temporal integration, $\tau = 0.18$. The radial distance is the normalised wavenumber (including the effect of angle), and the azimuthal distance is the angle of incidence to the element. The solid black line on the dissipation plots is the contour of zero dissipation.	72
4.18 CFL limit for 2D linear advection, at several orders. Varying correction function parameter, ι , and angle θ . Time integration is RK44. The value of ι_+ is shown as a dashed black line.	73
4.19 Condition number of various linear FR configurations	74
4.20 Variation of condition number with wave angles and wavenumber for upwinded 3D FR, $p = 3$, $\gamma_x = \gamma_y = \gamma_z = 1$, using Huynh g_2 correction functions.	76
4.21	77
4.22 For 3rd order and 5th order FR on an expanding grid with $\gamma = 1.1$ using RK44 time integration a spatial slice is shown. With the convected parameter u , the CFL number and the Nyquist normalised ($\hat{k} = \pi k/k_{nq}$).	79
4.23 Cross diagonal angle definition. $\alpha = \beta - 90^\circ$	79
4.24 19×19 quadrilateral meshes showing differing degrees of node jittered mesh warp.	80
4.25 Point averaged l_2 norm of error, $\frac{1}{N} \sum_{n=1}^N \theta_n _2$, against degrees of freedom (DoF) for $p = 4$ FR and nominally second order FV scheme. $CFL = 0.01$ for 3000 time steps.	80
4.26	81
4.27 Example slices through a 3D hexahedral mesh to illustrate the mesh quality metric.	84
4.28 Effect of jitter on turbulent kinetic energy dissipation of the TGV ($R_e = 1600$) for FR, $p = 2$, with Huynh g_2 correction functions on a 40^3 element mesh. Explicit time step size is $\Delta t = 1 \times 10^{-3}$	84
4.29 Effect of jitter on turbulent kinetic energy dissipation of the TGV ($R_e = 1600$) for FR, $p = 4$, with Huynh g_2 correction functions on a 24^3 element mesh. Explicit time step is $\Delta t = 1 \times 10^{-3}$	85
4.30 Dispersion and Dissipation relation for 1D upwinded FR, $p = 1$, with DG correction function.	86
4.31 Comparison of FR, $p = 1$ with DG correction functions with a second order central FV scheme with L2 Roe smoothing both with 170^3 degrees of freedom and $\Delta t \approx 5 \times 10^{-4}$. A reference DNS solution is provided from [18].	87

4.32 Comparison of FR, $p = 1$ with DG correction functions with a second order KEP FV scheme with L2 Roe smoothing both with 170^3 degrees of freedom and $\Delta t \approx 5 \times 10^{-4}$. A reference DNS solution is provide from [18].	87
5.1 Selected Gauss-Jacobi quadratures for $n = 4$.	100
5.2 Comparison of OSFR, ESFR and GSFR correction functions, $p = 3$.	105
5.3 Variation of the rate of error convergence with grid for qDG, $p = 4$.	113
5.4 CFL limit of various temporal integration methods for upwinded qDG, $p = 4$.	113
5.5 Example qGD, $p = 4$, correction function.	114
5.6 Variation of the rate of error convergence with grid for Jacobi-SD correction functions, $p = 4$.	114
5.7 CFL limit of various temporal integration methods for Jacobi SD with updinded interfaces, $p = 4$.	115
5.8 Dispersion and dissipation relations of convergence optimal Jacobi-SD and qDG correction function, $p = 4$.	117
5.9 CFL limit for upwinded FR with GSFR correction functions, $p = 3$, and RK44 temporal integration on a regular grid.	117
5.10 Dispersion and dissipation for selected $p = 3$ GSFR correction functions with interface upwinding.	118
5.11 CFL limit for upwinded FR with GSFR correction functions, $p = 4$, and RK44 temporal integration on a regular grid. ($\iota_1 = 1 \times 10^{-5}$)	119
5.12 Example GLSFR, $p = 4$, correction function with arbitary weights and wave propagating characteristics.	120
5.13 Maximum stable CFL number for GLSFR [$c = 1, \nu = 0$], with RK44 temporal integration.	120
5.14 Linear advection dispersion and dissipation comparison of spatial and temporal-spatial (T/S) analysis for upwinded GLSFR, $p = 4$.	121
5.15 Linear advection dispersion relations for central interface flux GLSFR, $p = 4$.	122
5.16 Maximum stable CFL number for GLSFR [$c = 10, \nu = 1$], with RK44 temporal integration.	122
5.17 Order of accuracy of GSFR, $p = 3$, applied to linear advection.	124
5.18 L^2 energy error of GSFR, $p = 3$, applied to linear advection.	126
5.19 Error in the domain integrated kinetic energy of the ICV for FR, $p = 3$, for various GSFR correction functions.	127
5.20 Jacobi-SD TGV dissipation and enstrophy comparison with OSFR correction function.	129

5.21 Jacobi SD, $p = 4$, time averaged dissipation and enstrophy error for TGV	130
5.22 Quasi-DG, $p = 4$, time averaged dissipation and enstrophy error for TGV	131
5.23 GLSFR $p = 4$, TGV dissipation rate error.	132
5.24 Optimal GLSFR $p = 4$ correction function dissipation rate for the TGV	133
5.25 Euler diagram to show the interconnection of the spaces of FR correction functions	134

Nomenclature

Roman Symbols

a	linear advection convective velocity
$b_p^{(\alpha,\beta)}$	the value of the p^{th} derivative of $J_p^{(\alpha,\beta)}$
\mathbf{C}_\bullet	interface correction matrix
C^n	unbounded n^{th} derivative continuity space
C_0^n	bounded n^{th} derivative continuity space
\mathbf{D}_η	differentiation matrix operator in η
\mathbf{D}_ξ	differentiation matrix operator in ξ
e_a	Aliasing error
\mathbf{F}	aggregate flux vector, used in one equation formulation
\mathbf{f}	x dimension flux vector
\mathbf{f}, \dots	conservative flux in x, \dots
$\mathbf{f}^{\text{inv}}, \dots$	conservative inviscid flux in x, \dots
$\mathbf{f}^{\text{vis}}, \dots$	conservative viscous flux in x, \dots
\mathbf{G}	Jacobian matrix
\mathbf{g}	y dimension flux vector
\mathbf{G}_n	Jacobian matrix for the n^{th} element
h	correction function
J_n	determinant of the n^{th} element's Jacobian matrix

$J_i^{(\alpha,\beta)}$	i^{th} order Jacobi polynomial, with control variables (α,β)
k	wavenumber
\hat{k}	Nyquist normalised wavenumber, k/k_{nq} ($[0, \pi]$ by convention)
k_{nq}	Nyquist wavenumber
$l_i(\xi)$	i^{th} Lagrange polynomial basis function in ξ
M_a	Mach Number
P_r	Prandtl Number
\mathbf{Q}	semi-discretised spatial scheme matrix
\mathbf{Q}_c	vector of conserved variables
$\nabla \mathbf{Q}_c$	gradient of conserved variables
\mathbf{Q}_{c+p}	vector of conserved variables, with E substituted with p
$q_n^{(\alpha,\beta)}$	the value of $(J_n^{(\alpha,\beta)})^2$ integrated over $[-1, 1]$ w.r.t the weight function w .
\mathbf{Q}_p	vector of primitive variables
$\nabla \mathbf{Q}_p$	gradient of primitive variables
\mathbf{R}	temporal update matrix
R_e	Reynolds Number
R	Specific gas constant
\mathbf{u}	primitive column vector
\mathbf{V}	Vector of velocity components
\mathbf{v}	eigenvector
W_2^{ι}	l_2 Sobolev space of u and $\iota u^{(p)}$
$W_2^{\iota,w}$	l_2 Sobolev space of u and $\iota u^{(p)}$ weighted by function w
y^+	wall normal distance normalised by viscous lengthscale

Greek Symbols

α	interface upwinding coefficient, $\alpha = 1$ implies upwinded, $\alpha = 0.5$ implies central differenced
γ	geometric expansion ratio
ϵ_1	global averaged kinetic energy decay rate
ϵ_2	global averaged enstrophy based decay rate
ζ	3 rd coordinate in reference domain
η	2 nd coordinate in reference domain
ι	correction function parameter, typically coefficient of p^{th} derivative in Sobolev norm
$\kappa(\mathbf{A})$	condition number of matrix \mathbf{A}
ν	rate of linear diffusion
ξ	1 st coordinate in reference domain
$\rho(\mathbf{A})$	spectral radius of matrix \mathbf{A}
ψ_i	i^{th} basis polynomial, typically Legendre polynomial of the first kind
ω	vorticity, $\nabla \times \mathbf{V}$
Ω	spatial domain
Ω_n	spatial domain partition
$\hat{\Omega}$	computational spatial domain

Superscripts

$\bar{\bullet}$	interpolated primitive transformed to physical domain
$y^{(i)}$	i^{th} derivative of y
$\hat{\bullet}$	value in computational domain
\bullet^δ	globally-continuous local polynomial approximation of value
$\bullet^{\delta C}$	correction to discontinuous values
$\bullet^{\delta D}$	local discontinuous polynomial approximation of value

$\bullet^{\delta Di}$	local discontinuous polynomial approximation of inviscid value
$\bullet^{\delta Dv}$	local discontinuous polynomial approximation of viscous value
$\bullet^{\delta I}$	common interface value

Subscripts

\bullet_b	property of bottom interface
\bullet_t	property of top interface

Other Symbols

$_n F_m(\mathbf{N}, \mathbf{M}; z)$	the n-m generalised hypergeometric function at z [11, 15]
\mathcal{L}_p	p^{th} order interpolation operator
\mathbb{N}	set of natural numbers, i.e. positive integers
$\hat{\nabla}$	gradient operator in computational space
O	big O notation showing limiting behaviour of function
$(x)_i$	rising Pochhammer function of x with i steps
$(\overline{x})_i$	falling Pochhammer function of x with i steps
\mathbb{R}	set of real numbers
\mathcal{R}_p	p^{th} order interpolation remainder operator
\mathbb{R}_+	set of positive real numbers
$\lceil \bullet \rceil$	ceiling function
$\lfloor \bullet \rfloor$	floor function
\bullet^T	vector or matrix transpose

Acronyms / Abbreviations

CFL	Courant–Friedrichs–Lewy number
CPR	Correction Procedure via Reconstruction
DFR	Direct Flux Reconstruction

DG	Discontinuous Galerkin
DNS	Direct Numerical Simulation
DRP	Dispersion Relation Preserving
ENO	Essentially Non-Oscillatory
ESFR	Extended range Stable Flux Reconstruction
FD	Finite Difference
FE	Finite Element
FLOP	FLoating point OPeration
FR	Flux Reconstruction
FV	Finite Volume
GJFR	Original Jacobi stable Flux Reconstruction
GLSFR	Generalised Lebesgue Stable Flux Reconstruction
GPU	Graphics Processing Unit
GSFR	Generalised Sobolev stable Flux Reconstruction
LCL	Lumped Chebyshev-Lobatto
LCP	Lifting Collocation Penalty
LES	Large Eddy Simulation
LSD	Legendre Spectral Difference
NDG	Nodal Discontinuous Galerkin
NSE	Navier-Stokes Equation
OSFR	Original Stable Flux Reconstruction
PDE	Partial Differential Equation
qDG	quasi Discontinuous Galerkin
RANS	Reynolds Averaged Navier-Stokes

RK	Runge-Kutta
SD	Spectral Difference
SV	Spectral Volume
TGV	Taylor-Green Vortex
WENO	Weighted Essentially Non-Oscillatory

Chapter 1

Introduction

1.1 Motivation for High-Order Methods

For a considerable time, engineers have been reliant on computational methods for simulating fluid flow. They use Computational Fluid Dynamics (CFD) to aid or improve design or advance knowledge about the behaviour and nature of fluid flow. This shift to computational methods has been necessary due to the immense cost of producing scale models or testing full-size rigs. However, this then makes the scale and scope of calculations dependent on the availability of computing resources. Although the throughput of high-performance computing has vastly increased since CFD's inception – the top supercomputer in November 2018 (the US DOE's Summit computer) having a peak LINPACK performance of 143.5 PFLOPS – NASA Vision 2030 [109] still lists FLOPS as a significant barrier to the 'use of CFD in the aerospace design process'.

Industry is confronted by a similar problem that caused the move away from experimental modelling. That is, to perform the far larger calculations that are becoming necessary, such as those of a full gas turbine engine, means that time must be sought on a large cluster or a new large supercomputer be built. The cost of this is enormous, with a project like 'Summit' only achievable by national governments. The alternative is that the algorithms that underpin CFD can be changed.

Fundamentally, the conservation form of the Navier-Stokes Equations (NSE) is a set of coupled PDEs, in which the differentiation operator can be defined in terms of the difference between two local values divided by the distance between their locations. Therefore from a purist's point of view, first-order schemes should do the job. This was the point explored in [46] and Godunov's Theorem reflects this. (NASA even used first-order methods as early as the 1950s to computationally calculate re-entry trajectories [73]). However, in reality, this leads to either very dense grids, the likes of which are impractical, or coarse grids that then suffer from high dissipation or dispersion. Therefore, it has been

ubiquitous within industry to use second order schemes, which are able to produce a well-converged solution to the Reynolds Averaged Navier-Stokes (RANS) equations.

Yet the fundamental flaw in RANS is that the closure problem means a model has to be inserted to get a full rank equation set. Hence, RANS solutions are strictly postdictive and can only inform the design process or understanding if prior knowledge of the outcome is known. In response to the inadequacies of RANS, Large Eddy Simulation (LES) has been coming to the forefront of CFD in the last few decades. NASA's CFD Vision 2030 [109] reflects this, while also highlighting the biggest barrier to ubiquity, which is that LES aims to resolve a large proportion of the energy contained in vortical structures directly on the grid (80-90%). This is a problem, because it gives rise to high grid requirements, albeit not as high as Direct Numerical Simulation (DNS), that stretch the limits of computing resources. Chow & Moin [28] and Ghosal [45] showed that the need to keep the truncation error small to enable the accurate use of sub-grid scale models meant the grid requirements were high, yet a move to higher order would mean that the scaling of the truncation error was to a higher power of grid spacing, thus lowering the grid requirements by decoupling the aliasing and truncation error.

Hence, higher-order methods have been gaining popularity. For example, at the AIAA SciTech Conferences on Aerospace Sciences the number of papers investigating or using high-order methods between 2014 and 2015 increased by $\approx 60\%$. What higher-order methods offer is a decrease in the number of degrees of freedom of a solution, as well as more freedom to tackle entrenched problems, such the handling of shock-waves including the carbuncle problem; complex boundary geometries [34]; and sub-grid scale modelling.

1.2 Motivation For The Current Study

The motivation for using higher order methods is clear - they allow for more accurate results and solution to problems that previously could not be considered due to computational limitations. Hence, the current work is to investigate one of these high order schemes. Yet, before schemes can be considered of industrial relevance two things need to be in place. Firstly, the scheme needs to have matured to a point such that there is sufficient understanding to design algorithms and data structures for it to be efficiently implemented. Secondly, the characteristics of a numerical scheme should be well enough understood that a practitioner can apply them in ways which take advantage of their abilities, whilst reducing the influence of their deficiencies. This second point is the area of interest for the current work.

Typically in industrial calculations, two effects are combined: a set of stiff equations which have been discretised on a reduced quality mesh; and equations which exhibit a

mix of advection, diffusion, and source terms - both linear and non-linear. In an industrial or engineering application the grid quality tends to suffer as the domains of interest are highly complex and far from canonical. Hence, it is firstly important that grids can be easily generated for complex geometries and then once a grid is produced, that the numerical scheme is not heavily degraded on non-ideal grids. This motivated the present study into how to characterise numerical methods to gain insight. The focus here is being placed on the characteristics on stretched grids for linear advection and diffusion. These categories will define the work going forward, as well as providing subdivision of topics in literature.

The key characteristics of a scheme that should be understood are its ability to resolve key features and its temporal stability. These metrics can then be passed down into ‘rules of thumb’ and subsequently used to inform the meshing process as well as further research. For example, if the temporal stability in some case is found to be too restrictive when using explicit methods it may be necessary to move to implicit time integration. This is a non-trivial matter and to ensure stability and efficient implementation further research would be needed. The evaluation of resolution can be broken down into wave resolution, energy decay rate, aliasing, and temporal stability. Wave resolving can be very informative for first and higher derivatives as potential solutions can be thought of as a superposition of waves. Furthermore, once wave transmission properties are known, deconvolution of the filter kernel can then be implemented to re-energise under-resolved wavenumbers. This links to the energy decay rate that can be utilised for finding new schemes as will be described later. More detail concerning existing evaluation techniques will be presented in Section 1.3.

So far, the justification for both the use of higher order methods and the present study has been kept very general. Becoming more specific, the family of schemes whose characteristics are explored in this work are based on Flux Reconstruction (FR) [55, 127]. Details of the development of the field that led to FR, the techniques currently used in analysis, and the state of the art will be laid out in Section 1.3. The overall structure will be: in Chapter 2 the numerical method of FR will be defined; in Chapter 3 the topic of aliasing at high order will be investigated; Chapter 4 will investigate the effect of mesh deformation in FR; Chapter 5 will look to define new types of FR; and in Chapter 6 conclusions will be made. Several appendices are included to aid the reader. These are: a brief introduction to orthogonal polynomials, a description of extended range FR, and pseudo code for some of the work included in Chapter 5. The remainder of this chapter is devoted to a review of the literature contributing to the development of ideas in this work.

1.3 Literature Review

We now present some of the key ideas and supporting literature that lead up to the present study. We will begin by introducing some contemporary numerical methods for conservation equations and how they went onto be extended to higher orders.

1.3.1 Development of High-Order Methods

Finite Difference Approaches

Much of the early work on the use of high-order methods was on a class of methods called Finite Difference (FD). This is owing to them being conceptually intuitive in their simplest form. FD can broadly take 2 forms: simple finite difference, the likes of which can be calculated from Taylor series; and compact difference or Padé schemes (so-called due to the use of the Padé approximation).

We will focus first on simple FD schemes with a significant historical account of techniques available in Harlow's memoirs [47]. Initially, these methods were applied to form first then second-order approximations of first and second derivatives [75, 76]. However, the first move towards high order was Roberts and Weiss [98] with a fourth order central difference scheme in space that was primarily developed for solving Maxwell's equations, but which was generalised for hyperbolic equations. This scheme's primary disadvantage was its mildly prohibitive CFL limit of 0.25. The restrictive CFL limits of high-order FD methods can be ameliorated in several ways, such as high order temporal integration, multi-grid [19], or implicit temporal methods. One such method that was developed is dual time stepping [60], which makes use of a real- and pseudo-time step to advance the solution. The philosophy of this method is to treat each time step as a steady problem in pseudo-time. Hence, converging each real-time step in pseudo-time, which subsequently allows the real-time steps to be very large. This method comes with significant computational overhead but has proved useful in high Reynolds number simulations or when integral time scales are large.

Commonly these simple FD schemes make use of their consistent stencil by having a structured grid. Indeed, all the original methods had structured grids, unstructured methods only coming later. Structured grids offer something of a compromise; due to knowing in advance the communication required, implementation can be highly optimised. For example, with tools such as GPU optimisation [20], making porting to heterogeneous architecture simpler. However, the other side of the compromise is that structured grids do mean that complex geometries are difficult to mesh and, in some cases, meshes may be impossible to produce.

Finally, FD schemes can be taken beyond what can formally be defined from Taylor series expansion via Dispersion Relation Preserving (DRP) schemes [83, 112]. DRP schemes modify the coefficients of an FD scheme of formal accuracy order, with the aim of improving the numerical properties of the method. For example, this could include reducing the dissipation rate of acoustic waves. The cost of this improvement is the loss of formal order of accuracy, but if the coefficients are chosen well this effect can be minimised, whilst still improving performance. For example, DRP schemes have been employed to provide high fidelity simulation of high-pressure turbine blades [135], something which has previously been challenging.

Next, we move on to what are commonly called compact finite difference schemes or compact schemes, which were introduced in a number of papers. Of note is Orszag et al. [91], in which a fourth order compact scheme is proposed and Lele [77], in which a more generalised set of compact schemes were introduced that could be adjusted for different wave propagation characteristics. Compact schemes make use of the interconnection of neighbouring points to give a wider stencil of differencing whilst maintaining a locally compact stencil. An example is shown in Fig. 1.1. This has the benefit of physically reducing the stencil required by each point in the implementation, whilst retaining a high-order spatial discretisation. Practically this is achieved by framing each block as a sparse banded matrix – for which there are highly optimised algorithms. Therefore, each block acts as a highly parallelisable region with a high degree of coupling that can propagate information quickly. Resultantly, compact schemes are best suited to large structured blocks. When applied to complex geometries, it becomes necessary to use a large number of blocks. The problem this poses is that it has been traditional for large overlap regions to be used at the interface of blocks, increasing inter-block communication and hence harming parallelism. More recently, methods of characteristics have come to be used together with one-sided differencing to remove the need for block overlaps [68], however characteristic based methods typically introduce excess diffusion at the interface. Other developments to solve the problem confronted by complex geometries have led to the use of other schemes to form an interface between blocks and between boundaries [41]. However, as problem size increases, hybrid approaches become less favourable due to the potential communication bottlenecks this could pose – as well as the load balancing issues introduced. The further issue of all these methods of block interfacing is that they can cause degradation to the solution quality.

Having introduced the two main branches of the FD method, it should have become clear that FD approaches lack any formal enforcement of conservation. This is common to many methods that work with the strong conservation form of equations. Instead, these methods rely on the accurate approximation of gradients to keep solution approximately conservative. This point links to later discussion of how other techniques differ.

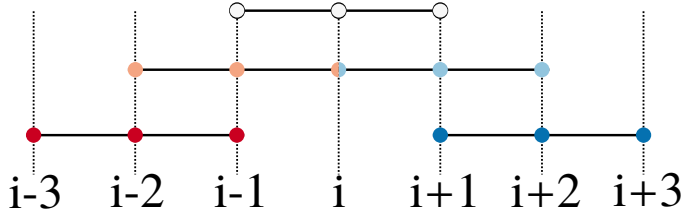


Fig. 1.1 An example stencil of a Compact FD scheme, showing the interconnection between node and how this can be leveraged to give a far wider stencil.

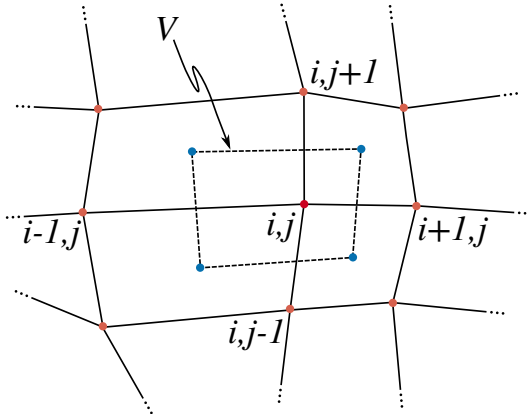


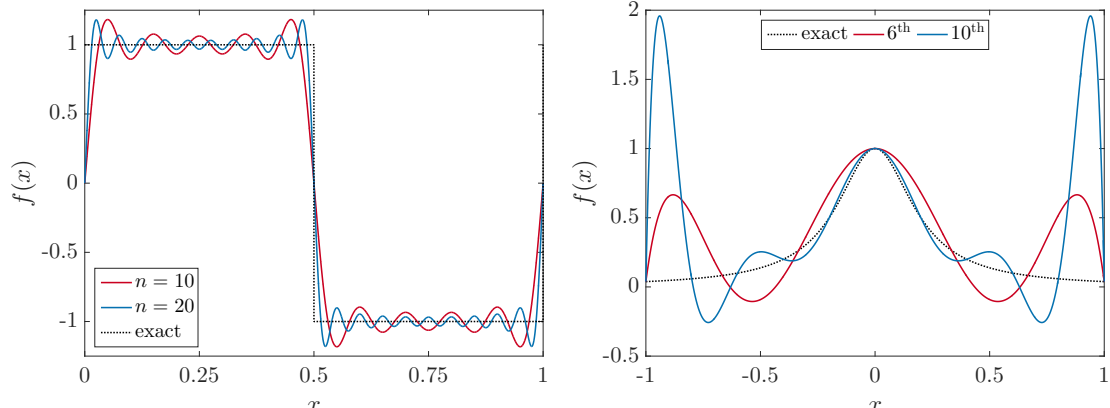
Fig. 1.2 Schematic of cell vertex finite volume grid, with dual generated via connecting centroids.

The final point for consideration on FD methods is their susceptibility to Gibbs' phenomenon, see Fig. 1.3. This is typical around flow features that inject high-frequency components into the flow field that are unable to be adequately resolved, such as shock waves. Finite difference methods are typically susceptible due to dispersion and low dissipation at high wavenumbers [77].

Finite Volume Approaches

The Finite Volume (FV) class of methods has been extremely popular for a considerable time and with good reason. If the derivation of the Navier-Stokes equations are considered, a common approach is to consider conservation of mass, momentum, and energy on a small control volume of fluid. FV approaches use this idea as the basis of the method. We begin by introducing the approach as taken for a second order accurate method, of which there are many techniques that have developed. We will focus on what is typically called a cell vertex centred method [120].

A typical set up of such a method is shown in Fig. 1.2. Here data is stored at the grid vertices (shown in red/orange) and a control volume is formed by linking the cell centroids. Simply put, to advance the solution at i, j in time, the flux through the control



(a) Gibbs' phenomenon when truncating the Fourier series of a square wave to n terms (b) Runge's phenomenon when polynomial fitting to Runge's function ($f(x) = 1/(1 + 25x^2)$)

Fig. 1.3 Examples of high frequency oscillation caused by discretisation approaches

volume, V , has to be calculated. This in turn is done by evaluating the flux on each edge. The method for evaluating the face flux is the primary component of an FV method and is where considerable effort has been focused, for example, the popular MUSCL scheme of Van Leer [122, 123]. However, we are concerned here with the development of high-order techniques so will go on to discuss how FV can be adapted to give higher order estimates of the face flux.

A key subset of high-order approaches we will focus on is the family of Essentially Non-Oscillatory schemes (ENO) [4, 48, 49]. These schemes are relatively representative of FV high order methods in their technique of achieving order, in that they use an extended stencil to form a polynomial that can be interpolated or integrated. Where the ENO family of schemes differs is in their approach to reducing spurious oscillation in the solution. As was mentioned earlier, around solution features that have large amounts of high wavenumber content there is a problem that fitting causes spurious oscillations. These spurious oscillations are caused by Gibb's/Runge's phenomena, manifesting itself in the numerical scheme as dispersion, i.e. changes to the speeds at which waves of different wavenumber propagate. Some examples of Gibb's/Runge's phenomena are shown in Fig. 1.3, and are ultimately due to sensitivity and ill-conditioning of the solution around large gradients. ENO attempts to counter this by downgrading the order of the solution in the presence of oscillations based on some criterion. This was taken further by Weighted ENO (WENO) [81, 107], where the various order solutions are blended together using a weighting function. We mention ENO and WENO as they marked an important change: polynomial fitting and extension of the technique to arbitrary orders.

Finite Volume methods have been found to be a useful and robust set of methods, consequently being used widely applied to problems beyond the research environment.

This is in part due to their simple nature and the fact that second-order methods lend themselves to unstructured grids and to a certain level of parallelism. However, as the approximation of face fluxes are moved to higher orders, the stencil increases. If then an unstructured method is also needed, forming stencils can become a complex task. For example, one extension of WENO to unstructured grids – that of Pringuey and Cant [94] – is highly complex. Furthermore, the extra communication and bespoke interpolation this requires can greatly reduce the efficiency of the method. This is also true of other high-order FV methodologies.

Element Based Approaches

Beyond FD and FV are a class of schemes that are commonly thought of as either Finite Element (FE) or Galerkin approaches. This class of schemes take the domain and subdivide it into elements. The FE approach [21], commonly called continuous Galerkin, uses these subdomains, a basis, and a weight function to find a global minimum to a variational form of the conservation equation that is to be solved. Weight functions form a necessary part of the method due to the inherent discretisation of numerical methods.

By contrast, Discontinuous Galerkin (DG), introduced by Reed and Hill in their seminal paper [97], aims to similarly find a global minimum to the variational form of a conservation equation. However, the difference is that DG only looks for a solution that is C^0 continuous. Since the inception of DG, the method has developed enormously and a comprehensive review can be found in Cockburn et al. [30]. The key development that these method introduced was localised polynomial fitting [40]. This removed the burden of large stencils common to other high-order approaches, although in some instances meant a large number of equations had to be solved due to the number of polynomial bases. As a consequence of the localised fitting, unstructured DG methods [12] can be implemented in ways that are more efficient than other high-order techniques.

1.3.2 Computational Considerations

Until now the discussion has largely been about numerical methods and their numerical characterisation. However, in all but the most trivial of cases, the method has to operate in hardware. This is the point at which the best numerical schemes can fail as there are four things that become important. These are the availability of FLOPs; memory availability; memory bandwidth; and memory latency. In early methods, such as FD, and to some extent continuing to the present time, the problems of computation were typically associated with FLOPs and memory availability. The solution to this was to increase the number of processors. However, the returns of this are diminishing, see Amdahl's

Law [7], due to most calculations having a serial element of computation at a fundamental level.

The development that has significantly changed scientific computing in the past decade has been the development and ubiquitous availability of multi-core CPUs and the utilisation of GPUs. Both of which have made more cores readily available for computing. Now GPUs are available with many thousands of single and double precision cores (see Nvidia's Volta architecture [90]) and CPUs are available with hundreds of threads (see Intel's Knights Landing architecture [110]). Hence, with careful crafting, a numerical method can be created with high levels of parallelism to utilise this hardware. Consequently, when designing a scheme, this has to be kept in mind. The end result is then that modern schemes can suffer from being memory bound, i.e insufficient memory bandwidth to feed the available FLOPs or slowing due to latency. In the case of Intel's KNL, latency can be a large problem with the onboard memory having very high bandwidth but at the cost of high latency. Therefore, to produce a numerical scheme that is computationally efficient, parallelism needs to be considered together with how memory can be kept contiguous and how the number of cache misses can be reduced.

This, then, is the current climate of high performance computing hardware, within which contemporary numerical methods in computational physics must reside.

1.3.3 Flux Reconstruction

The method under investigation in the current study is Energy-Stable Flux Reconstruction (shortened to FR) proposed by Huynh [55–57]. The energy stability of this method was proved initially by Vincent et al. [127] for linear advection via a modified Sobolev norm analysis. Further details of the use of Sobolev spaces in this context can be found in Kuskin and Lax [72, 78]. FR is related to the original Spectral Volume (SV) method proposed by Wang [132], which in turn drew on the work of Jiang and Shu [65] where nodal higher order polynomial fitting was used to accurately calculate values. Together with the work of Raviart and Thomas [96], a finite volume method was developed that used discrete elements with interface exchange to produce SV. As a result FR benefits from some of the same advantages as FE methods, primary the computational efficiency of elements coupled to high-order. This efficiency on large scale calculations was investigated by Vincent et al. [130] where it was found that FR could achieve 58% of peak LINPACK performance when run on a very large cluster.

Flux Reconstruction uses the same framework of finite elements with localised polynomials to reconstruct a high-order solution. To form a continuous solution an approximate Riemann solver, or similar technique, is used at the element interfaces to calculate a common value. Typical methods that have been applied to the first derivative component

of the calculation are those of Roe [100] or flux-vector splitting [79, 80, 111]. For the second order components of the calculation it has been typical to use methods such as BR1/BR2 [12, 14] or Local Discontinuous Galerkin (LDG) [32]. A paper of note to aid in the choice of Riemann solver is [95], which gives exhaustive detail of the pitfalls of various techniques. To propagate this information in a manner which preserves order, a correction function is used to apply small changes to the element interior points. Correction functions will be discussed further in a later section.

Successive extensions have been made to FR to allow for the handling of simplex geometries, such as by Williams et al. [137] that made use of triangle space and basis functions such as [39, 96]. Most recently the FR method has been adapted to ensure flow conservation [1–3], i.e that the scheme is conservative, which was previously not strictly the case.

Some recent further developments to FR, that are beyond the scope of this work, are Direct Flux Reconstruction (DFR) methods [101, 102]. These use interpolation together with thoughtful solution point placement to reduce the operation count of FR and may be of interest if they can be cast in such a way to give the same numerical character.

1.3.4 PDEs Characteristic of Industry

Advection Equations

The PDE to which FR was first applied was the advection equation [55], with the majority of analytical results being for linear advection, for example, Asthana et al. [8] and Vincent et al. [128]. The first major work in forming a more general approach to FR was, as has already been mentioned, that of Vincent et al. [127]. The generalised form was found as a result of imposing some assumptions on the stability analysis. The resulting stability analysis proved that for 1D linear advection the energy of the conserved variable is bounded and decreases with time, this is sufficient to say that the scheme is energy stable. If the underlying assumption made to find the generalised energy stable FR scheme is modified, as was done by Vincent et al. [129], then yet another, extended, range of stable correction functions can be found for linear advection. An extension of these stability analyses was performed by Sheshadri et al. [105], where the energy stability of quadrilaterals was explored. As a result of these efforts, there is now a large family of energy stable schemes that is broadly referred to as Flux Reconstruction.

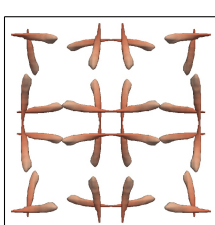
To broaden the knowledge about how FR transmits waves - and therefore arbitrary solutions - von Neumann analysis is a useful tool. This was first performed in the early paper by Huynh [55] in line with the earlier work on high-order methods by Lele [77] and Isaacson [58], with Vincent et al. [128] repeating this analysis for the previously discovered family of schemes. From this, they were able to show that the general form of

FR linked SD, Huynh, and DG methods. This work was two-fold, as it also explored the temporal stability of the fully discretised scheme, giving analytical CFL limits. Previously, Huynh [55] had only examined the semi-discrete form *i.e* exact temporal integration was used. From this spatio-temporal analysis correction functions were found that displayed super-convergence when temporal discretisation was carried out with a family of Runge-Kutta schemes. This property of super-convergence was found to be realised by DG methods by Cockburn et al. [31] when semi-discretised and therefore, what was found was a series of correction functions that could counter the dissipation and dispersion error of the temporal integration restoring the super-convergence characteristic of DG methods. The von Neumann analysis of linear advection was repeated by Asthana et al. [8] and yet another series of correction functions was found that gave minimal dispersion and dissipation errors. Moving to higher dimensionality problem Williams et al. [137] showed the beginnings of a 2D von Neumann analysis for linear advection. However, the scope of this investigation was severely limited as the main focus of the work was properties of FR on triangular elements, with solution point placement later optimised for advection on tetrahedra in the connected work by Witherden et al. [139]. It should be noted at this point that Huynh [55] proved for linear advection the stability of hypercube FR is not affected by solution point placement.

For industrially relevant problems, mesh quality is typically worse than for the idealised analytical problems that have up until now been considered, with typical domains being highly complex systems leveraging the unstructured nature of the scheme to mesh all manner of geometries. Some recent work [9] has begun to perform a more generalised von Neumann/Fourier analysis. With Mengaldo et al. [86] even purporting to have performed wavenumber free eigensolution analysis of DG for under-resolved LES. For example, they were focusing on the band on scheme performance were insufficient resolution causes more dramatic changes to the solution. Based on this there is still much to be found about the wave propagating behaviour in higher dimensions as well as the spatio-temporal stability on lower quality grids.

Diffusion Equations

Another important equation set to engineers is diffusion equations, which have parabolic behaviour. Flux Reconstruction of the diffusion equation was presented in Huynh [56] and was generalised and found to be energy stable in Williams and Jameson [137]. This analysis again used the modified Sobolev norm approach and found that diffusion terms add a stabilising effect proportional to the viscosity as expected. An extension was made to tetrahedral cells by Williams & Jameson [137]. An adapted von Neumann analysis can be performed on the linear advection-diffusion equation as was shown by



Watkins et al. [133]. A similar procedure was followed to fully discretise the scheme in order to find the CFL limits. The deficiency of this paper is that this was solely performed for nodal DG via FR, hence the scope of the insight gained was limited. Castonguay [23] did briefly show some results from von Neumann analysis however these are again narrow in scope. The more general von Neumann analysis of the linear diffusion and linear advection-diffusion in higher dimensions and on stretched grids is yet to be explored.

A more recent further development in the algorithms for solving fluid flows equations is hyperbolic diffusion [85, 88, 89]. This method aims to decrease the computational time of advection-diffusion equation by rewriting the governing equation such that only a first-order derivative is used, therefore transforming the diffusion equation from being a parabolic equation to hyperbolic. This is done by introducing another equation for each diffusion term and associating a diffusion timescale with each. The motivation for this in the present work is that, as will become clear once the numerical method is presented, when diffusion is incorporated within the FR scheme, a greater proportion of time is spent performing interface calculations. As the interface calculation cannot be vectorised the potential for parallelisation is not as great as the other steps in the algorithm. Hence, hyperbolic diffusion offers the possibility of optimisation, and if it can be incorporated into a full NSE solver, potential speed up.

A further advantage of hyperbolic diffusion is that when hyperbolised the diffusion equation is given a characteristic speed and direction of propagation. When applied to a parabolic equation, such as the diffusion of heat, this means that the solution has a front. This property that can be particularly useful when solving the Eikonal equation for wall distance, see Tucker et al. [121], although the Eikonal is already hyperbolic typical methods employ an adapted Hamilton-Jacobi form that contains diffusive terms. The advantage of hyperbolic diffusion being that the calculation can potentially be stopped once a sufficient wall distance is calculated, typically out to $y^+ = 60$ to 100.

1.3.5 Correction Functions

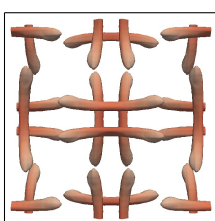
Underpinning the methodology of FR and CPR is a procedure in which the discontinuous local approximations of the solution have to be made globally continuous. It was through a generalisation of the procedure in which correction functions are calculated that unified stable FR schemes. As was described in the previous section, this was first performed by Vincent et al. [127], giving the family of FR that we will refer to as Original Stable FR (OSFR). Later, this family was extend using ideas from the spectral element community [129] giving rise to what we will call Extended Stable FR (ESFR).

These two works and subsequent investigations [6, 128, 130, 133, 136] have shown the importance of correction functions in defining the numerical characteristics of the

method. For example, by varying the correction function the CFL limit can be raised by $\approx 110\%$ compared to NDG methods. NDG methods give rise to super-convergence [5, 9, 31, 55, 138] and SD methods are somewhere between the two with slower convergence but higher CFL limits and more favourable dispersion and dissipation characteristics. This aims to show that the leverage of the correction functions can change the behaviour of the method through merely changing the entries of a matrix. Any development in this area is important in further unifying FR with other methods and could lead to the discovery of further performance improvements.

We leave the discussion of correction functions with a quote from Jameson's paper on the advances of using high-order methods in applied CFD [63]:

In the non-linear case, the FR schemes with appropriate correction polynomials are no longer exactly equivalent to the corresponding NDG and SD schemes. However, the FR methodology provides a rich framework for the design of high-order schemes of minimal complexity.



Chapter 2

Flux Reconstruction Methodology

2.1 Preliminaries

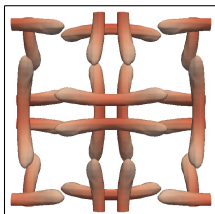
As has already been stated the Flux Reconstruction (FR) approach to be investigated is that of Huynh [55] and Vincent et al. [127]. An overview of the method is given here for the benefit of the reader. However, the exact implementation used follows that of Castonguay [23]. A cautionary note must be given that although the work of Castonguay [23] has many useful notes on efficient implementation there are also many typographical errors, and other peer reviewed sources should be consulted on implementation. Any of those already cited are of use, particularly Sheshadri et al. [106]. Over the next two sections, FR applied to the one dimensional linear advection equation and two dimensional second order PDEs on quadrilateral elements is presented.

Throughout the sections that follow domain subdivision, as is common to DG methods, will be utilised. Therefore this subdivision is presented here with the specifics of the domains to be subdivided given later where appropriate. If the domain of the calculation is Ω then the subdivision is:

$$\Omega = \bigcup_{n=1}^N \Omega_n \quad (2.1)$$

where $\Omega \in \mathbb{R}^d$, d is the dimensionality and N is the number of elements. The standardised sub-domain $\hat{\Omega}$ is used and will be called the computational space. In the case where the geometry is based on hypercubes, the computational space is taken as $\hat{\Omega} = [-1, 1]^d$. To transform from $\Omega_n \rightarrow \hat{\Omega}$ a Jacobian is defined as:

$$\mathbf{G}_n = \begin{bmatrix} \frac{\partial x_1}{\partial \xi_1} & \frac{\partial x_2}{\partial \xi_1} & \cdots & \frac{\partial x_d}{\partial \xi_1} \\ \frac{\partial x_1}{\partial \xi_2} & \frac{\partial x_2}{\partial \xi_2} & \cdots & \frac{\partial x_d}{\partial \xi_2} \\ \vdots & \vdots & \ddots & \vdots \\ \frac{\partial x_1}{\partial \xi_d} & \frac{\partial x_2}{\partial \xi_d} & \cdots & \frac{\partial x_d}{\partial \xi_d} \end{bmatrix} \quad \text{and} \quad J_n = |\mathbf{G}_n| \quad (2.2)$$



where x_i is the i^{th} spatial variable in the physical domain, Ω_n , and ξ_i is the i^{th} spatial variable in the computational domain, $\hat{\Omega}$. In lower dimension problems, the spatial variables will typically be notated as ξ , η , and ζ . Having set up the computational domain, for brevity, the computational gradient operator is defined as:

$$\hat{\nabla} = \begin{bmatrix} \frac{\partial}{\partial \xi_1} \\ \frac{\partial}{\partial \xi_2} \\ \vdots \end{bmatrix} \quad (2.3)$$

With these conventions in place the numerical method may now be defined.

2.2 One-Dimensional Approach for First-Order PDEs

We will begin by presenting the Flux Reconstruction (FR) methodology when applied to a first order conservative PDE. The precise manner in which we reconstruct the solution follows the work of Huynh [55] and Vincent et al. [127], where a more detailed view of the technique is presented. We set out to solve a 1D conservative equation of the form:

$$\frac{\partial u}{\partial t} + \frac{\partial f}{\partial x} = 0 \quad (2.4)$$

where u is the primitive and f is the flux variable. The aim of FR then is to take a polynomial approximation of the solution defined in each sub-domain, Ω_j , and form a continuous solution. Therefore, if we define a set of broken polynomials over the sub-domains we can then form a global solution as:

$$u^\delta = \bigcup_{n=1}^N u_n^\delta \approx u \quad \text{and} \quad f^\delta = \bigcup_{n=1}^N f_n^\delta \approx f. \quad (2.5)$$

Here we have defined u_j^δ and f_j^δ as being the approximate solution and flux in the j^{th} element. The work comes from ensuring that these represent a series of continuous polynomials. The stages in ensuring this are: first we transform Eq.(2.4) into reference domain:

$$\frac{\partial \hat{u}^\delta}{\partial t} + \frac{\partial \hat{f}^\delta}{\partial \xi} = 0 \quad (2.6)$$

defining

$$\hat{u}^\delta = J_n u^\delta \quad \text{and} \quad \hat{f}^\delta = J_n f^\delta \quad (2.7)$$

The next stage is then to actually form the polynomial for \hat{u}^δ in Eq.(2.7). To do this we define it as a sum over a basis:

$$\hat{u}^\delta = \sum_{i=0}^p \hat{u}_i^\delta(\xi) l_i(\xi) \quad (2.8)$$

where here we use the Lagrange basis defined as:

$$l_i = \prod_{\substack{j=0 \\ j \neq i}}^p \left(\frac{\xi - \xi_j}{\xi_i - \xi_j} \right). \quad (2.9)$$

Any basis could be used in place of l_i , however the advantage of the Lagrange basis is its natural application to nodal methods.

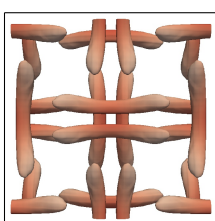
The third stage is to form a discontinuous flux polynomial in the reference domain – this is different from \hat{f}^δ , which is piecewise continuous. We will symbolise the discontinuous flux as $\hat{f}^{\delta D}$. The polynomial is then defined as:

$$\hat{f}^{\delta D} = \sum_{i=0}^p \hat{f}_i^{\delta D} l_i(\xi) \quad (2.10)$$

the advantage of this technique is that it is straightforward to calculate $\hat{f}_i^{\delta D}$ from \hat{u}^δ , and it is this that is the source of the inter-element discontinuities.

Step four begins the process of making a continuous flux polynomial. We initially interpolate the solution polynomial to the edges of the element as $\hat{u}_L^\delta = \hat{u}^\delta(-1)$ and $\hat{u}_R^\delta = \hat{u}^\delta(1)$. These interpolated values can then be used to calculate discontinuous interface values, $\hat{f}_L^{\delta D}$ and $\hat{f}_R^{\delta D}$. At every interface there are now pairs of collocated points that store the discontinuous flux on either side of the interface, e.g we have $\hat{f}_{j-1,R}^{\delta D}$ and $\hat{f}_{j,L}^{\delta D}$. Once the discontinuous collocated flux values are obtained they can then be used to calculate a common interface value for each pair of values. This can be done using many methods, however for hyperbolic equation sets it is often advantageous to use an upwinding methods via an appropriate approximate Riemann solver [114]. This is advantageous as the upwinding introduces diffusion that will act to stabilise the scheme, whereas if central differencing is used some smoothing/diffusion must be applied to ensure stability. For each element in 1D we then have a left and right common interface value, namely $\hat{f}_L^{\delta I}$ and $\hat{f}_R^{\delta I}$.

Step five is then the application of common interface value to build a correction to the discontinuous flux to form a continuous polynomial. At this stage we introduce the correction function, which is the means by which we propagate the common interface value into the element. In 1D we have a left and right correction function, corresponding



to the left and right element edge. The correction functions will be defined as $h_L(\xi)$ and $h_R(\xi)$ respectively, with the boundary conditions:

$$h_L(-1) = 1 \quad \text{and} \quad h_L(1) = 0; \quad (2.11)$$

$$h_R(-1) = 0 \quad \text{and} \quad h_R(1) = 1. \quad (2.12)$$

then forming the correction as:

$$\hat{f}^{\delta C} = (\hat{f}_L^{\delta I} - \hat{f}_L^{\delta D})h_L(\xi) + (\hat{f}_R^{\delta I} - \hat{f}_R^{\delta D})h_R(\xi) \quad (2.13)$$

Hence the continuous flux function is then:

$$\hat{f}^\delta = \hat{f}^{\delta D} + \hat{f}^{\delta C} = \hat{f}^{\delta D}(\xi) + (\hat{f}_L^{\delta I} - \hat{f}_L^{\delta D})h_L(\xi) + (\hat{f}_R^{\delta I} - \hat{f}_R^{\delta D})h_R(\xi) \quad (2.14)$$

at this stage we can discuss further the correction function and its order. Previously when defining $\hat{f}^{\delta D}$ because of the availability of data we could only fit an order p polynomial for $\hat{f}^{\delta D}$. However, at this stage we have the ability to introduce more information into our solution hence raising the order. Therefore, we take the order of h_L and h_R to be $p+1$ hence giving $\hat{f}^{\delta C}$ to be order $p+1$. This is perhaps a more philosophical view of the the order of the correction function, however later we will look at the how to define the correction function through a stability analysis, and see that only correction functions of order less than or equal to $p+1$ are stable.

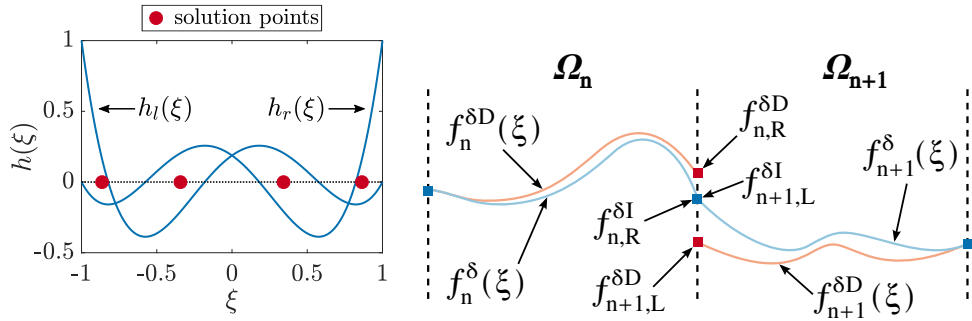
Finally, to calculate the continuous gradient of the flux we differentiate Eq.(2.14). First let us rewrite Eq.(2.14) to use the interpolation step of Eq.(2.10):

$$\hat{f}^\delta = \hat{f}^{\delta D} + \hat{f}^{\delta C} = \sum_{i=0}^p \hat{f}_i^{\delta D} l_i(\xi) + (\hat{f}_L^{\delta I} - \hat{f}_L^{\delta D})h_L(\xi) + (\hat{f}_R^{\delta I} - \hat{f}_R^{\delta D})h_R(\xi) \quad (2.15)$$

Upon differentiation this then becomes:

$$\frac{\partial \hat{f}^\delta}{\partial \xi} = \sum_{i=0}^p \hat{f}_i^{\delta D} \frac{dl_i(\xi)}{d\xi} + (\hat{f}_L^{\delta I} - \hat{f}_L^{\delta D}) \frac{dh_L(\xi)}{d\xi} + (\hat{f}_R^{\delta I} - \hat{f}_R^{\delta D}) \frac{dh_R(\xi)}{d\xi} \quad (2.16)$$

This is the last stage in the FR methodology and Eq.(2.16) can then be used in conjunction with a temporal integration method to advance the solution \hat{u}^δ in time. The simplest method for advancing Eq.(2.4) in time would be explicit temporal integration, commonly via explicit Runge-Kutta methods. Kennedy [67] gives a very comprehensive derivation and overview of explicit Runge-Kutta method when applied to the Navier-Stokes equation.



(a) Solution point layout for $p = 4$ in $\hat{\Omega}$, with corresponding left and right nodal DG correction functions.

(b) Schematic of flux polynomial correction, here only the interface between element n and $n + 1$ has been considered.

Fig. 2.1 Point layout in $\hat{\Omega}$ for $p = 4$ and example of flux correction.

2.3 Two-Dimensional Approach for Second-Order PDEs

Extension of the method to two dimensions is straightforward for quadrilateral elements, therefore the extension will be presented alongside an introduction to the procedure for second order PDEs. The method for generalised FR on second order PDEs is taken from Castonguay et al. [26] and Sheshadri et al. [106]. Here the second order PDE being solved is advection with linear diffusion, which can be written as:

$$\frac{\partial u}{\partial t} + \nabla \cdot \mathbf{F} = 0 \quad (2.17)$$

$$\mathbf{F} = \begin{bmatrix} f \\ g \end{bmatrix} = \begin{bmatrix} u - vq_x \\ u - vq_y \end{bmatrix} \quad (2.18)$$

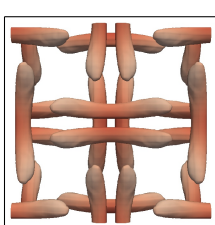
where v are the convective velocity and rate of diffusion respectively. q_x and q_y are then defined as:

$$q_x = \frac{\partial u}{\partial x}, \quad q_y = \frac{\partial u}{\partial y} \quad (2.19)$$

where $f = f(q_x, u)$ and $g = g(q_y, u)$.

The flux reconstruction process for an advection-diffusion problem will then differ from the purely advection case in that we have to also ensure that q_x and q_y are the gradient of a continuous solution. This is done using the same correction methodology as in Eq.(2.15):

$$\hat{u}^\delta = \hat{u}^{\delta D} + \sum_{i=0}^p \left[(\hat{u}_{L,i}^{\delta I} - \hat{u}_{L,i}^{\delta D})h_{L,i} + (\hat{u}_{R,i}^{\delta I} - \hat{u}_{R,i}^{\delta D})h_{R,i} + (\hat{u}_{T,i}^{\delta I} - \hat{u}_{T,i}^{\delta D})h_{T,i} + (\hat{u}_{B,i}^{\delta I} - \hat{u}_{B,i}^{\delta D})h_{B,i} \right] \quad (2.20)$$



where L, R, T and B subscripts are used to indicate the left, right, top and bottom interface values respectively. The common interface values, for example $u_{L,i}$, can simply be taken as the average across the interface, as the diffusion from the approximate Riemann solver is sufficient to prevent any instabilities here. The transformed values of q_x and q_y can simply be calculated then via differentiation of Eq.(2.20):

$$\hat{\nabla} \cdot \hat{u}^\delta = \begin{bmatrix} \hat{q}_x^\delta \\ \hat{q}_y^\delta \end{bmatrix} = \begin{bmatrix} \frac{\partial \hat{u}^{\delta D}}{\partial \xi} + \sum_{i=0}^p \left((\hat{u}_{L,i}^{\delta I} - \hat{u}_{L,i}^{\delta D}) \frac{\partial h_{L,i}}{\partial \xi} + (\hat{u}_{R,i}^{\delta I} - \hat{u}_{R,i}^{\delta D}) \frac{\partial h_{R,i}}{\partial \xi} \right) \\ \frac{\partial \hat{u}^{\delta D}}{\partial \eta} + \sum_{i=0}^p \left((\hat{u}_{T,i}^{\delta I} - \hat{u}_{T,i}^{\delta D}) \frac{\partial h_{T,i}}{\partial \eta} + (\hat{u}_{B,i}^{\delta I} - \hat{u}_{B,i}^{\delta D}) \frac{\partial h_{B,i}}{\partial \eta} \right) \end{bmatrix} \quad (2.21)$$

Once the transformed discontinuous gradient is calculated the discontinuous flux at the solution points can be calculated, and hence the discontinuous flux function can be formed as:

$$\hat{f}^{\delta D}(\xi, \eta) = \sum_{i=0}^{n_s} \hat{f}_i^{\delta D} l_i(\xi, \eta) \quad (2.22)$$

and in the case of a maximal order basis l_i then becomes the product of two 1D Lagrange polynomials.

The next stage is to extrapolate the solution to the flux points and calculate the inviscid and viscous interface fluxes, e.g. $\hat{f}_{L,i}^{\delta D_I}$ and $\hat{g}_{L,i}^{\delta D_V}$ for the left inviscid and viscous flux terms respectively. An appropriate method must then be used to calculate the the common interface value for the inviscid/hyperbolic and viscous/parabolic terms separately. The method for the inviscid/hyperbolic term was discussed in section 2.2. As for the viscous/parabolic term, methods such as BR1, BR2, LDG, could be used, with a more complete list of possibilities found in [26]. Finally the terms can be added together to find the common interface flux, e.g. $\hat{f}_{L,i}^{\delta I}$.

Now we can construct the divergence of the discontinuous flux and flux correction as:

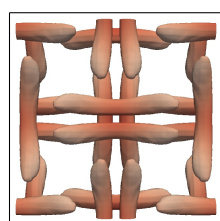
$$\hat{\nabla} \cdot \hat{\mathbf{F}}^{\delta D} = \sum_{i=0}^{n_s} \left(\hat{f}_i^{\delta D} \frac{\partial l_i(\xi, \eta)}{\partial \xi} + \hat{g}_i^{\delta D} \frac{\partial l_i(\xi, \eta)}{\partial \eta} \right) \quad (2.23)$$

$$\begin{aligned} \hat{\nabla} \cdot \hat{\mathbf{F}}^{\delta C} = & \sum_{i=0}^p \left((\hat{f}_{L,i}^{\delta I} - \hat{f}_{L,i}^{\delta D}) \frac{\partial h_{L,i}}{\partial \xi} + (\hat{f}_{R,i}^{\delta I} - \hat{f}_{R,i}^{\delta D}) \frac{\partial h_{R,i}}{\partial \xi} + \right. \\ & \left. (\hat{g}_{B,i}^{\delta I} - \hat{g}_{B,i}^{\delta D}) \frac{\partial h_{B,i}}{\partial \eta} + (\hat{g}_{T,i}^{\delta I} - \hat{g}_{T,i}^{\delta D}) \frac{\partial h_{T,i}}{\partial \eta} \right) \end{aligned} \quad (2.24)$$

With the discontinuous and corrected transformed flux gradient calculated the solution can then be moved forwards in time via:

$$\frac{\partial \hat{u}^\delta}{\partial t} = -\hat{\nabla} \cdot \hat{\mathbf{F}}^{\delta D} - \hat{\nabla} \cdot \hat{\mathbf{F}}^{\delta C} \quad (2.25)$$

To conclude, the key difference when considering an equation with second order derivatives is that the gradient has to be constructed from a continuous solution and hence FR must first be applied to u before being applied to f . The introduction of the last two sections is of course very terse, but does highlight the key features of FR, as well as the general paradigm being followed. For a more exhaustive explanation the reader is advised to consider the cited material. If any further detail is required beyond the overview given here, it will be presented in a later section as necessary.



Chapter 3

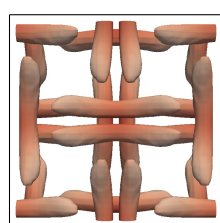
Implementation Aliasing

3.1 Introduction

Over the course of the last three decades Large Eddy Simulation (LES) has become increasingly used for the exploration of flow physics. Looking forward to how CFD will be used tomorrow, NASA CFD Vision 2030 [109] predicts that hybrid RANS/LES and wall-modelled LES will become increasingly used in aerospace design. With these methods likely to prevail until sufficient technological developments allow for wall-resolved LES to become feasible in the design process. The effect of this continuing shift from low fidelity modelling to high fidelity simulation is that the gap is bridged, in part, by adapting existing RANS tools for LES. For example, ANSYS Fluent began with its fluid calculation using RANS [131].

Soon into the development of numerical methods for computationally approximating solutions to PDEs, high order methods became of interest as they offered potentially lower mesh requirements and reduced error. For example, the development of Discontinuous-Galerkin by Reed and Hill [97] began a long journey of the method which has proved fruitful due to its super-convergence [31]. However, with the advent of LES, these high-order methods have become the focus of significant renewed research effort. Multiple tools capable of large high fidelity calculations becoming available, for example Nektar++[66], PyFR [138], etc.

In this process of adapting and developing methods, there seems to have been insufficient consideration of the effect implementation can have on the solution. Especially as methods become more sensitive via high order in the pursuit of higher fidelity. In particular, the investigation presented here is concerned with the form of the variables stored when solving a conservation equation. In the context of fluid mechanics, this commonly comes down to the question of whether the primitive or conservative variables are stored. To the knowledge of the authors, the only justification given for this choice



one way or the other comes from the Fluent's documentation where the arguments are 'it is a natural choice when solving incompressible flows' and 'to obtain more accurate velocity and temperature gradients in viscous fluxes, and pressure gradients in inviscid fluxes'. We, therefore, propose investigating this further, by answering the question: is the aliasing error introduced through the construction of the terms required in fluids dynamics sufficient for one method to be favourable? And then going explore the second point raised above, is there a significant difference in constructing the gradients required for viscous fluxes when different variables are stored?

A further point which we will explore is, whether the dogma that variables should be stored in double precision or if single precision is actually adequate. In most typical calculations the norm is to use double precision throughout, however, as the size of problems to be tackled grows so does the memory usage. Therefore, it would be beneficial to both reducing memory overhead and increasing computational speed if single precision were used. Further to this, some hardware, notably a large number of GPUs include only a small number of double precision arithmetic units and therefore the increase in computational speed can be as much as 32 times from the move from 32 to 64-bit precision. Some investigation into this question has been performed, notably by Homann et al. [53] on the DNS of incompressible homogeneous turbulence using a variable precision incompressible pseudo-spectral scheme. However they saw little to no difference when the precision was changed, but this may have been due to the explicit enforcement of incompressibility. Another investigation into precision was presented in the review paper by Bailey [10], that spanned several physics regimes. This investigation, however, was in the opposite direction, looking at the effect of 128-bit precision. It was found that it could be important and concluded that better support of adaptive precision should be made by software and hardware. Therefore, we wish to investigate if the same insensitivity to working precision is true for high order polynomial based methods, or like Bailey [10] it could, in fact, be important.

We therefore propose investigating this further, by answering the question: is the aliasing error introduced through the construction of the terms required in fluids dynamics sufficient for one method to be favourable? And then going explore the second point raised above, is there a significant difference in constructing the gradients required for viscous fluxes when different variables are stored? Lastly, then looking at the effect of floating point precision on turbulent flows when using polynomial based methods.

3.2 Discrete Polynomial Aliasing

In this section, we wish to introduce polynomial aliasing and how this error enters the solution of conservative equations. Let us start by studying a simple generalised conservative equation:

$$\frac{\partial u}{\partial t} + \frac{\partial f}{\partial x} = 0 \quad (3.1)$$

In this case, we will solve on the periodic domain $[-1, 1]$, for simplicity. Then the effect of solving this numerically is that we have some finite basis. Let us then set that the solution, u , may be constructed as some p^{th} order polynomial. In this case, we will use the Legendre basis:

$$u = \sum_{i=0}^p \tilde{u}_i \psi_i(x) \quad (3.2)$$

where ψ_m is the m^{th} order Legendre polynomial of the first kind. If the flux function is then $f = f(u^n)$ for $n \in \mathbb{N}$. Then for the flux we get:

$$f = \sum_{i=0}^{np} \tilde{f}_i \psi_i(x) \quad (3.3)$$

However, as previously stated, the functional space of the numerical solver is limited to be p^{th} order. To understand the error let us discretise Eq.(3.1) by using Eq.(3.2 & 3.3). We may then use the key result about Legendre polynomials, that simple truncation of the series gives the least squares projection of the polynomial. Therefore we may write:

$$\frac{\partial}{\partial t} \sum_{i=0}^p \tilde{u}_i \psi_i(x) = -\frac{\partial}{\partial x} \sum_{i=0}^p \tilde{f}_i \psi_i(x) \quad (3.4)$$

If we define the aliasing error, e_a , as:

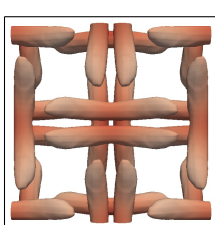
$$\frac{\partial}{\partial x} \sum_{i=0}^{np} \tilde{f}_i \psi_i = \frac{\partial}{\partial x} \sum_{i=0}^p \tilde{f}_i \psi_i + e_a \quad (3.5)$$

and then going on to define the differentiated polynomial coefficients as:

$$\frac{\partial}{\partial x} \sum_{i=0}^p \tilde{f}_i \psi_i = \frac{\partial}{\partial x} \sum_{i=0}^{p-1} \tilde{f}'_i \psi_i \quad (3.6)$$

Therefore :

$$\sum_{i=0}^{p-1} \tilde{f}'_i \psi_i(x) - \sum_{i=0}^{np-1} \tilde{f}'_i \psi_i(x) = - \sum_{i=p}^{np-1} \tilde{f}'_i \psi_i(x) = -e_a \quad (3.7)$$



The exact value of the coefficients \tilde{f} and \tilde{f}' are dependent on the numerical method and u , but we may write the energy as in the error term as:

$$\|e_a\|_{L_2}^2 = \int_{-1}^1 \left(\sum_{n=p}^{np-1} \tilde{f}_n' \psi_n(x) \right)^2 dx = \sum_{n=p}^{np-1} \frac{2(\tilde{f}_n')^2}{2n+1} \leq \frac{2}{2p+1} \|\tilde{f}'\|_\infty^2 \quad (3.8)$$

The aim of this has been to explain that in the context of a numerical method, the aliasing arises due to the inability of the method to resolve higher order terms. Furthermore, that the energy is removed as dissipation due to the sign of e_a .

This example demonstrates this, but it does not demonstrate the exact behaviour this paper is to investigate. Namely, the aliasing that occurs due to the way in which the variables are stored and used. In order to investigate this, we will modify the Burger's equation. First, we will introduce a key result in aliasing, first defining the interpolation remainder:

$$\mathcal{R}_p f = f - \mathcal{L}_p f \quad (3.9)$$

where \mathcal{L}_p is a p^{th} order linear *interpolation* operator. From Kress [71] it can then be stated that:

$$\mathcal{R}_p f(\xi) = \frac{f^{(p+1)}(\epsilon)}{(p+1)!} \prod_{i=0}^p (\xi - \xi_i) \quad (3.10)$$

where ξ_i are the interpolation points and ϵ is dependent on ξ . If we take the Burger's equation and now square the conserved variable such that we get the following:

$$\frac{\partial u^2}{\partial t} + \frac{\partial u^4}{\partial \xi} = 0 \quad (3.11)$$

this opens the opportunity for information to be stored in two ways comparable to methods used for Euler's equation. Namely, storing u or u^2 and forming the flux term by either: squaring u^2 or raising u to the power of four. This gives two possible flux polynomials when transformed into the computational domain:

$$\hat{u}^2(\xi) = \hat{f}_2 = \sum_{i=0}^{2p} \tilde{f}_{2,i} \psi_i \quad (3.12)$$

$$\hat{u}^4(\xi) = \hat{f}_4 = \sum_{i=0}^{4p} \tilde{f}_{4,i} \psi_i \quad (3.13)$$

To understand how errors may then enter the solution we wish to understand the scaling of the remainder of the flux interpolation to a finite polynomial space of order p . The

maximal norm can then be used to give an estimate as:

$$\|\mathcal{R}_p f\|_\infty \leq \frac{1}{(p+1)!} \|q_{p+1}\|_\infty \|f^{(p+1)}\|_\infty. \quad (3.14)$$

Here we define q_{p+1} as:

$$q_{p+1} = (\xi - \xi_0)(\xi - \xi_1) \dots (\xi - \xi_p) \quad (3.15)$$

with ξ_i being the points at which the value of f is stored. Taking the domain to be $[-1, 1]$ therefore $\|q_{p+1}\|_\infty \leq 2$. We now use Eq.(3.12 & 3.13) to refine the remainder estimates, which requires a bounding value of $\|f^{(p+1)}\|_\infty$. Firstly, it is known that the maximum absolute value of a Legendre polynomial is at $\xi = \pm 1$ and, due to the recursive definition of Legendre polynomials, the maximum value of the derivative is at $\xi = \pm 1$. If the value of a differentiated Legendre polynomial at ± 1 is:

$$\frac{d^m \psi_n(\pm 1)}{d\xi^m} = \frac{(\pm 1)^{n-m}(n+m)!}{2^n n!(n-m)!} \quad (3.16)$$

A consequence is that, for a given set of differentiated Legendre polynomials, $\{\psi'_n, \psi''_n, \dots, \psi_n^{(m)}\}$, the maximum value in this set is the edge value of the m^{th} derivative. Hence a bound can be placed on $\|f^{(p+1)}\|_\infty$ using Eq.(3.16) and the maximum Legendre mode coefficient as:

$$\|f_2^{(p+1)}\|_\infty \leq \left[\frac{2(3p+1)!}{2^{2p}(p)!(2p)!} \right] \max_{i \in \{0 \dots 2p\}} |\tilde{f}_{2,i}| \quad (3.17)$$

$$\|f_4^{(p+1)}\|_\infty \leq \left[\frac{2(5p+1)!}{2^{4p}(3p)!(4p)!} \right] \max_{i \in \{0 \dots 4p\}} |\tilde{f}_{4,i}| \quad (3.18)$$

Hence, the interpolation remainder may be bounded as:

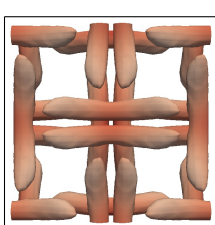
$$\|\mathcal{R}_p f_2\|_\infty \leq 4 \left[\frac{(3p+1)!}{2^{2p}(p)!(2p)!(p+1)!} \right] \max_{i \in \{0 \dots 2p\}} |\tilde{f}_{2,i}| \quad (3.19)$$

$$\|\mathcal{R}_p f_4\|_\infty \leq 4 \left[\frac{(5p+1)!}{2^{4p}(3p)!(4p)!(p+1)!} \right] \max_{i \in \{0 \dots 4p\}} |\tilde{f}_{4,i}| \quad (3.20)$$

It can be proved by induction that:

$$\frac{(3p+1)!}{2^{2p}(p)!(2p)!} \leq \frac{(5p+1)!}{2^{4p}(3p)!(4p)!}, \quad \forall p \in \mathbb{N} \quad (3.21)$$

From this, there are two conclusions that can be drawn. Firstly, the interpolation remainder of f_4 will always be bigger than f_2 . Secondly, the difference between the remainders will



grow factorially fast as the order is increased. Therefore, higher order methods will be more greatly affected by this mechanism of error introduction.

If we now consider FR in 1D for a conservative equation we get:

$$\frac{\partial \hat{u}^\delta}{\partial t} + \frac{\partial \hat{f}^\delta}{\partial \xi} = 0 \quad (3.22)$$

$$\frac{\partial \hat{f}^\delta}{\partial \xi} = \frac{\partial \hat{f}^{\delta D}}{\partial \xi} + (\hat{f}_L^{\delta I} - \hat{f}_L^{\delta D}) \frac{dh_L}{d\xi} + (\hat{f}_R^{\delta I} - \hat{f}_R^{\delta D}) \frac{dh_R}{d\xi}. \quad (3.23)$$

Therefore, we are concerned with two extensions of the remainder derived earlier: the remainder of the interpolation interpolated and the error of the interpolation to the left and right interfaces. To calculate this let us write:

$$\mathcal{R}'_p f = \frac{df}{dx} - \frac{d}{dx} \mathcal{L}_p f = \frac{d}{dx} \mathcal{R}_p f \quad (3.24)$$

Hence we can differentiate the result of Kress [71]:

$$\mathcal{R}'_p f(\xi) = \frac{f^{(p+1)}(\epsilon)}{(p+1)!} \frac{d}{d\xi} \prod_{i=0}^p (\xi - \xi_i), \quad \xi \in [-1, 1] \quad (3.25)$$

where $\epsilon \in [-1, 1]$. Finally we can write:

$$\|\mathcal{R}'_p f\|_\infty = \frac{p}{(p+1)!} \max_{i \in \{0..p\}} (\|q_p^i\|_\infty) \|f^{(p+1)}\|_\infty \quad (3.26)$$

defining q_p^i as:

$$q_p^i = \prod_{j=0, j \neq i}^p (\xi - \xi_j) \quad (3.27)$$

If we then apply the results of Eq.(3.19 & 3.20), it is demonstrated that the primary difference in the gradient remainder is a factor of p . If we then consider the more straight forward case of the remainder from interface interpolation, *i.e.* $\mathcal{R}_p f(\pm 1)$.

$$\mathcal{R}_p f(\pm 1) = \frac{f^{(p+1)}(\epsilon)}{(p+1)!} \prod_{i=0}^p (\pm 1 - \xi_i) \quad (3.28)$$

We will not consider the infinity norm in this case, as Eq.(3.28) gives sufficient details. The primary feature of note is that the behaviour of this remainder is primarily influenced by the interpolation point locations. For example, if $\xi_0 = -1$ and $\xi_p = 1$, as in a Gauss-Lobatto quadrature the aliasing error introduced through this mechanism would be zero. However, for other reasons explored by Castonguay [24] this is problematic in higher dimensions. By comparing the remainder due to differentiation and interface interpolation,

it can be seen that the differentiation gives a remainder that is approximately p times bigger. This indicates that the error that will dominate is due to the differentiation of polynomial experiencing aliasing.

3.3 Primitive and Conserved Variables

3.3.1 Euler's Equation

We will begin by considering the 1D Euler's equation in the conservative form.

$$\frac{\partial \mathbf{Q}}{\partial t} + \frac{\partial \mathbf{f}(\mathbf{Q})}{\partial x} = 0 \quad (3.29)$$

for

$$\mathbf{Q} = \begin{bmatrix} \rho \\ \rho u \\ E \end{bmatrix}, \quad \text{and} \quad \mathbf{f}(\mathbf{Q}) = \begin{bmatrix} \rho u \\ \rho u^2 + p \\ u(E + p) \end{bmatrix}. \quad (3.30)$$

The concern of this paper is what information should we store, while still solving this equation.

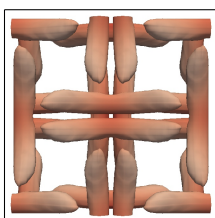
Conserved Variable Computation

In an implementation where the conserved variables are not stored directly, if the conserved form of Euler's equation is to be solved, then the conserved variables must be computed at some stage.

$$\mathbf{Q}_p \rightarrow \mathbf{Q}_c \quad (3.31)$$

$$\begin{bmatrix} \rho \\ u \\ p \end{bmatrix} \rightarrow \begin{bmatrix} \rho \\ \rho u \\ \frac{p}{\gamma-1} + \frac{1}{2}\rho(u^2) \end{bmatrix} = O \begin{bmatrix} \xi^p \\ \xi^{2p} \\ \xi^{3p} \end{bmatrix} \quad (3.32)$$

This transformation is shown in Eq.(3.31). It should be clear that if \mathbf{Q}_p is represented by a polynomial of order p , then the terms ρu , ρv , and ρw will be polynomials of order $2p$, while $u(E + p)$ will be of order $3p$. If the order of the scheme is greater than $3p$ this poses no issue. However, depending on how \mathbf{Q}_c is used this could pose a problem.



Inviscid Flux Computation

In most implementations seen by the authors, when the primitives are stored they are also subsequently used to form the flux, as opposed to using \mathbf{Q}_c . Therefore, the order of the flux formed from the primitives is:

$$\mathbf{Q}_p \rightarrow \mathbf{f} \quad (3.33)$$

$$\begin{bmatrix} \rho \\ u \\ p \end{bmatrix} \rightarrow \begin{bmatrix} \rho u \\ \rho u^2 + p \\ u(\frac{\gamma p}{\gamma-1} + \frac{1}{2}\rho(u^2)) \end{bmatrix} = O\begin{bmatrix} \xi^{2p} \\ \xi^{3p} \\ \xi^{4p} \end{bmatrix} \quad (3.34)$$

If instead the conserved variables are used we obtain:

$$\mathbf{Q}_c \rightarrow \mathbf{f} \quad (3.35)$$

$$\begin{bmatrix} \rho \\ \rho u \\ E \end{bmatrix} \rightarrow \begin{bmatrix} (\rho u) \\ \frac{(\rho u)^2}{\rho} + (\gamma - 1)\left(E - \frac{1}{2}\frac{(\rho u)^2}{\rho}\right) \\ \frac{(\rho u)}{\rho}\left(\gamma E - \frac{1}{2}(\gamma - 1)\frac{(\rho u)^2}{\rho}\right) \end{bmatrix} = O\begin{bmatrix} \xi^p \\ \xi^{2p}/\xi^p \\ \xi^{3p}/\xi^{2p} \end{bmatrix} \quad (3.36)$$

Here we have been somewhat careless with notation, here we intend $O(\xi^{2p}/\xi^p)$ to mean a $2p^{\text{th}}$ order polynomial divided by a p^{th} order polynomial. If the polynomial $1/O(\xi^p)$ is then expanded about zero to form a series of monomials, the series is $O(\xi^\infty)$. From this, we can see that in Eq.(3.35) we have avoided the ξ^{4p} term, but at the expense of dividing by ρ . This raises the question as to whether this formulation is more accurate, specifically, is the convergence of the $1/\rho$ series sufficiently fast to reduce aliasing? Importantly though, this method avoids a whole mechanism of the aliasing, introduced through the conversion in Eq.(3.31).

Another option that will be explored is storing the conserved variables but with energy substituted for pressure, \mathbf{Q}_{c+p} . The reason being that in industrial codes pressure is used frequently and this option would reduce the work involved in converting an implementation. Hence, the conversion from \mathbf{Q}_{c+p} to the flux, \mathbf{f} , is:

$$\mathbf{Q}_{c+p} \rightarrow \mathbf{f} \quad (3.37)$$

$$\begin{bmatrix} \rho \\ \rho u \\ p \end{bmatrix} \rightarrow \begin{bmatrix} (\rho u) \\ \frac{(\rho u)^2}{\rho} + p \\ \frac{(\rho u)}{\rho}\left(\frac{\gamma p}{\gamma-1} + \frac{1}{2}\frac{(\rho u)^2}{\rho}\right) \end{bmatrix} = O\begin{bmatrix} \xi^p \\ \xi^{2p}/\xi^p \\ \xi^{3p}/\xi^{2p} \end{bmatrix} \quad (3.38)$$

This method will also require a conversion step to retrieve the conserved variables if Eq.(3.29 & 3.30) are to be solved. This will then introduce aliasing of order:

$$\mathbf{Q}_{c+p} \rightarrow \mathbf{Q}_c \quad (3.39)$$

$$\begin{bmatrix} \rho \\ \rho u \\ p \end{bmatrix} \rightarrow \begin{bmatrix} (\rho) \\ (\rho u) \\ \frac{p}{\gamma-1} + \frac{1}{2} \frac{(\rho u)^2}{\rho} \end{bmatrix} = O \begin{bmatrix} \xi^p \\ \xi^p \\ \xi^{2p}/\xi^p \end{bmatrix} \quad (3.40)$$

This method has the potential to reduce the aliasing in forming the conserved variables and flux, as there is no longer the ξ^{4p} that is present in Eq.(3.33). However, this is again dependent on the nature of $1/\rho$.

3.3.2 Navier-Stoke's Equation

To confront more complex problems of fluid dynamical relevance, it is essential to consider the Navier-Stokes equation, written in for 3D in the conservative form as:

$$\frac{\partial \mathbf{Q}}{\partial t} + \nabla \cdot \mathbf{F}(\mathbf{Q}, \nabla \mathbf{Q}) = 0 \quad (3.41)$$

where

$$\nabla \cdot \mathbf{F} = (\mathbf{f}^{\text{inv}} - \mathbf{f}^{\text{vis}})_x + (\mathbf{g}^{\text{inv}} - \mathbf{g}^{\text{vis}})_y + (\mathbf{h}^{\text{inv}} - \mathbf{h}^{\text{vis}})_z \quad (3.42)$$

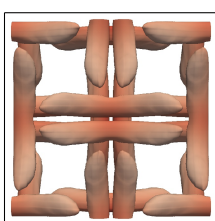
If we take the bulk viscosity, μ_b , to be zero, then \mathbf{f}^{vis} can be defined as:

$$\mu \begin{bmatrix} 0 \\ \tau_{xx} \\ \tau_{xy} \\ \tau_{xz} \\ u\tau_{xx} + v\tau_{xy} + w\tau_{xz} + \frac{\kappa}{\mu} T_x \end{bmatrix} = \mu \begin{bmatrix} 0 \\ \frac{4}{3}u_x - \frac{2}{3}(v_y + w_z) \\ u_y + v_x \\ w_x + u_z \\ u(\frac{4}{3}u_x - \frac{2}{3}(v_y + w_z)) + v(u_y + v_x) + w(w_x + u_z) + \frac{\kappa}{\mu} T_x \end{bmatrix} \quad (3.43)$$

with \mathbf{g}^{vis} and \mathbf{h}^{vis} similarly defined.

The importance of considering this equation is that, due to phenomena such as the energy cascade, in a method which does not suffer from implementation aliasing, aliasing will arise in LES due to the partial resolution of vortical motions. Hence, for turbulent flows, any difference is likely to be more marked as implementation aliasing amplifies the numerical aliasing.

Clearly for the case when primitive variables are stored, the gradients of the primitive can be directly calculated and used to form the viscous flux. However, when the conserved variables are stored there are two options available to form the gradients needed here:



convert the conserved variables to the primitives and calculate the gradients needed directly;

$$\begin{bmatrix} \rho \\ \rho u \\ \rho v \\ \rho w \\ E \end{bmatrix} \rightarrow \begin{bmatrix} \rho \\ u \\ v \\ w \\ p \end{bmatrix} \rightarrow \begin{bmatrix} \rho_x & \dots \\ u_x & \dots \\ v_x & \dots \\ w_x & \dots \\ \frac{c_v}{\gamma-1}(\rho^{-1}p_x - \rho^{-2}p\rho_x) & \dots \end{bmatrix}; \quad (3.44)$$

Or calculate the gradient of the conserved variables and use the product rule to convert them to what is needed,

$$\begin{bmatrix} \rho_x & \rho_y & \rho_z \\ (\rho u)_x & (\rho u)_y & (\rho u)_z \\ (\rho v)_x & (\rho v)_y & (\rho v)_z \\ (\rho w)_x & (\rho w)_y & (\rho w)_z \\ E_x & E_y & E_z \end{bmatrix} \rightarrow \begin{bmatrix} \rho_x & \rho_y & \rho_z \\ u_x & u_y & u_z \\ v_x & v_y & v_z \\ w_x & w_y & w_z \\ T_x & T_y & T_z \end{bmatrix}. \quad (3.45)$$

These two options can be simplified as:

$$\mathbf{Q}_c \rightarrow \mathbf{Q}_p \rightarrow \nabla \mathbf{Q}_p \quad (3.46)$$

$$\mathbf{Q}_c \rightarrow \nabla \mathbf{Q}_c \rightarrow \nabla \mathbf{Q}_p \quad (3.47)$$

where $\nabla \mathbf{Q}$ is the gradient of \mathbf{Q} . Here the final row of $\nabla \mathbf{Q}$ is the gradient of temperature, ∇T , for convenience in the calculation of the viscous flux.

The method for calculating the required gradients from the product rule applied to the conserved variable gradient formulation is:

$$\frac{1}{\rho} \begin{bmatrix} \rho \rho_x & \dots \\ ((\rho u)_x - \rho^{-1}(\rho u)\rho_x) & \dots \\ ((\rho v)_x - \rho^{-1}(\rho v)\rho_x) & \dots \\ ((\rho w)_x - \rho^{-1}(\rho w)\rho_x) & \dots \\ (E_x - \rho^{-1}E\rho_x) - ((\rho u)u_x + (\rho v)v_x + (\rho w)w_x) & \dots \end{bmatrix} = \begin{bmatrix} \rho_x & \rho_y & \rho_z \\ u_x & u_y & u_z \\ v_x & v_y & v_z \\ w_x & w_y & w_z \\ T_x & T_y & T_z \end{bmatrix} \quad (3.48)$$

The polynomial order of this step are then:

$$\frac{1}{\rho} \begin{bmatrix} \rho\rho_x \\ ((\rho u)_x - \rho^{-1}(\rho u)\rho_x) \\ ((\rho v)_x - \rho^{-1}(\rho v)\rho_x) \\ ((\rho w)_x - \rho^{-1}(\rho w)\rho_x) \\ (E_x - \rho^{-1}E\rho_x) - ((\rho u)u_x + (\rho v)v_x + (\rho w)w_x) \end{bmatrix} = O \begin{bmatrix} \xi^{p-1}(\eta\zeta)^p \\ \xi^{p-1}(\eta\zeta)^p / (\xi\eta\zeta)^p + \xi^{2p-1}(\eta\zeta)^{2p} / (\xi\eta\zeta)^{2p} + \xi^{2p-1}(\eta\zeta)^{2p} / (\xi\eta\zeta)^p \end{bmatrix} \quad (3.49)$$

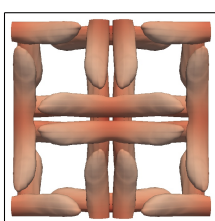
Again, it should be clear that the momentum and energy (rows 2-5) terms experience the most aliasing, although it is not clear of the effect that the division will have on aliasing. However, it is likely that the decay rate of the infinite quotient series will be fast in most cases.

The methods of data storage that will be investigated for the Navier-Stoke's equations and Euler's equations (where applicable) can the be summerised as, storing then:

- (A) Primitive variables
- Conserved variables, with the gradients for the Navier-Stokes equation calculated from the:
 - (B) conserved variables converted to primitive variables
 - (C) product rule applied to the gradient of the conserved variables
- (D) Conserved variables, but with pressure instead of energy

where the letters in brackets are shorthand identifiers that will be used in subsequent investigations.

At this point, we wish to link the ideas presented in section 3.2 with the methods of this section. It should be clear that in order for this form of aliasing error to be incorporated into the solution, then at some stage interpolation or polynomial fitting has to be used within the calculation. For FR, this comes when the gradient is calculated or the edge points are interpolated from the points inside the element. However, if only the nodal values are used, as is the case in second-order Finite Volume (FV) methods, then there is no mechanism by which this form of aliasing can affect the solution. Take the



example of converting primitive variables to conservative variables, and back again:

$$\mathbf{Q}_p \rightarrow \mathbf{Q}_c \rightarrow \mathbf{Q}'_p. \quad (3.50)$$

It should be apparent that beyond rounding error introduced, $\mathbf{Q}_p = \mathbf{Q}'_p$. Therefore, the means of variable storage will not affect FV but will affect any method that in some way interpolates or fits a polynomial.

3.4 Isentropic Convecting Vortex

To evaluate the impact of the changes suggested in section 3.3 we will begin by studying the effect on the error and total kinetic energy on the Isentropic convecting vortex (ICV). The ICV is of interest as it is an analytical solution to Euler's equations and hence allows for the error at a given time to be calculated. The problem that we are confronted with when using high order, the ICV, and a periodic domain, is the solution is only guaranteed to be C^0 continuous. This can be understood by considering the initial condition:

$$\rho = \left(1 - \frac{(\gamma-1)\beta^2}{8\gamma\pi^2} \exp(1-r^2)\right)^{\frac{1}{\gamma-1}} \quad (3.51)$$

$$u = u_0 + \frac{\beta}{2\pi} (y_0 - y) \exp\left(\frac{1-r^2}{2}\right) \quad (3.52)$$

$$v = v_0 + \frac{\beta}{2\pi} (x - x_0) \exp\left(\frac{1-r^2}{2}\right) \quad (3.53)$$

$$w = 0 \quad (3.54)$$

$$p = \left(1 - \frac{(\gamma-1)\beta^2}{8\gamma\pi^2} \exp(1-r^2)\right)^{\frac{\gamma}{\gamma-1}} \quad (3.55)$$

$$r^2 = (x - x_0)^2 + (y - y_0)^2 \quad (3.56)$$

where u_0 and v_0 are the advective velocities and β is the vortex strength (typically $\beta = 5$ is used). Hence, it can be seen that as the distance r is increased the vortex slowly decays and on a finite domain, this will lead to discontinuities in the gradient. This is a point that will be of importance later when reviewing results.

The metrics that we will use to review the accuracy are the point averaged absolute error in the density:

$$e(t) = \frac{1}{N_p} \sum_{i=1}^{N_p} |\rho_i - \rho(\mathbf{x}_i, t)|_2 \quad (3.57)$$

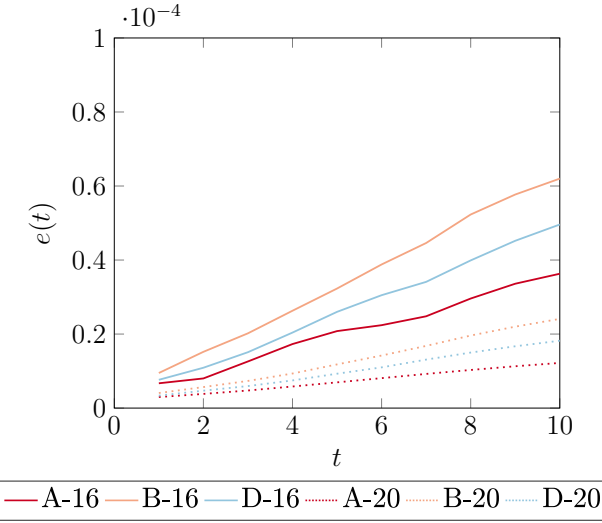


Fig. 3.1 Variation of error in ICV density with time for FR, $p = 4$, using methods A, B and D on $16 \times 16 \times 2$ and $20 \times 20 \times 2$ element grids.

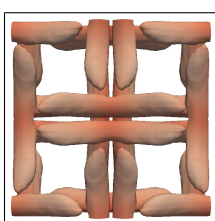
and the total kinetic energy:

$$E_k(t) = \frac{1}{2|\Omega|} \int_{\Omega} \rho \mathbf{V} \cdot \mathbf{V} d\mathbf{x} \quad (3.58)$$

where $|\Omega|$ is the domain volume.

We begin by investigating the effect of storing the primitive variables (A), conservative variables (B), and conservative variables with energy substituted for pressure (D) on the error. This is shown in Fig. 3.1. Clearly, method A has the lowest levels of error followed by D then B and this ordering does not change as the grid is refined. This results may be thought to be contrary to the expected outcome. However, to understand what is going on let us now consider how the kinetic energy changes with time.

Figure 3.2 shows how the kinetic energy in the domain changes with time. For both grid resolutions, the rate of kinetic energy dissipation of A is higher than B and D, while B and D are very similar. B and D show far less dissipation with the dissipation of method B being less than D in the higher resolution case, Fig. 3.2b. The importance of this is that, as was stated earlier, the ICV initial condition is only formally C^0 continuous. Therefore, the lower dissipation that methods B and D exhibit leads to the errors introduced via the discontinuities in the gradient not being as damped as in the case of A. Hence, the error grows faster while also showing less dissipation. Ultimately, it looks as though methods B and D can aid in the reduction of dissipation via aliasing, although this has some associated issues.



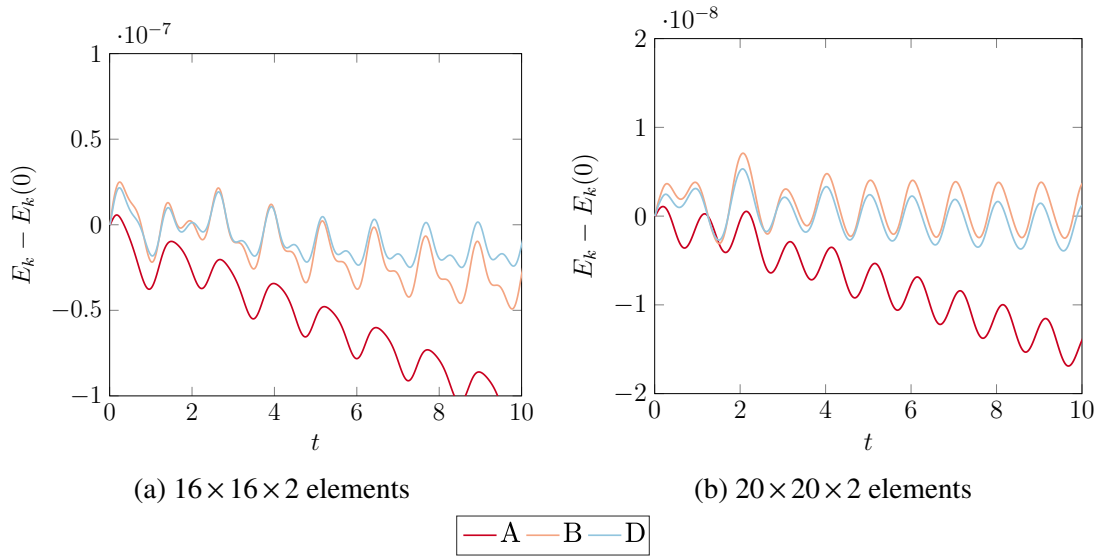


Fig. 3.2 Variation in total kinetic energy of the ICV, FR $p = 4$, for two grid resolutions. using methods A, B, and D.

3.5 Taylor-Green Vortex

The final investigation to be considered is the application of the various forms of stored variable to the full Navier-Stokes equation for a flow with turbulence. The flow of choice for this is the canonical Taylor-Green vortex [113, 18], where the exact flow field used is defined in [36, 27, 108]. This case is chosen as not only is it a case for the Navier-Stoke equation, but it exhibits transition from an Inviscid regime to a fully turbulent flow, via the mechanism of vortex stretching and shearing. This is key as not only is it more representative of real engineering flows, but transition will to turbulence will introduce the energy cascade to the flow and hence induce aliasing. We will go onto use this particular flow throughout this work and therefore some time will be devoted here to an explanation of its set up and behaviour.

The initial condition is taken to be:

$$u = U_0 \sin\left(\frac{x}{L}\right) \cos\left(\frac{y}{L}\right) \cos\left(\frac{z}{L}\right) \quad (3.59)$$

$$v = -U_0 \cos\left(\frac{x}{L}\right) \sin\left(\frac{y}{L}\right) \cos\left(\frac{z}{L}\right) \quad (3.60)$$

$$w = 0 \quad (3.61)$$

$$p = p_0 + \frac{\rho_0 U_0^2}{16} \left(\cos\left(\frac{2x}{L}\right) + \cos\left(\frac{2y}{L}\right) \right) \left(\cos\left(\frac{2z}{L}\right) + 2 \right) \quad (3.62)$$

$$\rho = \frac{p}{RT_0} \quad (3.63)$$

Where we define the case by the non-dimensional parameters as:

$$R_e = \frac{\rho_0 U_0 L}{\mu}, \quad P_r = 0.71 = \frac{\mu \gamma R}{\kappa(\gamma - 1)}, \quad M_a = \frac{U_0}{\sqrt{\gamma R T_0}} \quad (3.64)$$

with the free variable set as:

$$U_0 = 1, \quad \rho_0 = 1, \quad p_0 = 100, \quad R = 1, \quad \gamma = 1.4, \quad L = 1 \quad (3.65)$$

this is then solved on a domain $\Omega \in [-\pi, \pi]^3$ with periodic boundary conditions. Therefore, by varying R_e and M_a a series of different flow regimes can be explored, however first and foremost this case intended as an incompressible case. Hence, if we wish to explore that, it is typical to use a Mach number, M_a , of approximately 0.08. To give an appreciation of the flow field we have plotted iso-surfaces of q-criterion through time for $q = 0.5$, $R_e = 1600$ and $M_a = 0.08$ in the right corner as a flip-book. This shows the rapid decay of the vortex cores then the build up of vorticity through shear and then the transition to turbulence. If the simulation is continued, it is known that for $R_e \approx 500$ the turbulence exhibited is isotropic [18].

The metrics that we will use to study the behaviour of the numerical method applied to the TGV are rate kinetic energy dissipation and enstrophy dissipation:

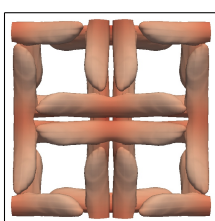
$$\epsilon_1 = -\frac{dE_k}{dt} = -\frac{d}{dt} \left(\frac{1}{2\rho_0 U_0^2 |\Omega|} \int_{\Omega} \rho \mathbf{V} \cdot \nabla \mathbf{V} d\mathbf{x} \right) \quad (3.66)$$

$$\epsilon_2 = \frac{\mu}{\rho_0^2 U_0^2 |\Omega|} \int_{\Omega} \rho (\boldsymbol{\omega} \cdot \boldsymbol{\omega}) d\mathbf{x} \quad (3.67)$$

where $\boldsymbol{\omega}$ is the vector is vorticity, μ is the shear viscosity, and where ϵ_1 & ϵ_2 have been normalised.

Aliasing is the main focus of this chapter, as such, we want to investigate if the different method of variable storage impacts the accuracy of the solution. As a result there two things that we will vary, first of which the Reynolds number. We proposed investigating $R_e = 400, 1600, 3000$, with reference DNS data (ref) available from [18]. This is because it will trigger a variety of different physics, as will be discussed later. The second variable we propose changing is the Mach number, where we will test the values $M_a = 0.08, 0.3$. The effect of compressibility on the TGV was investigated by [93] at various Mach numbers between 0.5 and 2, with 0.5 not being found to exhibit shocklets. Therefore, testing at $M_a = 0.3$ will test the introduction of aliasing due to larger spatial variations in ρ , but without triggering issues relating to shock capturing.

For the majority of the investigation, a 3D Navier-Stokes FR scheme will be used. The grid topology used will be hexahedral, constructed using a tensor product of construction



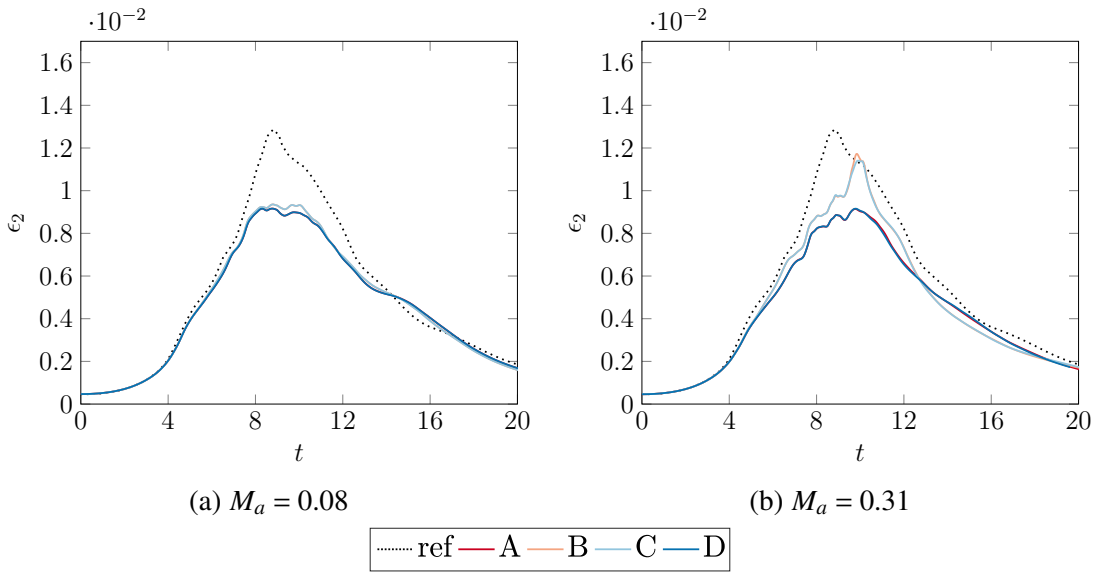


Fig. 3.3 Enstrophy of the Taylor-Green Vortex with $R_e = 1600$, $p = 4$ and 80^3 degrees of freedom for storage methods A-D.

of the 1D FR scheme. More details on this construction of FR can be found in [138, 24, 137] include the extension to diffusion equations. The method of calculating the inviscid common interface flux chosen is Rusanov flux with Davis wave speeds [103, 35]. The viscous common interface flux is found using Bassi and Rebays' BR1 scheme [12, 13]. The aim of this paper is not to explore the effect of FR correction function, but aliasing. Because of this, throughout we will use an FR correction function that recovers Nodal DG [55, 50].

Let us first consider the TGV case when $R_e = 1600$ at Mach numbers 0.08 and 0.31. We will look to compare the four methods presented in section 3.3 for FR with $p = 4$ on a mesh with 80^3 degrees of freedom, the results of which are shown in Fig. 3.3. It is seen that when $M_a = 0.08$, Fig. 3.3a, there is a small improvement when storing data as conserved variables over primitive variables. The results of the conservative variables with pressure instead of energy can be seen to be almost identical to the primitive variable results. It can also be noted that the largest difference is seen around the time of peak dissipation and not in the region $4 < t < 7$. This seems to indicate that the effect of changing the method of variable storage is to reduce the numerical/aliasing based dissipation at the smallest scales. It is apparent that it does not introduce extra sources of dispersion which would cause over dissipation around $4 < t < 7$ when small scales begin to enter the flow.

Moving onto the case when $M_a = 0.31$, the high Mach number will introduce larger spatial variation in the density as the flow becomes more compressible. This should increase the effect of aliasing error on the solution. The enstrophy is displayed in Fig. 3.3b and clearly shows a far larger change between the full conservative and the

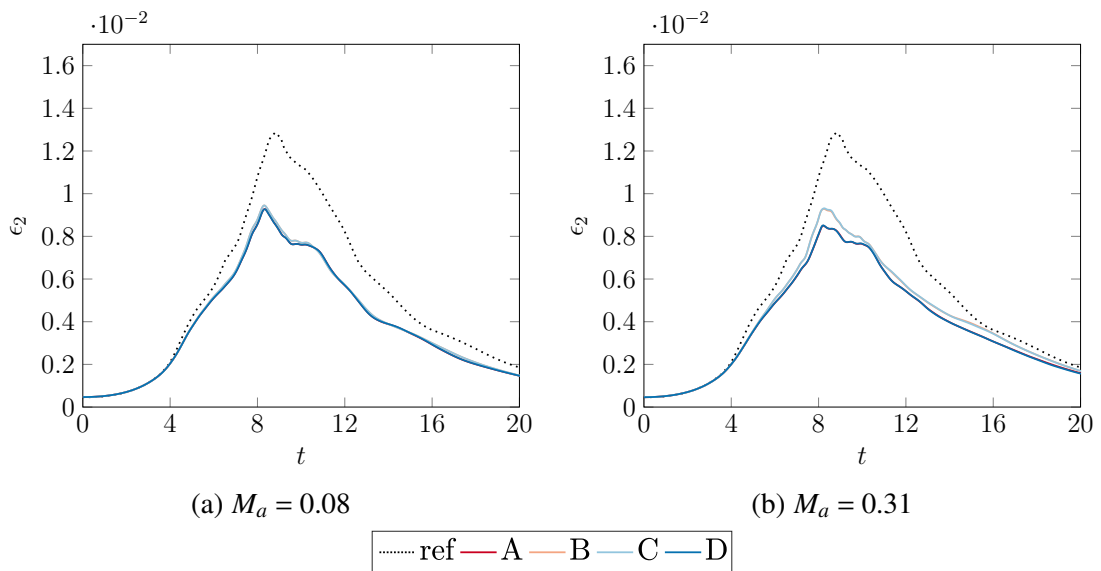


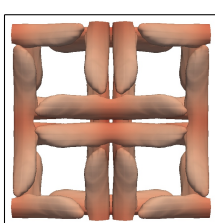
Fig. 3.4 Enstrophy of the Taylor-Green Vortex with $R_e = 1600$, $p = 3$ and 80^3 degrees of freedom.

primitive methods. Again the cases of primitive and partial conservative with pressure are very similar, this indicated that the improvement is largely originating from the change in the handling of the energy equation. The work in section 3.3 showed that when the primitive data is stored, the formulation of energy from pressure see aliasing error p orders higher than the momentum terms and hence it is to be expected that the largest contribution to the improving the scheme comes from the energy equation.

At the higher Mach number, there is a noticeable difference in Fig. 3.3b between the fully conservative with the gradient calculated from the converted primitives and the gradient calculated from the application of the product rule. It is hard to attribute this difference to a particular aspect, but we will explore this further.

In section 3.2 we showed analytically the dependency of interpolation rounding error on order and that it increases factorially as the order is increased. To investigate the effect of order we consider the case of $R_e = 1600$ run at $p = 3$ for the same number of degrees of freedom. The results of this are shown in Fig. 3.4. By comparison of Fig. 3.4a & 3.4b, we can see that there is still a larger difference between the methods in the high Mach number case than at low Mach number. However, when comparing Fig. 3.4 & 3.3, the difference between method is markedly smaller at lower order. This evidence is in agreement with the earlier analytical predictions. As we move to a higher order, this mechanism of aliasing becomes increasingly important.

We will now explore the effect of increasing the Reynolds numbers for the same grid resolution. In particular, we choose $R_e = 3000$, which was explored with DNS by Brachet et al. [18] and with DG by Chapelier et al. [27]. The results of the application of



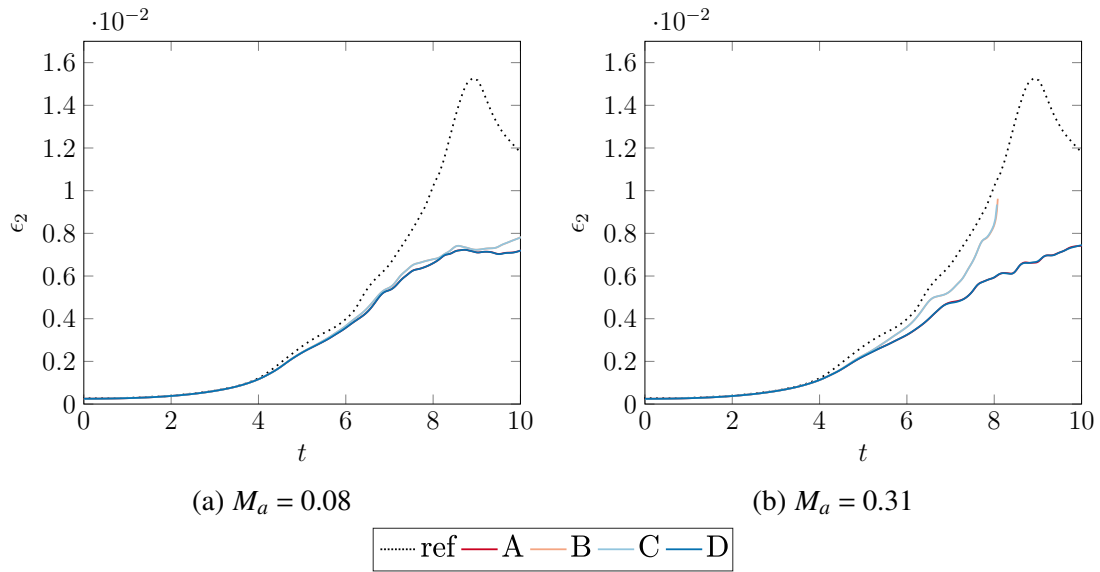


Fig. 3.5 Enstrophy of the Taylor-Green Vortex with $R_e = 3000$, $p = 4$ and 80^3 degrees of freedom.

$p = 4$ FR with the various methods of storage are presented in Fig. 3.5. Firstly studying the $M_a = 0.08$ case, there is again a noticeable difference between the conservative and primitive enstrophy. Which we can attribute to the decrease in numerical/aliasing based dissipation, due to the absence of over dissipation when small scales begin to be generated and the increase in dissipation at the expected peak. Hence, the small scales are being preserved for longer thus enabling there increased contribution to physical dissipation.

When the Mach number is increased to $M_a = 0.31$ we initially see a larger difference between the formulations, followed by the solution diverging. A similar divergence was observed by Chapelier et al. [27] when using DG on an under-resolved mesh. They attributed the divergence to insufficient numerical dissipation to stabilise the under-resolved grid. This adds weight to the argument that the change in the variables stored is mainly reducing numerical dissipation by reducing aliasing and not introducing dispersion. It should be noted that our results differ slightly from those of Chapelier et al. [27] as they are solving the filtered LES equations, whereas we are using implicit LES.

To highlight the impact of using the conserved variables with the product rule to calculate the gradient of the primitives, Eq.(3.47), we will reduce the Reynolds number to $R_e = 400$, such that the viscous terms become more important. Through testing, it was found that when 80^3 degrees of freedom were used the case was highly resolved, with the enstrophy based decay rate laying on the DNS results. Therefore, to introduce a source of aliasing, the grid resolution was reduced to a level that is more in keeping with LES. In this case to a $R_{e,\text{cell}} = 50$ at $p = 4$, or 40^3 degrees of freedom - the results of which are shown in Fig. 3.6.

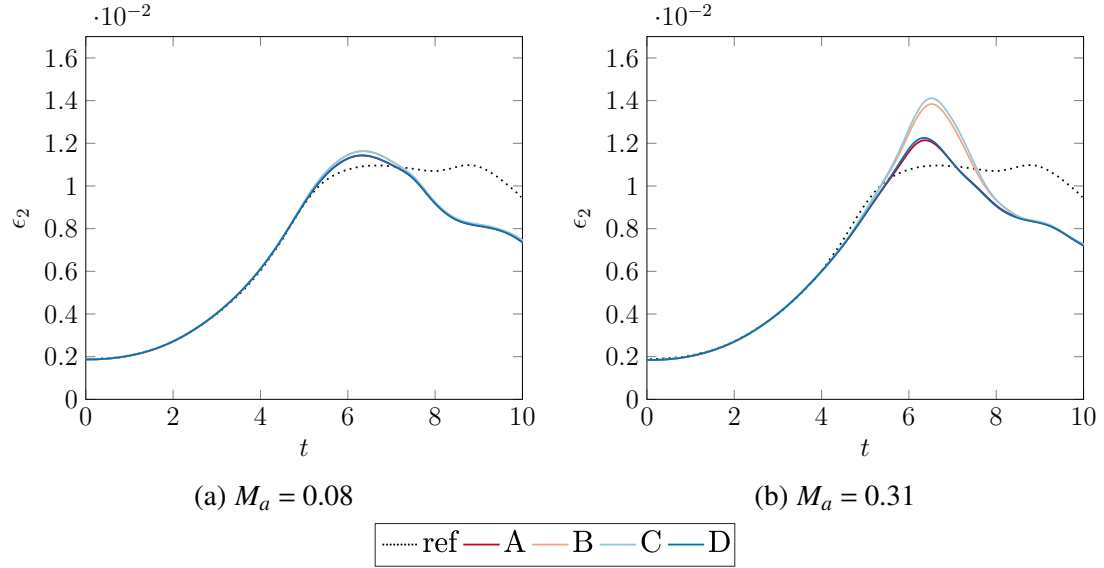
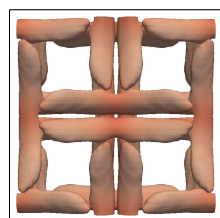


Fig. 3.6 Enstrophy of the Taylor-Green Vortex with $R_e = 400$, $p = 4$ and 40^3 degrees of freedom.

Table 3.1 Computation time comparison for one full RK44 explicit time step on a 8^3 , p=4, mesh.

Type	Computation time (ms)
A	6.423
B	5.832
C	5.634
D	6.757



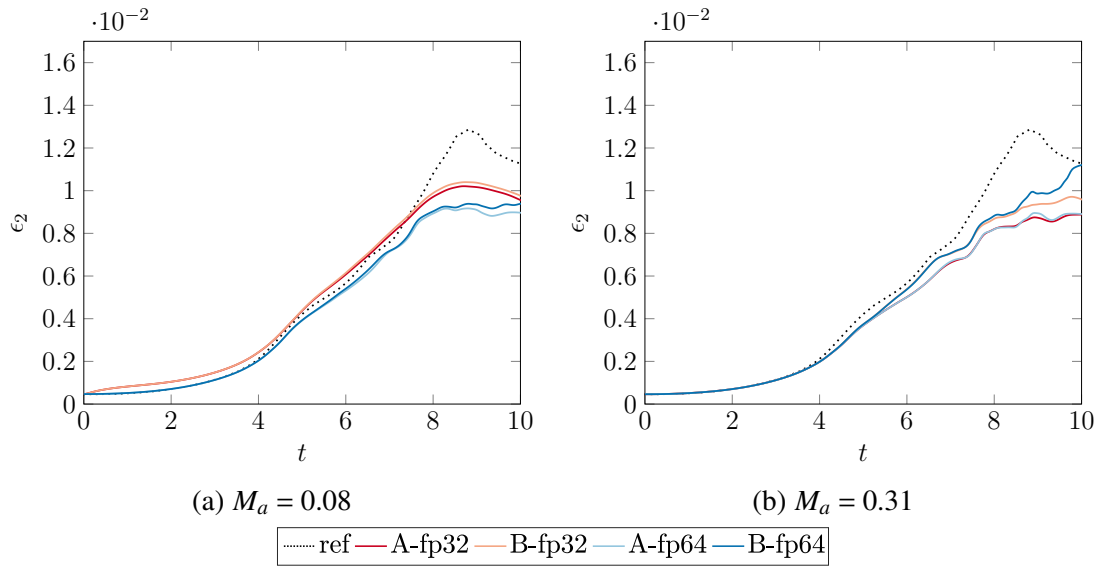


Fig. 3.7 Enstrophy of the Taylor-Green Vortex with $R_e = 1600$, $p = 4$ and 80^3 degrees of freedom for storage methods A and B in 32 (fp32) and 64 (fp64) bit precision.

The different methods outlined in section 3.3 will obviously require differing numbers of floating point operations as some conversion steps are required or different numbers of multiplications to build things like the flux terms. Therefore, we wish to understand what the impact on computational performance is, to this end we will profile the implementation. The implementation of FR used is an in house FR solver called Forflux, written in Fortran with Cuda Fortran and cuBLAS, both version 9.1, for GPU acceleration. The current implementation for small cases leads to the entire memory space being resident on the GPU and hence the CPU plays little to no role in the computation. The case profiled is a TGV, $p = 4$, with 8^3 elements run on a Titan Xp. Using the profiler, pgprof, the runtime for one complete explicit time step was found and is shown in Table 3.1.

It is clear that the continual conversion to or from the primitive variables has a noticeable impact on the computational time. In this case, the method that required the fewest number of conversions, method C (conservative variables using the product rule to calculate the gradient of the primitives), was the fastest. Method C gave a 12.3% reduction in computational time, which, all other things being equal, makes this a reasonable optimisation strategy to consider. Method D on the other hand, (conservative variables with E swapped for p), was slower as there are even more conversions required than the base primitive method.

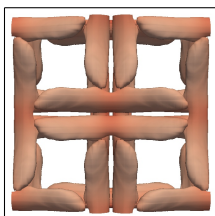
Finally, we will investigate the numerical impact of varying the working precision of the calculation when applied to turbulent and transitional flows. For this, we will limit our comparison to methods A and B, as it has previously been shown that the largest difference was between these two methods. The results of tests are shown in Fig. 3.7,

where 32-bit floating point (fp32) and 64-bit floating point (fp64) precisions were used. It is clear that the largest impact of changing the precision is at low Mach number. Coupled to the larger difference at higher Mach number being due to the variables stored, we believe that this is showing that at lower Mach number the scheme is more sensitive to numerical aliasing occurring in the interpolation. As the Mach number is increased and the physics begins to exhibit non-constant ρ , the small floating point errors in variables is more compatible with the physics and hence its effect appears to be lessened.

3.6 Conclusions

We investigated the effect of implementation on the accuracy of solving conservative PDEs. We found that the aliasing error when constructing conserved variables from primitive variables is factorially dependent on the order of the method. This result was exhibited through numerical tests, where the implementation error became more apparent as the order was increased. It was found that storing the primitive variables and constructing the conserved variables lead to higher dissipation and therefore it is recommended that the conserved variables are stored, as this method is also faster.

We also tested two methods for calculating the gradients required for forming the viscous flux in the Navier-Stokes equation, it was found that the different methods were very similar due to the small absolute value of the viscous flux. Therefore for most applications using the product rule on the gradient of the conserved variables is recommended as it was found to be fastest. Finally, the effect of working precision was investigated, finding that single precision has acceptable results, with the difference being more pronounced in low Mach number regimes for compressible schemes.



Chapter 4

Flux Reconstruction for First-Order PDEs on Stretched Grids

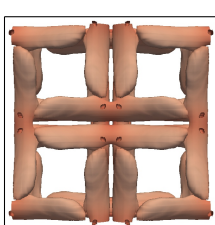
4.1 Introduction

First order PDEs are ubiquitous in the physical sciences, with first order spatial terms occurring in Euler's equations, Maxwell's equations, and the Cauchy momentum equation. Commonly these terms represent the spatial movement of information through the system and therefore the accuracy of their computation is key, as the error introduced by these terms will propagate throughout the domain. Further, it is common that the scale of the contribution of these terms in engineering equations dominates the solution.

The main advantage of high-order FR is its unstructured nature that makes parallelism straightforward owing to relatively few points in the algorithm that require inter-element communication. When applied to engineering problems this results in poorer quality meshes than canonical cases, for example Fig. 4.1 shows the trailing edge of a turbine blade. From this high levels of cell stretching, expansion, and skewness can be seen. It is also likely to have some cells around the tip of the trailing edge with flow incident at large angles. Hence, the performance characterisation of FR on poorer grids for first order PDEs is important, as knowledge of FR's behaviour can help to inform meshing requirements. This characterisation can also enable comparison to existing, lower order, techniques used and further shift the received wisdom of CFD practitioners towards high-order methods.

4.2 Analytical Techniques

The basis of the theoretical analysis to be performed is commonly called von Neumann analysis or Fourier analysis and follows the work of Lele [77], Hesthaven et al. [51],



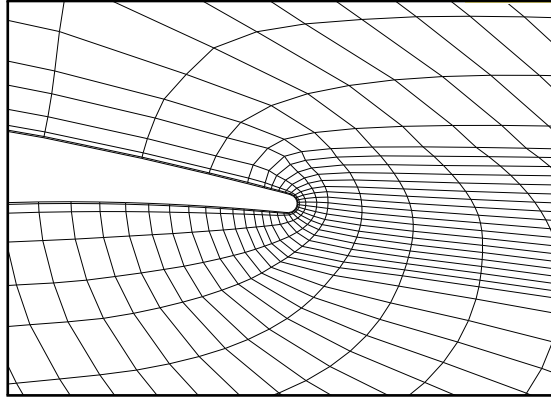


Fig. 4.1 Two-dimensional mesh slice of the trailer edge of a turbine blade. Showing how the grid in real calculations can undergo large expansion and skewing. (Mesh kindly reproduced with the permission of Bryn Ubald)

Huynh [55], Vincent et al. [128], and Asthana et al. [8]. These works have applied the methodology to a broad range of techniques, with this analysis often being the first port-of-call when trying to understand a new numerical method. However, the scope of these investigations has so far been limited to uniform grids. We therefore propose to relax this assumption and retain the generality of the technique. The advantage being that the important effects of grid stretching can be investigated.

4.2.1 One-Dimensional von Neumann Analysis

We will begin by generalising the FR Von Neumann analysis in one dimension. Consider then the domain as $\Omega \in \mathbb{R}^1$ with N sub-domains Ω_n , with flux points of Ω_n located at $\mathbf{x}_j \forall \{j \in \mathbb{N}, j \leq N\}$. The 1D linear advection equation can be written as Eq. (4.1).

$$\frac{\partial u}{\partial t} + a \frac{\partial u}{\partial x} = 0 \quad (4.1)$$

By projecting Eq. (4.1) onto the space Ω_n , and using the FR methodology of Eq. (2.15) we get:

$$\frac{\partial \mathbf{u}_j}{\partial t} = -J_j^{-1} \left(\mathbf{D}\mathbf{f}_j + (\hat{f}_{j,L}^{\delta I} - \hat{f}_{j,L}^{\delta D}) \mathbf{h_L} + (\hat{f}_{j,R}^{\delta I} - \hat{f}_{j,R}^{\delta D}) \mathbf{h_R} \right) \quad (4.2)$$

Here we have not yet applied simple linear advection to the flux term. This is presented in a matrixised form that is compatible with that set out initially in [128], taking \mathbf{D}_{mn} as the contribution from the first derivative on the m^{th} Lagrange basis function to the n^{th} solution point. $\mathbf{h_L}$ and $\mathbf{h_R}$ are taken as $dh_L(\xi)/d\xi$ and $dh_R(\xi)/d\xi$ respectively, where ξ are the reference coordinates of the solution points. By setting $a = 1$ and applying upwinding

at the interfaces we can set the common interface values to:

$$J_j^{-1} \hat{f}_L^{\delta I} = J_{j-1}^{-1} \hat{u}_{j-1}^{\delta}(1) \quad (4.3)$$

$$J_j^{-1} \hat{f}_R^{\delta I} = J_j^{-1} \hat{u}_j^{\delta}(1) \quad (4.4)$$

By substituting Eq. (4.3) & (4.4) into Eq. (4.2) and collecting the matrix operators into \mathbf{C}_0 and \mathbf{C}_{-1} :

$$\frac{\partial \mathbf{u}_j}{\partial t} = -J_j^{-1} \mathbf{C}_0 \mathbf{u}_j - J_{j-1}^{-1} \mathbf{C}_{-1} \mathbf{u}_{j-1} \quad (4.5)$$

$$\mathbf{C}_0 = \mathbf{D} - \mathbf{h}_L \mathbf{l}_R^T \quad (4.6)$$

$$\mathbf{C}_{-1} = \mathbf{h}_L \mathbf{l}_R^T \quad (4.7)$$

where \mathbf{l}_L and \mathbf{l}_R are again compatible with [128] and defined such that \mathbf{l}_L^i is the contribution of the i^{th} Lagrange basis function evaluated at the left interface. \mathbf{l}_R is similarly defined.

Defining the continuous input as a Bloch wave, and projecting onto the discrete solution domain:

$$u(x, t) = v \exp(i(kx - \omega t)) \quad (4.8)$$

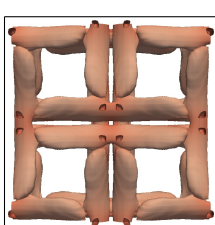
$$\mathbf{u}_j = \mathbf{v}_j \exp(ik(0.5(\xi + 1)\delta_j + x_j - ct)) \quad (4.9)$$

Inputting this result into Eq. (4.5), and setting $\delta_j = x_j - x_{j-1}$ gives:

$$c(k)\mathbf{v} = -\frac{i}{k} (J_j^{-1} \mathbf{C}_0 + J_{j-1}^{-1} \mathbf{C}_{-1} \exp(-ik\delta_j)) \mathbf{v} \quad (4.10)$$

Equation (4.10) shows that the modified phase velocity $c(k)$, is one of the complex eigenvalues of a matrix describing the spatial transformation performed by the scheme. For an FR scheme with order p there will be p eigenvalues to this problem, of which one is the physical result and the other modes being phase shifted values to give an orthogonal set. The physical interpretation of $c(k)$ is that a wave number's dispersion factor is $\Re(c(k))$ and its dissipation factor is $\Im(c(k))$. With dispersion and dissipation formally being $k\Re(c(k)) = \Re(\omega'(k))$ and $k\Im(c(k)) = \Im(\omega'(k))$ respectively, where $\omega'(k)$ is the modified wavenumber. Throughout our investigation we will also normalise the wavenumber k by the Nyquist wavenumber, k_{nq} such that $\hat{k} = k/k_{nq}$.

The special case that $\delta_j = \text{const.}$ implies that $J^{-1} = \text{const.}$ which was the case investigated in [8, 128]. However, the more general form of Eq. (4.10) allows von Neumann analysis to be performed on stretched meshes. Importantly, Eq. (4.10) shows that the stencil of cells affecting the dissipation and dispersion of an upwinded FR scheme is just



the current cell and its immediate neighbour and hence only the local expansion rate is important for behaviour. This is clearly not the case for finite difference schemes above second order. Repeating the analysis for an FD scheme will give a basis of comparison and an example of the modified wavenumber for a 4th order central difference scheme is given in Eq. (4.11):

$$c(k) = \frac{i}{k} (b_{-2,j} \exp(-ik(\delta_j + \delta_{j-1})) + b_{-1,j} \exp(-ik(\delta_j)) + b_{2,j} \exp(ik(\delta_{j+2} + \delta_{j+1})) + b_{1,j} \exp(ik(\delta_{j+1}))) \quad (4.11)$$

where $b_{-2,j}$ is a weighting factor from the derivative of the Lagrange polynomial basis function corresponding to the point $j-2$ evaluated at the point x_j , and so on.

A further implication of Eq. (4.9) is that Eq. (4.2) can be rewritten in a semi-discrete form:

$$\frac{\partial \mathbf{u}_j}{\partial t} = \mathbf{Q} \mathbf{u}_j \quad (4.12)$$

And for the case of pure upwinding at the interface it follows that $\mathbf{Q} = -J_j^{-1} \mathbf{C}_0 - J_{j-1}^{-1} \mathbf{C}_{-1} \exp(-ik\delta_j)$. Putting the result into this form allows the analytical framework of Asthana [8] to be used, hence the explicit update form can be found as:

$$\mathbf{u}_j(t + \tau) = \mathbf{R}(\mathbf{Q}) \mathbf{u}_j(t) \quad (4.13)$$

$$\mathbf{R}_{33} = \mathbf{I} + \frac{(\tau \mathbf{Q})^1}{1!} + \frac{(\tau \mathbf{Q})^2}{2!} + \frac{(\tau \mathbf{Q})^3}{3!} \quad (4.14)$$

Equation (4.14) is an example definition of \mathbf{R} for a 3rd-order 3-step low storage Runge-Kutta [67]. The form of Eq. (4.13) implies the von Neumann condition of \mathbf{R} 's spectral radius, $\rho(\mathbf{R}) \leq 1 \forall k \in \mathbb{R}$.

From the analytical form the main derived quantity to be considered is the Points Per Wavelength (PPW) for dispersion error < 1% , defined as:

$$\text{PPW} = \frac{2\pi}{\|\hat{k}\| \inf(|\Re(c(\hat{k})) - 1|_2, \epsilon)} \quad (4.15)$$

where, ϵ is the error level and $c(k)$ is the convective velocity from Eq.(4.10). This definition of PPW is based on the points being the solution points in the case of FR. Consider the case of a wave whose wavelength is the length of an element. The normalised Nyquist wavenumber would then be $2\pi/(p + 1)$ and hence the use solution points is contained within the definition. PPW is particularly interesting as it can be used to produce minimum point requirements for a given region, if the scale of flow features or the explicit filter width is known. A further derived quantity that will be touched on

briefly is the implicit filter kernel, Trefethen [115]:

$$\hat{G}(\hat{k}) \propto e^{t\Im(c(\hat{k}))} \quad (4.16)$$

Although this is not the main subject of this paper it can be illuminating to briefly look at the implicit filter.

To validate the analytical methods presented and gain insight into the fully discretised scheme behaviour, a numerical approach is proposed similar to Lele's [77] analytical method. The methodology is to apply a scalar wave to a one dimensional domain and allow the wave to be convected downstream. By choosing a low CFL number of 0.01, the spatial terms dominate the overall error. (CFL numbers of 0.05 and 0.005 were also tested, and the results were found to be largely unchanged, only affected by the discrete Fourier transform as the sampling rate will vary with CFL. Hence a CFL number of 0.01 was used to mitigate this error and give fast test turnover time). Fourier analysis is then performed on the prescribed wave after convection through the grid. The transform of the field u is:

$$\tilde{u}(x) = \sum_{k=-N/2}^{N/2} A_k \exp\left(\frac{2\pi i k x}{L}\right) \quad (4.17)$$

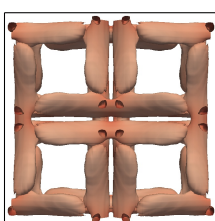
The method by Lele [77] would have, however, taken the spatial derivative of the wave after convection to give:

$$\tilde{u}'(x) = \sum_{k=-N/2}^{N/2} A_k \left(\frac{2\pi i k}{L}\right) \exp\left(\frac{2\pi i k x}{L}\right) \quad (4.18)$$

By dividing Eq. (4.18) by Eq. (4.17) the modified wavenumber can be obtained as in Eq. (4.19). In practice this approach has low throughput, due to need to calculate the derivative and as the full wavenumber space has explored. Furthermore, this method was found to be prone to the introduction of additional sources of error caused by the method used to calculate the derivative. Therefore, a direct comparison is made between the Fourier Transform (FT) of the prescribed input wave and the FT of the prescribed wave after convection through the grid. This is schematically represented in Fig. 4.2.

$$k' = \left(\frac{L}{2\pi i}\right) \frac{\tilde{u}'(x)}{\tilde{u}(x)} \quad (4.19)$$

where k' is the modified wave number and equals $\omega/c(k)$. This method is utilised for calculation of the PPW for numerical test cases in accordance with Eq.(4.15).



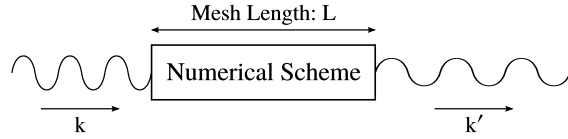


Fig. 4.2 Schematic of numerical scheme with incoming and outgoing wave showing wavenumber transformation over mesh of length L .

4.2.2 Two-Dimensional von Neumann Analysis

For reasons that should be clear from FRs applications, it is important to extend the theoretical techniques of the previous section to higher spatial dimensions. This extension from the 1D analysis to higher spatial dimensions does greatly increases the complexity of the theoretical procedures, however in a finite element framework this is somewhat reduced. We this cautionary remake, we will begin our extension by restating the 2D linear advection equation:

$$\frac{\partial u}{\partial t} + \nabla \cdot \mathbf{F} = 0 \quad (4.20)$$

$$\mathbf{F} = \begin{bmatrix} f \\ g \end{bmatrix} = u \mathbf{a} = \begin{bmatrix} au \\ bu \end{bmatrix} \quad (4.21)$$

Again, flux reconstruction then uses the superposition of the discontinuous and corrected flux divergence, meaning Eq. (4.21) can be rewritten as:

$$\frac{\partial \mathbf{u}_{i,j}}{\partial t} = -\nabla \cdot \mathbf{F}_{i,j}^{\delta D} - \nabla \cdot \mathbf{F}_{i,j}^{\delta C} \quad (4.22)$$

here the subscript i, j is taken to mean the i^{th} element in x and the j^{th} element in y . Although, this implies a structured grid the localised nature of the stencil means this simplification is acceptable in an analytical framework, as later it will only be used to keep track of connectivity in a simple manner.

Taking the following definition of the Jacobian, the computational-physical domain transformation can be defined:

$$\mathbf{G} = \begin{bmatrix} \frac{\partial x}{\partial \xi} & \frac{\partial y}{\partial \xi} \\ \frac{\partial x}{\partial \eta} & \frac{\partial y}{\partial \eta} \end{bmatrix} = \begin{bmatrix} G_1 & G_2 \\ G_3 & G_4 \end{bmatrix} \quad \text{and} \quad J = |\mathbf{G}| \quad (4.23)$$

$$u = J^{-1} \hat{u}, \quad \mathbf{F} = J^{-1} \mathbf{G} \hat{\mathbf{F}}, \quad \nabla \cdot \mathbf{F} = J^{-1} \hat{\nabla} \cdot \hat{\mathbf{F}} \quad (4.24)$$

where we use $\hat{\nabla}$ to mean $[\frac{\partial}{\partial \xi}, \frac{\partial}{\partial \eta}]^T$ in 2D. From the work of Huynh [55], Castonguay [23], and Sheshadri et al. [106], Eq.(4.21) is written in two dimensions as:

$$\hat{\nabla} \cdot \hat{\mathbf{F}}^{\delta D} = \sum_{i=0}^p \sum_{j=0}^p \hat{f}_{i,j}^{\delta D} \frac{\partial l_i(\xi)}{\partial \xi} l_j(\eta) + \sum_{i=0}^p \sum_{j=0}^p \hat{g}_{i,j}^{\delta D} \frac{\partial l_j(\eta)}{\partial \eta} l_i(\xi) \quad (4.25)$$

$$\begin{aligned} \hat{\nabla} \cdot \hat{\mathbf{F}}^{\delta C} = & \sum_{i=0}^p \left((\hat{f}_{L,i}^{\delta I} - \hat{f}_{L,i}^{\delta D}) \frac{dh_{L,i}}{d\xi} + (\hat{f}_{R,i}^{\delta I} - \hat{f}_{R,i}^{\delta D}) \frac{dh_{R,i}}{d\xi} + \right. \\ & \left. (\hat{g}_{B,i}^{\delta I} - \hat{g}_{B,i}^{\delta D}) \frac{dh_{B,i}}{d\eta} + (\hat{g}_{T,i}^{\delta I} - \hat{g}_{T,i}^{\delta D}) \frac{dh_{T,i}}{d\eta} \right) \end{aligned}$$

where we use L , R , B , and T subscripts to mean left, right, bottom, and top respectively. This is the same technique as was set out in chapter 2, reiterated here for clarity. We will then impose that grid transformations are purely rectilinear, *i.e.* $G_2 = G_3 = 0$. We may now use Eq. (4.25) and convert it into a matrix form:

$$\hat{\nabla} \cdot \hat{\mathbf{F}}^{\delta D} = \mathbf{D}_\xi \hat{\mathbf{f}}_{i,j}^\delta + \mathbf{D}_\eta \hat{\mathbf{g}}_{i,j}^\delta \quad (4.26)$$

$$\nabla \cdot \mathbf{F}^{\delta D} = G_{1,i,j}^{-1} \mathbf{D}_\xi \mathbf{f}_{i,j}^\delta + G_{4,i,j}^{-1} \mathbf{D}_\eta \mathbf{g}_{i,j}^\delta \quad (4.27)$$

To apply the correction function, we need to calculate the interface values around the element. For the case of generalised central/upwinding with upwinding ratio α , the common interface fluxes may be written as:

$$G_{4,i,j}^{-1} \hat{f}_L^{\delta I} = a(\alpha G_{4,i-1,j}^{-1} \hat{u}_{i-1,j,R}^\delta + (1-\alpha) G_{4,i,j}^{-1} \hat{u}_{i,j,L}^\delta) \quad (4.28)$$

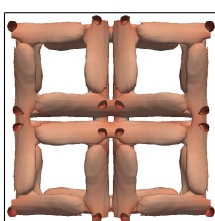
$$G_{4,i,j}^{-1} \hat{f}_R^{\delta I} = a(\alpha G_{4,i,j}^{-1} \hat{u}_{i,j,R}^\delta + (1-\alpha) G_{4,i+1,j}^{-1} \hat{u}_{i+1,j,L}^\delta) \quad (4.29)$$

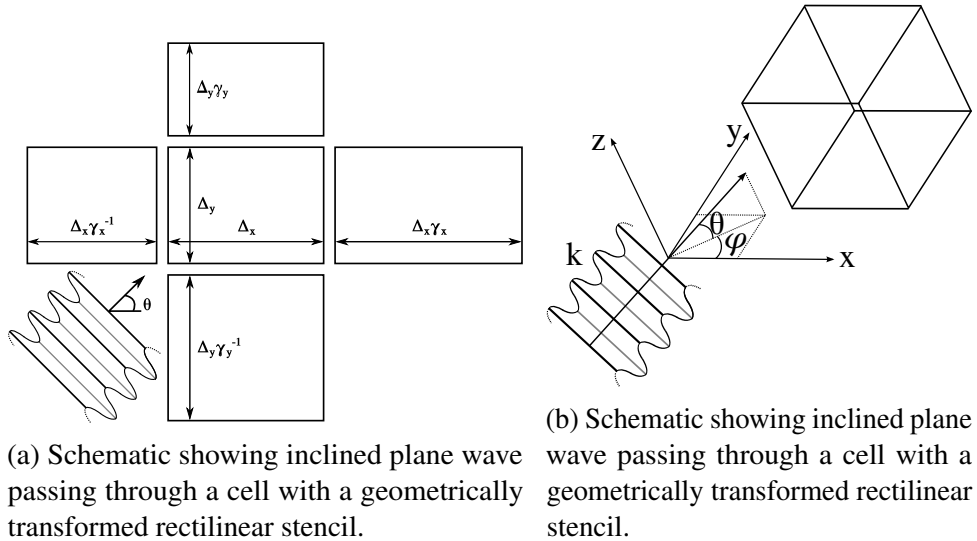
$$G_{1,i,j}^{-1} \hat{g}_B^{\delta I} = b(\alpha G_{1,i,j-1}^{-1} \hat{u}_{i,j-1,T}^\delta + (1-\alpha) G_{1,i,j}^{-1} \hat{u}_{i,j,B}^\delta) \quad (4.30)$$

$$G_{1,i,j}^{-1} \hat{g}_T^{\delta I} = b(\alpha G_{1,i,j}^{-1} \hat{u}_{i,j,T}^\delta + (1-\alpha) G_{1,i,j+1}^{-1} \hat{u}_{i,j+1,B}^\delta) \quad (4.31)$$

where $\alpha = 1$ gives rise to upwinding and $\alpha = 0.5$ produces central difference. Hence the divergence correction can be written as:

$$\begin{aligned} \hat{\nabla} \cdot \hat{\mathbf{F}}_{i,j}^{\delta C} = & a\alpha \left(G_{4,i-1,j}^{-1} \mathbf{h_L} \mathbf{l_R}^T \hat{\mathbf{u}}_{i-1,j}^\delta - G_{4,i,j}^{-1} \mathbf{h_L} \mathbf{l_L}^T \hat{\mathbf{u}}_{i,j}^\delta \right) + \\ & a(1-\alpha) \left(G_{4,i+1,j}^{-1} \mathbf{h_R} \mathbf{l_L}^T \hat{\mathbf{u}}_{i+1,j}^\delta - G_{4,i,j}^{-1} \mathbf{h_R} \mathbf{l_R}^T \hat{\mathbf{u}}_{i,j}^\delta \right) + \\ & b\alpha \left(G_{1,i,j-1}^{-1} \mathbf{h_B} \mathbf{l_T}^T \hat{\mathbf{u}}_{i,j-1}^\delta - G_{1,i,j}^{-1} \mathbf{h_B} \mathbf{l_B}^T \hat{\mathbf{u}}_{i,j}^\delta \right) + \\ & b(1-\alpha) \left(G_{1,i,j+1}^{-1} \mathbf{h_T} \mathbf{l_B}^T \hat{\mathbf{u}}_{i,j+1}^\delta - G_{1,i,j}^{-1} \mathbf{h_T} \mathbf{l_T}^T \hat{\mathbf{u}}_{i,j}^\delta \right) \end{aligned} \quad (4.32)$$





(a) Schematic showing inclined plane wave passing through a cell with a geometrically transformed rectilinear stencil.

(b) Schematic showing inclined plane wave passing through a cell with a geometrically transformed rectilinear stencil.

Fig. 4.3

where \mathbf{h}_L is the *gradient* of the left correction function at the solution points and again \mathbf{l}_L are the values of the polynomial basis at the left interface and so on for R , T , and B . Therefore, by grouping terms by their cell indexing and transforming each term into the physical domain:

$$\begin{aligned} \frac{\partial \mathbf{u}_{i,j}}{\partial t} = & -a(G_{1,i-1,j}^{-1} \mathbf{C}_L \mathbf{u}_{i-1,j}^\delta + G_{1,i,j}^{-1} \mathbf{C}_{0\xi} \mathbf{u}_{i,j}^\delta + G_{1,i+1,j}^{-1} \mathbf{C}_R \mathbf{u}_{i+1,j}^\delta) \\ & -b(G_{4,i,j-1}^{-1} \mathbf{C}_B \mathbf{u}_{i,j-1}^\delta + G_{4,i,j}^{-1} \mathbf{C}_{0\eta} \mathbf{u}_{i,j}^\delta + G_{4,i,j+1}^{-1} \mathbf{C}_T \mathbf{u}_{i,j+1}^\delta) \end{aligned} \quad (4.33)$$

where

$$\mathbf{C}_L = \alpha \mathbf{h}_L \mathbf{l}_R^T \quad \mathbf{C}_R = (1-\alpha) \mathbf{h}_R \mathbf{l}_L^T \quad \mathbf{C}_{0\xi} = \mathbf{D}_\xi - \alpha \mathbf{h}_L \mathbf{l}_L^T - (1-\alpha) \mathbf{h}_R \mathbf{l}_R^T \quad (4.34)$$

$$\mathbf{C}_B = \alpha \mathbf{h}_B \mathbf{l}_T^T \quad \mathbf{C}_T = (1-\alpha) \mathbf{h}_T \mathbf{l}_B^T \quad \mathbf{C}_{0\eta} = \mathbf{D}_\eta - \alpha \mathbf{h}_B \mathbf{l}_B^T - (1-\alpha) \mathbf{h}_T \mathbf{l}_T^T \quad (4.35)$$

Finally, we are here interested in the frequency response of the system, and, importantly to engineers and technicians, how the cell's orientation relative to an oncoming wave affects performance. Therefore, we impose a trial solution of the form:

$$u(x, y; t) = \exp(ik(x \cos \theta + y \sin \theta - ct)) \quad (4.36)$$

and by substitution into Eq.(4.21), the advection velocity, \mathbf{a} , can be found, which is shown schematically in Fig. 4.3a.

$$\mathbf{a} = \begin{bmatrix} a \\ b \end{bmatrix} = \begin{bmatrix} \cos \theta \\ \sin \theta \end{bmatrix} \quad (4.37)$$

The plane wave can then be projected into the computational domain and discretised as:

$$\mathbf{u}_{i,j} = \mathbf{v} \exp\left(ik((0.5(\xi+1)\delta_i + x_i)\cos\theta + (0.5(\eta+1)\delta_j + y_j)\sin\theta - ct)\right) \quad (4.38)$$

where, for brevity, $\delta_i = x_i - x_{i-1}$ and $\delta_j = y_j - y_{j-1}$ are defined. Inserting Eq.(4.38) into Eq.(4.33), an Eigenvalue problem can be obtained as:

$$\begin{aligned} -ikc(k)\mathbf{v} = & -\cos\theta(G_{1,i-1,j}^{-1}\mathbf{C}_L \exp(-ik\delta_{i-1}\cos\theta) + G_{1,i,j}^{-1}\mathbf{C}_{0\xi} + G_{1,i+1,j}^{-1}\mathbf{C}_R \exp(ik\delta_i\cos\theta))\mathbf{v} \\ & -\sin\theta(G_{4,i,j-1}^{-1}\mathbf{C}_B \exp(-ik\delta_{j-1}\sin\theta) + G_{4,i,j}^{-1}\mathbf{C}_{0\eta} + G_{4,i,j+1}^{-1}\mathbf{C}_T \exp(ik\delta_j\sin\theta))\mathbf{v} \end{aligned} \quad (4.39)$$

where $\Re k(c(k)) = \Re(\omega)$ and $\Im(kc(k)) = \Im(\omega)$ are the dispersion and dissipation, respectively, and ω is the modified angular frequency response of the system. By studying the trial solution of Eq.(4.36) it can be understood that if $\Im(\omega) > 0$ then the amplitude of the wave will increase and vice versa. Furthermore, if $\Re(\omega) \neq k$ then a wave will move at a different speed compared to the other waves inside the packet, causing the quality of the interpolation to be affected as the solution is advanced in time as the components that make it up move at different speeds. An important point is the difference between phase velocity ω/k and group velocity $d\omega/dk$. Phase velocity is the speed of a wave in a packet of waves. Group velocity is the speed of the packet. Therefore, changes to $d\omega/dk$, i.e can be thought of more as a change to the physics due to the numerical method.

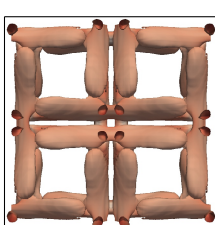
To form a semi-discrete operator matrix for FR we can combine Eq.(4.33) with Eq.(4.38), resulting in a matrix we will call, $\mathbf{Q}_{i,j}$. This is defined as:

$$\frac{\partial \mathbf{u}_{i,j}}{\partial t} = \mathbf{Q}_{i,j} \mathbf{u}_{i,j} \quad (4.40)$$

$$\begin{aligned} \mathbf{Q}_{i,j} = & -J_{i,j} \cos\theta(G_{4,i-1,j}^{-1}\mathbf{C}_L \exp(-ik\delta_{i-1}\cos\theta) + G_{4,i,j}^{-1}\mathbf{C}_{0\xi} + G_{4,i+1,j}^{-1}\mathbf{C}_R \exp(ik\delta_i\cos\theta)) \\ & -J_{i,j} \sin\theta(G_{1,i,j-1}^{-1}\mathbf{C}_B \exp(-ik\delta_{j-1}\sin\theta) + G_{1,i,j}^{-1}\mathbf{C}_{0\eta} + G_{1,i,j+1}^{-1}\mathbf{C}_T \exp(ik\delta_j\sin\theta)) \end{aligned} \quad (4.41)$$

The semi-discrete FR operator, \mathbf{Q} , can again be used to define an update matrix when combined with a temporal discretisation as in Eq.(4.13). Von Neumann's theorems [58, 74] and Banach's fixed point theorem [71] can again be used to explore the linear stability of the scheme.

In recent works by Vermerie et al. [126] and Trojak et al. [119], this Fourier analysis was extended by fully discretising the equation. This is performed by taking Eq.(4.13)



and again applying Eq.(4.36). This results in:

$$\exp(-ik(c-1)\tau)\mathbf{v} = \lambda\mathbf{v} = \exp(ik\tau)\mathbf{R}(k, \tau)\mathbf{v} \quad (4.42)$$

where the explicit time step from n to $n+1$ is τ . Hence, rearranging for the modified wave speed:

$$c = \frac{i \log(\lambda)}{k\tau} + 1 \quad (4.43)$$

where λ are the eigenvalues of $\exp(ik\tau)\mathbf{R}$. The advantage of this further analysis is that it gives the dispersion and dissipation relations of the full scheme as would be experienced when applied as implicit LES.

Lastly, the linear FR operator matrix, $\mathbf{Q}_{i,j}$, can be diagonalised as:

$$\mathbf{Q}_{i,j} = ik\mathbf{W}_{i,j}\mathbf{\Lambda}_{i,j}\mathbf{W}_{i,j}^{-1} \quad (4.44)$$

where \mathbf{W} is a matrix of eigenvectors and $\mathbf{\Lambda}$ is a diagonal matrix of normalised eigenvalues. From this, the weights of modes used to reconstruct the solution can be found as:

$$\mathbf{u}_{i,j} = \mathbf{W}_{i,j}\boldsymbol{\beta}_{i,j} \quad (4.45)$$

where $\boldsymbol{\beta}$ is an array of mode weights used to project $\mathbf{u}_{i,j}$ into the functional space of FR. The posedness of the projection can then be measured for wavenumbers using the number of the matrix of modes defined as:

$$\kappa(\mathbf{W}_{i,j}) = \frac{\sigma_{\max}(\mathbf{W}_{i,j})}{\sigma_{\min}(\mathbf{W}_{i,j})} \quad (4.46)$$

where $\sigma(\mathbf{W}_{i,j})$ is a singular value of $\mathbf{W}_{i,j}$, with the matrix becoming singular as $\kappa \rightarrow \infty$.

The results of this section can then be extended to n-dimensions and, in particular, the three-dimensional case will be investigated to show the continuation of trends with higher dimensionality. The analysis can broadly be repeated and is excluded for brevity, but importantly the prescribed solution is taken as:

$$u = \exp(ik(x\cos\phi\cos\theta + y\cos\phi\sin\theta + z\sin\phi - ct)) \quad (4.47)$$

where the angles are as shown in Fig. 4.3b, and hence the 3D convective velocities for linear advection are:

$$\mathbf{a} = \begin{bmatrix} \cos\phi\cos\theta \\ \cos\phi\sin\theta \\ \sin\phi \end{bmatrix} \quad (4.48)$$

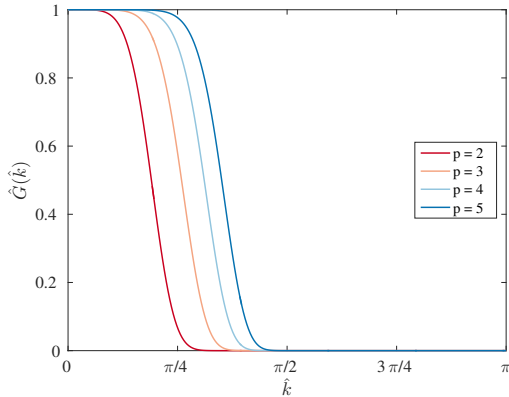


Fig. 4.4 Analytical filter kernel, $\hat{G}(\hat{k})$, against Nyquist normalised wavenumber, \hat{k} for various orders of upwinded FR with Huynh, g_2 , correction functions. The is for $t = 100$ in Eq. (4.16).

4.3 Analytical Findings

4.3.1 One-Dimensional Analytic Results

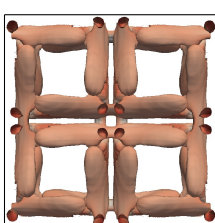
Spatial Characteristics

The analytical methods presented in section 4.2.1 makes the implicit assumption that there is a linear mapping between solution point placement in the real and physical domain. The analysis did, however, carry through the ability for the relative scaling of adjacent cells to be varied. Hence, this allows for the characteristics of non-uniform grids to be investigated, with the geometric expansion being one such linear transformation in common usage, for example in the meshing of a boundary layer. The geometric expansion is defined as:

$$x_{j+1} = x_j + \gamma(x_j - x_{j-1}) \quad (4.49)$$

where γ is the grid expansion rate. The points that this transformation defines are then used as the flux points for the element and linear interpolation gives the solution points physical domain coordinates, using the computational quadrature as weights to ensure a linear mapping. Proceeding to analytically calculate the modified wave speed from Eq. (4.10), a preliminary result that can be qualitatively informative is the filter kernel and is shown in Fig. 4.4. In each case the convolution kernel is normalised independently by the Nyquist wavenumber, k_{nq} . This is included as it clearly shows that while there is merit in going to much higher orders ($p > 4$), this does result in a case of diminishing returns.

Figure 4.5 shows normalised wavenumbers against normalised modified wavenumbers for differing levels of mesh stretching. The results for the uniform grid case can be



compared to those found by Huynh [55] and found to be in agreement. What the new results broadly exhibit is dispersion overshoot for expanding grids, while contracting grids cause dispersion undershoot. For expanding meshes this physically means that for a central band of wavenumbers, where the group velocity ($\partial\omega/\partial k$) is not approximately constant, the upwind group velocity is higher. This is caused by the change in the Nyquist wavenumber between the smaller upwind and larger downwind elements in an expanding mesh. Resultantly, as the solution advects downwind, this small increase in the group velocity between elements means that a wave will be advected into an element faster than it will exit. This gives rise to anti-dissipation, seen in Fig 4.6. The opposite behaviour is exhibited in contractions. At wavenumbers above this central band, Lagrange fitting becomes ineffective at sufficiently projecting the prescribed wave into the functional space, and so the dispersion relation goes zero regardless, and the dissipation becomes high.

To highlight the practical impact of mesh deformation the PPW resulting in a dispersion error $< 1\%$, Eq.(4.15) with $\epsilon = 0.01$, is plotted against expansion factor in Fig. 4.7. Over the range of expansion factors, there are some clear optimal PPW at varying polynomial orders. When Fig. 4.5 is considered, it can be seen that the dispersion over- or under-shoot present under some conditions can be counteracted by mesh warping. Therefore, depending on mesh conditions, it may be beneficial to directionally vary the spatial order, as this may reduce the point requirements locally. For example, for an eddy passing through a complex mesh, fewer points would be needed while passing through a contraction with $p = 5$ compared to $p = 4$ and vice versa. It is proposed that this could be achieved by maintaining the order of the polynomial interpolation, reflected in the number of solution points, but the order of the correction function could be varied. Clearly, this can only be used as a means of dropping the order accuracy, and not as a means of increasing order. From Vincent et al. [127] it can be seen that this method results in a special case of the energy stability criterion and that the correction functions proposed by Vincent et al. [127] with reduced order, will still fulfil this criterion. A study was carried out to this effect, and it was found that using a p^{th} order, as opposed to $p + 1^{\text{th}}$ order, correction function on a p^{th} order sub-domain results in a stable degradation of the spatial order, pointing to the feasibility of this method.

Coupled Spatial-Temporal Characteristics

The preceding analysis was predicated on using an analytical solution to the linear advection equation that allowed the time derivative for the semi-discrete linear system to be exactly calculated. This is of course a simplification that cannot be used practically and Eq.(4.13) is far more representative of a real implementation. The family of temporal

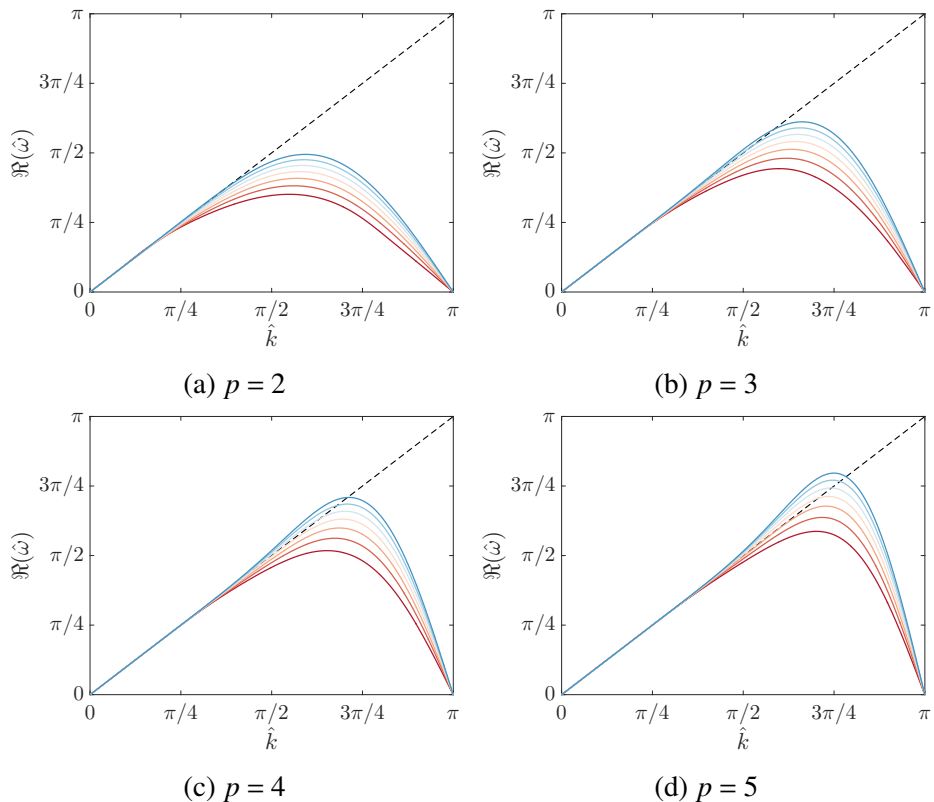
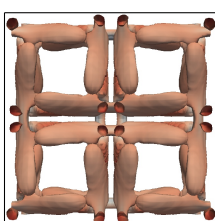


Fig. 4.5 Dispersion relations for FR, with Huynh, g_2 , correction functions, on various geometrically stretched meshes.

-- spectral performance, — $\gamma = 0.4$, — $\gamma = 0.6$, — $\gamma = 0.8$, — $\gamma = 1.0$, — $\gamma = 1.2$, — $\gamma = 1.4$, — $\gamma = 1.6$



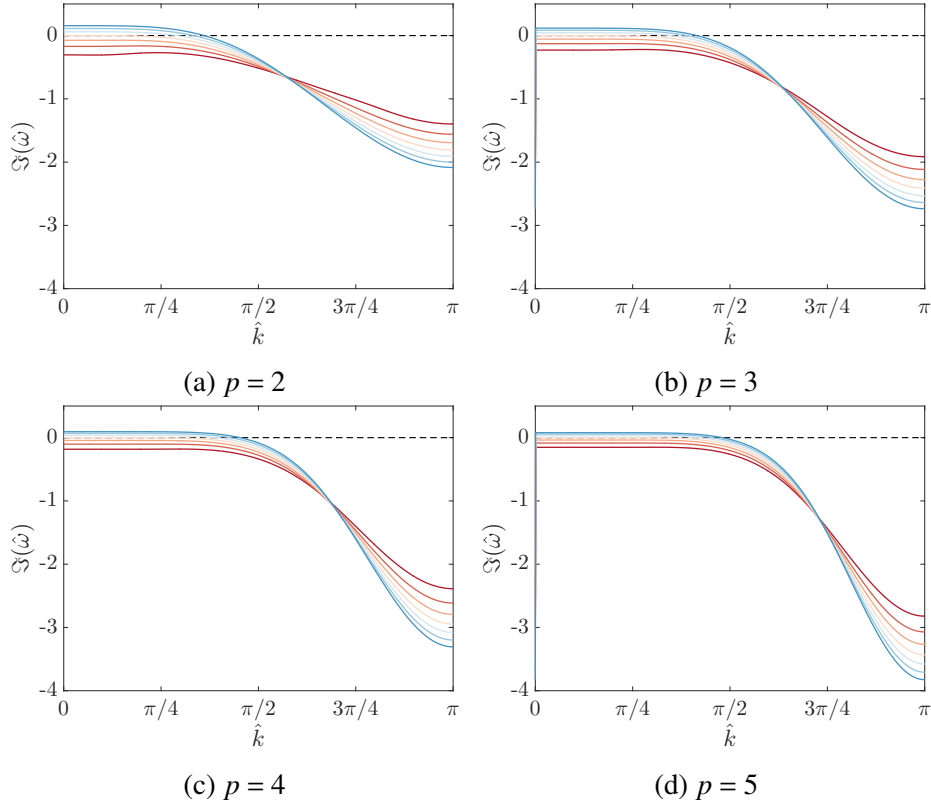


Fig. 4.6 Dissipation relations for FR, with Huynh, g_2 , correction functions, on various geometrically stretched meshes.

-- spectral performance, — $\gamma = 0.4$, — $\gamma = 0.6$, — $\gamma = 0.8$, — $\gamma = 1.0$, — $\gamma = 1.2$, — $\gamma = 1.4$, — $\gamma = 1.6$

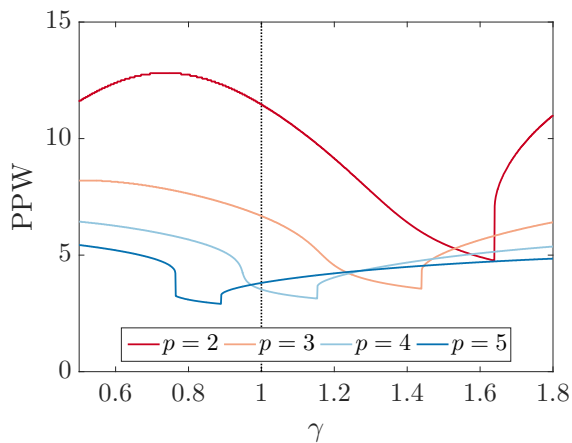


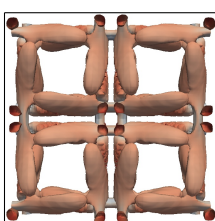
Fig. 4.7 Points Per Wavelength (PPW) for error $< 1\%$ against expansion rate, γ , for various spatial orders of upwinded FR with Huynh, g_2 , correction functions.

integration schemes to be coupled to FR here are low-storage Runge-Kutta [67], commonly called RK33, RK44, etc.. The analysis performed is primarily in search of the maximum stable CFL number, τ/δ_j for $a = 1$, obtained via varying the time step, τ , and calculation of the spectral radius of the update matrix, \mathbf{R} . This is plotted in Fig. 4.9 for various geometric expansion ratios. Initially focusing on contracting grids, the maximum stable CFL number is shown to be higher than in the case of uniform grids. This could have been expected from observation of Fig. 4.6, and furthermore it can be reasoned that as a wave is swept from one cell to its smaller upwind neighbour, the ability of the neighbouring element to resolve that wave improves. This is due to the wave's Nyquist normalised wavenumber, \hat{k} , decreasing as it is advected through successively smaller elements.

Focusing on expanding grids, if third order is considered, $p = 2$, $\rho(\mathbf{R}) \not< 1 \forall \{k \in \mathbb{R} : \gamma > 1\}$, this means that while being strictly unstable, some wavenumbers are in practice stable. This is displayed in Fig. 4.8b with $\rho(\mathbf{R}(k))$ being both less than and greater than one. The practical implication is that a wave, k , fed into the expanding grid can cause an instability if $\rho(\mathbf{R}(k)) > 1$, however, as the wave advects the relative wavenumber increases due to a decreasing k_{nq} . Hence a band of $\rho(\mathbf{R}(k)) < 1$ will be encountered by the wave and the instability will be attenuated. This procedure would be expected to repeat until the wave is beyond the grid resolution.¹

For $p > 2$, different expanding mesh characteristics are seen with $\rho(\mathbf{R}) \geq 1 \forall \{k \in \mathbb{R} : \gamma > 1\}$, Fig. 4.8c. Later numerical tests will show that for $p > 2$ instability is also encountered, but this is likewise attenuated as the wave advects. This result can be seen analytically by observing the dissipation relation in Fig. 4.6 and using the same logic as before. The full impact on stability that this implies will be discussed later alongside numerical findings. However, for simplicity, the scheme stability limit (as shown in Table. 4.1) will be taken as the higher point between either the point of the sharp increase in the spectral radius or the point at which the spectral radius increases above 1, (see Fig. 4.9).

¹Also of note from Fig. 4.8 is that the spectral radius is a periodic function which depends on the element Nyquist wavenumber, rather than the solution point Nyquist wavenumber.



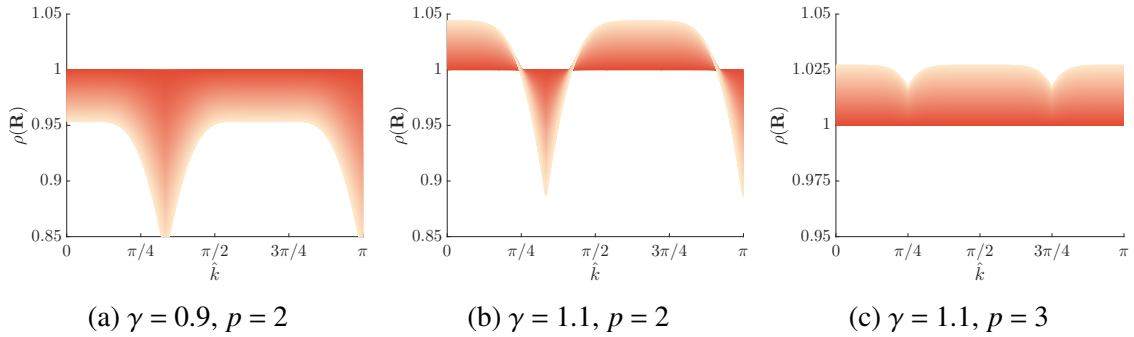


Fig. 4.8 Spectral radius of \mathbf{R} for RK44, upwinded FR with Huynh, g_2 , correction functions, against Nyquist normalised wavenumber for $\gamma = 0.9$ and $\gamma = 1.1$. with various time steps τ . τ increasing is shown as a decrease in colour intensity.

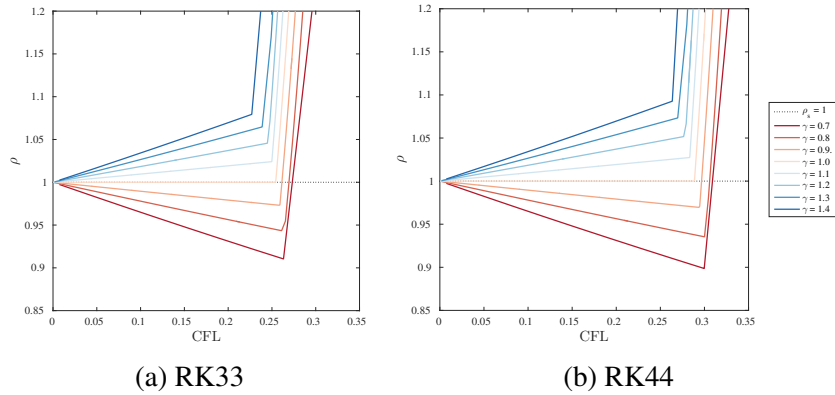


Fig. 4.9 Spectral radius of time scheme specific update matrix, \mathbf{R} , for $p = 3$ upwinded FR with Huynh, g_2 , corrections, against CFL number on various grid.

Table 4.1 Analytical CFL limit of FR for various grid expansion factors and temporal integration schemes. Using the Huynh correction function.

Time Scheme	Spatial Order	CFL							
		$\gamma = 0.7$	0.8	0.9	1.0	1.1	1.2	1.3	
RK33	3	0.519	0.482	0.463	0.448	0.442	0.436	0.424	
	4	0.284	0.269	0.261	0.254	0.250	0.245	0.239	
	5	0.183	0.177	0.172	0.167	0.164	0.161	0.159	
RK44	3	0.592	0.547	0.531	0.513	0.505	0.495	0.507	
	4	0.318	0.307	0.297	0.288	0.282	0.278	0.270	
	5	0.218	0.199	0.194	0.189	0.186	0.182	0.179	
RK55	3	0.702	0.634	0.611	0.590	0.579	0.567	0.558	
	4	0.353	0.352	0.342	0.332	0.326	0.320	0.311	
	5	0.246	0.230	0.224	0.217	0.214	0.210	0.204	

4.3.2 Two-Dimensional Analytical Results

Preliminaries

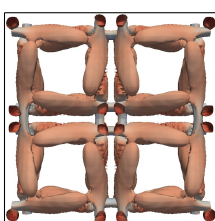
The analytical methods presented in section 4.2.2 allow us to investigate many properties of FR, however from Eq.(4.13 & 4.41) it can be seen that the functional space of \mathbf{Q} is 8 dimensional, leading to the functional space of $\rho(\mathbf{R})$ being 9 dimensional ($\tau, \gamma_x, \gamma_y, \Delta_x, \Delta_y, k, \theta, \iota, p$). Therefore we need to restrict our investigation to some key results relating to grid deformation. Firstly, understanding the dispersion and dissipation ($\Re(\omega)$ & $\Im(\omega)$) in 2D for both uniform and stretched grids will be important. Secondly, we wish to understand how higher dimensionality and grid deformations affect the temporal stability of FR through evaluation of the CFL limits [33]. Here, the dispersion and dissipation relations will be useful in explaining the trends seen and will aid in linking this work to that of Trojak et al. [118]. The definition of the CFL number in higher dimensions will be taken as:

$$\text{CFL}_d = \tau \sum_{i=1}^d \frac{a_i}{\Delta_i} \quad (4.50)$$

where d is the dimensionality, τ is the time step and, a_i and Δ_i are the characteristic velocity and grid spacing in the i^{th} dimension, respectively. The CFL limit is then the maximum value of CFL at which the scheme is stable in a von Neumann sense. Finally, we wish to understand if correction functions can be used to alleviate any effects of deformation by understanding how the scheme properties vary with correction function. Within this study, the link to the posed nature of the linear system will be explored with regard to how this relates to the other properties.

Before proceeding with the analysis in higher dimensions, it will be useful to review the key result of the previous 1D investigations. A key point was that expanding grids cause dispersion overshoot, as is seen by the dispersion relation going above the line $\hat{\omega} = 1$ in Fig. 4.5. While contractions cause dispersion to undershoot. More interesting is the impact of the grid on the dissipation as is shown in Fig. 4.6. Here expanding grids are shown to have a region where $\Im(\hat{\omega}) > 0$ at low wavenumbers, while contracting grids in the same wavenumber range have $\Im(\hat{\omega}) < 0$. This implies that a wave propagating across a contracting grid is more quickly dissipated, whereas on an expanding grid the amplitude of the wave is increased. Hence, expanding grids are strictly unstable.

This characteristic is obviously of importance as it could lead to the scheme being non-conservative. Hence, the importance of studying this phenomena in higher dimensions.



Effect of Grid Expansion on Dispersion and Dissipation

For the higher dimensional case, we begin by considering the dispersion and dissipation on a uniform grid in two dimensions. We are concerned here with the primary mode — as FR has multiple modes, this is the one that physically represents the wave. Although, as was found by Asthana [9], this may not be how the energy distributes itself. We identify the physical mode as the mode whose dispersion relation that goes through zero and dissipation relation similar to those seen in Fig. 4.5.

The dispersion and dissipation relations are then shown in Figs. 4.10 and 4.11. It is clear that for all orders FR becomes more dispersive and dissipative at $\theta = 45^\circ$. This is more easily seen for the dissipation relation, but in the case of dispersion is displayed by the indent at $\hat{k} \approx 3\pi/4$. Furthermore, there doesn't seem to be any widening in the range of angles over which FR becomes more dispersive and dissipative as the order is reduced. By comparison with the results of Lele [77], where a similar test is performed for standard and compact difference schemes, FR shows a comparatively smaller change in performance as the angle is varied. It is thought that this due to the method of polynomial fitting used by FR, namely that this implementation of FR used a tensor grid of monomials *i.e.*, the number of solution points is $(p+1)^d$ and hence the monomials in the interpolation go from $(\xi^0\eta^0, \xi^1\eta^0 \dots \xi^p\eta^p)$. By contrast, finite differences do not include the cross product terms, which will become increasingly dominant as the angle is increased.

Moving on, we then consider the impact of non-uniform grids on the character of the dispersion and dissipation. There are two cases that have been identified from previous work as being of interest. Firstly, when the grid is expanding, does this give the same positive dissipation in higher dimensions as seen in the 1D case, Fig. ??? Secondly, if positive dissipation is seen in the 2D case, will an orthogonal contraction help to stabilise the grid? For example, if $\gamma_x = 1.1$ then will setting $\gamma_y = 0.9$ help to reduce the positive dissipation?

The first of these questions is explored in Figs. 4.12a & 4.12b. It is observed in Fig. 4.12b that expanding grids do cause positive dissipation in higher dimensions. This is more clearly displayed for some specific angles in Fig. 4.13d, where the dissipation is seen to be slightly positive at low wavenumbers. In one dimension, this behaviour was previously explained that as a wave moves through elements of different size the group velocity ($d\omega/dk$) will change. For an expanding grid, this leads to low wavenumber energy collecting in elements. The same mechanism looks to be responsible in higher dimensions.

The next question of whether a contraction orthogonal to the expansion will help to stabilise the situation is considered in Figs. 4.12c and 4.12d. From Fig. 4.12d, it can be seen that the answer is yes. However, there is still a region of positive dissipation for

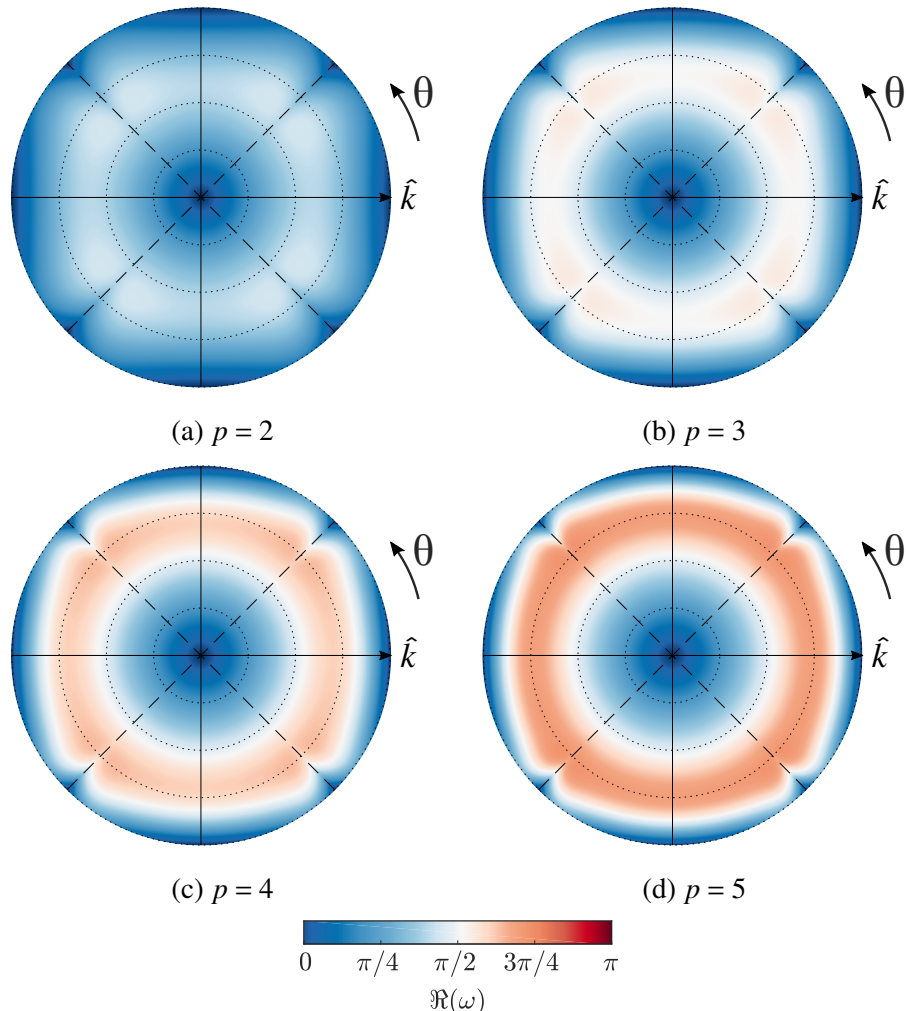
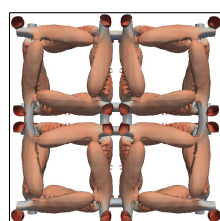


Fig. 4.10 Primary mode dispersion for 2D upwinded FR, with Huynh g_2 corrections, at various orders. Normalised wavenumber as radial distance (markers at $\pi/4$ intervals), and element angle of incidence as azimuthal distance.



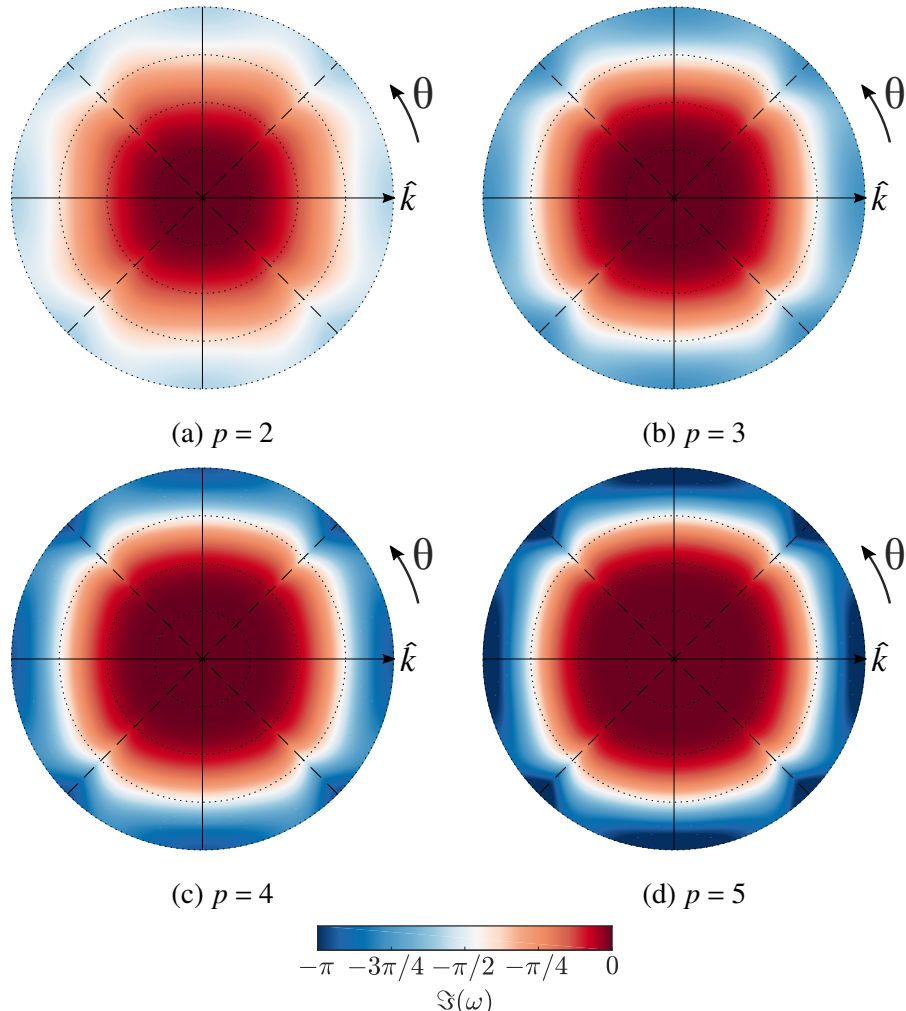


Fig. 4.11 Primary mode dissipation for 2D upwinded FR, with Huynh g_2 corrections, at various orders. Normalised wavenumber as radial distance (markers at $\pi/4$ intervals), and element angle of incidence as azimuthal distance.

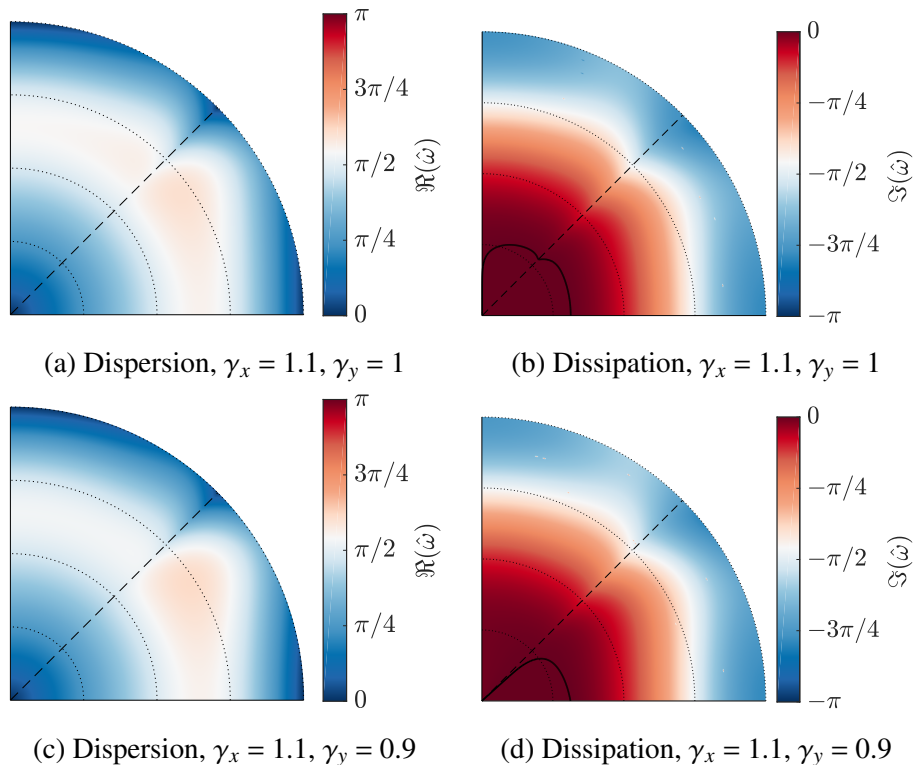
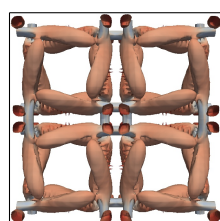


Fig. 4.12 Two dimensional upwind FR, $p = 3$ with Huynh g_2 corrections, for different grid expansion factors. Normalised wavenumber as radial distance (markers at $\pi/4$ intervals), and element angle of incidence as azimuthal distance. The solid black line on the dissipation plots is the contour of zero dissipation.



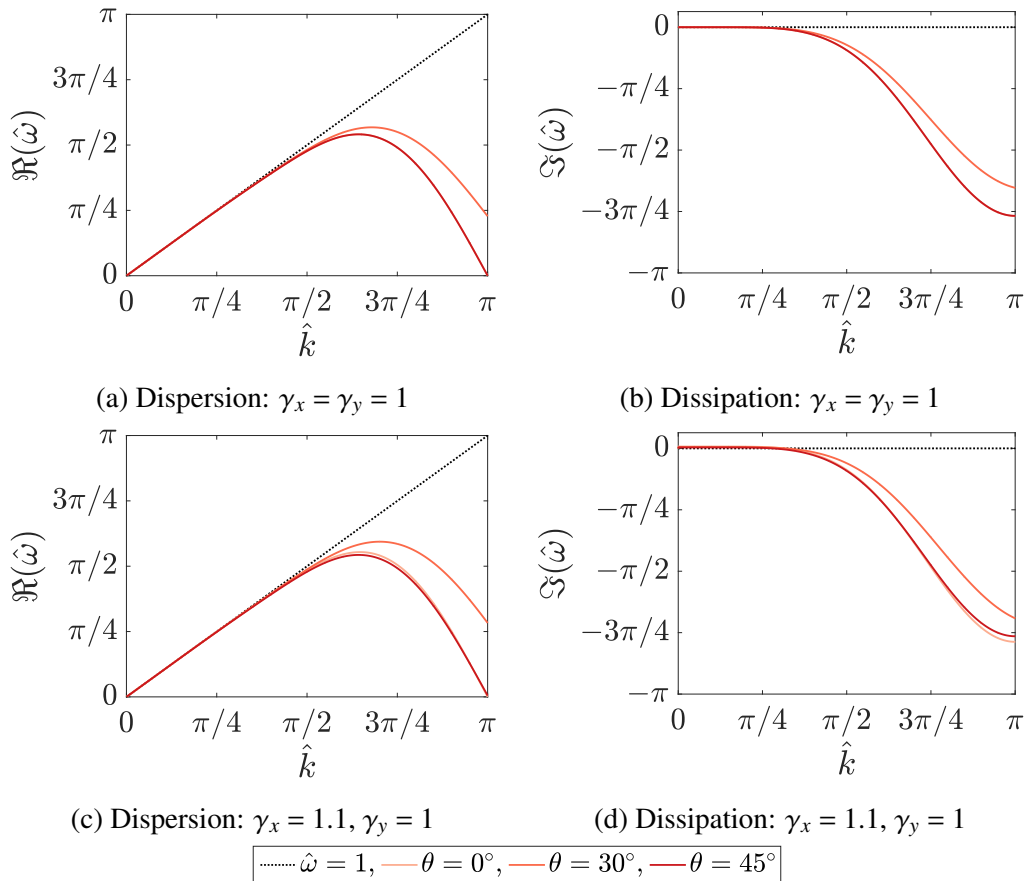


Fig. 4.13 Two dimensional upwinded FR, $p = 3$, with Huynh g_2 corrections at selected incident angles.

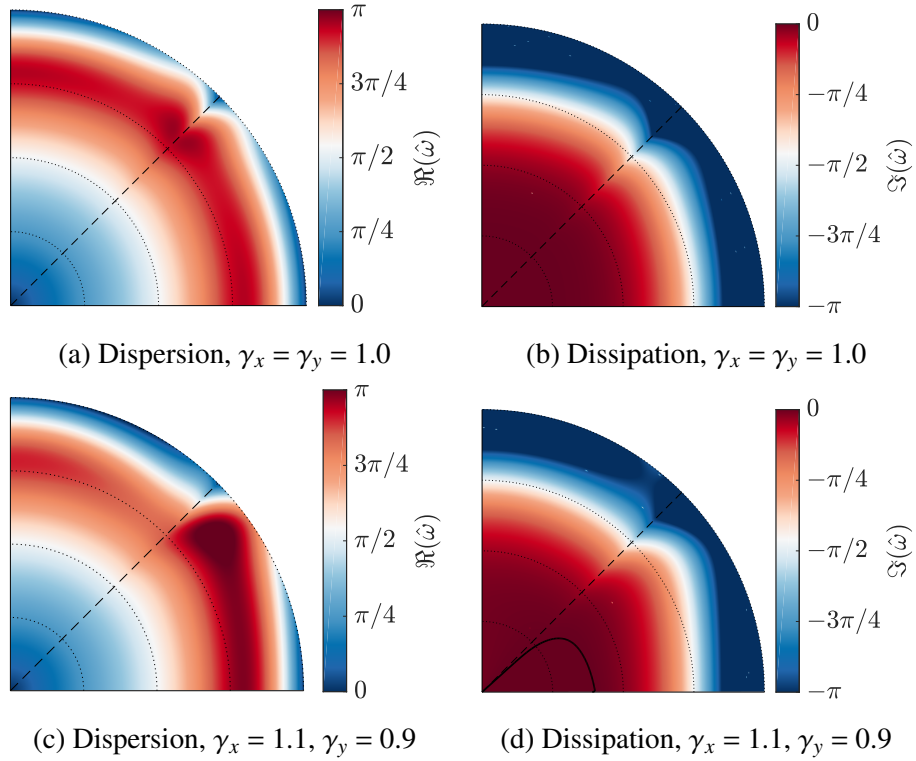
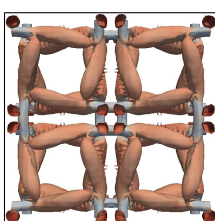


Fig. 4.14 Two dimensional upwind FR, $p = 3$ with NDG corrections, for different grid expansion factors. Normalised wavenumber as radial distance (markers at $\pi/4$ intervals), and element angle of incidence as azimuthal distance. The solid black line on the dissipation plots is the contour of zero dissipation.

$\theta < 45^\circ$ and as the incidence angle of the wave approaches $\theta = 0$ the stabilisation brought about by the contraction decays. The $\theta = 0$ case is identical to the case of $\gamma_y = 1$.

For completeness, we have included plots of the dispersion and dissipation for NDG in Fig. 4.14. By comparing the un-stretched and stretched results of Fig. 4.14a-4.14b to those of Fig. 4.14c-4.14d it is clear that the effect of stretching is similar to that seen with the Huynh g_2 corrections in Fig. 4.12. However, the notable between NDG and Huynh's g_2 corrections is that NDG exhibits more dissipation at higher wavenumbers, as well as dispersion overshoot. This is difficult to see precisely in Fig. 4.14, but is indicated by the darker band at $\hat{k} \approx 3\pi/4$. Furthermore, the location of the zero dissipation contour is different between the two correction functions, which for NDG is at a higher wavenumber. This is caused by the unstretched NDG having lower dissipation at lower wavenumbers. As is seen by comparing Fig. 4.14b and Fig. 4.12b.

Lastly, for this investigation into the dispersion and dissipation characteristics of FR, we wish to make a note on the Nyquist frequency of the elements. As was also the case for 1D stretched elements, the Nyquist frequency has a dependency on the expansion ratio. This is found from the harmonic mean of the 1D Nyquist frequencies, then normalised by



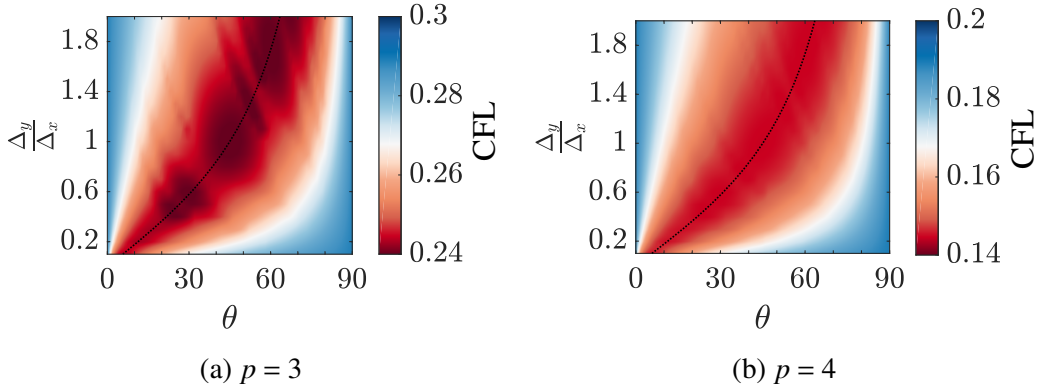


Fig. 4.15 Effect of varying: the relative size an element in x and y ; the angle of incidence; and CFL in 2D for upwind FR. The method of temporal integration used here was RK44. (.....) $\Delta_y/\Delta_x = \tan\theta$

the element size at that angle. Hence, the normalised wavenumber is then:

$$\hat{k} = k/k_{\text{nq}} = k \max \{ \cos(\theta), \sin(\theta) \} \left(\frac{1}{p+1} \right) \sqrt{\left(\frac{\cos(\theta)}{\gamma_x} \right)^2 + \left(\frac{\sin(\theta)}{\gamma_y} \right)^2} \quad (4.51)$$

Effect of Grid Aspect Ratio on CFL Limit

Beyond the resolution of the scheme, is the question of setting up a case and running it on some machine. For this, knowledge of the temporal stability is key and we will begin by looking at the effect of the relative size of an element in x and y on the CFL limits of FR. In this case, the grid is not expanding or contracting, merely the ratio of Δ_x to Δ_y is varied.

As can be seen from Fig. 4.15 there is a clear impact on the CFL limit of FR when elements are rectangular, with no change in the CFL limit when the waves are aligned with the grid. What is evident is that the angle of incidence where the CFL limit is smallest, for a given size ratio, is when a wave is incident at an angle of $\tan^{-1}(\Delta_y/\Delta_x)$. This angle corresponds to the maximum length across the element and hence, when the wave is decomposed into x and y components, the wavenumbers are lowest — *i.e.*, $\inf_{\theta \in \mathbb{R}} (\sup \{ \Delta_y \cos(\theta), \Delta_x \sin(\theta) \})$ when $\theta = \tan^{-1}(\Delta_y/\Delta_x)$. As the wavenumbers will be at their lowest necessary to form the wave, from the 1D dissipation of FR, the dissipation will also be at its lowest. Therefore, there is less dissipation in the spatial scheme available to counteract the negative dissipation of the temporal scheme, hence reducing temporal stability at $\theta = \tan^{-1}(\Delta_y/\Delta_x)$.

Effect of Grid Expansion on CFL Limit

Now we introduce to the grid an expansion or contraction in x and y , with varying incident angles. The results of these distortions are shown in Fig. 4.16. The minimum CFL limit is seen to be at $\theta = 45^\circ$, with temporal performance peaking as expected at $\theta = 0^\circ, 90^\circ$. This result agrees with that of Fig. 4.15. However, this also shows that the angle of minimum CFL is only dependent on the local element shape, and in the case investigated here the central element is always square. Furthermore, when the CFL limit in the quasi-1D case ($\theta = 0^\circ, 90^\circ$) is compared to the results of Trojak et al. [118], the CFL limit is found to be lower than the 1D case. This may be due in part to the increased modes of the system and their coupling leading to a less stable system. This decrease is corroborated by numerical tests, and the analytical reasoning will follow shortly.

A second point to note is that for non-grid-aligned waves the expansion or contraction in both components affects stability. With a contraction orthogonal to expansion again helping to stabilise the scheme. This point is subtle, because if the decomposition of the wave into x and y were linearly independent then it would be expected that the lowest CFL limit would dominate. However, this result demonstrates that there is coupling between the x and y components — which could be used advantageously, as was discussed earlier.

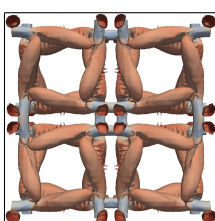
Throughout the analytical tests in which waves were injected at incidence on a square central element, the Nyquist wavenumber was found to be $k_{nq,\theta} = k_{nq,0}/\cos(\theta)$ for $0^\circ \leq \theta \leq 45^\circ$. This result can be understood in one of two ways. Firstly that a wave at an angle can draw on more points in the normal direction to form a fit of higher wavenumbers. Or that the wave can be thought of as being a coupled decomposition of the wave into the x and y directions, and although it has been said that these are not independent, this does mean that higher wavenumbers can be supported.

To understand further why expanding meshes are less stable and contracting meshes more stable it can be illuminating to consider the 1D linear advection equation, which for upwinded FR can be written as:

$$\frac{\partial \mathbf{u}_j}{\partial t} = -J_j^{-1} \mathbf{C}_0 \mathbf{u}_j - J_{j-1}^{-1} \mathbf{C}_{-1} \mathbf{u}_{j-1} \quad (4.52)$$

where \mathbf{C}_{-1} and \mathbf{C}_0 are defined similarly to \mathbf{C}_L and $\mathbf{C}_{0,\xi}$ in Eq.(??). Then using Euler's method to temporally integrate this equation, we find:

$$\mathbf{u}_j^{n+1} = \mathbf{u}_j^n - \tau(J_j^{-1} \mathbf{C}_0 \mathbf{u}_j^n + J_{j-1}^{-1} \mathbf{C}_{-1} \mathbf{u}_{j-1}^n) = (\mathbf{I} - \tau J_j^{-1} \mathbf{C}_0) \mathbf{u}_j^n - \tau J_{j-1}^{-1} \mathbf{C}_{-1} \mathbf{u}_{j-1}^n \quad (4.53)$$



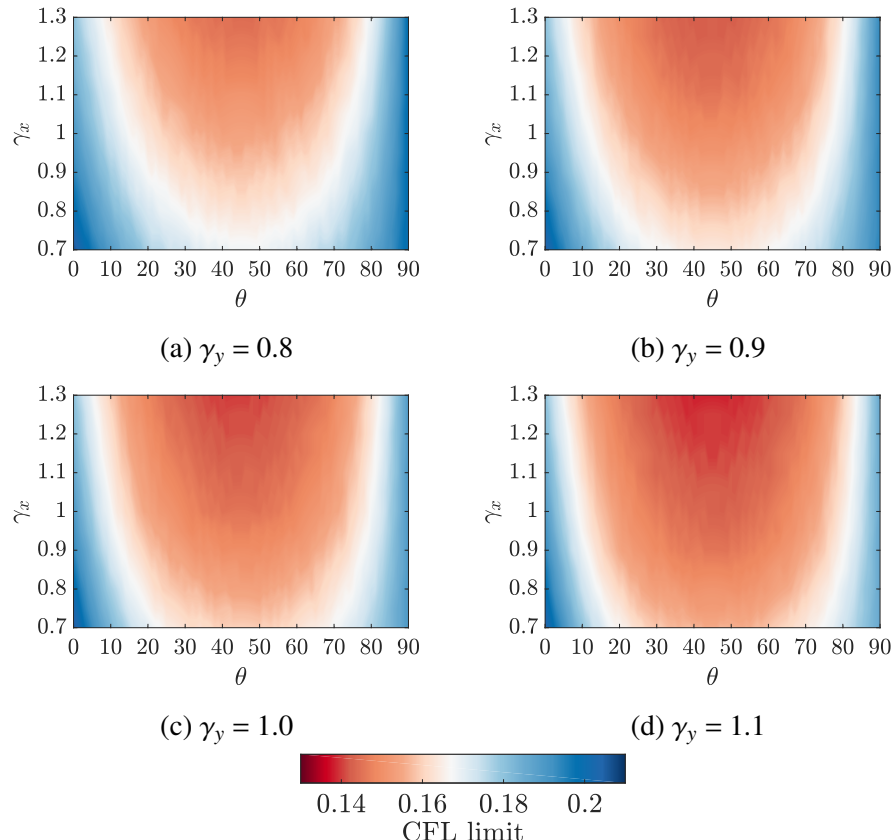


Fig. 4.16 CFL limit for 2D linear advection with FR ($p = 4$) using Huynh correction function, showing variation with θ and γ_x for some set values of γ_y . Time integration is RK44.

where the superscript n denotes the time step. If $u_{j-m-1}^{n-m} (\forall m \in \mathbb{N})$ is then recursively substituted, the final form is then:

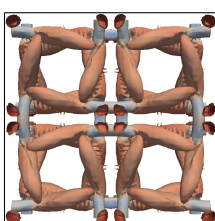
$$\mathbf{u}_j^{n+1} = \frac{1}{2} \sum_{m=0}^{\infty} (\mathbf{I} - \tau(2\gamma)^m \mathbf{C}_0) \underbrace{(-2\gamma\tau \mathbf{C}_{-1})^m}_{\mathbf{T}} \mathbf{u}_{j-m}^{n-m} \quad (4.54)$$

where we assume the solution is on a geometrically expanding grid in order to substitute for the Jacobian — hence being only valid for linearly transformed elements. If we consider that \mathbf{C}_0 and \mathbf{C}_{-1} are linear operators, then rather than prescribing a solution, the dynamics of linear operators can be used [16]. So, if the mesh extends infinitely downwind, then it is sufficient to say that Eq.(4.54) is stable when it is a hypercyclic orbit. Hence, the stability criterion is that $-2\gamma\tau \mathbf{C}_{-1} = \mathbf{T}$ is a matrixable linear hypercyclic operator. The definition of which is that $\sup \|\mathbf{T}^n\| \leq 1, \forall n \in \mathbb{N}$, which in turn implies that $\rho(\mathbf{T}) = 1$. What this aims to show is that the stability criterion is dependent on the product of τ and γ , as well as on \mathbf{C}_0 . Therefore, as γ increases the maximum stable τ decreases, for constant \mathbf{C}_{-1} . This also explains that although the scheme may be formally unstable, correct setting of τ for a given γ can lead to a \mathbf{T} that is still hypercyclic and give a bounded solution. However because of the $(-1)^m$ this does mean that if $\mathbf{U}_{n-1} \subset \mathbb{R}$ is the set of solutions at some time step $n-1$, then the solution $\mathbf{u}_j^n \notin \mathbf{U}_{n-1}$ i.e, for a sinusoidal solution the computed value may exceed the prescribed magnitude.

Effect of Grid Expansion of Fully Discrete Dispersion and Dissipation

Following on from the exploration of grid expansion on temporal stability limits, we will present the fully discretised Fourier analysis in two dimensions. In this investigation, we look at the dispersion and dissipation of Huynh g_2 correction functions for several expansion ratios. Throughout this investigation as the angle is swept through from $0 - 90^\circ$ the time step will be held constant as this is reflective of practical applications.

Figure 4.17 displays the dispersion and dissipation relation for Huynh g_2 correction functions when fully discretised with RK44 explicit temporal integration. It should be noted that there are some anomalous artefacts in the data due to the complexity of sorting and selecting the eigenvalues. Primarily this shows that when fully discretised, the instability on expanding grids is still present. This is then coupled to the same behaviour that was observed by Vermerie et al. [126] and Trojak et al. [119]. Namely that the gradient of the dispersion can be much larger and hence the magnitude group velocity can be very large. Also observed, which is seen here, is that as the explicit time step is increased the dissipation is reduced, with the largest difference seen at higher wavenumbers. As a result the wavenumber at which $\Im(\hat{\omega}) = 0$ (the solid black lines) in Fig 4.17d & 4.17f is not appreciably changed compared to the semi-discrete results.



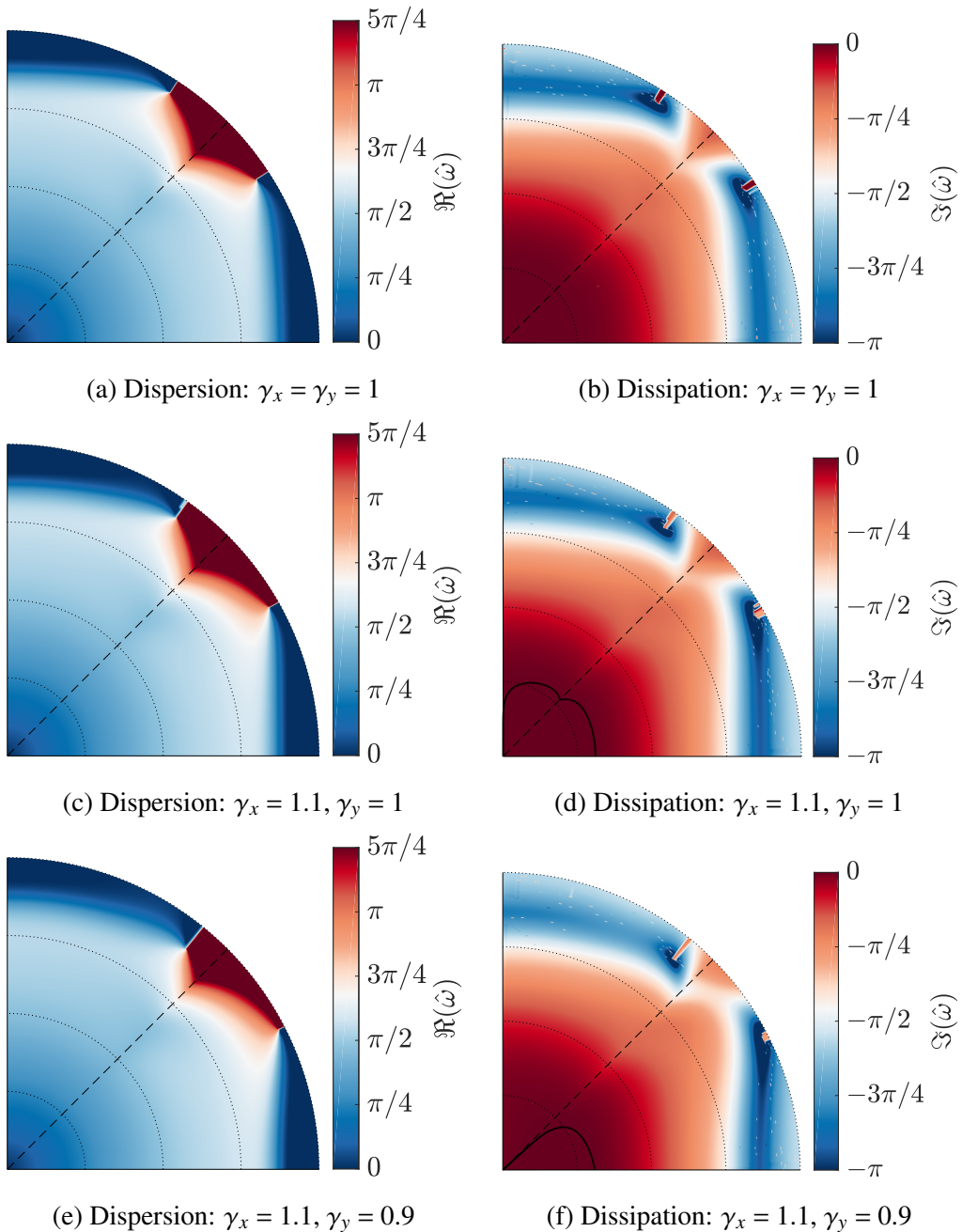


Fig. 4.17 Dispersion and dissipation of upwinded FR, $p = 3$, with Huynh g_2 corrections and explicit RK44 temporal integration, $\tau = 0.18$. The radial distance is the normalised wavenumber (including the effect of angle), and the azimuthal distance is the angle of incidence to the element. The solid black line on the dissipation plots is the contour of zero dissipation.

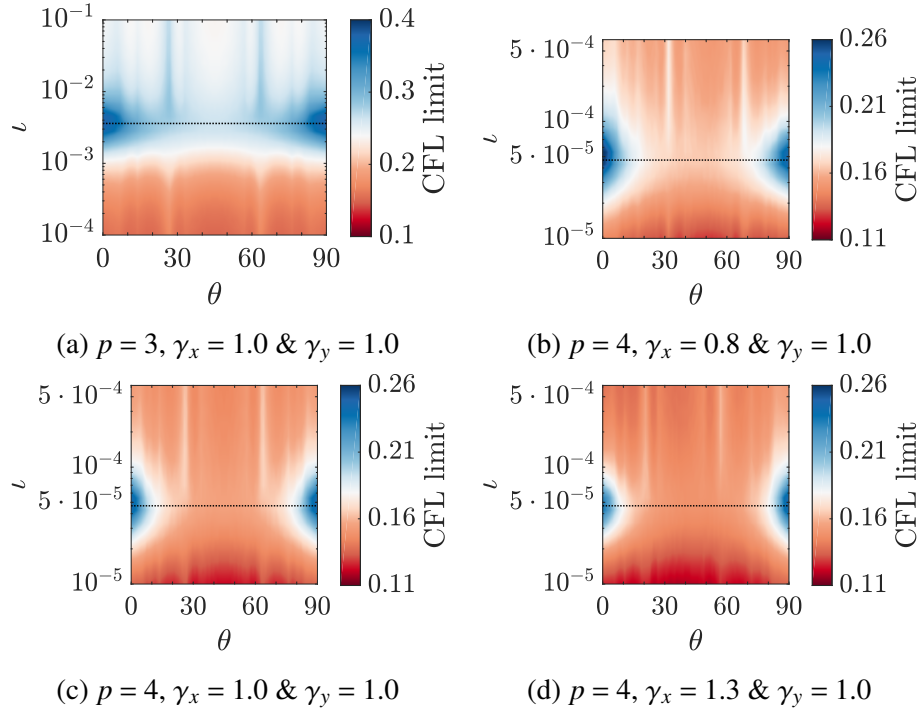
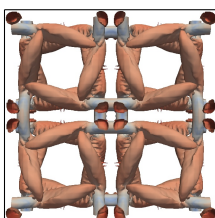


Fig. 4.18 CFL limit for 2D linear advection, at several orders. Varying correction function parameter, ι , and angle θ . Time integration is RK44. The value of ι_+ is shown as a dashed black line.

However, in Fig 4.17 there are regions of significantly increased and decreased dissipation at high wavenumbers. The general impact that these results show is that, when fully discretised, FR becomes more heterogeneous.

Effect of Correction Functions with Grid Expansion

As was mentioned in section ??, a series of correction functions with peak temporal stability and spatial accuracy was proposed by Vincent et al. [128], defined by a correction parameter, ι_+ . These correction functions exhibited the superconvergence expected of Nodal DG (Cockburn et al. [31]), however $\iota_+ \neq \iota_{\text{DG}}$ as they account for the variation in the dispersion caused by the discrete temporal integration. We wish to investigate if the advantage of this family of correction functions is maintained in 2D or if an analogue can be found. Therefore, the correction function parameter is varied for different angles and grid expansion rate, the results of which are presented in Fig. 4.18. Using Fig. 4.18c as an example, the peak CFL at ι_+ can be seen clearly in the case of $\theta = 0^\circ$, with its peak value reduced in comparison to the 1D case. (This was discussed in section 4.3.2. However, the clear peak at $\theta = 0^\circ, 90^\circ$ does not significantly persist as the wave angle increases to $\theta = 45^\circ$, with the peak becoming substantially flattened. Therefore, the balancing effect that the modification of correction function has on the dispersion of the scheme



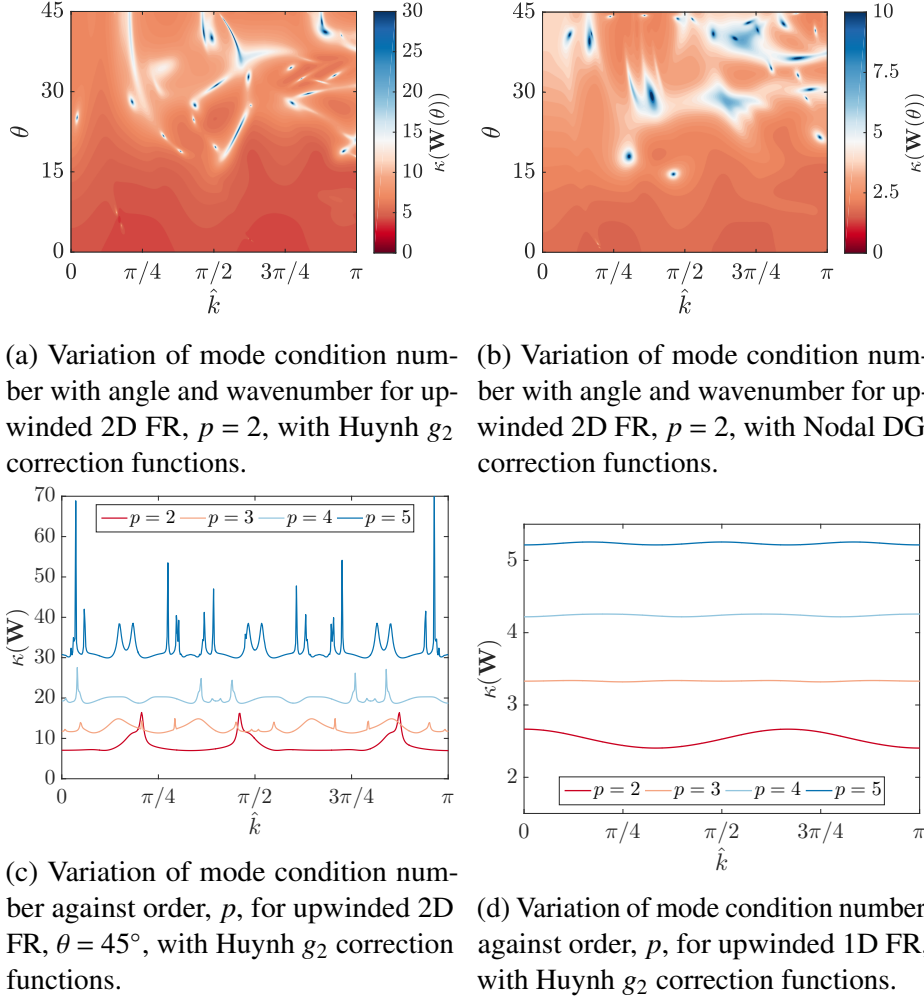


Fig. 4.19 Condition number of various linear FR configurations

seems to have a limited scope. Also, it seems there is no other correction function able to achieve the same effect at the intermediate range of angles. Furthermore, the persistence of the peak CFL limit is not seen as the expansion rate and order is varied, with ι_+ , in fact, suffering the most appreciable decay in performance as the angle is varied, when compared to the other correction functions.

To investigate further the impact of varying correction functions on higher dimensional problems, we will consider the projection of the solution into the functional space of FR for linear advection. The method for understanding this is by studying the posedness of the linear operators. The process of projection was outlined in section 4.2.2. Presented here are the several results showing how the posedness varies with angle, correction function, and order.

Several insights into the different multidimensional behaviour of FR can be gained by studying Fig. 4.19. By comparison of Fig. 4.19a & 4.19b it can be seen that Huynh's

g_2 correction function causes the projection to be more ill-posed on average compared to Nodal DG methods. Hence, the superconvergent DG recovering scheme of Vincent et al. [128] has decreased temporal stability. This is because the ill-posedness indicates the sensitivity of the reconstruction to change, a more sensitive reconstruction means that error can result in energy being transferred to more dissipative modes. This point is important as it means to show that ill-conditioning is not directly the mechanism for loss. But the movement of energy to other more dissipative modes is, and the condition number is symptomatic of that.

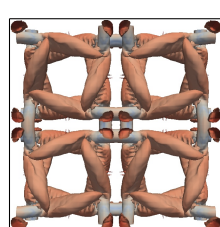
Furthermore, in both cases as, across all wavenumbers, the condition number can be seen to increase with incident angle. When compared with Fig. 4.16 and Fig. 4.18c it can be seen that for a given correction function the CFL limit reaches its minimum at $\theta = 45^\circ$, therefore a stark increase in condition number can also cause a decrease in temporal stability, potentially due to too much transport between modes.

A result presented by Trojak et al. [118] was that for FR the best points per wavelength (PPW) performance was seen for $p = 4$ with the PPW increasing for orders higher than this. A result that is exhibited by Fig. 4.19c is that the condition number for $p = 5$ schemes is higher than for lower orders and may have passed a point where increased order is out weighted by inaccuracy in ill-conditioning. This may explain the optimal result seen and is touching on the fundamental problem characterised by Runge's phenomena, that high-order may introduce accuracy through high-order but may also introduce inaccuracy reflected by a high condition. A result that cannot be clearly seen in either Fig. 4.19a or 4.19b, however, was exhibited by FR was for $\theta = 0$ the condition number was significantly higher than that found for 1D FR owing to the naturally poor conditioning of a 2D system acting as a quasi-1D one. This is linked to the lower CFL number experienced in this case, as was shown in Fig. 4.16. To show that the results found in this section extend to higher dimensions, the von Neumann analysis was repeated for 3D 'hexi-linear' grids. The primary result of interest is the increased condition number of the functional projection and this can be seen in Fig. 4.20. The message is that, as expected, the ill-posedness of the reconstruction increases with the order. While small increases in the condition number can give increased temporal stability, larger increases in condition number tend to act to destabilise the coupled spatial-temporal scheme.

4.4 Numerical Experiments

4.4.1 One-Dimensional Linear Advection Equation on Stretched Grids

The analytical procedures set out up to this point have been semi-discrete and idealised. For CFD practitioners the comparative performance and implemented performance of



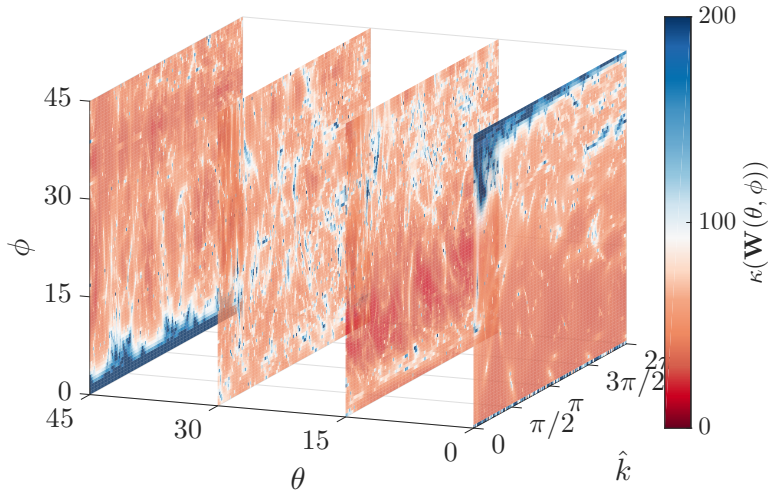
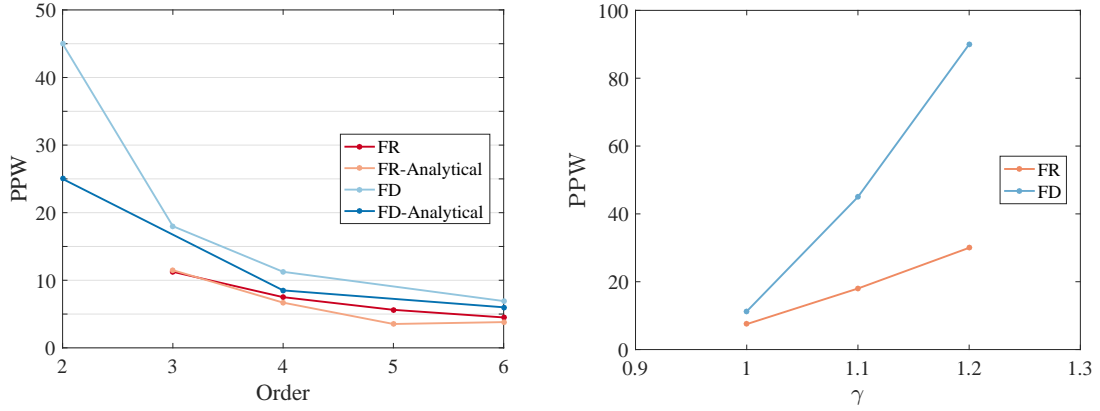


Fig. 4.20 Variation of condition number with wave angles and wavenumber for upwinded 3D FR, $p = 3$, $\gamma_x = \gamma_y = \gamma_z = 1$, using Huynh g_2 correction functions.

FR is highly important. From this the process of mesh generation can be informed as well as greater understanding of the expected results gained. To this end, numerical tests are performed for wavenumbers $0 \leq k \leq k_{nq}$, where k_{nq} is the Nyquist wavenumber for a uniform mesh of unit length. For the purposes of comparison, k and k' (the modified wavenumber) are normalized by the mesh averaged Nyquist wavenumber. This gives $0 \leq \hat{k} = \pi k / k_{nq} \leq \pi$ and $0 \leq \Re(\hat{k}') = k' / k_{nq} \leq \pi$.

Finite Difference (FD) schemes are used to provide a comparison akin to high quality industrial codes. At higher orders, central difference schemes begin to become unstable as, for unstretched grids, second order and greater central difference schemes offer no dissipation. Therefore, the only sources of numerical error are from dispersion and temporal integration. Because of this, and as increasing order leads to better dispersion performance, the cell Reynolds number increases. The result is that FD schemes at intermediate wave numbers become unable to damp out disturbances. (It must be noted that due to the very low CFL number, the temporal scheme introduces negligible numerical error). This is combated by adding smoothing to the solution, a common practice in industry, and is here accomplished by adding a small amount (0.5 – 2%) of Lax-Friedrichs differencing.

Two key points are highlighted by Fig. 4.21a. The first of these is that FR requires fewer PPW than FD schemes at equivalent order. Importantly, this means that coarser meshes can be utilised by FR for similar wave resolving characteristics to FD schemes at the same order. It is believed that the increased accuracy of FR originates from the polynomial reconstruction in a reference sub-domain, hence the propagation of information in FR is largely controlled by the correction function, which can lead to



(a) Points per wavelength (PPW) for 1% error against spatial order of FD and FR schemes. FD schemes are central differencing except order 3, which is upwinding. DoF = const. = 180 and $\tau = 1 \times 10^{-4}$ s. The analytical results shown are found from Eq. (4.10) and similar analysis.

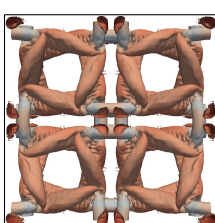
(b) PPW against mesh stretching factor for 4th order FD and FR schemes. DoF = 180 and $\tau = 1 \times 10^{-5}$ s.

Fig. 4.21

superior performance. Whereas, FD methods use a stencil, for which information can freely propagate through, hence a less coherent solution is produced due to each point effectively producing its own polynomial fit of the solution.

Secondly, Fig. 4.21a shows a discrepancy between the theoretical and analytical results for both FR and FD. The origin of the error in both of these schemes is the numerical diffusion. For FD, this is due to the scheme's subtle instability, meaning that for useful implementation, some diffusion must be added to ensure the survival of the solution. FR is also affected by numerical diffusion, but this is caused by its own intrinsic dissipation, apparent in Fig. 4.6. When numerical tests are run, the dispersion and dissipation are inseparable and although a dispersion relationship of sorts can be found, it is impacted by the dissipation of the scheme damping out higher wavenumbers. This is the reality of any application of a scheme and so it can be informative to run both analytical and numerical tests as the numerically derived PPW shown in Fig. 4.21a are those that an end user will experience. The same effect can be seen in Fig. 4.21b: as the mesh becomes stretched the PPW rises more quickly than the analytical results would predict. This is caused by the onset of dissipation at lower wavenumbers for deformed meshes, but, importantly, a wave passed through a multi-element mesh will have the transfer function applied multiple times, thereby causing greater attenuation.

Results of great significance displayed both numerically and analytically show that FR has the ability to resolve waves better than FD schemes and that FR is more numerically robust when applied to geometrically stretched meshes, with FR requiring 33% of the



mesh points compared to FD in 1D for severely stretched meshes ($\gamma = 1.2$ at fourth order). Moving to two or three dimensions, this result, in the most extreme examples, can be 11% or 4% respectively. The increased ability of FR to handle stretched meshes is again because of the localised fitting within sub-domains, and here the linear transformation caused by the stretching of the elements is exactly captured in the Jacobian. For this case the impact of adjacent cell stretching is felt only through convection of the solution through one interface. However, for a fully compressible Euler or Navier-Stokes implementation the effect of adjacent cells could be increased as Riemann solvers at all interfaces would be necessary and will give rise to more inter-cell communication.

To further understand the stability of the full numerical scheme it is necessary to consider the spatio-temporal coupling. In the previous section the effect of this coupling was considered and it was said that for $p \geq 3$ on expanding grids, the behaviour is slightly different, *i.e.* $\rho(\mathbf{R}) \geq 1 \forall k$. The implication this has for the stability of higher order expanding grids is not clear from the spectral radius, however, because as the wave moves through the expanding grid \hat{k} will increase, so the scheme dissipation will add a stabilising effect. To show this, a similar numerical method is used, however now taking a spatial slice for various orders, wavenumbers, and grids. Figure 4.22 shows two such slices. Initially, the fed wave shows some instability but advection through the grid means dissipation from the spatial scheme will begin to cancel some of the negative dissipation of the time scheme. The result is that after an initial band of instability both orders show recovery of the solution before beginning to decay on the sparser cells.

This also illustrated a limitation of the analytical approach adopted here - that taking a solution of the form of Eq. (4.8) means that the solution is static, *i.e.* evolutions of the solution from far upstream are not permitted. Again, this emphasises the importance of running numerical tests alongside analytical ones.

4.4.2 Two-Dimensional Eulers Equation with Randomised Grids

Few problems confronted in engineering are ever sufficiently simple that they can be solved with sufficient accuracy by 1D methods, making extension to higher dimensionality crucial. Two dimensions also allows for a greater range of geometrical deformations to occur, even while maintaining a linear transformation of elements. Included within this, each element has a higher number of degrees of freedom, revealing a potential mechanism for inaccuracies to enter the solutions. To evaluate the effect of higher dimensionality the isentropic convecting vortex (ICV) test case is used, as it has a known analytical solution, so numerical error can be straightforwardly calculated for the Euler equations. A mixture of mesh qualities are to be tested, so mesh quality was artificially reduced by stochastically jittering corner nodes of a uniform grid via time seeded random

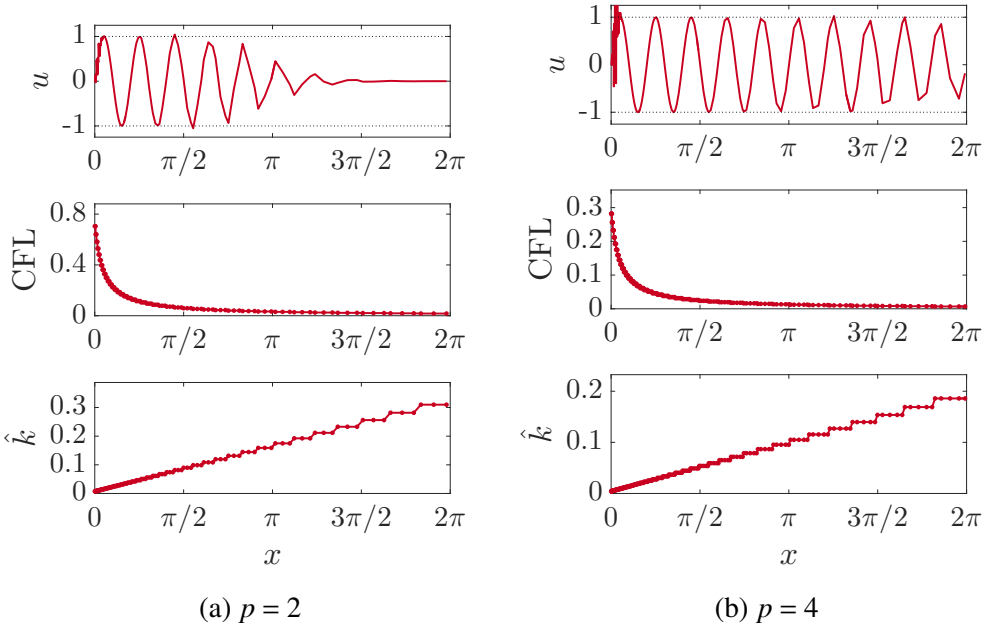


Fig. 4.22 For 3rd order and 5th order FR on an expanding grid with $\gamma = 1.1$ using RK44 time integration a spatial slice is shown. With the convected parameter u , the CFL number and the Nyquist normalised ($\hat{k} = \pi k / k_{nq}$).

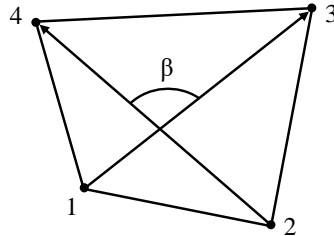
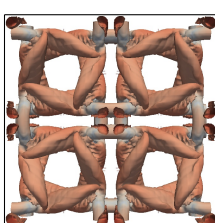


Fig. 4.23 Cross diagonal angle definition. $\alpha = \beta - 90^\circ$.

numbers. The degree of jitter is controlled by a multiplying factor and the mesh quality and warp is then characterised by a skew angle. This is defined as the mesh average absolute angle by which the element cross diagonals deviate from square (Fig. 4.23) and encompasses both the skewness and aspect ratio of a mesh. Some sample meshes are shown in Fig. 4.24a - 4.24c.

A finite volume (FV) scheme (a simplified version of T-block), with the same explicit time integration as used in the FR calculation was used for performance comparison, as it is representative of a family of schemes widely used in industry. To evaluate the spatial error, the temporal error has to be minimised by use of an appropriately small time step, which in this case corresponds to $CFL = 0.01$. ($CFL = 0.05$ & 0.005 were also tested and the error was found to be independent of the temporal scheme at this level). By



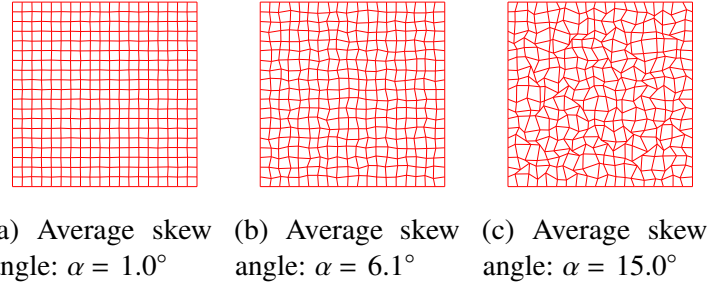


Fig. 4.24 19×19 quadrilateral meshes showing differing degrees of node jittered mesh warp.

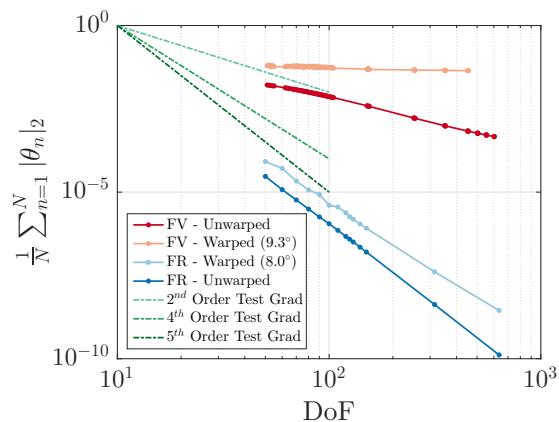


Fig. 4.25 Point averaged l_2 norm of error, $\frac{1}{N} \sum_{n=1}^N |\theta_n|_2$, against degrees of freedom (DoF) for $p = 4$ FR and nominally second order FV scheme. $CFL = 0.01$ for 3000 time steps.

comparing the exact solution, u , and computed solution, u' , the error, θ , can be calculated and the spatial order of accuracy (OOA) can be obtained:

$$\theta = u - u' = O(\delta^{p+1}) \quad (4.55)$$

Recovery of the spatial OOA is shown in Fig. 4.25, *i.e.*, $OOA = p + 1$, and a comparison can be made with the 5^{th} order test gradient to see this. The plotted results for the FV scheme display an $OOA \approx 2$, as well as a large increase in the cell averaged l_2 error compared to FR for the same number of Degrees of Freedom (DoF). Also shown in Fig. 4.25 are the results of moderate mesh warping. In FR's case, a move towards $OOA \approx 4$ occurs, and the FV scheme result becomes unphysical, *i.e.* $OOA = 0$.

A more detailed investigation into the deterioration of the spatial order is performed via variation of the degree of node jittering. Tests were run with $CFL = 0.01$ for 500 time steps (again, results were found to be independent of CFL number at this level). The results of numerical tests and a predictive procedure are shown in Fig. 4.26. The predictive procedure uses the error data from a mesh of fewer degrees of freedom together

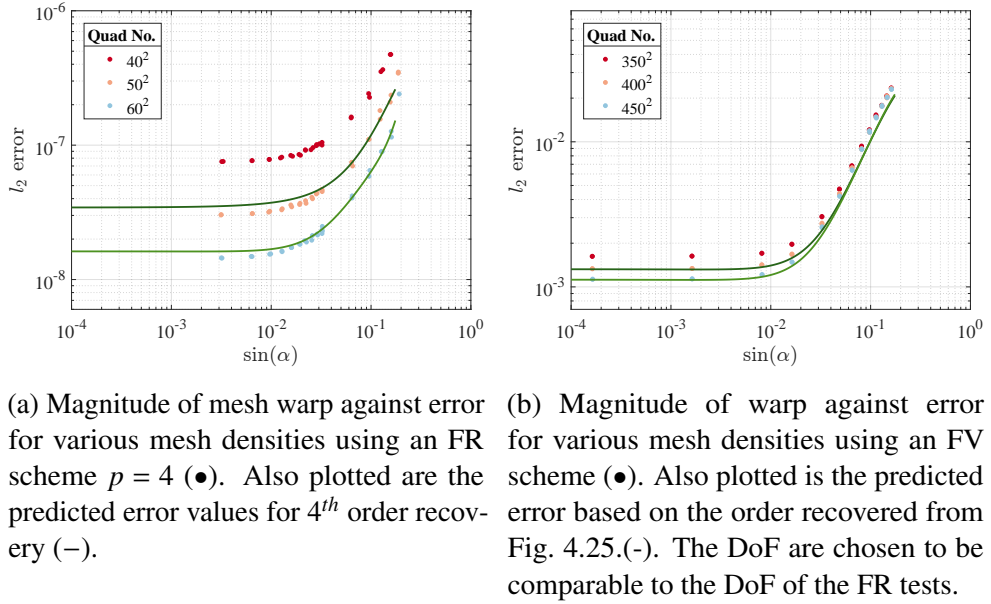


Fig. 4.26

with the desired OOA to make a prediction of the error at a higher quantity of degrees of freedom.

Figure 4.26 shows that, consistent with Fig. 4.25, at low skew angles, FR's OOA is unaffected by mesh quality: $\text{OOA} \rightarrow p + 1$ as $\alpha \rightarrow 0^\circ$. Figure 4.26a then confirms that on poorer quality meshes the OOA drops by approximately one, here shown as a drop from $\text{OOA} = 5$ to $\text{OOA} \approx 4$, this is shown by comparison to the 4th order predicted error line. This warp induced change occurs at $\alpha \approx 1.5^\circ$, and as mesh skewness increases to its maximum, FR is still able to give an accurate solution. By comparison the FV scheme (Fig. 4.26b) undergoes warp induced error change at $\alpha \approx 0.55^\circ$, transitioning from $\text{OOA} \approx 2$ to $\text{OOA} = 0$. Although the FV scheme is much simpler, this shows that the performance of such schemes widely used in industry can be rapidly eroded by a lack of mesh quality.

The root cause of the loss of order accuracy of FR on warped grids is not fully revealed by these tests. The Jacobian that maps between the physical and computational domain in this case provides an exact mapping due to the node jittering providing a linear transformation. Hence, error is not introduced to the convective velocity through the Jacobian. The additional error has two potential sources. Firstly the linear component of FR could introduce error via ill-conditioning of the projection to the functional space when waves are advected at an angle. Secondly, Jameson et al. [64] derived the aliasing error for 1D non-linear problems in the FR framework, yet in higher dimensions, on arbitrary grids, cross multiplication of projection terms will be present. Therefore, as the

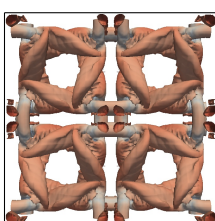


Table 4.2 Comparable errors in a 2D ICV test for FR and FV schemes.

	Flux Reconstruction	Finite Volume
Point Averaged Error	4.7×10^{-5}	4.01×10^{-5}
Wall Time	1.6 s	639 s
Cells	64, $p = 4$	4,000,000

mesh become skewed aliasing has the scope to introduce larger quantities of error. Both of these topics are quite expansive and are left for further investigation.

As a final aside to illustrate the increase in performance that FR offers compared to a typical FV method, the ICV test case on a uniform mesh was used. For this test the number of degrees of freedom was varied such that the grid averaged l_2 error was comparable - this was done with a CFL = 0.01 for 100 time steps. (A small variation of the CFL number was made and the results were found to be invariant with CFL number). The test was carried out on a single core of an Intel® Xeon® L5630 which was otherwise idle. The results of testing are shown in Table 4.2, and show that FR requires ~ 2.6 orders of magnitude less wall time for the same error in 2D as the FV method used here.

4.4.3 Three-Dimensional Navier-Stokes Equations with Randomised Grids

In the preceding analysis, the focus has been on theoretically exploring the linear advection equation. However, this has limited scope when applied to the equation sets that are considered practically. Therefore, we wish to understand what the effect of grid deformation is when we move to a full non-linear implementations of the Navier-Stokes equations, and how the behaviour observed for linear advection carries across.

It is very common within the CFD community to use the canonical Taylor-Green Vortex (TGV) [113] test case to assess the numerics of a solver applied to the Navier-Stokes equations with turbulence — and to that end there is a plethora of DNS data available for comparison [18, 36]. However, this case is quite contrived and ultimately will favour spectral or structured methods due to the Cartesian and periodic domain, whilst also being unrepresentative of engineering flows that are often wall bounded and/or have complex geometries. Hence, we propose linearly deforming the elements of the mesh by jittering the corner nodes to be more representative of real mesh conditions. Importantly, these deformation will introduce cross multiplication into the Jacobian, as well as local regions of expansion and contraction.

The initial conditions of the TGV being used here are those of DeBonis [36], where the character of the flow is controlled by the non-dimensional parameters defined as:

$$R_e = \frac{\rho_0 U_0 L}{\mu}, \quad P_r = 0.71 = \frac{\mu \gamma R}{\kappa(\gamma - 1)}, \quad M_a = 0.08 = \frac{U_0}{\sqrt{\gamma R T_0}} \quad (4.56)$$

where we will use the standard set of free-variables for the velocity, density, pressure, and gas characteristics:

$$U_0 = 1, \quad \rho_0 = 1, \quad p_0 = 100, \quad R = 1, \quad \gamma = 1.4, \quad L = 1 \quad (4.57)$$

Here, due to the solver implementation, we use a specific gas constant of unity and hence, to achieve the required Reynolds and Prandtl numbers, the dynamic viscosity and thermal conductivity can be set appropriately.

As has been stated, we will take the uniform periodic mesh on the domain $\Omega \in [-\pi, \pi]^3$, and jitter the corner nodes of the elements that are interior to the domain. The amount of jitter is calculated using a time seeded random number shifted to be centred about zero and scaled by a global factor between zero and unity. The scaling factor is such that zero gives a uniform mesh and unity could lead to edges of zero length. After jittering, the solution points are then linearly positioned within the element using the thin plate spline radial basis function together with the mapping from the uniform to jittered corner nodes. This gives a linear mapping of uniform solution points to solution points within the jittered elements. Finally, a quality metric is needed to describe, in a single number, the relative quality of the meshes produced. We opted for a volume ratio shape factor, slightly redefined as:

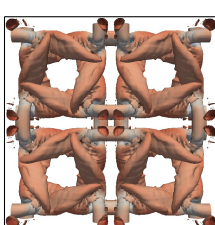
$$q_h = \frac{6 \sqrt{\pi} V_h}{S_h^{3/2}} \quad (4.58)$$

where S_h is the surface area of the hexahedral element and V_h is the volume of the hexahedral elements. The quality metric, q_h , is then defined as the ratio of the volume of the element to the volume of a sphere with the same surface area, with $q_h = \sqrt{\pi}/6$ for a perfect cube. To put this parameter into context, some example meshes are shown in Fig. 4.27.

The statistics that will be studied here are the decay of the kinetic energy and the enstrophy decay rate, which are defined respectively as:

$$-\frac{dE_k}{dt} = -\frac{1}{2\rho_0 |\Omega|} \frac{d}{dt} \int_{\Omega} \rho(u^2 + v^2 + w^2) d\mathbf{x} \quad (4.59)$$

$$\epsilon = \frac{\mu}{\rho_0^2 |\Omega|} \int_{\Omega} \rho(\omega \cdot \omega) d\mathbf{x} \quad (4.60)$$



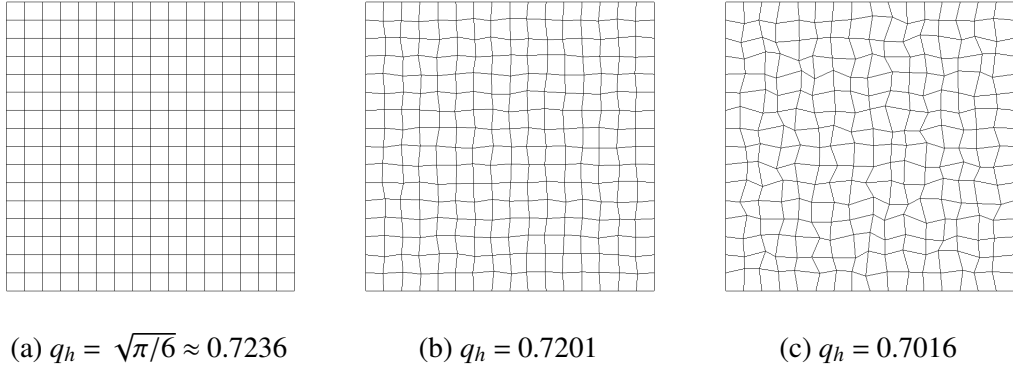


Fig. 4.27 Example slices through a 3D hexahedral mesh to illustrate the mesh quality metric.

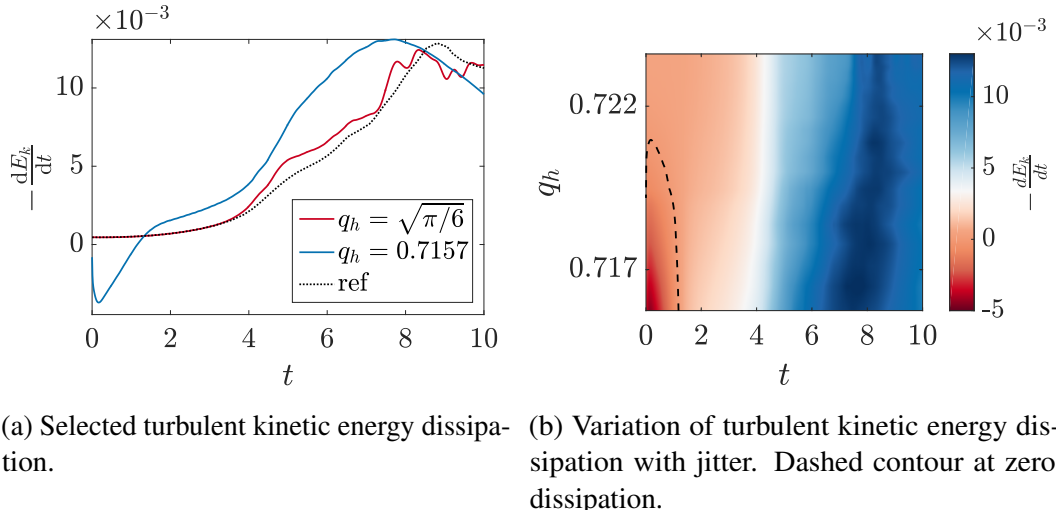


Fig. 4.28 Effect of jitter on turbulent kinetic energy dissipation of the TGV ($R_e = 1600$) for FR, $p = 2$, with Huynh g_2 correction functions on a 40^3 element mesh. Explicit time step size is $\Delta t = 1 \times 10^{-3}$.

where $\omega = \nabla \times [u, v, w]^T$ is vorticity and $|\Omega|$ is the domain volume.

Fig. 4.29 shows the first of these results. It may be observed that as the grid quality decreases there appears a period of time near the start of the simulation where the turbulent kinetic energy increases. As time progresses, dissipation is again seen and the point of peak dissipation arrives early, moving from $t \approx 8.5$ to $t \approx 7.5$.

The explanation of this is believed to be that initially the regions in the mesh that are locally expanding cause an increase in the energy due to the positive dissipation. This was discussed in Section 4.3.2, that for the linear advection equation, dissipation is positive at low wavenumbers for expanding grids and negative for contracting grids at the same wavenumber. It is thought that as the simulation progresses, the energy cascade of large scales to small scales then means that more of the solution lies in the

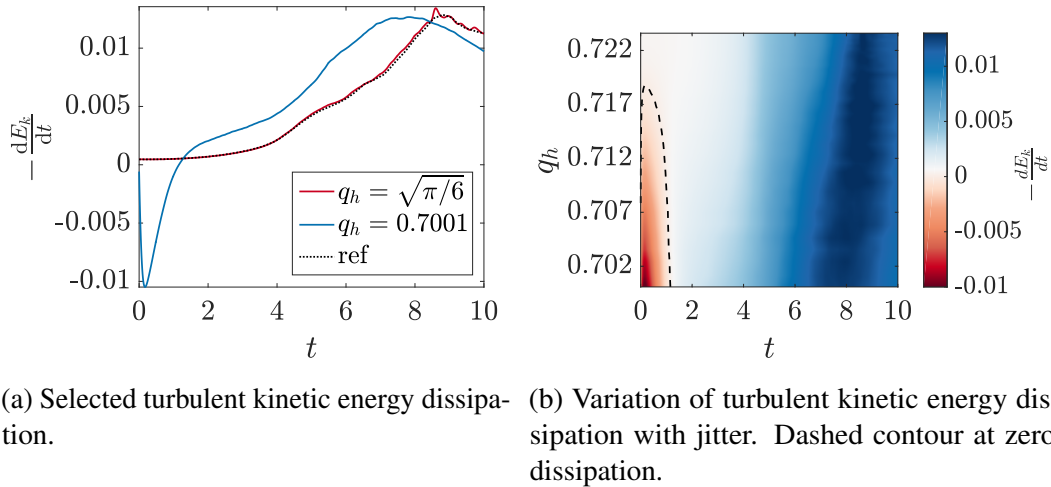
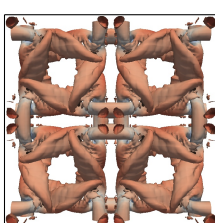


Fig. 4.29 Effect of jitter on turbulent kinetic energy dissipation of the TGV ($R_e = 1600$) for FR, $p = 4$, with Huynh g_2 correction functions on a 24^3 element mesh. Explicit time step is $\Delta t = 1 \times 10^{-3}$.

more dissipative higher wavenumber region for both expanding and contracting grids. Therefore, the net dissipation at later time is higher than the uniform case and hence the peak dissipation is earlier. This is consistent with a lower R_e and hence higher global dissipation. We can conclude that the stability of this case is brought about by the physics of the Navier-Stokes and cascade of energy from low to high wavenumbers, which side steps the problem of positive dissipation of low wavenumbers on expanding meshes. This result is interesting as it is in slight contradiction to the result of Trojak et al. [118] and the previous section, where FR was found to be more robust to grid for Euler's equations. However, in that investigation the Isentropic Convecting Vortex was considered where there was a large convective velocity. This may expose slightly different properties, although a full explanation is not known.

To provide some reference as to how FR performs relative to an established method we will use an edge-based Finite Volume (FV) method for comparison. The FV method is a standard central second order method with L2 Roe smoothing [92] for stabilisation, which has been validated previously [104]. The particular FR scheme used in this comparison is $p = 1$, giving second order, the same as the FV scheme. However, this puts FR at a significant disadvantage as its numeric characteristics at low order are particularly poor. For example, consider the dispersion and dissipation relations in Fig. 4.30, which, by comparison to the result of Lele [77], show that FR has noticeably lower resolving abilities when compared against a second order FD scheme.

With this in mind, we present the results of tests on various jittered grids with a total of 170^3 degrees of freedom in Fig. 4.31. For the uniform case the enstrophy clearly shows that FR is underresolved compared to FV, which is also shown by a slightly increased rate



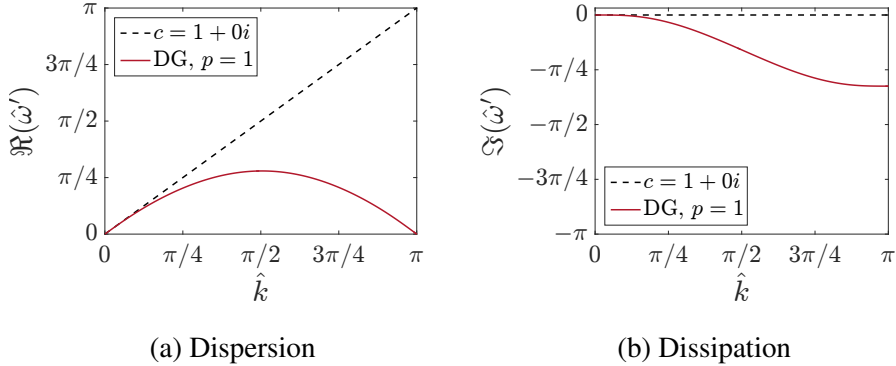


Fig. 4.30 Dispersion and Dissipation relation for 1D upwinded FR, $p = 1$, with DG correction function.

of dissipation earlier — indicating that the implicit filter is too narrow. If we now consider the effect of jittering, several things may be concluded. Firstly, we were unable to run FR with $j_f = 0.5$ as the simulation quickly became unstable. Secondly, for $-dE_k/dt$ it seems that the peak value is less sensitive with FR than with FV, with central FV seeing some very large amplitude oscillation in $-dE_k/dt$. This is likely to be rooted in the central differencing at the interfaces, as if we change to a kinetic energy preserving formulation [61, 134], as is displayed in Fig. 4.32, these oscillations are removed and the sensitivity to jitter is reduced. The enstrophy (Fig. 4.32b) seems to indicate that a large amount of what seemed to be resolved energy may have in fact been dispersion induced fluctuations. However, in both cases FV was able to run with grids up to $j_f = 0.9$ and $q_h = 0.6382$ — not shown — it appears that in these cases the added stability of the smoothing has greatly helped FV, especially in the central difference case where running without smoothing caused the case to fail even at low levels of jitter.

Before moving on it must be noted that in FR we once again see a dip in dE_k/dt , which is also present to a lesser extent in both versions of FV tested. This is again linked to the instability caused by locally expanding grids, but in the case of FV the dip is smaller and is aided by the use of smoothing. The conclusion for this comparison is that FV is somewhat resilient to degradation to the mesh quality, with the resilience coming from smoothing for central differenced FV. This allowed highly warped meshes to be run, but at the expense of accuracy with excess dissipation affecting the solution. KEP was found to be far more resilient and could even run without smoothing. FR, when run at low order, was unsuited to this problem, but did see less degradation compared to central FV and there is the potential for $p = 1$ FR to equally benefit on poorer quality meshes from smoothing via a different Riemann solver, such as Roe, or from the use of KEP [3].

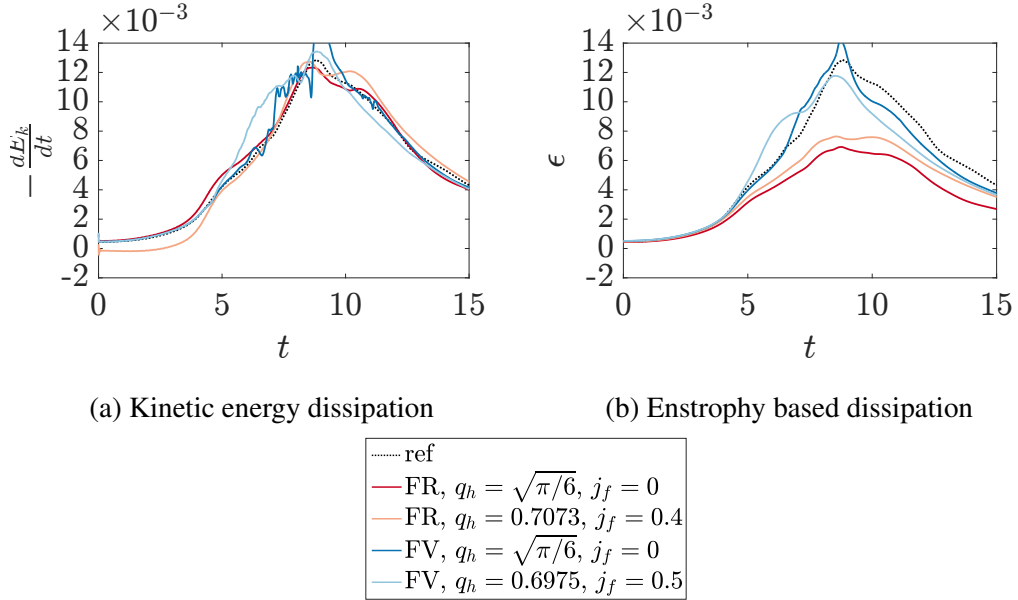


Fig. 4.31 Comparison of FR, $p = 1$ with DG correction functions with a second order central FV scheme with L2 Roe smoothing both with 170^3 degrees of freedom and $\Delta t \approx 5 \times 10^{-4}$. A reference DNS solution is provided from [18].

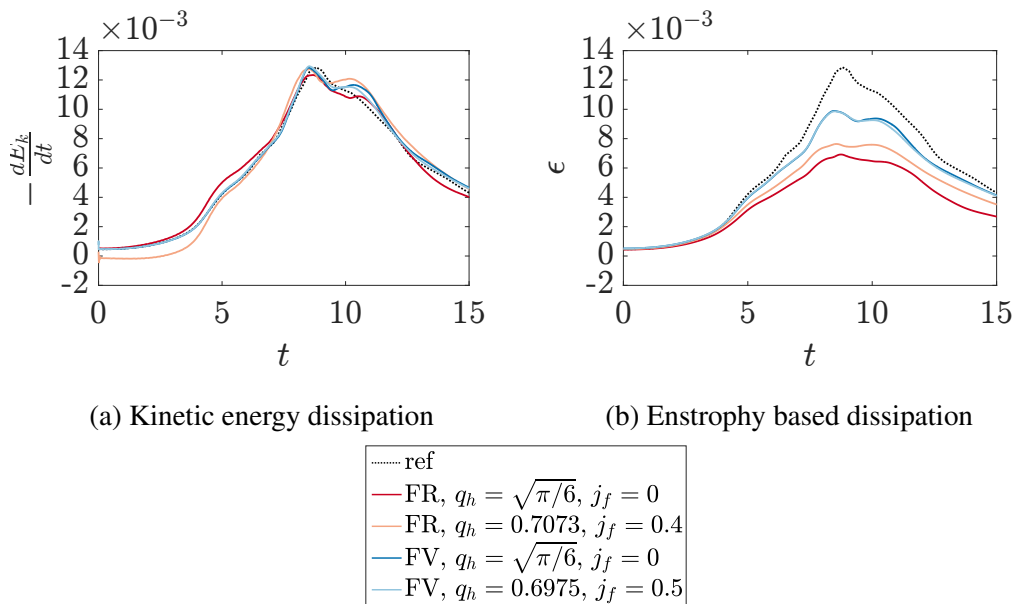
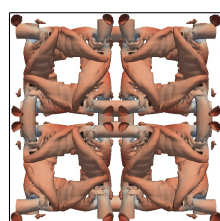


Fig. 4.32 Comparison of FR, $p = 1$ with DG correction functions with a second order KEP FV scheme with L2 Roe smoothing both with 170^3 degrees of freedom and $\Delta t \approx 5 \times 10^{-4}$. A reference DNS solution is provide from [18].



4.5 Conclusions

The use of FR on warped meshes is important for the likely future applications of the scheme. It has been shown that FR is more resilient to distorted meshes than some FD and FV families of schemes which are currently widely used in industry. A detailed look at the PPW of FR on stretched grids with varying order, as well as study of the FR stability criterion, shows that, depending on geometry, the order of the scheme can be varied to increased performance. In particular, within a given cell the correction function order can be directionally varied to increase wave resolving ability. It is also shown from the linear advection equation that the CFL limit with non-regular grids is dependent on the dominant wave direction, with contracting grids providing a stabilising effect. This is a feature of FR that will impact boundary layer meshes. It was proposed that the ill-conditioning of the functional projection of FR causes the degradation in accuracy for warped meshes. A more complete study of this is left as future work. Lastly, in some runtime comparisons, FR was found to require ~ 2.6 orders of magnitude less wall time for the same error in two dimensional test, compared to a widely used FV method.

Through this work we have presented a theoretical extension of the FR von Neumann analysis to higher dimensions. This allowed us to understand the character of the dispersion and dissipation relations of FR as the incident angle of a wave was varied. Differences were noted between the behaviours of FR and finite differencing methods, primarily that FR saw lower variation in character with angle. The effect of higher dimensionality on the CFL limit was also found, with higher dimensionality causing a reduction in the CFL limit.

Investigations were then performed on deformed meshes and theoretically the same behaviour was seen in two dimensions as in one. Specifically, that expanding meshes cause instability and contracting mesh cause excess dissipation, however when coupled together the effects can act to cancel each other out. Numerical experiments were subsequently performed using the Taylor-Green vortex case, however with the element corner node positions jittered. Tests showed 5th order to be more resilient to mesh poor quality meshes than 3rd order, but in both cases the effect of localised regions of expansion are thought to be responsible for an initial increase in the kinetic energy of the solution. The appearance of smaller turbulent scales within the TGV solution as time progressed then counteracted this effect, as high wavenumbers on locally contracting regions experience excess dissipation. Lastly, comparison was made between FR and a second order FV method. It was found that FR was more resilient to mesh deformation than FV methods, however FR is far from optimal when running at second order. In both cases it is recommended that kinetic energy preserving methods should be used as they will greatly increase resilience to mesh quality.

Chapter 5

Novel Correction Functions

5.1 Introduction

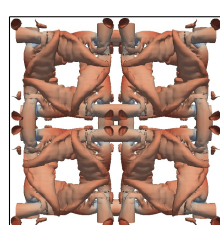
The numerical method of Flux Reconstruction (FR) was introduced in chapter 2. What should have been apparent is that within the FR methodology, the correction function plays an important part in the solution and has a large impact on the exact character of the scheme. To reiterate this, consider FR applied to the 1D conservation law to give:

$$\frac{d\hat{u}^\delta}{dt} = - \sum_{j=0}^p \hat{f}_j^{\delta D} \frac{dl_j}{d\xi}(\xi) - (\hat{f}_L^{\delta I} - \hat{f}_L^{\delta D}) \frac{dh_L}{d\xi}(\xi) - (\hat{f}_R^{\delta I} - \hat{f}_R^{\delta D}) \frac{dh_R}{d\xi}(\xi) \quad (5.1)$$

These values can then be used to advance \hat{u}^δ in time via a suitable temporal discretisation of this semi-discrete expression.

In 2011, Vincent et al. [128] discovered a one-parameter family of correction functions, herein referred to as original stable FR (OSFR) schemes, that lead to stable FR schemes for linear advection problems. This work was subsequently extended to linear advection-diffusion problems by Castonguay et al. [26]. More recently Vincent et al. [129] identified a multi-parameter family of linearly stable FR correction functions which are herein referred to as the extended stable FR (ESFR) schemes. In a series of numerical experiments, Vermeire and Vincent [125] observed that several of these schemes are more stable for ILES simulations than NDG. However, despite this progress, several questions around what exactly a correction function is, and more aptly, how one should be chosen, remain. To this end, we aim to extend the theoretical understanding of FR correction functions.

By this work we aim to enable correction functions to be found that can increase the: accuracy; temporal stability, or both for FR. The advantage that this possesses is that, in



the framework of FR, changing the correction function is straightforward resulting in only limited work for the end user to see benefits.

5.2 Stability Definition

5.2.1 Preliminaries

In order to form a numerical scheme that is energy stable, we need to find a functional space whose energy does not increase with time when the method is applied to a linear problem. This condition is similar to treating FR as a linear operator and imposing that the operator is a contraction in the sense of Banach's fixed point theorem [71]. This condition is dependent on us being able to define a functional space. A necessary and sufficient condition for this is we must be able to find a valid norm, $\|x\|$, that meets the following conditions [71]:

- $\|x\| \geq 0$ *(positivity)*
- $\|x\| = 0 \iff x = 0$ *(definiteness)*
- $\|ax\| = |a|\|x\|$ *(homogeneity)*
- $\|x + y\| \leq \|x\| + \|y\|$ *(triangle inequality)*

Having found a norm that satisfies these conditions, and taking a solution in the FR reference domain to be $\hat{u}^\delta(\xi)$, we can then define the energy stability criterion as:

$$\frac{d}{dt} \|\hat{u}^\delta\| \leq 0 \quad (5.2)$$

The question then becomes, how to create the norm and when is the condition of Eq. (5.2) met? There are several candidates that will be presented and then explored for FR in the remainder of this chapter. It should be noted that this was not the technique used by Vincent et al. [129], who employed arguments based around the finite element nature of the FR method to produce a multi-parameter family of FR correction functions. A posteriori, the effective norms that this method implied were then found. The exact formulation of these functions is contained in appendix B.

At this stage it will be useful to define the form of the solution, \hat{u}^δ , as one of two polynomial interpolations:

$$\hat{u}^\delta = \sum_{i=0}^p \tilde{u}_i \psi_i(\xi) \quad (5.3)$$

or

$$\hat{u}^\delta = \sum_{i=0}^p \tilde{u}_i J_i^{(\alpha,\beta)}(\xi) \quad (5.4)$$

where ψ_n is the n^{th} order Legendre polynomial of the first kind and $J_n^{(\alpha,\beta)}$ is the n^{th} order Jacobi polynomial, with (α,β) as control variables. Both forms of the interpolation will be used throughout this chapter depending on the circumstance.

5.2.2 Sobolev Norm

The original norm used to define a set of FR correction functions [127] was a modified finite Sobolev norm:

$$\|\hat{u}^\delta\|_{W_2^\iota} = \sqrt{\int_{-1}^1 (\hat{u}^\delta)^2 + \iota \left(\frac{\partial^p \hat{u}^\delta}{\partial \xi^p} \right)^2 d\xi} \quad (5.5)$$

The key step that was taken in defining a set of FR schemes was the modification of multiplying the p^{th} derivative by a free parameter. This gave an adjustable variable that would alter the numerical method. The associated condition on stability was then:

$$\frac{d}{dt} \|\hat{u}^\delta\|_{W_2^\iota}^2 = \frac{d}{dt} \int_{-1}^1 (\hat{u}^\delta)^2 + \iota \left(\frac{\partial^p \hat{u}^\delta}{\partial \xi^p} \right)^2 d\xi \leq 0 \quad (5.6)$$

For this to be a valid norm it must satisfy the conditions of section 5.2.1. However, as differentiation is linear, the satisfaction of these criterion will follow naturally if positivity is proven, namely if:

$$0 < \|\hat{u}^\delta\|_{W_2^\iota} < \infty \quad \forall \hat{u}^\delta \neq 0 \quad (5.7)$$

Then by making use of Eq.(5.3) it was then shown that:

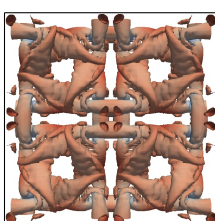
$$\frac{-1}{(2p+1)(a_p p!)^2} < \iota < \infty. \quad (5.8)$$

where $a_p = (2p)!/(2^p(p!)^2)$.

5.2.3 Weighted Sobolev Norm

Following on from the definition of OSFR, we may define a weighted Sobolev norm [140] in the reference domain. Here we will use the Jacobi weight function, giving:

$$\|\hat{u}^\delta\|_{W_2^{\iota,w}} = \sqrt{\int_{-1}^1 \left((\hat{u}^\delta)^2 + \iota \left(\frac{\partial^p \hat{u}^\delta}{\partial \xi^p} \right)^2 \right) (1-\xi)^\alpha (1+\xi)^\beta d\xi} \quad (5.9)$$



Thus, the criterion on energy stability in time for a finite polynomial solution is that:

$$\frac{d}{dt} \|\hat{u}^\delta\|_{W_2^{\ell,w}}^2 = \frac{d}{dt} \int_{-1}^1 \left((\hat{u}^\delta)^2 + \iota \left(\frac{\partial^p \hat{u}^\delta}{\partial \xi^p} \right)^2 \right) w_{\alpha,\beta}(\xi) d\xi \leq 0 \quad (5.10)$$

where

$$w_{\alpha,\beta}(\xi) = (1-\xi)^\alpha (1+\xi)^\beta \quad (5.11)$$

and for brevity we will define the average as:

$$\frac{1}{2} \int_{-1}^1 w_{\alpha,\beta}(\xi) d\xi = \bar{w}_{\alpha,\beta} \quad (5.12)$$

This weight function is that used for the orthogonality definition of Jacobi polynomials and, before proceeding, we will lay out some results for Jacobi polynomials that will be used throughout. Firstly the orthogonality condition:

$$\int_{-1}^1 J_m^{(\alpha,\beta)} J_n^{(\alpha,\beta)} w_{\alpha,\beta} d\xi = \underbrace{\frac{2^{\alpha+\beta+1}}{2n+\alpha+\beta+1} \frac{\Gamma(n+\alpha+1)\Gamma(n+\beta+1)}{n!\Gamma(n+\alpha+\beta+1)}}_{q_n^{(\alpha,\beta)}} \delta_{mn} \quad (5.13)$$

where $\Gamma(x)$ is the gamma function and δ_{mn} is the Kronecker delta function. Secondly, it will be useful to differentiate a Jacobi polynomial and express the result as a series of Jacobi polynomials on the same basis. From Doha [37] we find:

$$\frac{d^m J_n^{(\alpha,\beta)}}{d\xi^m} = 2^{-m} (n+\alpha+\beta+1)_m \sum_{i=0}^{n-m} D_{n-m,i}(\alpha+m, \beta+m, \alpha, \beta) J_i^{(\alpha,\beta)} \quad (5.14)$$

where

$$D_{j,i}(\gamma, \delta, \alpha, \beta) = \frac{(j+\gamma+\delta+1)_i (i+\gamma+1)_{j-i} \Gamma(i+\alpha+\beta+1)}{(j-i)! \Gamma(2i+\alpha+\beta+1)} \times {}_3F_2 \left(\begin{matrix} i-j, & j+i+\gamma+\delta+1, & i+\alpha+1 \\ i+\gamma+1, & 2i+\alpha+\beta+2 \end{matrix}; 1 \right) \quad (5.15)$$

We define here that that $(x)_i$ is the rising Pochhammer function and ${}_3F_2(\dots; z)$ is the 3-2 generalised hypergeometric function [11, 15]. In the interest of brevity in later sections we will also define the constant:

$$b_p^{(\alpha,\beta)} = \frac{\partial^p J_p^{(\alpha,\beta)}}{\partial \xi^p} = 2^{-p} (p+\alpha+\beta+1)_p \quad (5.16)$$

Proceeding without describing a specific numerical method, the norm described by Eq.(5.9) must then indeed be a norm; *i.e.* it must be positive, definite, homogeneous, and obey the triangle inequality. Of particular concern to us is the positivity condition for the remaining conditions, again, follow immediately due to the linear nature of differentiation. Hence, it is required that:

$$0 < \|\hat{u}^\delta\|_{W_2^{\iota,w}}^2 = \int_{-1}^1 \left((\hat{u}^\delta)^2 + \iota \left(\frac{\partial^p \hat{u}^\delta}{\partial \xi^p} \right)^2 \right) (1 - \xi)^\alpha (1 + \xi)^\beta d\xi < \infty \quad (5.17)$$

for $\hat{u}^\delta \neq 0$. Therefore, following the method of [127] we can substitute Eq.(5.4) into Eq.(5.17) as:

$$0 < \sum_{i=0}^p \tilde{u}_i^2 q_i^{(\alpha,\beta)} + \iota (b_p^{(\alpha,\beta)})^2 q_0^{(\alpha,\beta)} < \infty \quad (5.18)$$

Then grouping terms of the same order:

$$0 < \sum_{i=0}^{p-1} \tilde{u}_i^2 q_i^{(\alpha,\beta)} + \left(q_p^{(\alpha,\beta)} + \iota (b_p^{(\alpha,\beta)})^2 q_0^{(\alpha,\beta)} \right) \tilde{u}_p^2 < \infty \quad (5.19)$$

As \tilde{u}_i^2 is always positive, the limit on the value of ι is:

$$-\iota_{\text{crit}} = -\frac{q_p^{(\alpha,\beta)}}{(b_p^{(\alpha,\beta)})^2 q_0^{(\alpha,\beta)}} \leq \iota < \infty \quad (5.20)$$

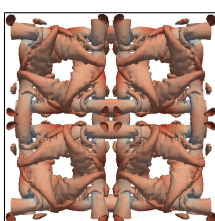
The value of ι_{crit} can be evaluated in a closed form that shows it is always positive, and hence quasi-DG (qDG) schemes ($\iota = 0$) will always have a positive norm, leading us expect a large region of stability.

$$\begin{aligned} \iota_{\text{crit}} &= \frac{q_p^{(\alpha,\beta)}}{(b_p^{(\alpha,\beta)})^2 q_0^{(\alpha,\beta)}} = \left(\frac{\alpha + \beta + 1}{2p + \alpha + \beta + 1} \right) \left(\frac{(\alpha + 1)_p (\beta + 1)_p}{(\alpha + \beta + 1)_p} \right) \times \\ &\quad \left(\frac{2^p}{(p + \alpha + \beta + 1)_p} \right)^2 \end{aligned} \quad (5.21)$$

To show this is compatible with previous work, let us suggest $(\alpha, \beta) = (0, 0)$. Remembering that $(1)_p = p!$, we get:

$$\frac{q_p^{(0,0)}}{(b_p^{(0,0)})^2 q_0^{(0,0)}} = \frac{(p!)^3}{(2p+1)(2p)!} \left(\frac{2^p}{(2p)!} \right)^2 \quad (5.22)$$

Which is identical to the result of section 5.2.2.



5.2.4 Generalised Sobolev Norm

In sections 5.2.2 & 5.2.3 the norm was defined with the zeroth and p^{th} order derivatives. This is sufficient to define the topology of the functional space, however, if we wish to generalise this further, we can include all derivatives in the norm. First defining the general modified Sobolev norm as:

$$\|u\|_{n,W^{p,2}} = \sqrt{\int_{-1}^1 \sum_{i=0}^p (u^{(i)})^2 d\xi} \quad (5.23)$$

where $u^{(i)}$ is the i^{th} spatial derivative of u and $W^{p,2}$ is the p^{th} order l_2 Sobolev space. (In this case $W^{p,2} = H^p$, where H is a Hilbert space). This can then be modified to form:

$$\|u\|_{n,W^{p,2,\iota}} = \sqrt{\int_{-1}^1 \sum_{i=0}^p \iota_i (u^{(i)})^2 d\xi} \quad (5.24)$$

Before applying an particular numerical scheme, we can constrain the values of ι_i such that positivity can be insured, *i.e.* $0 < \|\hat{u}^\delta\|_{n,W^{p,2,\iota}}^2 < \infty$. From the definition of the norm, thus:

$$0 < \int_{-1}^1 \sum_{i=0}^p \iota_i (\hat{u}^{\delta,(i)})^2 d\xi < \infty \quad (5.25)$$

If we then apply Eq.(5.3):

$$0 < \int_{-1}^1 \sum_{i=0}^p \iota_i \left(\sum_{j=0}^p \tilde{u}_j \frac{\partial^i \psi_j}{\partial \xi^i} \right)^2 d\xi < \infty \quad (5.26)$$

which can then be simplified to:

$$0 < \sum_{j=0}^p \iota_0 \left(\frac{2}{2j+1} \right) \tilde{u}_j^2 + \int_{-1}^1 \sum_{i=1}^{p-1} \iota_i \left(\sum_{j=0}^p \tilde{u}_j \frac{\partial^i \psi_j}{\partial \xi^i} \right)^2 d\xi + \iota_p \left(\frac{(2p)!}{2^p p!} \right)^2 v_p^2 < \infty \quad (5.27)$$

The limit will then vary depending on a given order, therefore specific examples will be given later.

5.2.5 Lebesgue Norm

Finally, for both the generalised Sobolev norm and the standard Sobolev norm there is a special case that may be considered degenerate. This is the Lebesgue norm which is

formed when taking $\iota_i = 0 \forall i \neq 0$ and $\iota_0 = 1$:

$$\|u\|_{n,L^2} = \sqrt{\int_{-1}^1 u^2 d\xi} \quad (5.28)$$

We say this is a ‘degenerate’ norm as later when exploring it and the generalised Sobolev norm, it will be shown to be a degenerate solution to a linear problem.

5.3 Finding Stable Correction Functions

5.3.1 Sobolev Norm – Original Stable FR

In the preceding sections, we introduced the FR approach, how correction functions are used to form a piecewise continuous solution and how FR’s stability can be defined through norms. We now wish to take these ideas and apply them to fulfil the primary aim of discovering new correction functions. Before presenting our extensions of the OSFR schemes it is useful to review the key results from the original OSFR paper of Vincent et al. [127]. Specifically, the OSFR corrections functions are obtained by setting:

$$h_L = \frac{(-1)^p}{2} \left(\psi_p - \frac{\eta_p \psi_{p-1} + \psi_{p+1}}{1 + \eta_p} \right), \quad (5.29)$$

and

$$h_R = \frac{1}{2} \left(\psi_p + \frac{\eta_p \psi_{p-1} + \psi_{p+1}}{1 + \eta_p} \right), \quad (5.30)$$

where $\psi_p = \psi_p(\xi)$ is a Legendre polynomial of order p and

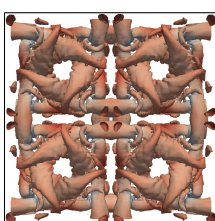
$$\eta_p = \iota(2p+1)(a_p p!)^2 \quad \text{and} \quad a_p = \frac{(2p)!}{2^p (p!)^2},$$

where the range of values taken by ι is limited by Eq.(5.8).

5.3.2 Weighted Sobolev Norm – Generalised Jacobi Stable FR

Moving onto the definition of the Jacobi stable FR correction functions, let us now consider applying FR to a linear advection problem. Without loss of generality we shall assume a unit convection velocity such that $f(u) = u$. It follows that:

$$\frac{d\hat{u}^\delta}{dt} = -\frac{\partial \hat{u}^\delta}{\partial \xi} - (\hat{u}_L^{\delta I} - \hat{u}_L^\delta) \frac{dh_L}{d\xi} - (\hat{u}_R^{\delta I} - \hat{u}_R^\delta) \frac{dh_R}{d\xi} \quad (5.31)$$



Previously, for the proof of OSFR [127], Eq.(5.31) would be multiplied by \hat{u}^δ and integrated over the reference domain. However, as we want to use a weight function, we shall defer this integration step, as this simplifies the use of the product rule. Multiplying Eq.(5.31) by \hat{u}^δ we obtain:

$$\hat{u}^\delta \frac{d\hat{u}^\delta}{dt} = -\hat{u}^\delta \frac{\partial \hat{u}^\delta}{\partial \xi} - (\hat{u}_L^{\delta I} - \hat{u}_L^\delta) \hat{u}^\delta \frac{dh_L}{d\xi} - (\hat{u}_R^{\delta I} - \hat{u}_R^\delta) \hat{u}^\delta \frac{dh_R}{d\xi} \quad (5.32)$$

and applying the product rule, this can be written as:

$$\begin{aligned} \frac{1}{2} \frac{d(\hat{u}^\delta)^2}{dt} &= -\frac{1}{2} \frac{\partial(\hat{u}^\delta)^2}{\partial \xi} - (\hat{u}_L^{\delta I} - \hat{u}_L^\delta) \left(\frac{\partial h_L \hat{u}^\delta}{\partial \xi} - h_L \frac{d\hat{u}^\delta}{d\xi} \right) \\ &\quad - (\hat{u}_R^{\delta I} - \hat{u}_R^\delta) \left(\frac{\partial h_R \hat{u}^\delta}{\partial \xi} - h_R \frac{d\hat{u}^\delta}{d\xi} \right) \end{aligned} \quad (5.33)$$

This step is important as it allows the formation of the conserved variable at the interface, as well ensuring that only derivatives of \hat{u}^δ are present. We may now proceed to multiply by the weight function and integrate over the reference domain:

$$\begin{aligned} \frac{1}{2} \frac{d}{dt} \int_{-1}^1 (\hat{u}^\delta)^2 w_{\alpha,\beta} d\xi &= -\frac{1}{2} \int_{-1}^1 \frac{\partial(\hat{u}^\delta)^2}{\partial \xi} w_{\alpha,\beta} d\xi \\ &\quad - (\hat{u}_L^{\delta I} - \hat{u}_L^\delta) \int_{-1}^1 \left(\frac{\partial h_L \hat{u}^\delta}{\partial \xi} - h_L \frac{d\hat{u}^\delta}{d\xi} \right) w_{\alpha,\beta} d\xi \\ &\quad - (\hat{u}_R^{\delta I} - \hat{u}_R^\delta) \int_{-1}^1 \left(\frac{\partial h_R \hat{u}^\delta}{\partial \xi} - h_R \frac{d\hat{u}^\delta}{d\xi} \right) w_{\alpha,\beta} d\xi \end{aligned} \quad (5.34)$$

Now proceeding to form the second component of the weighted Sobolev norm, we first take the p^{th} spatial derivative of Eq.(5.31):

$$\frac{d}{dt} \frac{\partial^p \hat{u}^\delta}{\partial \xi^p} = -\frac{\partial^{p+1} \hat{u}^\delta}{\partial \xi^{p+1}} - (\hat{u}_L^{\delta I} - \hat{u}_L^\delta) \frac{d^{p+1} h_L}{d\xi^{p+1}} - (\hat{u}_R^{\delta I} - \hat{u}_R^\delta) \frac{d^{p+1} h_R}{d\xi^{p+1}}, \quad (5.35)$$

Given \hat{u}^δ is a p^{th} order polynomial, Eq.(5.35) may be multiplied by the p^{th} derivative of \hat{u}^δ and integrated over the reference domain with the weighting function to give:

$$\begin{aligned} \frac{1}{2} \frac{d}{dt} \int_{-1}^1 \left(\frac{\partial^p \hat{u}^\delta}{\partial \xi^p} \right)^2 w_{\alpha,\beta} d\xi &= -2(\hat{u}_L^{\delta I} - \hat{u}_L^\delta) \frac{\partial^p \hat{u}^\delta}{\partial \xi^p} \frac{d^{p+1} h_L}{d\xi^{p+1}} \bar{w}_{\alpha,\beta} \\ &\quad - 2(\hat{u}_R^{\delta I} - \hat{u}_R^\delta) \frac{\partial^p \hat{u}^\delta}{\partial \xi^p} \frac{d^{p+1} h_R}{d\xi^{p+1}} \bar{w}_{\alpha,\beta} \end{aligned} \quad (5.36)$$

This simplification can be made due to the respective orders of \hat{u}^δ , h_L , and h_R . To now form the complete weighted Sobolev norm, we take Eq.(5.34) and add ι times Eq.(5.36)

as:

$$\begin{aligned} \frac{1}{2} \frac{d}{dt} \int_{-1}^1 \left((\hat{u}^\delta)^2 + \iota \left(\frac{\partial^p \hat{u}^\delta}{\partial \xi^p} \right)^2 \right) w_{\alpha, \beta} d\xi &= -\frac{1}{2} \int_{-1}^1 \frac{\partial(\hat{u}^\delta)^2}{\partial \xi} w_{\alpha, \beta} d\xi \\ &\quad - (\hat{u}_L^{\delta I} - \hat{u}_L^\delta) \int_{-1}^1 \left(\frac{\partial h_L \hat{u}^\delta}{\partial \xi} - h_L \frac{d\hat{u}^\delta}{d\xi} \right) w_{\alpha, \beta} d\xi \\ &\quad - (\hat{u}_R^{\delta I} - \hat{u}_R^\delta) \int_{-1}^1 \left(\frac{\partial h_R \hat{u}^\delta}{\partial \xi} - h_R \frac{d\hat{u}^\delta}{d\xi} \right) w_{\alpha, \beta} d\xi \quad (5.37) \\ &\quad - 2(\hat{u}_L^{\delta I} - \hat{u}_L^\delta) \iota \frac{\partial^p \hat{u}^\delta}{\partial \xi^p} \frac{d^{p+1} h_L}{d\xi^{p+1}} \overline{w}_{\alpha, \beta} \\ &\quad - 2(\hat{u}_R^{\delta I} - \hat{u}_R^\delta) \iota \frac{\partial^p \hat{u}^\delta}{\partial \xi^p} \frac{d^{p+1} h_R}{d\xi^{p+1}} \overline{w}_{\alpha, \beta} \end{aligned}$$

Hence, by analogy to Vincent et al. [127] and section 5.3.1, if the following conditions are imposed on the correction function:

$$\int_{-1}^1 \left(h_L \frac{d\hat{u}^\delta}{d\xi} \right) w_{\alpha, \beta} d\xi - \iota \frac{\partial^p \hat{u}^\delta}{\partial \xi^p} \frac{d^{p+1} h_L}{d\xi^{p+1}} \int_{-1}^1 w_{\alpha, \beta} d\xi = 0 \quad (5.38)$$

$$\int_{-1}^1 \left(h_R \frac{d\hat{u}^\delta}{d\xi} \right) w_{\alpha, \beta} d\xi - \iota \frac{\partial^p \hat{u}^\delta}{\partial \xi^p} \frac{d^{p+1} h_R}{d\xi^{p+1}} \int_{-1}^1 w_{\alpha, \beta} d\xi = 0 \quad (5.39)$$

then

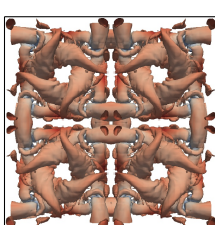
$$\begin{aligned} \frac{1}{2} \frac{d}{dt} \int_{-1}^1 \left((\hat{u}^\delta)^2 + \iota \left(\frac{\partial^p \hat{u}^\delta}{\partial \xi^p} \right)^2 \right) w_{\alpha, \beta} d\xi &= -\frac{1}{2} \int_{-1}^1 \frac{\partial(\hat{u}^\delta)^2}{\partial \xi} w_{\alpha, \beta}(\xi) d\xi \\ &\quad - (\hat{u}_L^{\delta I} - \hat{u}_L^\delta) \int_{-1}^1 \left(\frac{\partial h_L \hat{u}^\delta}{\partial \xi} \right) w_{\alpha, \beta} d\xi \quad (5.40) \\ &\quad - (\hat{u}_R^{\delta I} - \hat{u}_R^\delta) \int_{-1}^1 \left(\frac{\partial h_R \hat{u}^\delta}{\partial \xi} \right) w_{\alpha, \beta} d\xi \end{aligned}$$

In order to find correction functions that can meet the conditions of Eq.(5.38 & 5.39) we need to define the projection of \hat{u}^δ , h_L , and h_R into the Jacobi polynomial basis, for this we will use Eq.(5.4) and:

$$h_L = \sum_{i=0}^{p+1} \tilde{h}_{L,i} J_i^{(\alpha, \beta)} \quad \text{and} \quad h_R = \sum_{i=0}^{p+1} \tilde{h}_{R,i} J_i^{(\alpha, \beta)} \quad (5.41)$$

With these definitions, we may now substitute Eq.(5.41) into Eq.(5.38) to get:

$$\int_{-1}^1 \left(\sum_{i=0}^{p+1} \sum_{j=0}^p \tilde{h}_{L,i} \tilde{u}_j J_i^{(\alpha, \beta)} \frac{dJ_j^{(\alpha, \beta)}}{d\xi} \right) w_{\alpha, \beta} d\xi - \iota \tilde{u}_p \tilde{h}_{L,p+1} b_p^{(\alpha, \beta)} b_{p+1}^{(\alpha, \beta)} q_0^{(\alpha, \beta)} = 0 \quad (5.42)$$



To solve this integral condition we may constrain \tilde{h}_L , without loss of generality, to only have terms in $p-1$, p and, $p+1$. We then observe that the only contribution to the equality in Eq.(5.42) is from the $p-1^{\text{th}}$ term of \tilde{h}_L . Therefore, if we can find a closed form of $D_{p-1,p-1}(\alpha+1,\beta+1,\alpha,\beta)$ we can relate $\tilde{h}_{L,p-1}$ to $\tilde{h}_{L,p+1}$ through ι . Hence, substituting the values into Eq.(5.15) we find that the hypergeometric function component becomes ${}_3F_2(0,\dots;1)$ and, from the definition of the rising Pochhammer function, this must have a value of unity, hence we may write:

$$D_{p-1,p-1}(\alpha+1,\beta+1,\alpha,\beta) = \frac{(2p+\alpha+\beta-1)(2p+\alpha+\beta)}{2(p+\alpha+\beta)} \quad (5.43)$$

which leads to:

$$\iota = \frac{\tilde{h}_{L,p-1}}{\tilde{h}_{L,p+1}} \underbrace{\left(\frac{(p+\alpha+\beta+1)(p+\alpha+\beta+2)_{p-1} q_{p-1}^{(\alpha,\beta)}}{2(p+\alpha+\beta)_{p-1} b_p^{(\alpha,\beta)} b_{p+1}^{(\alpha,\beta)} q_0^{(\alpha,\beta)}} \right)}_{A_p} \quad (5.44)$$

Using the fact that $h_L(-1) = 1$ and $h_L(1) = 0$ we find:

$$(-1)^p = \tilde{h}_{L,p} \underbrace{\left(\frac{(\beta+1)_p}{p!} \left[\left(\frac{p+\alpha}{p+\beta} \right) \frac{\iota p(p+1) + (p+\beta)(p+\beta+1) A_p}{\iota p(p+1) + (p+\alpha)(p+\alpha+1) A_p} + 1 \right] \right)}_{\kappa_p^{(\alpha,\beta)}} \quad (5.45)$$

$$\tilde{h}_{L,p+1} = -\frac{A_p J_p^{(\alpha,\beta)}(1) \tilde{h}_{L,p}}{\iota J_{p-1}^{(\alpha,\beta)}(1) + A_p J_{p+1}^{(\alpha,\beta)}(1)} = -\frac{A_p(p+1)(p+\alpha) \tilde{h}_{L,p}}{\iota p(p+1) + (p+\alpha+1)(p+\alpha) A_p} \quad (5.46)$$

Putting this all together we obtain:

$$h_L = \frac{(-1)^p}{\kappa_p^{(\alpha,\beta)}} \left(J_p^{(\alpha,\beta)} - \frac{\iota(p+1)(p+\alpha) J_{p-1}^{(\alpha,\beta)} + (p+1)(p+\alpha) A_p J_{p+1}^{(\alpha,\beta)}}{\iota p(p+1) + (p+\alpha+1)(p+\alpha) A_p} \right) \quad (5.47)$$

$$h_R = \frac{1}{\kappa_p^{(\alpha,\beta)}} \left(J_p^{(\alpha,\beta)} + \frac{\iota(p+1)(p+\alpha) J_{p-1}^{(\alpha,\beta)} + (p+1)(p+\alpha) A_p J_{p+1}^{(\alpha,\beta)}}{\iota p(p+1) + (p+\alpha+1)(p+\alpha) A_p} \right) \quad (5.48)$$

Spectral Difference Schemes

We will now use the results found for GJFR to define a useful subset of correction functions. It has been shown [55, 62, 127] that FR is able to recover SD schemes for equation sets with homogeneous linear flux functions. The implication being that the treatment of aliasing, introduced by non-linear or heterogeneous flux functions, is different in FR to a native SD scheme. To obtain an SD scheme within FR the roots of

the left and right corrections functions must be symmetric about $\xi = 0$. The simplest method of achieving this is by prescribing the interior zeros to be a set of quadrature points. In the first proof of energy stability of SD schemes the canonical Gauss–Legendre quadrature [62] was utilised, but other quadratures have been considered, for example, Lui et al. [82] saw the potential for a Gauss–Legendre–Lobatto quadrature. As the choice of quadrature is arbitrary, it is proposed that this is extended to the full set of Gauss–Jacobi quadratures, where the p^{th} Gauss–Jacobi points are the roots of the p^{th} order Jacobi polynomial [71]. This gives rise to the correction functions:

$$h_{L,\text{SD}} = \frac{(1-\xi)}{2} \frac{J_p^{(\alpha,\beta)}(\xi)}{J_p^{(\alpha,\beta)}(-1)} \quad \text{and} \quad h_{R,\text{SD}} = \frac{(1+\xi)}{2} \frac{J_p^{(\alpha,\beta)}(\xi)}{J_p^{(\alpha,\beta)}(1)} \quad (5.49)$$

where the correction functions are normalised for the edge value, as Jacobi polynomials do not guarantee unit magnitude at ± 1 . The recurrence relation for Jacobi polynomials [17] leads us to the following form:

$$\begin{aligned} h_{L,\text{SD}} = & \left(-\frac{(p+\alpha)(p+\beta)}{(2p+\alpha+\beta+1)(2p+\alpha+\beta)} J_{p-1}^{(\alpha,\beta)} \right. \\ & + \frac{1}{2} \left(1 + \frac{\alpha^2 - \beta^2}{(2p+\alpha+\beta+2)(2p+\alpha+\beta)} \right) J_p^{(\alpha,\beta)} \\ & \left. - \frac{(p+1)(p+1+\alpha+\beta)}{(2p+\alpha+\beta+1)(2p+\alpha+\beta+2)} J_{p+1}^{(\alpha,\beta)} \right) \frac{(-1)^p \Gamma(p+1) \Gamma(\beta+1)}{\Gamma(p+\beta+1)} \end{aligned} \quad (5.50)$$

and

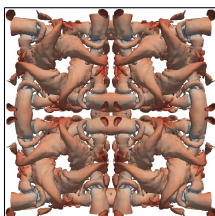
$$\begin{aligned} h_{R,\text{SD}} = & \left(\frac{(p+\alpha)(p+\beta)}{(2p+\alpha+\beta+1)(2p+\alpha+\beta)} J_{p-1}^{(\alpha,\beta)} \right. \\ & + \frac{1}{2} \left(1 - \frac{\alpha^2 - \beta^2}{(2p+\alpha+\beta+2)(2p+\alpha+\beta)} \right) J_p^{(\alpha,\beta)} \\ & \left. + \frac{(p+1)(p+1+\alpha+\beta)}{(2p+\alpha+\beta+1)(2p+\alpha+\beta+2)} J_{p+1}^{(\alpha,\beta)} \right) \frac{\Gamma(p+1) \Gamma(\alpha+1)}{\Gamma(p+\alpha+1)} \end{aligned} \quad (5.51)$$

This methods advantage in extending the set of SD correction functions is that we may use the work of the previous section in order to prove the theoretical energy stability. We therefore assert:

Lemma 5.3.1. *SD Energy Stability. A given SD correction function with $\alpha, \beta \in (-1, \infty)$ will always give the norm $\|\hat{u}^\delta\|_{W_2^{\ell,w}}$ to be positive.*

Proof. Using Eq.(5.44) to produce an expression of ι for SD schemes, which, after normalisation by ι_{crit} , gives:

$$\frac{\iota_{\text{SD}}}{\iota_{\text{crit}}} = \frac{p}{p+1} \quad (5.52)$$



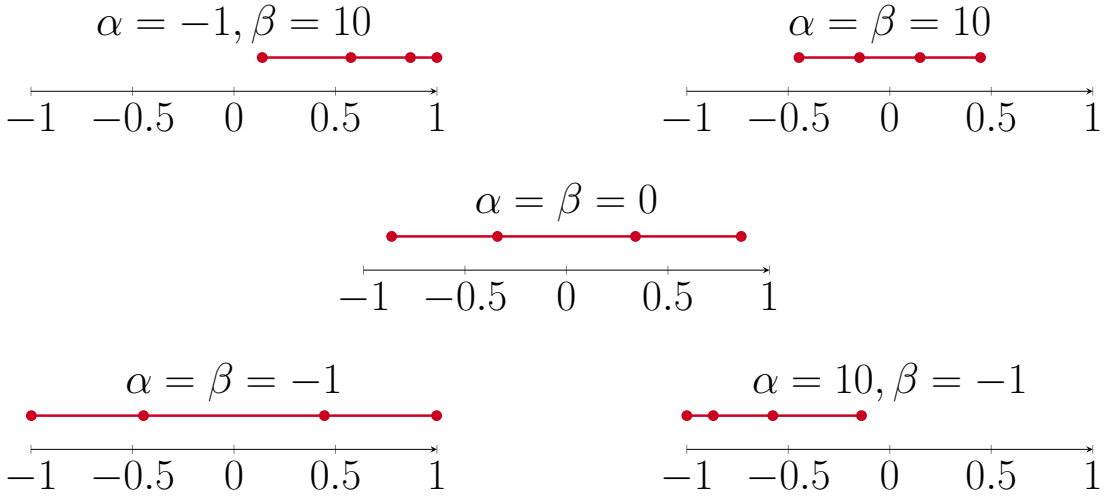


Fig. 5.1 Selected Gauss-Jacobi quadratures for $n = 4$.

As ι_{crit} is always positive, so must ι_{SD} always be positive. \square

Lastly, we will note that this definition of SD schemes may be extended to include all quadratures in $[-1, 1]$ by defining the correction function as:

$$h_L = \frac{(1-\xi)}{2} \frac{J_m^{(\alpha,\beta)}(\xi)}{J_m^{(\alpha,\beta)}(-1)} \quad \text{for } |m|_1 = p \quad (5.53)$$

where $m = (m_1, m_2 \dots)$ is a multiindex and (α, β) may vary with m_i . This is included for completeness, however the focus will put on the Jacobi SD function of Eq.(5.49).

To briefly touch on some of the characteristics of the Jacobi SD correction function, consider the Gauss–Jacobi quadratures that make up the interior zeros of the correction function. Figure 5.1 aims to demonstrate how the quadrature is affected by the variation of α and β , primarily that for $\alpha = \beta$ the quadrature is symmetric. Furthermore, in the limit as $\alpha, \beta \rightarrow -1$ the quadrature gets pinned to the edges and as $\alpha, \beta \rightarrow \infty$ the quadrature gets compressed to the middle. The effect this has for the case when $\alpha \neq \beta$ is that the left and right correction functions are not symmetric, with the zeros biased towards one of the edges.

5.3.3 Generalised Sobolev Norm – Generalised Sobolev Stable FR

We now move onto defining GSFR correction functions, for which we again use the flux reconstructed form of the first order conservation law with unit convective velocity ($\hat{f}^\delta = \hat{u}^\delta$):

$$\frac{\partial \hat{u}^\delta}{\partial t} = -\frac{\partial \hat{u}^\delta}{\partial \xi} - (\hat{u}_L^{\delta I} - \hat{u}_L^\delta) \frac{dh_L}{d\xi} - (\hat{u}_R^{\delta I} - \hat{u}_R^\delta) \frac{dh_R}{d\xi} \quad (5.54)$$

Hence, we undertake defining the modified broken Sobolev norm from Eq.(5.78), which is performed via summation of recursive differentiation and multiplication of the variable. With subsequent integration over the sub-domain to give:

$$\frac{1}{2} \frac{d}{dt} \int_{-1}^1 \sum_{i=0}^p \iota_i (\hat{u}^{\delta(i)})^2 d\xi = -\frac{1}{2} \underbrace{\int_{-1}^1 \sum_{i=0}^p \iota_i \frac{\partial}{\partial \xi} \left(\frac{\partial^i \hat{u}^\delta}{\partial \xi^i} \right)^2 d\xi}_{I_s} - (\hat{u}_L^{\delta I} - \hat{u}_L^\delta) \underbrace{\int_{-1}^1 \sum_{i=0}^p \iota_i \frac{\partial^i \hat{u}^\delta}{\partial \xi^i} \frac{d^{i+1} h_L}{d\xi^{i+1}} d\xi}_{I_L} \\ - (\hat{u}_R^{\delta I} - \hat{u}_R^\delta) \underbrace{\int_{-1}^1 \sum_{i=0}^p \iota_i \frac{\partial^i \hat{u}^\delta}{\partial \xi^i} \frac{d^{i+1} h_R}{d\xi^{i+1}} d\xi}_{I_R} \quad (5.55)$$

When I_s is combined with one round of integration by parts of I_l and I_r for $i = 0$, it becomes the conservation portion of the equation. Hence, after the integration by parts required to form the conversation integral, the necessary conditions on stability are:

$$\sum_{i=0}^p \iota_i \int_{-1}^1 \frac{d^i h_L}{d\xi^i} \frac{\partial^{i+1} \hat{u}^\delta}{\partial \xi^{i+1}} d\xi = \sum_{i=1}^p \iota_i \left| \frac{\partial^i \hat{u}^\delta}{\partial \xi^i} \frac{d^i h_L}{d\xi^i} \right|_{-1}^1 \quad (5.56)$$

$$\sum_{i=0}^p \iota_i \int_{-1}^1 \frac{d^i h_R}{d\xi^i} \frac{\partial^{i+1} \hat{u}^\delta}{\partial \xi^{i+1}} d\xi = \sum_{i=1}^p \iota_i \left| \frac{\partial^i \hat{u}^\delta}{\partial \xi^i} \frac{d^i h_R}{d\xi^i} \right|_{-1}^1 \quad (5.57)$$

If the correction function and solution are taken as being a series of Legendre polynomials:

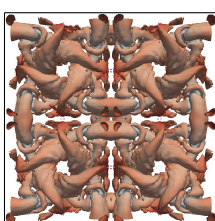
$$h_L(\xi) = \sum_{i=0}^{p+1} \tilde{h}_{L,i} \psi_i(\xi) \quad \text{and} \quad \hat{u}^\delta(\xi) = \sum_{i=0}^p \tilde{u}_i \psi_i(\xi) \quad (5.58)$$

then it is possible to find a closed set of equations that define $\tilde{h}_{L,i}$ in terms of ι_i . Legendre polynomials are chosen as their weighting function for the orthogonality condition is unity, greatly simplifying later derivations. Therefore, substitution of Eq.(5.58) into Eq.(5.56) gives:

$$\sum_{i=0}^p \iota_i \int_{-1}^1 \left[\sum_{n=0}^{p+1} \sum_{m=0}^p \tilde{h}_{L,n} \tilde{u}_m \frac{d^i \psi_n}{d\xi^i} \frac{\partial^{i+1} \psi_m}{\partial \xi^{i+1}} \right] d\xi = \sum_{i=1}^p \iota_i \left| \sum_{n=0}^{p+1} \sum_{m=0}^p \tilde{h}_{L,n} \tilde{u}_m \frac{d^i \psi_n}{d\xi^i} \frac{\partial^i \psi_m}{\partial \xi^i} \right|_{-1}^1 \quad (5.59)$$

This may be cast as a closed set of linear equations of the form:

$$\mathbf{L}_p \tilde{\mathbf{h}}_{\mathbf{L}} = [0 \quad \dots \quad 0 \quad 1]^T \quad (5.60)$$



where the penultimate entries of Eq.(5.60) are the enforcement of the boundary conditions on h_L , and, due to these boundary conditions, \mathbf{L}_p is a square matrix. The general form of the entries of \mathbf{L}_p can be written as:

$$\mathbf{L}_p[m-1][n] = \sum_{i=0}^p \iota_i \int_{-1}^1 \frac{d^i \psi_n}{d\xi^i} \frac{d^{i+1} \psi_m}{d\xi^{i+1}} d\xi - \sum_{i=1}^p \iota_i \left| \frac{d^i \psi_n}{d\xi^i} \frac{d^i \psi_m}{d\xi^i} \right|_{-1}^1 \quad (5.61)$$

where $m, n \in \mathbb{N}$ with $1 \leq m \leq p$ and $0 \leq n \leq p+1$. The $m=0$ case is removed as it is identically zero, and the final two rows will come from the boundary conditions on $h_L(\xi)$. To evaluate Eq.(5.61), it can be useful to consider the following result of Miller [87], which we modify to consider Legendre polynomials and the prescribed relationship of the derivatives.

$$\int_{-1}^1 \frac{d^m \psi_n}{d\xi^m} \frac{d^{m+1} \psi_k}{d\xi^{m+1}} d\xi = \sum_{i=0}^{\lfloor \frac{n-m}{2} \rfloor} \sum_{j=0}^{\lfloor \frac{k-m-1}{2} \rfloor} \frac{b_i(m, n) b_j(m+1, k)}{n+k-2(m+i+j)} [1 - (-1)^{n+k-2(m+i+j)}] \quad (5.62)$$

where we define:

$$b_i(m, n) = \frac{(-1)^i (2(n-i))!}{2^n (n-m-2i)! (n-i)! i!} \quad (5.63)$$

Then for the gradient of Legendre polynomials at the end point:

$$\frac{\partial^n \psi_j(-1)}{\partial \xi^n} = \frac{(-1)^{j-n} (j+n)!}{2^n n! (j-n)!} \quad \text{and} \quad \frac{\partial^n \psi_j(1)}{\partial \xi^n} = \frac{(1)^{j-n} (j+n)!}{2^n n! (j-n)!} \quad \text{for } j \geq n \quad (5.64)$$

which can be inferred from the work of Garfinkel [42] and Holdeman [52]. With these identities established specific examples may now be evaluated.

GSFR for $p = 2$

For the case of $p = 2$ the generalised correction function equation can be found to be:

$$\mathbf{L}_2 \tilde{\mathbf{h}}_L = \begin{bmatrix} -\iota_0 & 0 & 3\iota_1 & 0 \\ 0 & -\iota_0 & 0 & 15(\iota_1 + 3\iota_2) \\ 1 & 1 & 1 & 1 \\ 1 & -1 & 1 & -1 \end{bmatrix} \tilde{\mathbf{h}}_L = \begin{bmatrix} 0 \\ 0 \\ 0 \\ 1 \end{bmatrix} \quad (5.65)$$

And upon assessment of the limits presented by Eq.(5.27), the limits on \mathbf{I}_2 can be found to be:

$$\begin{bmatrix} 0 \\ -\frac{1}{2} \left(\frac{2}{3} \iota_0 \right) \\ -\frac{1}{3} \left(\frac{2}{5} \iota_0 + 6\iota_1 \right) \end{bmatrix} < \mathbf{I}_2 < \infty \quad (5.66)$$

GSFR for $p = 3$

$$\begin{bmatrix} -\iota_0 & 0 & 3\iota_1 & 0 & 10\iota_1 \\ 0 & -\iota_0 & 0 & 15(\iota_1 + 3\iota_2) & 0 \\ -\iota_0 & 0 & -(\iota_0 - 3\iota_1) & 0 & 15(3\iota_1 + 35\iota_2 + 105\iota_3) \\ 1 & 1 & 1 & 1 & 1 \\ 1 & -1 & 1 & -1 & 1 \end{bmatrix} \tilde{\mathbf{h}}_L = \begin{bmatrix} 0 \\ 0 \\ 0 \\ 0 \\ 1 \end{bmatrix} \quad (5.67)$$

Evaluating Eq.(5.27), the condition necessary for valid correction functions is:

$$0 < 2\iota_0 v_0^2 + \left(\frac{2}{3}\iota_0 + \iota_1\right)v_1^2 + \left(\frac{2}{5}\iota_0 + 6\iota_1 + 18\iota_2\right)v_2^2 + \left(\frac{2}{7}\iota_0 + 8\iota_1 + 150\iota_2 + 255\iota_3\right)v_3^2 + \iota_1(v_1 + 2v_3)^2 < \infty \quad (5.68)$$

Due to the final term in Eq.(5.68), the transformation of this to a necessary condition on \mathbf{I}_3 is difficult. However, it can lead to a sufficient condition on the range of validity for \mathbf{I}_3 :

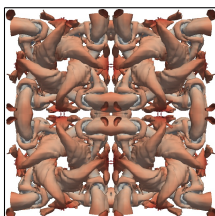
$$\begin{bmatrix} 0 \\ 0 \\ -\frac{1}{18}\left(\frac{2}{5}\iota_0 + 6\iota_1\right) \\ -\frac{1}{255}\left(\frac{2}{7}\iota_0 + 8\iota_1 + 150\iota_2\right) \end{bmatrix} < \mathbf{I}_3 < \infty \quad (5.69)$$

GSFR for $p = 4$

$$\begin{bmatrix} \iota_0 & 0 & 3\iota_1 & 0 & 10\iota_1 & 0 \\ 0 & \iota_0 & 0 & 15(\iota_1 + 3\iota_2) & 0 & (42\iota_1 + 315\iota_2) \\ \iota_0 & 0 & (\iota_0 + 3\iota_1) & 0 & 15(3\iota_1 + 35\iota_2 + 105\iota_3) & 0 \\ 0 & \iota_0 & 0 & (-\iota_0 + 15\iota_1 + 150\iota_2) & 0 & 105(\iota_1 + 31\iota_2 - 63\iota_3 + 945\iota_4) \\ 1 & 1 & 1 & 1 & 1 & 1 \\ 1 & -1 & 1 & -1 & 1 & -1 \end{bmatrix} \tilde{\mathbf{h}}_L = \begin{bmatrix} 0 \\ 0 \\ 0 \\ 0 \\ 0 \\ 1 \end{bmatrix} \quad (5.70)$$

Evaluating Eq.(5.27) to find the necessary limits on validity:

$$\begin{aligned} 0 < 2\iota_0 v_0^2 + \left(\frac{2}{3}\iota_0 + \iota_1\right)v_1^2 + \left(\frac{2}{5}\iota_0 + 2\iota_1 + 9\iota_2\right)v_2^2 + \left(\frac{2}{7}\iota_0 + 8\iota_1 + 150\iota_2 + 450\iota_3\right)v_3^2 \\ + \left(\frac{2}{9}\iota_0 + 11\iota_1 + 290\iota_2 + 7350\iota_3 + 11025\iota_4\right)v_4^2 \\ + \iota_1(2v_2 + 3v_4)^2 + \iota_1(v_1 + 2v_3)^2 + \iota_2(3v_2 + 20v_4)^2 < \infty \end{aligned} \quad (5.71)$$



And hence, with the same reasoning as for $p = 3$, the sufficient conditions on \mathbf{I}_4 for valid correction functions are:

$$\begin{bmatrix} 0 \\ 0 \\ 0 \\ -\frac{1}{450}\left(\frac{2}{7}\iota_0 + 8\iota_1 + 150\iota_2\right) \\ -\frac{1}{105^2}\left(\frac{2}{9}\iota_0 + 11\iota_1 + 290\iota_2 + 7350\iota_3\right) \end{bmatrix} < \mathbf{I}_4 < \infty \quad (5.72)$$

At this point it is worth noting the recursive nature of the matrix \mathbf{L}_p . Hence the set of correction functions at p is the union of p^{th} order correction functions and the correction functions defined by \mathbf{L}_{p-1} and so on recursively down to the empty set. So if the p^{th} order correction function is defined by some eigenfunction \mathbf{c}_p then the space of correction functions is defined as $\bigoplus_{i=0}^p \mathbf{c}_i$, i.e each time the order is increased, one extra eigenfunction is introduced. However, in the special case of $\mathbf{I}_p = [1, 0, \dots]^T$, the set of correction functions collapse to a single value, unique for each p . This is an interesting property that will be explored in future work.

To show that these correction functions are in fact unique by comparison to both the OSFR of Vincent et al. [127] and the ESFR of Vincent et al. [129], an attempt must be made to reconstruct the GSFR correction functions in both the ESFR and the OSFR setting . Starting with OSFR, this method defines only the free parameter ι , as described in Eq.(5.29). Taking $p = 3$ and defining some arbitrary stable value of \mathbf{I}_3 , the equivalent value of ι can be found using the value of $\tilde{\mathbf{h}}_{L,p+1}$ found from Eq.(5.67). Hence:

$$\iota = \frac{1}{(2p+1)(a_p p!)^2} \left(\frac{(-1)^{p+1}}{\tilde{\mathbf{h}}_{L,p+1}} - 2 \right) \quad (5.73)$$

To then compare to ESFR, it is easier to consider the gradient of h_L , defined in Eq.(B.1), and defining the Legendre polynomial weights of GSFR similarly as $\tilde{\mathbf{g}}_L$. Then for the case of $p = 3$ the corresponding ESFR weights can be found, using Eq.(B.11) from Vincent et al. [129], as:

$$\kappa_1 = -\left(\frac{1}{\tilde{\mathbf{g}}_{L,2}} + \frac{2}{5}\right) \quad (5.74)$$

$$\kappa_0 = \frac{175\kappa_1^2 \tilde{\mathbf{g}}_{L,1} + 105\kappa_1 - 12\tilde{\mathbf{g}}_{L,1} + 18}{42\tilde{\mathbf{g}}_{L,1} - 63} \quad (5.75)$$

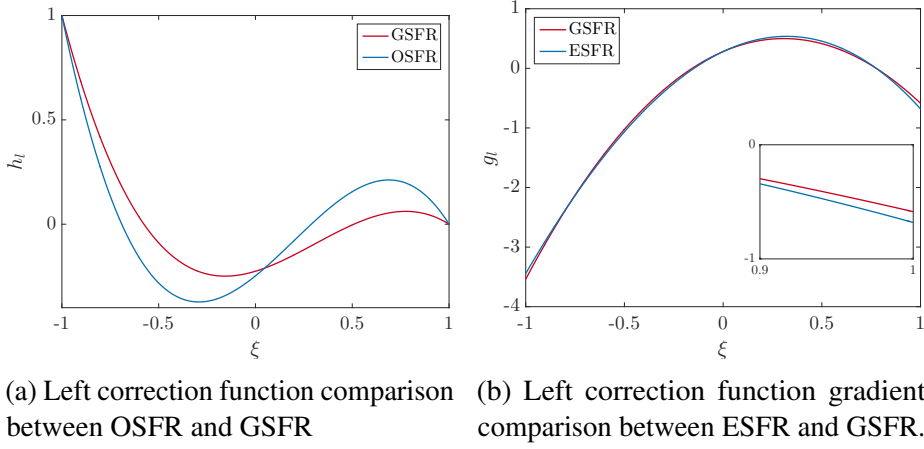


Fig. 5.2 Comparison of OS, ES and GS correction functions. For $p = 3$ and taking $\mathbf{I}_3 = [1, 0.01, 0.01, 0.1]^T$

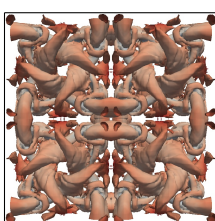
It can then be further shown that to be an ESFR correction function for $p = 3$, together with Eq.(5.74), the following must be satisfied:

$$\frac{175\kappa_1^2 \tilde{\mathbf{g}}_{L,3} + 105\kappa_1 + 42 - 12\tilde{\mathbf{g}}_{L,3}}{42\tilde{\mathbf{g}}_{L,3}} = \frac{175\kappa_1^2 \tilde{\mathbf{g}}_{L,1} + 105\kappa_1 - 12\tilde{\mathbf{g}}_{L,1} + 18}{42\tilde{\mathbf{g}}_{L,1} - 63} \quad (5.76)$$

where κ_1 is defined by Eq.(5.74). As is shown in Fig. 5.2 the correction functions found by satisfying Eq.(5.56 & 5.57) are in fact different from those defined by OSFR and ESFR. Furthermore, for OSFR it is trivial to show that it is a sub-set of GSFR, from there respective definitions, OSFR can be constructed when $\mathbf{I}_p = [1, \dots, 0.5t]^T$. The ESFR norm definition detailed in [129] can be used to show ESFR is a subset of GSFR. This result could be expected as both OSFR and ESFR were found to be Sobolev stable. To find the corresponding values of \mathbf{I}_p for a given h_L , originating from either OSFR or ESFR, the subject of the equation defining the GSFR correction must be change to \mathbf{I}_p . In the case of $p = 3$ and setting $t_0 = 1$, this takes the form:

$$\underbrace{\begin{bmatrix} 3\tilde{\mathbf{h}}_{L,2} + 10\tilde{\mathbf{h}}_{L,4} & 0 & 0 \\ 15\tilde{\mathbf{h}}_{L,3} & 45\tilde{\mathbf{h}}_{L,3} & 0 \\ 3\tilde{\mathbf{h}}_{L,2} + 45\tilde{\mathbf{h}}_{L,4} & 525\tilde{\mathbf{h}}_{L,4} & 1575\tilde{\mathbf{h}}_{L,4} \end{bmatrix}}_{\mathbf{H}_3} \begin{bmatrix} t_1 \\ t_2 \\ t_3 \end{bmatrix} = \begin{bmatrix} \tilde{\mathbf{h}}_{L,0} \\ \tilde{\mathbf{h}}_{L,1} \\ \tilde{\mathbf{h}}_{L,0} + \tilde{\mathbf{h}}_{L,2} \end{bmatrix} \quad (5.77)$$

Hence, ESFR and OSFR are both recoverable from GSFR. The exception to the invertibility of \mathbf{H}_3 over the set of ESFR and OSFR is when either $\tilde{\mathbf{h}}_{L,3} = 0$ or $\tilde{\mathbf{h}}_{L,4} = 0$, as GSFR has multiple ways of constructing these lower order correction functions.



5.3.4 Lebesgue Norm – Generalised Lebesgue Stable FR

We will now look for corrections that satisfy the stability criterion, $d(\|u\|_{n,L^2})/dt \leq 0$, in this norm for the 1D FR conservation law:

$$\frac{\partial \hat{u}^\delta}{\partial t} = -\frac{\partial \hat{f}^\delta}{\partial \xi} - (\hat{f}_L^{\delta I} - \hat{f}_L^\delta) \frac{dh_L}{d\xi} - (\hat{f}_R^{\delta I} - \hat{f}_R^\delta) \frac{dh_R}{d\xi}$$

If the flux function is set such that linear advection is solved then $\hat{f}^\delta = \hat{u}^\delta$. This then implies that:

$$\frac{\partial \hat{u}^\delta}{\partial t} = -\frac{\partial \hat{u}^\delta}{\partial \xi} - (\hat{u}_L^{\delta I} - \hat{u}_L^\delta) \frac{dh_L}{d\xi} - (\hat{u}_R^{\delta I} - \hat{u}_R^\delta) \frac{dh_R}{d\xi} \quad (5.78)$$

Multiplying Eq.(5.78) by the discontinuous conserved variable and integrating over the sub-domain:

$$\int_{-1}^1 \hat{u}^\delta \frac{\partial \hat{u}^\delta}{\partial t} d\xi = - \int_{-1}^1 \hat{u}^\delta \frac{\partial \hat{u}^\delta}{\partial \xi} d\xi - (\hat{u}_L^{\delta I} - \hat{u}_L^\delta) \int_{-1}^1 \hat{u}^\delta \frac{dh_L}{d\xi} d\xi - (\hat{u}_R^{\delta I} - \hat{u}_R^\delta) \int_{-1}^1 \hat{u}^\delta \frac{dh_R}{d\xi} d\xi \quad (5.79)$$

Applying the product rule and integration by parts to Eq.(5.79), the rate of energy decay of FR which may also be recognised as the rate of change of the Lebesgue norm is:

$$\begin{aligned} \frac{1}{2} \frac{d}{dt} \int_{-1}^1 (\hat{u}^\delta)^2 d\xi &= -\frac{1}{2} \int \frac{\partial (\hat{u}^\delta)^2}{\partial \xi} \xi + (\hat{u}_L^{\delta I} - \hat{u}_L^\delta) \hat{u}_L^\delta - (\hat{u}_R^{\delta I} - \hat{u}_R^\delta) \hat{u}_R^\delta \\ &\quad + (\hat{u}_L^{\delta I} - \hat{u}_L^\delta) \underbrace{\int_{-1}^1 h_L \frac{\partial \hat{u}^\delta}{\partial \xi} d\xi}_{I_L} \\ &\quad + (\hat{u}_R^{\delta I} - \hat{u}_R^\delta) \underbrace{\int_{-1}^1 h_R \frac{\partial \hat{u}^\delta}{\partial \xi} d\xi}_{I_R} \end{aligned} \quad (5.80)$$

If the integrals I_L and I_R are set equal to zero, then Eq.(5.80) may be reduced to:

$$\frac{1}{2} \frac{d}{dt} \int_{-1}^1 (\hat{u}^\delta)^2 d\xi = \frac{1}{2} ((\hat{u}_L^\delta)^2 - (\hat{u}_R^\delta)^2) + (\hat{u}_L^{\delta I} \hat{u}_L^\delta - \hat{u}_R^{\delta I} \hat{u}_R^\delta) \quad (5.81)$$

This can be further simplified into an expression for the transfer of energy across the boundary.

$$\frac{1}{2} \frac{d}{dt} \int_{-1}^1 (\hat{u}^\delta)^2 d\xi = \frac{1}{2} (2\hat{u}_L^{\delta I} - \hat{u}_L^\delta) \hat{u}_L^\delta - \frac{1}{2} (2\hat{u}_R^{\delta I} - \hat{u}_R^\delta) \hat{u}_R^\delta \quad (5.82)$$

and hence the energy stability after setting of the correction is controlled by the method used for interface calculation. In order to extract a condition in which $I_L = I_R = 0$, it is useful to consider the orthogonal polynomial basis, by using Eq.(5.3) and using the

similar basis for the correction function as in Eq.(5.58). It may be useful at this point to be reminded of the result for Legendre polynomials [52], caused by their alternating odd-even nature:

$$\int_{-1}^1 \psi_l(\xi) \frac{d\psi_m(\xi)}{d\xi} d\xi = \begin{cases} 2, & \text{for } l/2 - \lfloor l/2 \rfloor \neq m/2 - \lfloor m/2 \rfloor, \quad l \leq m \\ 0, & \text{otherwise} \end{cases} \quad (5.83)$$

Hence, applying this to I_L and I_R , the family of correction functions is found by satisfaction of the following conditions:

$$\sum_{\substack{i=0 \\ i=\text{even}}}^{p-1} \tilde{h}_{L,i} = 0 \quad \text{and} \quad \sum_{\substack{i=0 \\ i=\text{odd}}}^{p-1} \tilde{h}_{L,i} = 0 \quad (5.84)$$

By enforcing the boundary conditions namely: $h_L(-1) = 1$ and $h_L(1) = 0$, the final conditions on $\tilde{\mathbf{h}}_L$ may be found as:

$$\tilde{h}_{L,p+1} = \frac{(-1)^{p+1}}{2} \quad \text{and} \quad \tilde{h}_{L,p} = \frac{(-1)^p}{2} \quad (5.85)$$

It can be seen by comparison to the OSFR scheme of Eq.(5.29), that this new set of correction functions are coincident with the previous family of corrections at only one point, $\eta_p = 0$, corresponding to Nodal DG or when the terms of Eq.(5.84) are all zero. Owing to space of stability this scheme inhabits, this new set of corrections will henceforth be called Generalised Lebesgue Stable FR, GLSFR.

It may at this point be thought that the highly arbitrary family of correction functions that satisfy Eq.5.84 may lead to the injection or sink of mass into the sub-elements. To placate this fear we consider the integration of Eq.(5.1) over the sub-domain, *i.e.* the rate of change of mass in the sub-domain:

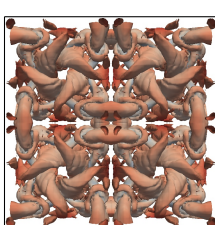
$$\frac{d}{dt} \int_{-1}^1 \hat{u}^\delta d\xi = - \int_{-1}^1 \frac{\partial \hat{f}^\delta}{\partial \xi} d\xi - (\hat{f}_L^{\delta I} - \hat{f}_L^\delta) \int_{-1}^1 \frac{dh_L}{d\xi} d\xi - (\hat{f}_R^{\delta I} - \hat{f}_R^\delta) \int_{-1}^1 \frac{dh_R}{d\xi} d\xi \quad (5.86)$$

and considering the constraints on h_L and h_R , this becomes:

$$\frac{d}{dt} \int_{-1}^1 \hat{u}^\delta d\xi = (\hat{f}_L^\delta - \hat{f}_R^\delta) + (\hat{f}_L^{\delta I} - \hat{f}_L^\delta) - (\hat{f}_R^{\delta I} - \hat{f}_R^\delta) \quad (5.87)$$

$$= \hat{f}_L^{\delta I} - \hat{f}_R^{\delta I} \quad (5.88)$$

Hence, the rate of mass accumulation within an element is dependent on the interface calculation, the flux function and, as was shown in Chapter 4, mesh deformation. But is



not dependent on the correction function, so long as the boundary conditions are fully enforced.

5.4 Analytical Findings

The investigation of correction functions has, so far, been focused on functional analysis, sitting at a very high level ensuring an abstract form of stability. To give more meaningful insight into the behaviour of the sets of FR schemes defined, we wish to perform a Fourier and von Neumann analysis. Where we will inspect the spectral properties and ergodicity of FR applied to the linear advection and advection-diffusion equations for harmonic solutions. This form of analysis was outlined by Lele [77], for finite difference and applied to DG by Hu et al. [54] and Hesthaven & Warburton [50].

The analytical techniques were then adapted to FR by Huynh [55] and Vincent et al. [128]. With the techniques extended to the fully discrete equations by Vermeire et al. [124] and Trojak et al. [119]. The formulation and structure of the analysis presented here follow that of Trojak et al. [118], which was also presented in chapter 4. We reiterate the outline of the analysis here for ease and to allow presentation of the extension to diffusion equations. Starting with the semi-discrete matrixised form of FR applied to the linear advection equation:

$$\frac{\partial \mathbf{u}_j}{\partial t} = -J_{j+1}^{-1} \mathbf{C}_+ \mathbf{u}_{j+1} - J_j^{-1} \mathbf{C}_0 \mathbf{u}_j - J_{j-1}^{-1} \mathbf{C}_- \mathbf{u}_{j-1} \quad (5.89)$$

where the matrixised operators are defined as:

$$\mathbf{C}_+ = (1 - \alpha) \mathbf{g}_R \mathbf{l}_L^T \quad (5.90)$$

$$\mathbf{C}_0 = \mathbf{D} - \alpha \mathbf{g}_L \mathbf{l}_L^T - (1 - \alpha) \mathbf{g}_R \mathbf{l}_R^T \quad (5.91)$$

$$\mathbf{C}_- = \alpha \mathbf{g}_L \mathbf{l}_R^T \quad (5.92)$$

As before, \mathbf{D} is the discrete differentiation operator, \mathbf{g}_L and \mathbf{g}_R are respectively the left and right correction function gradients at the solution points, \mathbf{l}_L and \mathbf{l}_R are respectively the interpolation coefficients to the left and right flux points from the solution points. α is then defined to be the upwinding ratio, ($\alpha = 1$ meaning fully upwinded and $\alpha = 0.5$ meaning central differenced). A harmonic solution can then be imposed on this by using the bloch wave:

$$u = v \exp(i(kx - \omega t)) \quad (5.93)$$

which, upon substitution into Eq.(5.89), the harmonic solution to linear advection via FR is thus:

$$\frac{\partial \mathbf{u}_j}{\partial t} = -\left(J_{j+1}^{-1}\mathbf{C}_+ \exp(-ik\delta_j) + J_j^{-1}\mathbf{C}_0 + -J_{j-1}^{-1}\mathbf{C}_- \exp(-ik\delta_{j-1})\right)\mathbf{u}_j = \mathbf{Q}_a\mathbf{u}_j \quad (5.94)$$

In the semi-discrete form this allows for the temporal derivative to be calculated, thus giving the eigenvalue problem:

$$c(k)\mathbf{v} = \frac{i}{k}\mathbf{Q}_a(k)\mathbf{u}_j \quad (5.95)$$

where the dispersion and dissipation can be found as $\Re(\hat{\omega}) = \Re(c)\hat{k}$ and $\Im(\hat{\omega}) = \Im(c)\hat{k}$ respectively.

Taking this analysis one step further, most problems of practical interest involve second order derivatives. Therefore, we wish to understand the behaviour and stability of this branch of correction functions when applied to diffusion and advection-diffusion problems. If we introduce the linear diffusion equation written as:

$$\frac{\partial u}{\partial t} = \nu \frac{\partial^2 q}{\partial x^2} \quad (5.96)$$

$$q = \frac{\partial u}{\partial x} \quad (5.97)$$

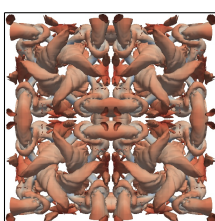
where ν is viscosity. Thus from Eq.(5.94) we may write:

$$\frac{\partial \mathbf{u}_j}{\partial t} = J_{j-1}^{-1}\mathbf{C}_{-1}J_{j-1}^{-1}\mathbf{q}_{j-1} + J_j^{-1}\mathbf{C}_0J_j^{-1}\mathbf{q}_j + J_{j+1}^{-1}\mathbf{C}_{+1}J_{j+1}^{-1}\mathbf{q}_{j+1} \quad (5.98)$$

By applying the same spatial discretisation to \mathbf{q} , \mathbf{q}_j can be written as:

$$J_j^{-1}\mathbf{q}_j = J_{j-1}^{-1}\mathbf{C}_{-1}\mathbf{u}_{j-1} + J_j^{-1}\mathbf{C}_0\mathbf{u}_j + J_{j+1}^{-1}\mathbf{C}_{+1}\mathbf{u}_{j+1} \quad (5.99)$$

This implies that the same correction function is used for both the diffusion correction and advection correction. This was found to give optimal performance [26, 23] and has the benefit of easier practical implementation. Proceeding, the semi-discretised linear



diffusion equation for FR is then:

$$\frac{\partial \mathbf{u}_j}{\partial t} = \underbrace{J_{j-2}^{-1} J_{j-1}^{-1} \mathbf{C}_{-1}^2}_{\mathbf{B}_{-2}} \mathbf{u}_{j-2} + \underbrace{J_{j-1}^{-1} (J_{j-1}^{-1} \mathbf{C}_{-1} \mathbf{C}_0 + J_j^{-1} \mathbf{C}_0 \mathbf{C}_{-1})}_{\mathbf{B}_{-1}} \mathbf{u}_{j-1} + \underbrace{J_j^{-1} (J_{j-1}^{-1} \mathbf{C}_{-1} \mathbf{C}_{+1} + J_j^{-1} \mathbf{C}_0^2 + J_{j+1}^{-1} \mathbf{C}_{+1} \mathbf{C}_{-1})}_{\mathbf{B}_0} \mathbf{u}_j + \underbrace{J_{j+1}^{-1} (J_j^{-1} \mathbf{C}_0 \mathbf{C}_{+1} + J_{j+1}^{-1} \mathbf{C}_{+1} \mathbf{C}_0)}_{\mathbf{B}_{+1}} \mathbf{u}_{j+1} + \underbrace{J_{j+1}^{-1} J_{j+2}^{-1} \mathbf{C}_{+1}^2}_{\mathbf{B}_{+2}} \mathbf{u}_{j+2} \quad (5.100)$$

where the matrices \mathbf{C}_{-1} , \mathbf{C}_0 and \mathbf{C}_{+1} are defined as before. This form is very similar to that shown in [133], although parts of there method is presented erroneously. In this case, we will use BR1 for the calculation of the common interface flux, hence $\alpha = 0.5$. Applying a trial solution of $u = v \exp(ikx_j) \exp(-k^2 c_d t)$ to Eq.(5.100) and simplifying:

$$c_d \mathbf{v} = -\frac{1}{k^2} (e^{ik(x_{j-2}-x_j)} \mathbf{B}_{-2} \mathbf{v} + e^{ik(x_{j-1}-x_j)} \mathbf{B}_{-1} \mathbf{v} + \mathbf{B}_0 \mathbf{v} + e^{ik(x_{j+1}-x_j)} \mathbf{B}_{+1} \mathbf{v} + e^{ik(x_{j+2}-x_j)} \mathbf{B}_{+2} \mathbf{v}) \quad (5.101)$$

If $\delta_j = x_j - x_{j-1}$, then this can be further simplified to:

$$c_d \mathbf{v} = -\frac{1}{k^2} (e^{-ik(\delta_{j-1}+\delta_j)} \mathbf{B}_{-2} + e^{-ik\delta_j} \mathbf{B}_{-1} + \mathbf{B}_0 + e^{ik\delta_{j+1}} \mathbf{B}_{+1} + e^{ik(\delta_{j+2}+\delta_{j+1})} \mathbf{B}_{+2}) \mathbf{v} \quad (5.102)$$

Which can also allow us to define the FR diffusion matrix as:

$$\mathbf{Q}_d = (e^{-ik(\delta_{j-1}+\delta_j)} \mathbf{B}_{-2} + e^{-ik\delta_j} \mathbf{B}_{-1} + \mathbf{B}_0 + e^{ik\delta_{j+1}} \mathbf{B}_{+1} + e^{ik(\delta_{j+2}+\delta_{j+1})} \mathbf{B}_{+2}) \quad (5.103)$$

Equation (5.102) is again an eigenvalue problem, albeit a non-trivial one, where from [115, 133] the dissipation and dispersion are defined as $\Re(\hat{k}^2 c_d)$ and $\Im(\hat{k}^2 c_d)$ respectively, due to the of the second derivative. The physical mode is extracted from the $p + 1$ dimensional eigenproblem following the procedure of [133]. Finally for the case of linear advection-diffusion, the fully discrete form may be written using the update matrix, which

encompasses the temporal integration method.

$$\mathbf{Q}_{\text{ad}} = 2c\mathbf{Q}_a + 4\nu\mathbf{Q}_d \quad (5.104)$$

$$\mathbf{u}_j^{n+1} = \mathbf{R}(\mathbf{Q}_{\text{ad}})\mathbf{u}_j^n \quad (5.105)$$

$$\mathbf{R}_{33}(\mathbf{Q}_{\text{ad}}) = \sum_{m=0}^3 \frac{(\tau\mathbf{Q}_{\text{ad}})^m}{m!} \quad (5.106)$$

where τ is the explicit time step. From the update matrix \mathbf{R} the fully discrete dispersion and dissipation can then be found by further substitution of the trial solution of Eq.(5.93) into Eq.(5.104).

$$\underbrace{e^{-ik(c-1)\tau}}_{\lambda} \mathbf{v} = e^{ik\tau} \mathbf{R} \mathbf{v} \quad (5.107)$$

$$c(k; \tau) = \frac{i \log(\lambda)}{k\tau} + 1 \quad (5.108)$$

Hence, from von Neumann's theorem [58], for temporal stability of the fully discrete scheme the spectral radius of the update matrix must be less than or equal to one, $\rho(\mathbf{R}) \leq 1$. For comparative purposes we then define the normalised time step for advection-diffusion as:

$$\hat{\tau} = \left(\frac{2c}{h} + \frac{4\nu}{h^2} \right) \tau \quad (5.109)$$

and this will be used to define the CFL limit.

The final analytic method that will be used, is the rate of convergence of the solution error with grid spacing. In order to calculate the error with time we first define the diagonalisation of \mathbf{Q}_a as:

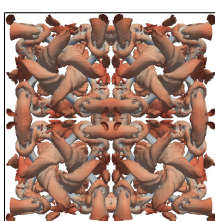
$$\mathbf{Q}_a = ik\mathbf{W}\Lambda\mathbf{W}^{-1} \quad (5.110)$$

By diagonalising the semi-discrete operator in this manner, where \mathbf{W} is the eigenvector matrix and $\Lambda = \text{diag}(\lambda_0 \dots \lambda_p)$, we may form the initial interpolation of the solution as:

$$\mathbf{u}_j^\delta(t=0) = \exp(ikx_j)\mathbf{W}\mathbf{v}_0 = \exp\left(ik(J_j(\zeta+1) + x_j)\right) \quad (5.111)$$

To calculate the rate of convergence, we need to monitor the semi-discrete error of the solution for different grid spacings. The derivation of the analytical semi-discrete and fully-discrete error can be found in [9, 119] and as the derivation is secondary to the aim, here we will jump to the end result for the semi-discrete error.

$$\mathbf{e}_j(t, J) = \mathbf{u}_j^\delta(t) - \mathbf{u}_j(t) = \exp(ik(x_j - t)) \sum_{n=0}^p \left(\exp(ikt(\lambda_n + 1)) - 1 \right) \mathbf{w}_{0,n} \mathbf{w}_n \quad (5.112)$$



where \mathbf{w}_n is the n^{th} column vector of \mathbf{W} . If we define the l_2 norm of the error as $\|\mathbf{e}(t, J)_j\|_2 = E(t, J)_j$ then the grid convergence rate is:

$$r_h(t) = \frac{\log(E(t, J_1)_j) - \log(E(t, J_2)_j)}{\log J_1 - \log J_2} \quad (5.113)$$

where J_1 and J_2 are the Jacobians of the two grids over which the convergence rate is to be calculated. With the tools needed having been defined we may now move onto presenting various findings for the classes of correction functions.

5.4.1 GJFR Results

We will begin the analysis of GJFR by studying qDG which, for a given α & β , the correction parameter is set as $\iota = 0$. In the case of $\alpha = \beta = 0$ this is known to be equivalent to Nodal DG. Therefore, when the space of correction functions is extended using the Jacobi weighting function, the set of schemes may be considered to be quasi-DG (qDG) for the different bases. The property that sets DG apart from other correction functions is that it achieves super-convergence [55, 9, 31, 5, 138], *i.e.* for sufficiently smooth and well resolved specific cases, the rate of error convergence can be of order $2p + 1$, whereas other FR schemes would normally be expected to obtain less.

Because of this feature we will initially look at the rate of convergence of the qDG, with a focus on the case when $\alpha = \beta$, *i.e.* symmetric weight functions. There are two rates of convergence that can be considered, the initial rate as $t \rightarrow 0$ and the long time rate as $t \rightarrow \infty$, with the initial rate being dictated by the secondary modes and the long time rate by the primary mode. Due to the secondary modes having very short half-lives at a well-resolved wavenumbers [119], we consider the most important convergence rate to be $r_h(t) \rightarrow \infty$, and this is shown in Figure 5.3. It is evident then that for both the central difference and upwinded interface case improvement may be made to the rate of convergence over standard DG schemes. It may be possible, then, to improve the practical performance of FR using a qDG scheme.

Second, we go on to study the stability of the qDG once the temporal integration is discretised. For this we will make use of low storage RK schemes [67] as they can be simply added to FR schemes practically and do not prohibitively increase memory usage, a major concern with the current cost of graphics RAM.

Figure 5.4 then shows that for both RK33 and RK44, as α or β is decreased the CFL limit is reduced. Furthermore, as $\beta \rightarrow -1$ temporal stability is lost, and in order to understand this it can be useful to consider the shape of the correction function as $\beta \rightarrow -1$ which is shown in Figure 5.5. From this it is evident that the maximum gradient increases, with significant changes occurring across the whole domain. This is the opposite of

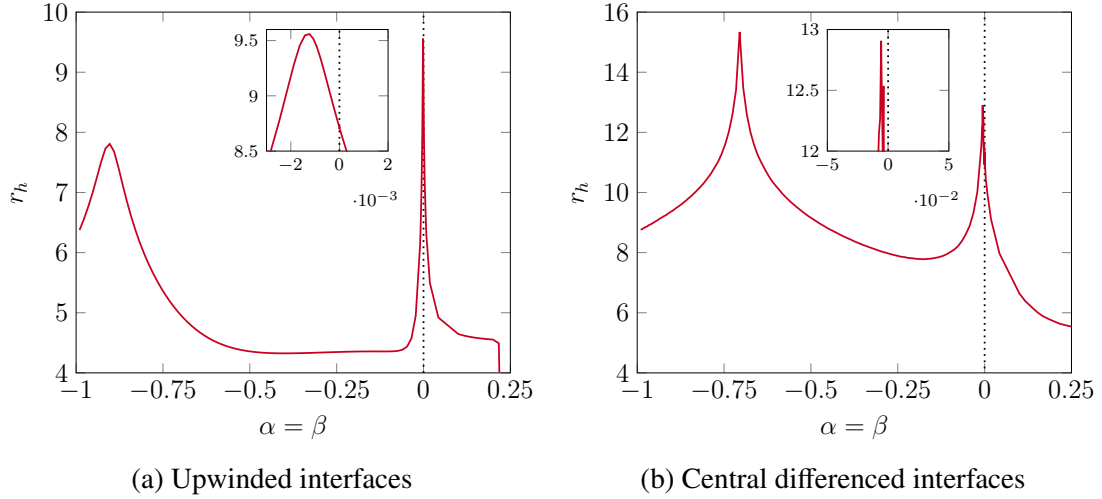


Fig. 5.3 Variation of the rate of error convergence with grid for quasi-DG correction functions, ($\iota = 0$) when, $p = 4$, $\alpha = \beta$, $J_2/J_1 = 0.5$, $k = 3\pi/4$ and, $t/T = 1000$. The dotted line is for $\alpha = \beta = 0$.

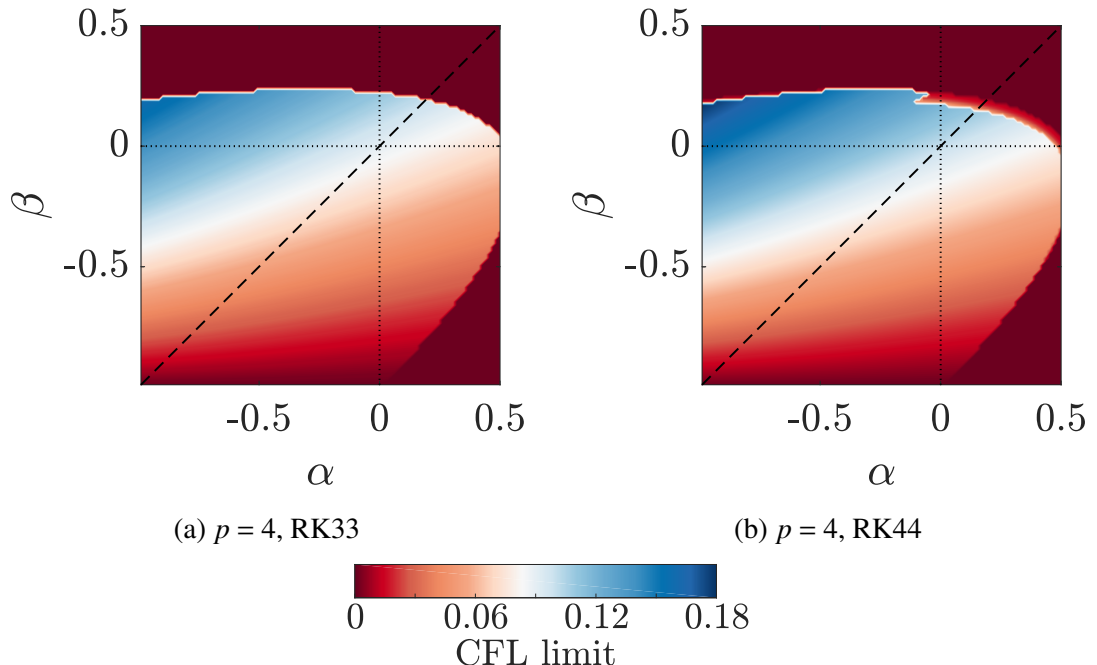
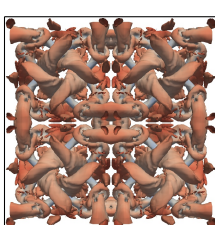


Fig. 5.4 CFL limit of various temporal integration methods for $\iota = 0$ with upwinded interfaces. The dashed line is for $\alpha = \beta$ and the dotted lines are $\alpha = 0$ and $\beta = 0$.



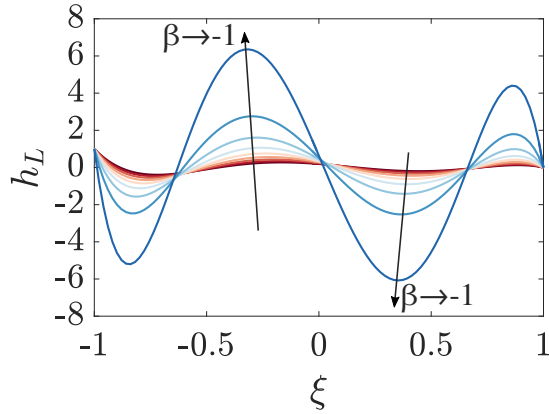


Fig. 5.5 qDG, $p = 4$, correction functions for $\alpha = 0$ as $\beta \rightarrow -1$ from $\beta = 0$.

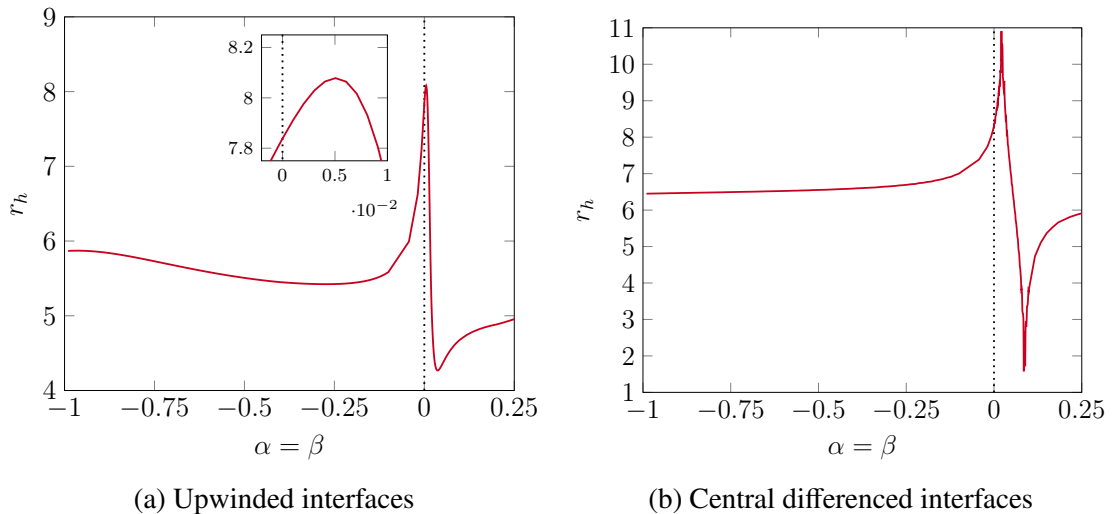


Fig. 5.6 Variation of the rate of error convergence with grid for SD correction functions when, $p = 4$, $\alpha = \beta$, $J_2/J_1 = 0.5$, $k = \pi/2$ and, $t/T = 1000$. The dotted line is for $\alpha = \beta = 0$.

what Huynh [55] proposed as good characteristics for temporal stability, where most of gradient was lumped at one end.

Moving on now to study another subset of GJFR, SD. Spectral Difference via FR is often considered in some sense as being a canonical FR correction function [55, 127, 22, 125]. This is with good reason as its dispersion and dissipation characteristics are quite favourable [128]. Yet the Jacobi generalisation allows us to extend the definition of the SD correction functions, allowing us to investigate whether yet more favourable characteristics can be achieved. To restrict the space of possible functions we will use a detail outlined in section 5.3.2, that in the case of $\alpha \neq \beta$ the correction functions are not symmetric about $\zeta = 0$. This will bias convection due to directional variation in the phase and group velocities, which for most practical calculations would be unacceptable. Because of this our study into the rate of convergence will focus on the case of $\alpha = \beta$.

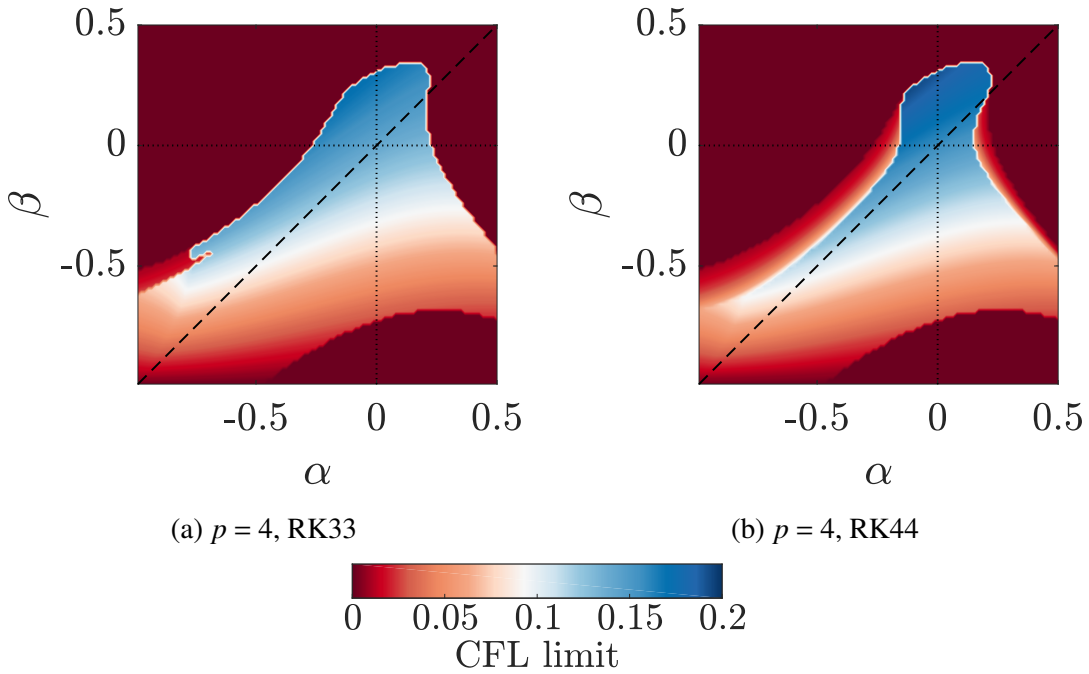
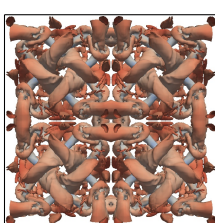


Fig. 5.7 CFL limit of various temporal integration methods for Jacobi SD with upwind interfaces. The dashed line is for $\alpha = \beta$ and the dotted lines are $\alpha = 0$ and $\beta = 0$.

The long time rate of convergence is then presented in Figure 5.6 for both upwinded and central differenced interfaces. In both cases, it is clear that improvements may be made. This improvement is only minor in the case of upwinded interfaces, however when the interface is centrally differenced, a three order increase in the rate of convergence can be seen for $\alpha = \beta \approx 2 \times 10^{-2}$. This is similar in size to the increase seen for qDG with central differencing.

After the peak rate of convergence, there is a sharp drop off in the rate of convergence towards unity order. A similar drop off in Figure 5.6a is also seen but closer to the peak value. When practically implemented, an approximate Riemann solver is used across the interface, which is likely to give a mix of upwinding and central flux - so the rate of convergence will vary somewhere between the Figure 5.3a & 5.3b. Because of this, to avoid hitting the penalty of the sharp decrease in order as the degree of upwinding changes, it may be more robust to use an $\alpha = \beta$ value closer to 5×10^{-3} (the upwind optimal) rather than the central optimal value.

Again, when using these correction functions practically, a method of discrete time integration will be used. Figure 5.7 displays the CFL limit for $p = 4$ for two low storage RK explicit temporal integration schemes. It is evident that, although previously we showed that ι_{SD} would lead to the norm always being positive. This, together with the result for qDG, indicates that the critical value of ι is a necessary but not sufficient condition for stability and that additional contributions from Eq.(5.40) will further restrict



the stability. This is not unexpected, as when $\alpha, \beta < 0$ it is clear that the weight function is ill-defined at the end-points; something which is not reflected in the value of ι_{crit} . However, ι_{crit} is not without merit and Figures 5.4 & 5.7 clearly show that there is a well defined stable region of correction functions which contain the optimal points found in Figures 5.3 & 5.6. In the case of optimal SD, the CFL limit is approximately the same as for the original SD scheme ($\alpha = \beta = 0$) and the performance will be further explored in the next section.

For completeness, we include in Figure 5.8 the dispersion and dissipation relationships for the correction functions that give optimal rates of convergence. These relations can be extracted from the diagonal matrix Δ and for the case of central differenced interfaces the dissipation is zero. The dispersion relations for central differenced interfaces are also split between two modes, one active at low frequencies and the other active at high frequencies. Because of this we have included both modes. Comparison made between these relations and their OSFR counterparts found previously by Vincent et al. [128] show that the difference is only slight. This should give us confidence that the correction functions found will at least provide a reasonable answer practically.

5.4.2 GSFR Results

We will now present the analytic findings of GSFR, with the focus being on the temporal stability. This is due to the high dimensionality of the correction function space and the computational expense of calculating the convergence.

As was discussed in Section 5.3.3, the cross product between some of the solution weights, for example the last term in Eq.(5.68), leads to difficulty in transforming the necessary condition for a positive definite norm to a condition on \mathbf{I}_p . Although a sufficient condition on \mathbf{I}_p can be found, \mathbf{I}_p will be allowed to vary beyond these bounds to aid understanding in the underlying necessary condition. Throughout this analysis ι_0 will also be taken as one; it should be understood that this is an arbitrary choice, but that choosing a different value will simply lead to a linear scaling of all other ι_i values shown here.

Beginning with the case of $p = 3$, Fig. 5.9 shows the variation of CFL number with \mathbf{I}_3 for low storage RK44 temporal integration. In this figure positive and negative log axes in ι_2 and ι_3 are used to clearly show the CFL manifold, the join is at $\pm 10^{-5}$. This chiefly shows the extent of the domain of \mathbf{I}_3 and also highlights some regions of interest. The first region to consider is that as $\iota_3, \iota_2 \rightarrow \infty$, in this case the correction function converges upon $p = 2$ correction functions. This is similar to the properties of the ESFR scheme. Secondly, in Fig.5.9a, a region at $\iota_1 = 5 \times 10^{-2}$ as $\iota_2 \rightarrow \infty$. Here an almost one dimensional region of high CFL is present, where the correction function order drops further to $p = 1$. Lastly consider the region where $\mathbf{I}_3 \approx [1, 0, 10^{-3}, 10^{-3}]^T$, here the CFL

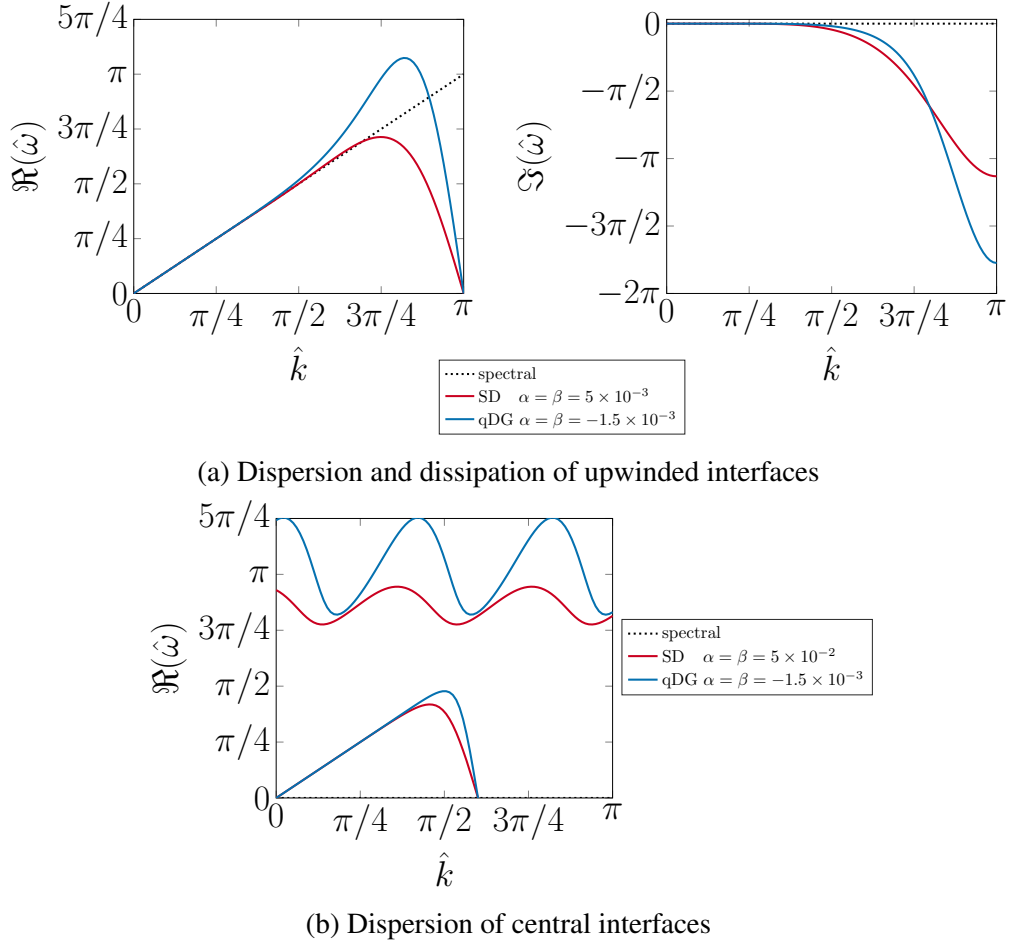


Fig. 5.8 Dispersion ($\Re(\hat{\omega})$) and dissipation ($\Im(\hat{\omega})$) relations of the SD and qDG $p = 4$ correction functions found to give improved rates of convergence.

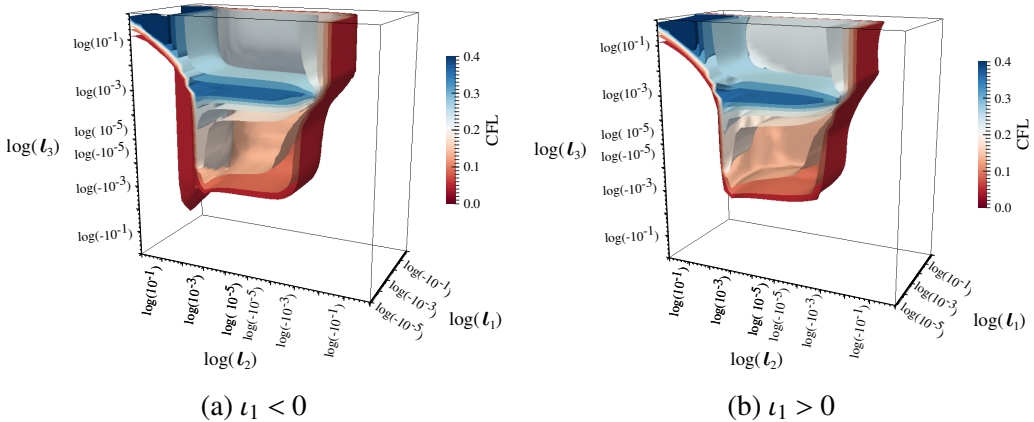
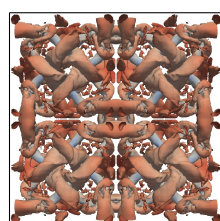


Fig. 5.9 CFL limit for upwinded FR with GSFR correction functions, $p = 3$, and RK44 temporal integration on a regular grid.



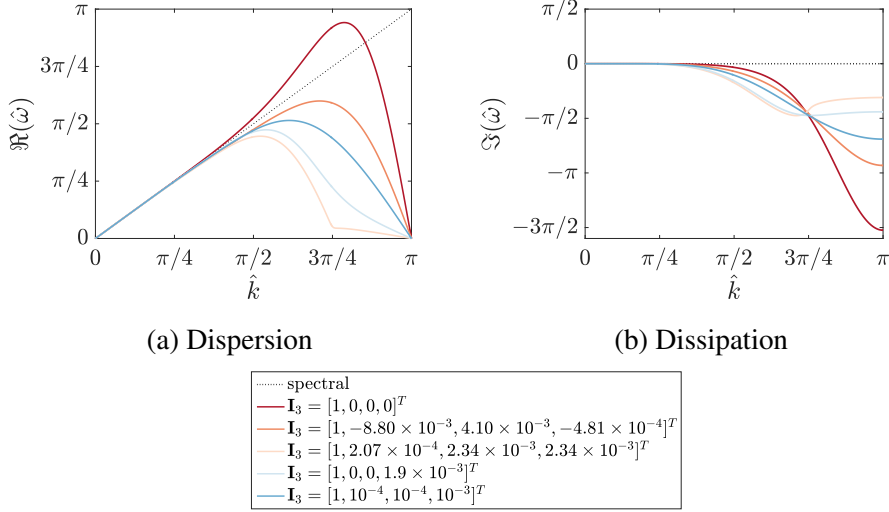


Fig. 5.10 Dispersion and dissipation for selected $p = 3$ GSFR correction functions with interface upwinding.

limit can be seen to have a local maximum. This region of local maximum is believed to give recovery of high-order due to the scale of the Legendre weights, which can be shown analytically through the position of the Nyquist wavenumber of the semi-discretised form, with degradation in the Nyquist limit indicating a drop in order of accuracy (OOA). To exactly find the OOA a numerical method will be introduced in Section 5.5.1.

The investigation of the dispersion and dissipation for some selected correction functions when $p = 3$ is presented in Fig. 5.10. The third correction function tested is that which gives peak CFL performance. In this case the Nyquist wavenumber is maintained at that for an OOA of four. However, a drop in the phase velocity, $c_p = \omega/k$, at high wavenumber is exhibited, but associated with this there has been a significant reduction in the dissipation. The combination of these has then given rise to an increased CFL limit, but at the cost of spectral performance.

Returning to the investigation of CFL limits, Fig. 5.11 shows two regions of interest for $p = 4$ which are similar to those shown for $p = 3$. However, now with the first region found in $-\iota_3$ half plan, which may have been predicted by the interaction of the odd and even powers. Although a localised maximum CFL limit can be seen, the free parameter is four dimensional, and hence a search method will have to be used to find the global high-order recovering maximum CFL limit. This method will be explored fully in Section 5.5.1.

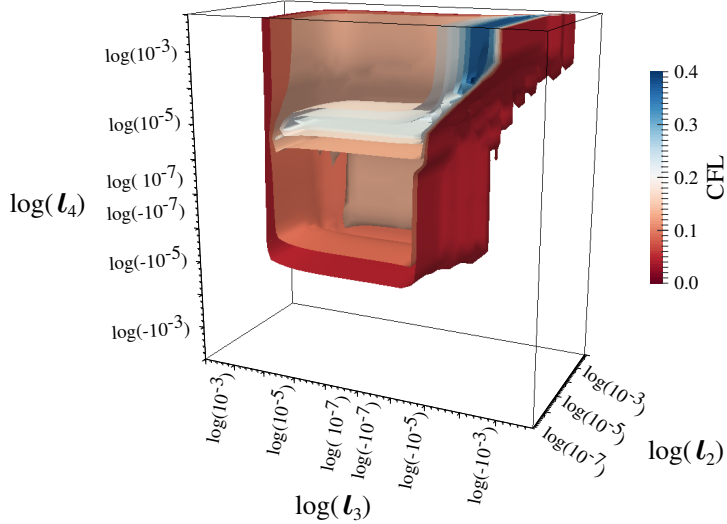


Fig. 5.11 CFL limit for upwinded FR with GSFR correction functions, $p = 4$, and RK44 temporal integration on a regular grid. ($\iota_1 = 1 \times 10^{-5}$)

5.4.3 GLSFR Results

GLSFR presents us with a far broader scope of correction functions owing to the almost arbitrary nature of the variables defining them. As a result we will initially study the dispersion and dissipation of linear advection, with the primary aim of showing how, for what may be traditionally considered an inappropriate correction function, we are able to recover a stable scheme. Take the following example, when $p = 4$ and the correction weights are chosen arbitrarily to be:

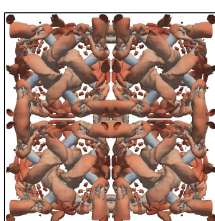
$$\tilde{h}_{l0} = (5.22943203125 \times 10^4) \times 10^{-5} \quad (5.114)$$

$$\tilde{h}_{l1} = 0.1\sqrt{2} \quad (5.115)$$

where Eq.(5.114) is 10^{-5} times the floating point representation of the ASCII string ‘GLFR’. It is clearly apparent that this arbitrary correction function that satisfies Eq. (5.84) is stable and although wave propagating characteristic of this arbitrary example are not optimal. However, this aims to demonstrate initially that a correction function may be defined that was previously unproduicible, leading to an incredibly general family of schemes.

In order to understand the space of temporally stable GLSFR correction functions the 1D linear-advection von Neumann analysis is first investigated for various orders, correction functions and interface calculations.

Figure 5.13 shows the region of stable correction function when RK44 temporal integration is used, with a clear region of overlap between the upwinded and central cases. For previous correction function sets, the existence of the Sobolev norm was



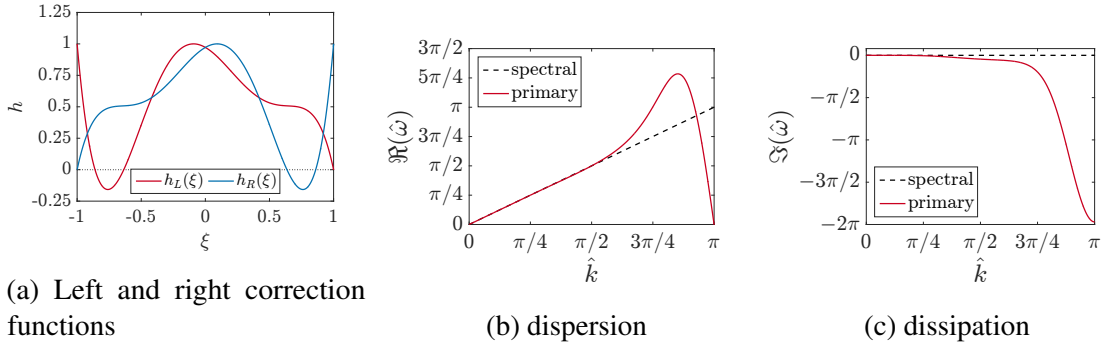


Fig. 5.12 Correction function and wave propagating characteristics for arbitrary correction weights as in Eq.(5.114 & 5.115), for $p = 4$ on a uniform grid with upwinded cell interfaces applied to linear advection.

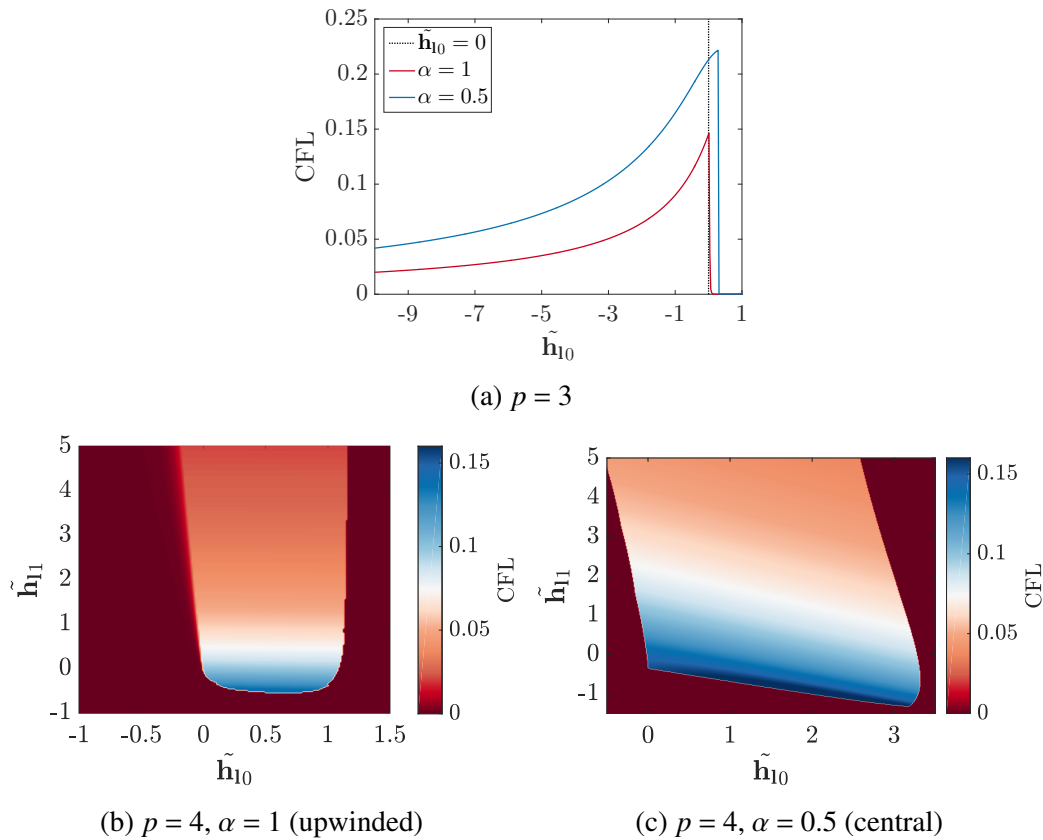


Fig. 5.13 Maximum stable CFL number for GLSFR [$c = 1, \nu = 0$], with RK44 temporal integration.

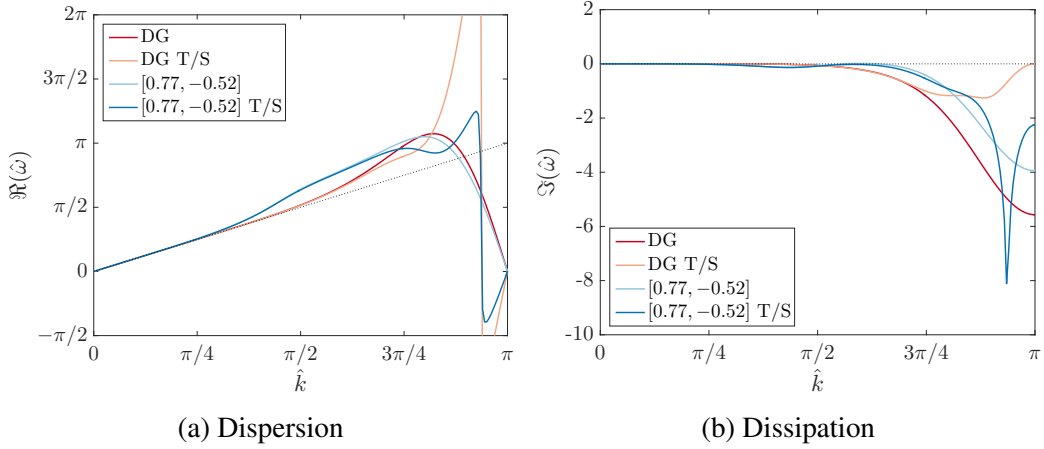
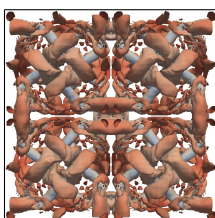


Fig. 5.14 Linear advection dispersion and dissipation comparison of spatial and temporal-spatial (T/S) analysis for upwinded FR, $p = 4$. This compares DG and with GLSFR with $\mathbf{H}_4 = [0.77, -0.52]$. The temporal-spatial analysis uses RK44 temporal integration at $\tau = 0.1$ in both cases.

used to determine the region of stable correction functions, however due to the nature of the GLSFR Sobolev norm, in that it collapses onto the L^2 norm, this approach could not be taken. Instead the results of Fig. 5.13 may be used to heuristically bound the correction function set. To demonstrate the wave propagation properties of GLSFR we perform a semi-discrete and fully discrete von Neumann analysis. We will take the case when $p = 4$ and compare the correction function that gives the highest CFL limit for both the upwinded and central case to DG. We chose DG as this is a commonly used scheme even within FR [130] due to the complexity currently with the simplex correction definition [25]. The CFL optimal case corresponds to $\mathbf{H}_4 = [\tilde{\mathbf{h}}_{10} = 0.77, \tilde{\mathbf{h}}_{11} = -0.52]$, with the DG comparison at $\mathbf{H}_4 = [0, 0]$.

It should be clear from Fig. 5.14 that GLSFR in the fully discrete case is able to greatly reduce the wave group velocity, however at the expense of dispersion overshoot. Furthermore, by comparison of the dispersion and dissipation it can be seen that this GLSFR correction function has a very localised region of high dissipation around the wavenumber where the dispersion leads us to have a very large negative group velocity. It can be concluded that such a scheme may give improved performance when applied to explicit LES.

Lastly for the advection study, the semi-discrete dispersion relation for DG and $\mathbf{H}_4 = [0.77, -0.52]$ with central interfaces are included for completeness. It can be seen that the regions in DG where the dispersion relation is discontinuous has been greatly reduced, from [133, 9], it can be understood that the smaller regions of discontinuity in the dispersion relation, leads to less energy transfer to spurious modes.



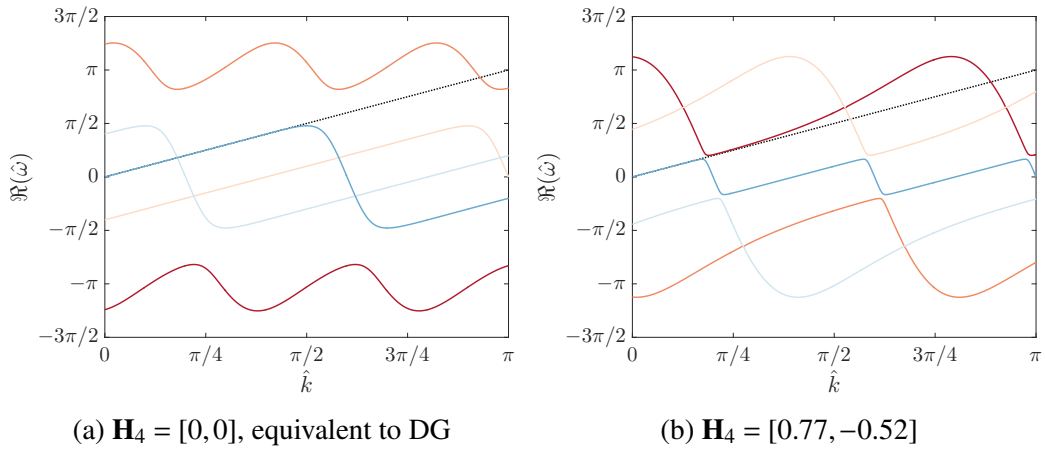


Fig. 5.15 Linear advection dispersion relations for central interface flux FR, $p = 4$, with the dispersion shown for all modes.

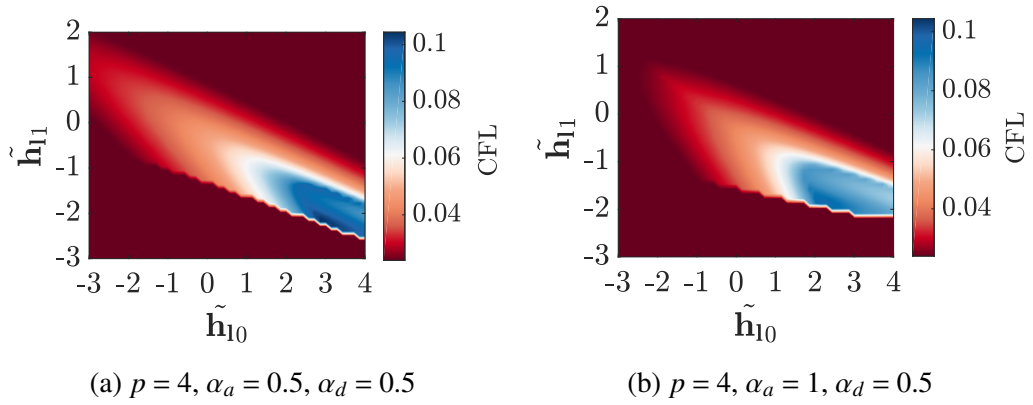


Fig. 5.16 Maximum stable CFL number for GLSFR [$c = 10, v = 1$], with RK44 temporal integration.

To study the general trend in the CFL limit of the combined advection diffusion equation we use the case of $a = 10$ and $v = 1$, which was similarly used in the investigation by Watkins et al. [133]. Figure 5.16 shows the CFL limits for $p = 4$ for various correction functions for the case when the both advection and diffusion interface calculation are central differenced and the case when advection is upwinded and diffusion is central differenced. In both cases it can be seen that the stability profile is of a different character than pure advection, with higher values of \tilde{h}_{l0} being stable due to the additional stability brought by the diffusion terms. The motivation of this test is the understanding it can bring to later tests. With the main observation being the slant to the CFL profile, although this will be affected by the relative scale of the advection-diffusion terms.

5.5 Numerical Experiments

5.5.1 Linear Problems - GSFR

Generalised Sobolev stable correction function have a large number of variables that define there shape. Therefore it is not practical to explore the behaviour of the whole space of correction function on a non-linear equation set. Therefore, we will examine the behaviour an a set of linear cases. These test are were undertaken to validate analytical findings and provide useful further insight. The first such numerical test was contrived to calculate the OOA of the scheme while solving the linear advection equation with wave speed of unity. The domain set-up for this case was a periodic domain with $x \in [0, 2\pi]$, with the number of elements allowed to vary such that varying degrees of freedom could be tested. The interfaces were fully upwinded and a time step was chosen such that the temporal integration was not the primary source of error. The initial solution was taken to be a plane wave, with a wavenumber that would be expected to be well resolved on the grids:

$$u(x; t = 0) = u^e(x; t = 0) = \cos(kx), \quad k = \frac{1}{2\pi} \quad (5.116)$$

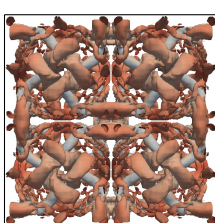
where $u^e(x, t)$ is the exact solution and $u(x, t)$ is the approximate solution from FR. Taking the solution after some number of time integrations, the point averaged error can be calculated for several grid densities, with n_s points:

$$e_2 = \frac{1}{n_s} \sum_{i=1}^{n_s} |u^e(x_i, t) - u(x_i, t)| \quad (5.117)$$

$$e_2 = |u^e(x, t) - u(x, t)| = O(n_s^{-k}) \quad (5.118)$$

where k is the numerically realised OOA, which can be found through taking logs of Eq.(5.118). With this established, the correction functions can now be varied to to show the effect of \mathbf{I}_p on OOA.

Figure 5.17 shows one of the regions of interest for the case of $p = 3$. What can be noted is that the analytically predicted decrease in order as $\iota_3 \rightarrow \infty$ is demonstrated numerically, with $\text{OOA} \rightarrow p$. Reassuringly, the order accuracy in the region of $\iota_3 \approx 10^{-3}$, where peak temporal stability is believed to lie, is shown to have $\text{OOA} = p + 1$ and hence the maximum CFL limit may be increased without an apparent loss in order accuracy. It may, therefore, be productive to perform a search of correction functions, in order to find the peak CLF limit. The domain of \mathbf{I}_p is sufficiently small, permitting an exhaustive search that couples the numerical OOA calculation and analytic CFL calculation to find the maximum CFL limit. The results of this search are shown in Table 5.1, in all cases the OOA recovered was $p + 1$, consistent with the expected order. It may be noted that in



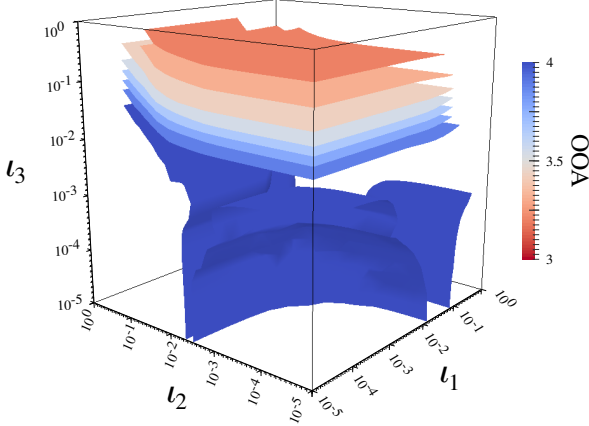


Fig. 5.17 Order of accuracy of GSFR, $p = 3$ for linear advection of a wave with $k = 1/2\pi$, at $t = \pi$.

Table 5.1 Peak CFL of Order recovering GSFR

p	RK Scheme	\mathbf{I}_p	τ
3	RK33	$[1, 1.274 \times 10^{-3}, 1.438 \times 10^{-2}, 7.848 \times 10^{-3}]^T$	0.385
	RK44	$[1, 2.069 \times 10^{-4}, 2.336 \times 10^{-3}, 2.336 \times 10^{-3}]^T$	0.390
	RK55	$[1, 6.952 \times 10^{-4}, -6.158 \times 10^{-5}, 2.336 \times 10^{-3}]^T$	0.443
4	RK33	$[1, 4.833 \times 10^{-4}, 2.336 \times 10^{-5}, -1.438 \times 10^{-4}, 2.637 \times 10^{-4}]^T$	0.431
	RK44	$[1, 1.624 \times 10^{-3}, 2.637 \times 10^{-4}, -2.637 \times 10^{-4}, 2.637 \times 10^{-4}]^T$	0.430
	RK55	$[1, 1.624 \times 10^{-3}, 1.274 \times 10^{-5}, -2.637 \times 10^{-4}, 8.859 \times 10^{-4}]^T$	0.354

some cases a significant improvement upon the CFL limit may be made by comparison to Vincent et al. [128].

Thus far, the investigation has focused exclusively on the linear advection equation. However, for practical applications, non-linear conservation equations will be encountered. Other than the introduction of shock-waves, for which there treatment is still an open question, non-linear equations also introduce aliasing error due to the multiplication of polynomials. This results in a solution that lies beyond the spectral resolution of the grid. Further insight into the origin and effect of order and aliasing was investigated by Kravchenko and Moin [70]. Previously, to investigate this problem, a flux function used by Hesthaven and Warburton [51] and Vincent et al. [127] was defined as:

$$f(x; t) = ((1 - x^2)^5 + 1)u(x, t) \quad (5.119)$$

However, when applied to a periodic domain $\Omega = [-1, 1]$ the flux function of Eq.(5.119) is only C^0 continuous. Hence, it is proposed that it would be more suitable to use a flux

function defined as:

$$f(x; t) = (\sin(\pi x) + 2)u(x; t) \quad (5.120)$$

This flux function is strictly linear in u , however the spatial dependence of the flux function, results in the triggering of aliasing error. Therefore, this gives useful insight into GSFR's application to full non-linear problems, without the associated problems of shock formation. To understand the mechanism of production for aliasing error, consider the finite spatial Fourier series of an approximate solution $u(x, t)$:

$$u(x, t) = \sum_{n=-N/2}^{N/2-1} w_n(t) \exp\left(\frac{n\pi i x}{l}\right) \quad (5.121)$$

where $w_n(t)$ are time dependent Fourier weights, and l is the domain half length. The half length can be used to generalise Eq.(5.120), such that, together with application of the product rule, one has:

$$\frac{\partial(\sin(\frac{\pi x}{l}) + 2)u}{\partial x} = \left(\sin\left(\frac{\pi x}{l}\right) + 2 \right) \frac{\partial u}{\partial x} + \frac{\pi}{l} \cos\left(\frac{\pi x}{l}\right) u \quad (5.122)$$

By subsequent application of the Fourier series of Eq.(5.121):

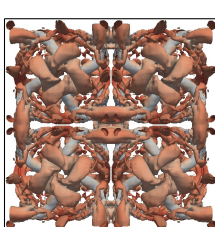
$$\begin{aligned} \frac{\partial(\sin(\frac{\pi x}{l}) + 2)u}{\partial x} &= \frac{\pi}{2l} \sum_{n=-N/2}^{N/2-1} w_n(t) \left(4ni \exp\left(\frac{nx}{l}\right) \right. \\ &\quad \left. + \exp\left(\frac{(n-1)\pi i x}{l}\right) (1+ni) \right. \\ &\quad \left. + \exp\left(\frac{(n+1)\pi i x}{l}\right) (1-ni) \right) \end{aligned} \quad (5.123)$$

hence, aliasing is injected only by the highest frequency mode and will propagate down through the modes. As opposed to the flux function of Eq.(5.119), which would cause aliasing error injection at all modes. For the numerical experiment, the domain set up was $\Omega = [-1, 1]$ with periodic boundaries. The method of temporal integration used was low storage RK44, with τ set to be sufficiently small that the temporal integration had a negligible effect on the error. To illustrate the effect on the solution, the domain L^2 energy of the conserved variable is used, defined as:

$$E(t) = \int_{\Omega} u(x, t)^2 dx \quad (5.124)$$

and the initial condition will be taken as:

$$u(x; t = 0) = \sin(4\pi x) \quad (5.125)$$



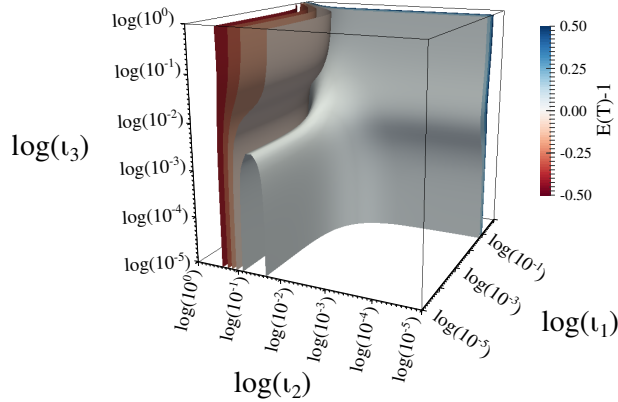


Fig. 5.18 L^2 energy error for FR, $p = 3$, using RK44 temporal integration with $CFL = 0.06$, for $\alpha = 1$ (upwinded) $t = T = 2/\sqrt{3}$.

The effect of having a flux function that is C^∞ continuous on Ω is that the periodic boundaries are analogous to solving the same equation on an infinite domain. Hence, the time period of the solution can be found analytically to be $T = 2/\sqrt{3}$. To evaluate the relative performance of correction functions, the L^2 energy error relative to some known value of the L^2 energy is compared for various correction functions. Due to the periodicity of the solution, the error at some time nT , $n \in \mathbb{N}$ may be straightforwardly calculated, *i.e.* analytical energy $E_a(nT) = 1$.

Figure 5.18 shows just such an error in the L^2 energy, for $p = 3$ with upwinded interfaces. Central differenced interfaces are not shown as, for all correction functions, the scheme had gone unstable within $t = 15T = 30/\sqrt{3}$. This is due to the coupling of the aliasing error to the zero dissipation associated with central difference. The result is that any error introduced into the solution does not become damped and hence instability arises. However, when considering the case of upwinded interfaces, the implicit dissipation in the scheme can be sufficient to stabilise the errors introduced through aliasing. It may also be noted that, from Fig. 5.9, the region of localised peak CFL number lies within a region of low aliasing error and hence correction functions in this region ($\iota_3 \approx 1 \times 10^{-3}$, $\iota_1 \approx 0$) may be good candidates for practical applications.

5.5.2 Isentropic Convecting Vortex - GSFR

Owing again to the high level of dimensionality of the GSFR definition, we will conclude the investigation of GSFR with application to the 3D Euler equations, defined as:

$$\frac{\partial \mathbf{U}}{\partial t} + \nabla \cdot \mathbf{F} = 0 \quad (5.126)$$

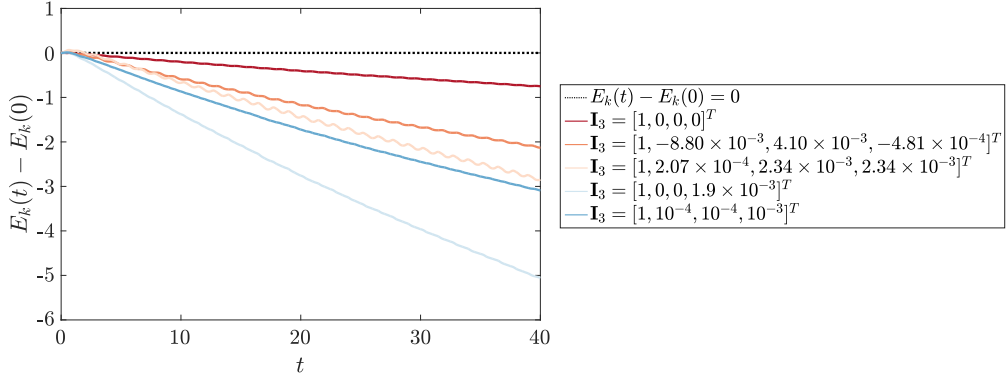


Fig. 5.19 Error in the domain integrated kinetic energy of the ICV for FR, $p = 3$, for various correction functions. Using RK44 temporal integration with $\tau = 10^{-3}$ on $\Omega = [-10, 10]^3$ with $16 \times 16 \times 1$ elements. For the error calculation, $E_k(0)$ was calculated on a $256 \times 256 \times 1$ grid. Finally the convective velocity was taken as $u_0 = v_0 = 1$, $w_0 = 0$.

where

$$\mathbf{F} = [\mathbf{f} \quad \mathbf{g} \quad \mathbf{h}]^T \quad (5.127)$$

$$\mathbf{f} = \begin{bmatrix} \rho u \\ \rho u^2 + p \\ \rho u v \\ \rho u w \\ u(\frac{1}{2}\rho \mathbf{V} \cdot \mathbf{V} + \rho e + p) \end{bmatrix} \quad \mathbf{g} = \begin{bmatrix} \rho v \\ \rho u v \\ \rho v^2 + p \\ \rho v w \\ v(\frac{1}{2}\rho \mathbf{V} \cdot \mathbf{V} + \rho e + p) \end{bmatrix} \quad \mathbf{h} = \begin{bmatrix} \rho w \\ \rho u w \\ \rho v w \\ \rho w^2 + p \\ w(\frac{1}{2}\rho \mathbf{V} \cdot \mathbf{V} + \rho e + p) \end{bmatrix} \quad (5.128)$$

with $\mathbf{V} = [u, v, w]^T$. The case used to numerically investigate the performance of FR on Euler's Equations is the Isentropic Convecting Vortex (ICV) [29]:

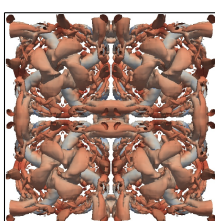
$$u = u_0 + \frac{\beta(y_c - y)}{2\pi} \exp\left(\frac{1 - r^2}{2}\right) \quad (5.129)$$

$$v = v_0 + \frac{\beta(x - x_c)}{2\pi} \exp\left(\frac{1 - r^2}{2}\right) \quad (5.130)$$

$$w = w_0 \quad (5.131)$$

$$T = 1 - \frac{(\gamma - 1)\beta^2}{8\gamma\pi^2} \exp(1 - r^2) \quad (5.132)$$

where, β is the vortex strength, x_c and y_c are the grid centre coordinates, γ is the ratio of specific heats, $r = \sqrt{x^2 + y^2}$ and T is temperature. The domain of the solution is taken as $\Omega \in [-10, 10]^3$ with periodic boundaries and the vortex strength $\beta = 5$. For this case the common interface flux calculation used is the Rusanov flux [103] with characteristic speed from Davis [35].



As is shown in Fig.5.19, all the correction functions taken from the region deemed stable for linear advection, are stable when applied to the ICV. For all correction functions tested, there is a small region, $0 \leq t \leq 2$, where the kinetic energy increases above the initial value, this is likely due to the smoothing of the higher order discontinuities in the solution. The origin of these discontinuities is, although the domain is large, the solution is not strictly C^p continuous on a periodic domain, and the effect of these discontinuities were seen to reduce as the domain is widened. The oscillation that is also seen in all the error plots of Fig.5.19 is due to the grid affecting integration accuracy and has a frequency that reflects this. The correction functions considered here are: DG; the CFL optimal correction function presented by Vermeire and Vincent [125]; the CFL optimal correction function from Table.5.1; the correction function found by Vincent et al. [128] to give best temporal stability this combination of spatial-temporal scheme; and lastly a stable correction function chosen arbitrarily.

It can be clearly seen that DG gives the best performance. Although, it may be expected that the CFL optimal correction function would give best performance, as is shown in Fig.5.10, this is not the case. The grid used here is sufficient for the solution to be primarily formed of lower wavenumbers, where, as can be seen from the mid section of Fig.5.10b, DG has the least dissipation. An interesting comparison can be made between the performance of the optimal CFL correction functions for OSFR, ESFR, and GSFR. The OSFR case is clearly far more dissipative, from which it could be postulated that the lower order Sobolev terms present in ESFR and GSFR can lead to the cancelling out of unwanted dissipation.

5.5.3 Taylor-Green Vortex

Lastly for GLSFR and GJFR we will build on the theoretical and linear work carried out in earlier sections by again using the Taylor-Green vortex test case [113, 18, 36]. Restating the reasoning for using this case, it is a well known canonical case for the full incompressible Navier-Stokes equations and is highly important as it exhibits: inviscid, transitional, and turbulent flow regimes. Therefore, if improvements can be made via correction function selection on such a case this will translate well onto an engineering CFD problem.

The physics of this case are controlled by the setting of three no-dimensional parameters, the Reynolds, Prandtl, and Mach numbers. With Reynold and Prandtl numbers controlled through setting the dynamic viscosity and thermal conductivity and Mach number controlled through setting the stagnation density relative to a reference velocity. The typical condition we will use, unless otherwise stated is, $R_e = 1600$, $P_r = 0.71$ and $M_a = 0.081$. To give an understanding of the flow field of this case the iso-surfaces of

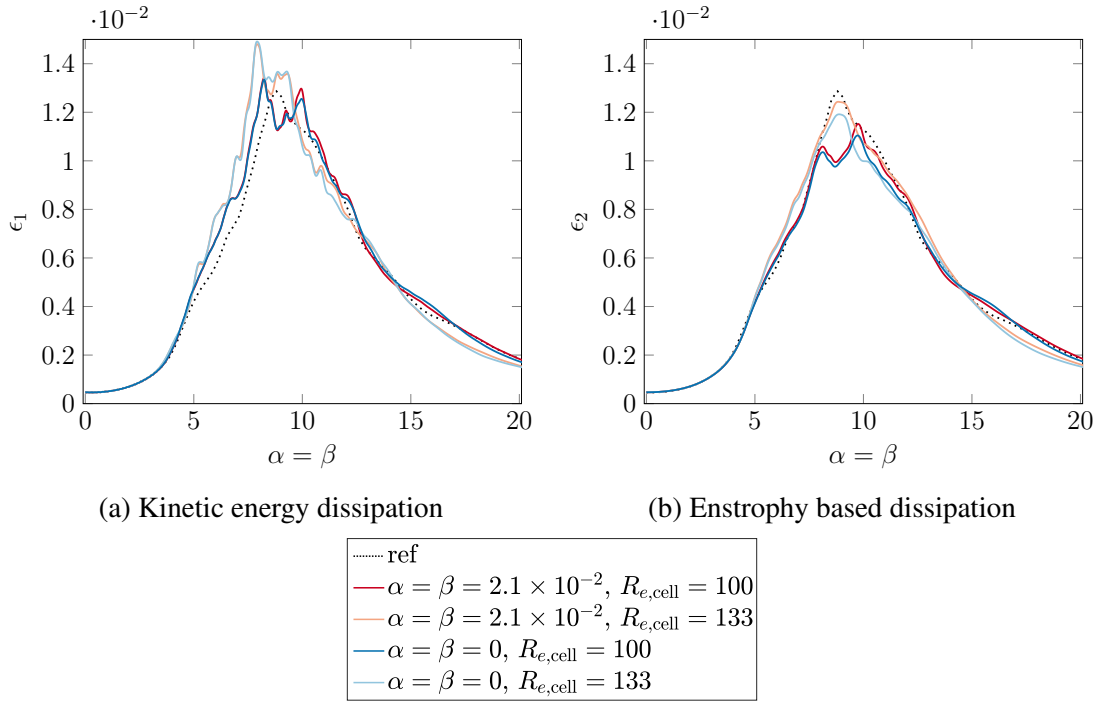


Fig. 5.20 Comparison of the Jacobi SD correction function ($\alpha = \beta = 2.1 \times 10^{-2}$) with the SD correction function recovered by OSFR for two under-resolved grids.

the q-criterion at $q = 0.5$ are shown in the right hand corner as a flip book. The time interval between frames is 0.1 normalised time units.

The aim of this case is to display the impact of changing the correction function by evaluating two metrics. The metrics to be evaluated were introduced earlier in chapter 3, and are kinetic energy dissipation and enstrophy based dissipation:

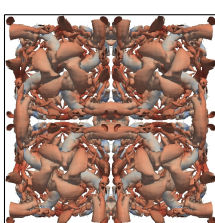
$$\epsilon_1 = -\frac{dE_k}{dt} = -\frac{d}{dt}\left(\frac{1}{2\rho_0 U_0^2 |\Omega|} \int_{\Omega} \rho \mathbf{V} \cdot \nabla \mathbf{V} d\mathbf{x}\right)$$

$$\epsilon_2 = \frac{\mu}{\rho_0^2 U_0^2 |\Omega|} \int_{\Omega} \rho (\boldsymbol{\omega} \cdot \boldsymbol{\omega}) d\mathbf{x}$$

We will also evaluate the time averaged error in these terms, but will introduce the exact definition on a case by case basis.

GJFR Results

We will begin by evaluating the performance of the SD correction function found in section 5.4.1. Again, we note here that SD via FR and native SD are only identical for linear homogeneous equation sets. In Figure 5.20, we compare two grids that are marginally underresolved. For the TGV small scales are generated at times approximately in the range $3 < t < 7$, with moderate levels of over-dissipation around these times are



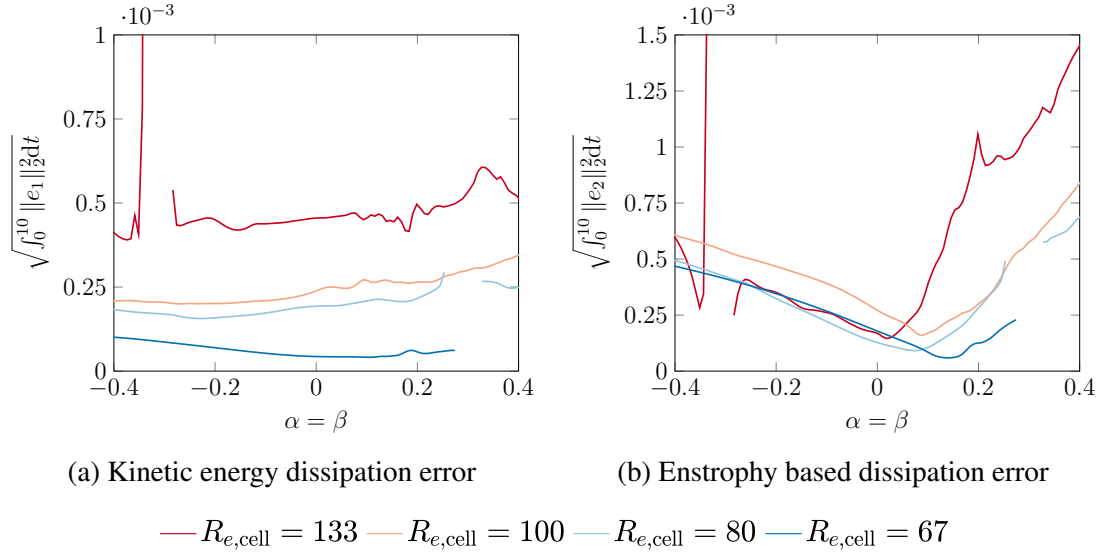


Fig. 5.21 Time averaged error in dissipation rates for the Taylor–Green Vortex, $p = 4$, with symmetric Jacobi SD correction functions.

indicative of dispersion due to under-resolution. Looking at ϵ_1 and comparing against the reference line we observe similar performance for both SD schemes. However, looking at ϵ_2 it is clear that on both grids the Jacobi SD correction function has an improved dissipation rated compared with the SD scheme recovered by OSFR. This suggests that the extra flexibility provided by our Jacobi correction functions may enable us to obtain more physical sub grid-scale dissipation.

In order to explore this further, we will investigate how the error in the dissipation varies with time over a range of Jacobi SD correction functions at different grid resolution levels. For this investigation we will us the l_2 error in ϵ_1 and ϵ_2 which we will define as $\|\epsilon_1\|_2 = \|\epsilon_1 - \epsilon_{1,\text{ref}}\|_2$ and similarly for ϵ_2 , where $\epsilon_{1,\text{ref}}$ is the dissipation rate of the reference DNS solution [36, 18]. The resulting errors for several grid resolutions over the range of correction functions $-1 < \alpha = \beta \leq 0.5$ are shown in Figure 5.21.

Before analysing the results further we will remark on the temporal integration method. RK44 [67] explicit temporal integration was used with a time step at $R_{e,\text{cell}} = 100$ of $\Delta t = 10^{-3}$. This explicit time step was then linearly scaled as the grids were refined or coarsened, such that the acoustic CFL number remains approximately constant. A time step of $\Delta t = 10^{-3}$ has previously been used for high resolution DNS simulations and is understood to be more than sufficient to resolve the temporal dynamics of the TGV [36]. As such we shall opt to discard any correction function which is found to be temporally unstable with this time step—for such functions are unlikely to be of practical utility. Finally, we note that in the case of $R_{e,\text{cell}} = 133$, some of the schemes with particularly large errors were found to blow up at some time $t > 10$.

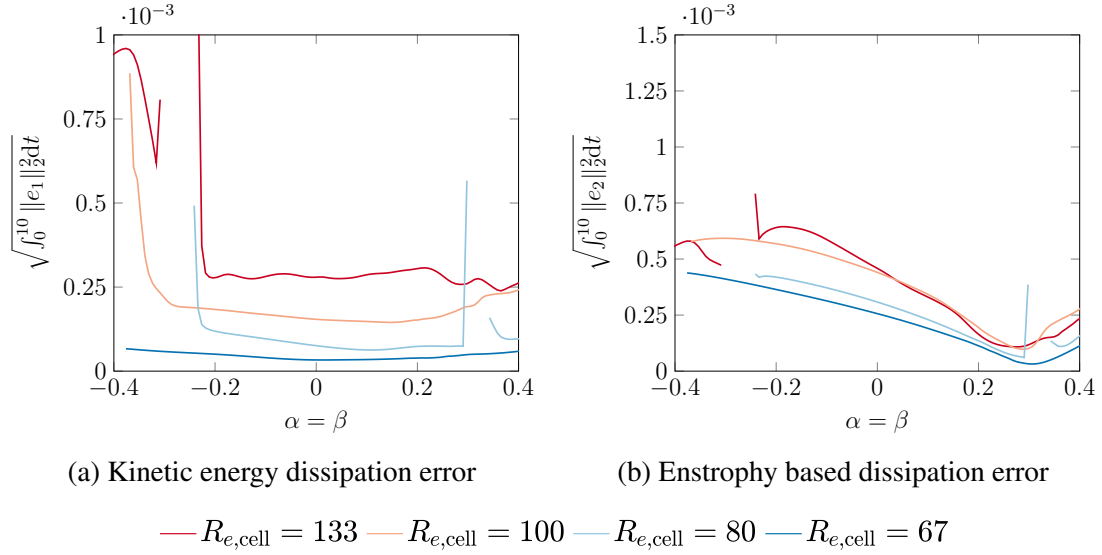
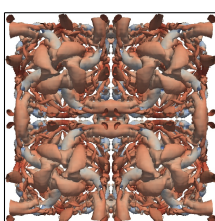


Fig. 5.22 Time averaged error in dissipation rates for the Taylor–Green Vortex, $p = 4$, with qDG correction functions for $\alpha = \beta$.

Looking at Figure 5.21a it is apparent that the integrated ϵ_1 error is less sensitive to variations in the correction function. As a result this may be useful in giving more general information about grid resolution and order and will be discussed later. However, far higher sensitivity in the integrated ϵ_2 error is observed. There is clearly an optimal region around $0 < \alpha = \beta < 0.2$, which is similar to the region that was found theoretically to give optimal convergence for linear advection.

Repeating this series of tests for qDG, we can see from comparison of Figure 5.22 & 5.21 that for a range of α values the error of qDG is less than that on SD schemes. In some cases, $\alpha \approx 0.25$, the error in the enstrophy is very low and moderately invariant with $R_{e,\text{cell}}$. Referencing section 5.4.1, there is no appreciable degradation in CFL limit at this point although it is near to the limit of theoretical stability. Thus the Jacobi SD schemes trade a small amount of accuracy for an appreciable gain in the CFL limit.

A key point to note about both the Jacobi SD and qDG tests is that in both cases correction functions were found that performed better when considering ϵ_2 than in ϵ_1 , this seems to indicate that the resolved turbulence and the implicit sub-grid model—which comes from the correction function—lead to physical vortical motions. However, the larger ϵ_1 means that there is still non-physical dissipation, but this must be in the larger bulk movement of the fluid, and hence not displayed in the gradients. As was mentioned previously, the variation ϵ_1 is smaller than ϵ_2 when considering changes in correction function. This indicates that ϵ_1 is controlled more by other factors such as the polynomial order, or as this investigation shows, $R_{e,\text{cell}}$.



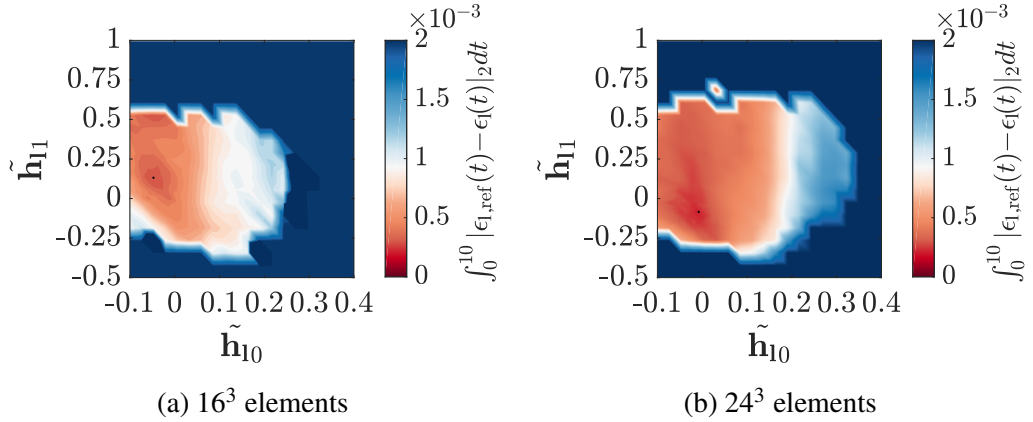


Fig. 5.23 Time integrated error in the kinetic energy dissipation of the Taylor-Green vortex, $R_e = 1600$ $P_r = 0.71$ $M_a = 0.08$, for FR, $p = 4$, with 800 GLSFR correction functions compared to DNS data for each grid resolution. RK44 temporal integration was used with a fixed time step of 1×10^{-3} . A point indicates the correction function tested with the lowest error.

GLSFR Results

We now move on to study the GLSFR correction function set applied to the TGV.

Figure 5.23 shows the approximate error for two different grid spacing as the correction function is varied with a constant time step of 1×10^{-3} . This time step was chosen as it should be sufficient to run with such a time step [84] and any reduction beyond this would symbolise that a correction function is not sufficiently temporally stable to be considered applicable for industrial problems. As was observed in Fig. 5.13b & 5.13c as the parameter \mathbf{h}_{l1} is increased the temporal stability is reduced and this trend is also seen in the TGV case. There is also large asymmetry between positive and negative values of $\hat{\mathbf{h}}_{l0}$ which was also seen in Fig. 5.16. However, for Fig. 5.16 the opposite behaviour is seen, but this was for CFL limit. The implication of a higher CFL limit is a more dissipative scheme, whereas for reduced error a less dissipative scheme is necessary. Hence, the location of the error optimal correction function lying in the left-hand half plane. A secondary point that may be made about GLSFR correction functions is that for both grid resolution correction functions were found in broadly the same range of \mathbf{H}_4 that gave lower error than Nodal DG via FR. Hence, these correction functions are not merely a mathematical exercise but can provide improved performance for real fluid dynamical simulations.

Lastly the kinetic energy dissipation of the optimal and DG correction function is compared for the two grid refinement levels in Fig. 5.24. In both cases the peak turbulent dissipation is better matched, but in both cases there is a region at $t \approx 7.5$ in which correction function tuning appear to make only modest or no improvement. In the case of

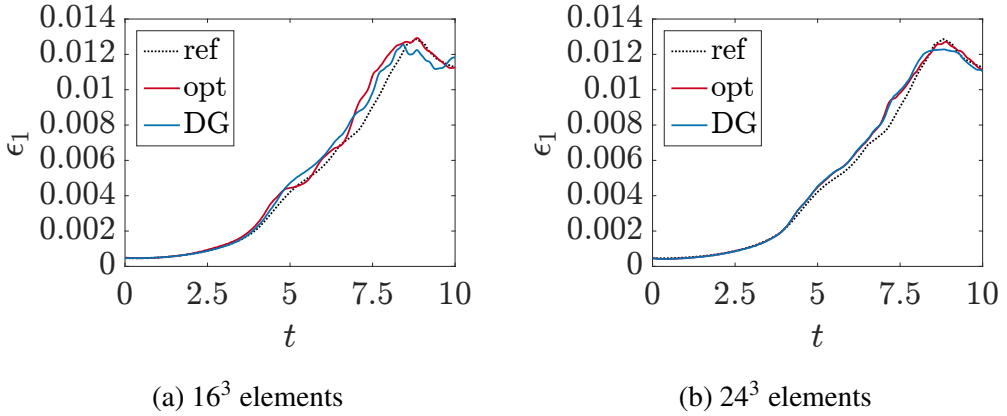


Fig. 5.24 Optimal GLSFR correction functions, $p = 4$, found in Fig.5.23 compared to Nodal DG via FR, with reference data taken from DeBonis [36]. RK44 temporal integration was used with a fixed time step of 1×10^{-3} .

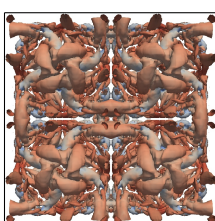
Fig. 5.24a, tuning the correction function has resulted in extra dissipation at this time. The importance of $t \approx 7.5$ is due to the rate of change of dissipation being at its highest and the flow can be said to be transitioning to turbulence with turbulent structures forming. The factor can be seen to have the greatest impact on improving the simulation of the physics at this time is increased grid resolution. For the mildly under-resolved case of 16^3 , extra dissipation seems to be important in producing extra shear to correctly form turbulence for the subsequent decay.

5.6 Conclusions

Several new energy stable families of correction functions have been found for FR. These were derived by a novel approach to generalising Sobolev energy stability. In some instances these sets were found to contain the previously defined OSFR [127] and ESFR [129] correction function sets. For a full picture of how these sets of correction functions intersect diagrammatically see Fig 5.25. Further work is needed to explore the full potential of the correction functions discovered, however some conclusions may be drawn from each of the sets defined.

5.6.1 GJFR

Theoretical convergence studies and von Neumann analysis were then used to show that these new schemes can be used to increase accuracy without impacting temporal stability relative to previous FR schemes. Moreover, the newly derived schemes also enable the definition of quasi-DG schemes which correspond to DG schemes with a different



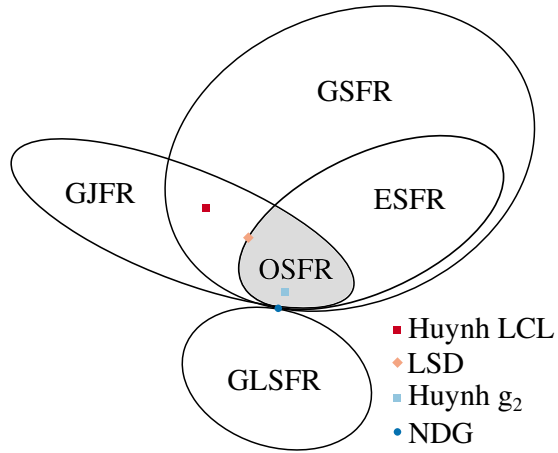


Fig. 5.25 Euler diagram to show the interconnection of the spaces of FR correction functions: Nodal DG (NDG) [55]; Original Stable FR (OSFR) [127]; Extended range Stable FR (ESFR) [129]; Generalised Sobolev stable FR (GSFR) [117]; Generalised Lebesgue Stable FR (GLSFR) [116] and, the Generalised Jacobi stable FR (GJFR) of the present work. Some specific examples of specific schemes are given, notably Huynh's Lumped Chebyshev-Lobatto (LCL) [55] scheme and the original Legendre spectral difference (LSD) scheme [69, 55, 62]

polynomial basis. The same convergence study showed that these have the potential to increase the order of accuracy of DG, and in the case of $p = 4$ with central interfaces, an increase in the rate of convergence of two orders was found. Using the Generalised Jacobi approach it is all possible to recover, at least for a linear flux function, a range of spectral difference schemes. Numerical experiments were then performed to validate some of the findings, which showed that the optimal correction function for the full Navier–Stokes equation lay in the same region predicted by theoretical linear investigations.

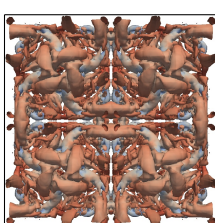
5.6.2 GSFR

Study of the linear advection equation, via a von Neumann analysis, was then used to show that for $p = 3$ a correction function could be found that led to an increase in the CFL number for RK44 temporal integration. It was also demonstrated that this correction function recovers numerically the expected OOA, with GSFR also enabling the recovery of functions from the lower order spaces. A one dimensional linear heterogeneous PDE was proposed to numerically investigate the performance of GSFR when applied to an equation that causes aliasing. The investigation showed that the region of high CFL limit for the case of $p = 3$ was within a stable area of low error. Finally, the solution of Euler's equations on the ICV test case was used to compare the relative performance when applied to fully non-linear PDEs. Of the correction functions tested all remained

stable with reasonable performance, however it was found that DG gave the minimal decay in the kinetic energy for this test.

5.6.3 GLSFR

Von Neumann analysis for both the linear advection and linear advection-diffusion was then presented for this new set of corrections and a region of temporally stable correction function was found to exist for both upwinded and centrally difference interfaces, when Runge-Kutta temporal integration is used. Through exploration of the dispersion and dissipation characteristics of some of the correction function, it was shown that GLSFR may be able to provide improved performance for implicit LES calculations. Lastly, a series of Taylor-Green vortex test are performed for two grid spacing and it was found that in both case a similar region of corrections gave good performance for minimising the error in the turbulent kinetic energy dissipation. In both cases correction functions were found that reduced the error when compared to DG. Therefore, it is concluded that GLSFR may be able improve the accuracy of FR when applied to real fluid-dynamical problems.

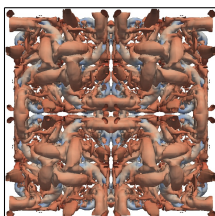


Chapter 6

Conclusions and Future Work

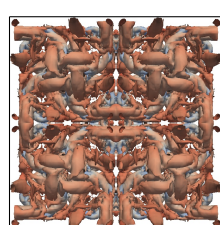
6.1 Conclusions

6.2 Future Work



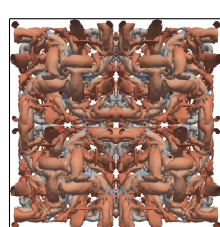
References

- [1] Y. ABE, T. HAGA, T. NOMOURA, AND K. FUJII, *On the Freestream Preservation of High-Order Conservative Flux-Reconstruction Schemes*, Journal of Computational Physics, 281 (2015), pp. 28–54.
- [2] ——, *Conservative High-Order Flux-Reconstruction Schemes on Moving and Deforming Grids*, Computers and Fluids, 139 (2016), pp. 2–16.
- [3] Y. ABE, I. MORINAKA, T. HAGA, T. NOMOURA, H. SHIBATA, AND K. MIYAJI, *Stable, Non-Dissipative, and Conservative Flux-Reconstruction Schemes in Split Forms*, Journal of Computational Physics, 353 (2018), pp. 193–227.
- [4] R. ABGRALL, *On Essentially Non-Oscillatory Schemes on Unstructured Meshes: Analysis and Implementation*, Journal of Computational Physics, 114 (1994), pp. 45–58.
- [5] S. ADJERID, K. D. DEVINE, J. E. FLAHERTY, AND L. KRIVODONOVA, *A Posteriori Error Estimation for Discontinuous Galerkin Solutions of Hyperbolic Problems*, Computer Methods in Applied Mechanics and Engineering, 191 (2002), pp. 1097–1112.
- [6] M. ALHAWWARY AND Z. J. WANG, *Fourier Analysis and Evaluation of DG, FD and Compact Difference Methods for Conservation Laws*, Journal of Computational Physics, 373 (2018), pp. 835–862.
- [7] G. M. AMDAHL, *Validity of the Single Processor Approach to Achieving Large Scale Computing Capabilities*, in AFIPS Spring Jopint Computer Conference, 1967, pp. 1–4.
- [8] K. ASTHANA AND A. JAMESON, *High-Order Flux Reconstruction Schemes with Minimal Dispersion and Dissipation*, Journal of Scientific Computing, 62 (2014), pp. 913–944.
- [9] K. ASTHANA, J. WATKINS, AND A. JAMESON, *On Consistency and Rate of Convergence of Flux Reconstruction For Time-Dependent Problems*, Journal of Computational Physics, 334 (2017), pp. 367–391.
- [10] D. H. BAILEY, *High-Precision Floating-Point Arithmetic in Scientific Computing*, Computing in Science and Engineering, 7 (2005), pp. 54–61.
- [11] W. N. BAILEY, *On The Product of Two Legendre Polynomials*, Mathematical Proceedings of the Cambridge Philosophical Society, 29 (1933), pp. 173–176.



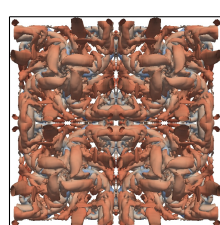
- [12] F. BASSI AND S. REBAY, *A High-Order Accurate Discontinuous Finite Element Method for the Numerical Solution of the Compressible Navier–Stokes Equations*, Journal of Computational Physics, 131 (1997), pp. 267–279.
- [13] ——, *An Implicit High-Order Discontinuous Galerkin Method for the Steady State Compressible Navier-Stokes Equations*, in Computational Fluid Dynamics '98, Athens,Greece, 1998, John Wilery & Sons Ltd., pp. 1226–1233.
- [14] F. BASSI, S. REBAY, G. MARIOTTI, S. PEDINOTTI, AND M. SAVINI, *A High Order Accurate Discontinuous Finite Element Method for Inviscid and Viscous Turbomachinery Flows*, in Turbomachinery - Fluid Dynamics and Thermodynamics, 2nd European Conference, Antwerpen, Mar 5-7, 1997, pp. 99–108.
- [15] H. BATEMEN, A. ERDELYI, W. MAGNUS, F. OBERHETTINGER, AND F. TRICOMI, *Higher Transcendental Functions, Volume 1*, McGraw-Hill Book Company, New York Toronto London, first ed., 1953.
- [16] F. BAYART AND E. MATHERON, *Dynamics of Linear Operators*, Cambridge University Press, New York, first ed., 2009.
- [17] R. BEALS AND R. WONG, *Special Functions and Orthogonal Polynomials*, Cambridge University Press, Cambridge, first ed., 2016.
- [18] M. E. BRACHET, S. A. ORSZAG, B. G. NICKEL, R. H. MORF, AND U. FRISCH, *Small-Scale Structure of the Taylor-Green Vortex*, Journal of Fluid Mechanics, 130 (1983), pp. 411–452.
- [19] A. BRANDT, *Multi-Level Adaptive Solutions to Boundary-Value Problems*, Mathematics of Computation, 31 (1977), pp. 333–390.
- [20] T. BRANDVIK AND G. PULLAN, *An Accelerated 3D Navier–Stokes Solver for Flows in Turbomachines*, Journal of Turbomachinery, 133 (2009), pp. 1–9.
- [21] S. C. BRENNER AND L. RIDGWAY-SCOTT, *The Mathematical Theory of Finite Element Methods*, Springer-Verlag, New York, third ed., 2008.
- [22] J. R. BULL AND A. JAMESON, *Simulation of the Compressible Taylor Green Vortex using High-Order Flux Reconstruction Schemes*, AIAA Journal, 53 (2014), pp. 1–17.
- [23] P. CASTONGUAY, *High-order Energy Stable Flux Reconstruction Schemes For Fluid Flow Simulations on Unstructured Grids*, PhD thesis, Stanford University, 2012.
- [24] P. CASTONGUAY, P. E. VINCENT, AND A. JAMESON, *Application of High-Order Energy Stable Flux Reconstruction Schemes to the Euler Equations*, 49th AIAA Aerospace Sciences Meeting including the New Horizons Forum and Aerospace Exposition, 686 (2011).
- [25] ——, *A New Class of High-Order Energy Stable Flux Reconstruction Schemes for Triangular Elements*, Journal of Scientific Computing, 51 (2012), pp. 224–256.
- [26] P. CASTONGUAY, D. M. WILLIAMS, P. E. VINCENT, AND A. JAMESON, *Energy Stable Flux Reconstruction Schemes for Advection-Diffusion Problems*, Computer Methods in Applied Mechanics and Engineering, 267 (2013), pp. 400–417.

- [27] J.-B. CHAPELIER, M. DE LA LLAVE PLATA, AND F. RENAC, *Inviscid and Viscous Simulations of the Taylor-Green Vortex Flow Using a Modal Discontinuous Galerkin Approach*, in 42nd AIAA Fluid Dynamics Conference and Exhibit, no. June, 2012, pp. 1–17.
- [28] F. K. CHOW AND P. MOIN, *A Further Study of Numerical Errors in Large-Eddy Simulations*, Journal of Computational Physics, 184 (2003), pp. 366–380.
- [29] B. COCKBURN, C. JOHNSON, C. W. SHU, AND E. TADMOR, *Advanced Numerical Approximation of Nonlinear Hyperbolic Equations*, Springer-Verlag, Berlin Heidelberg, first ed., aug 1997.
- [30] B. COCKBURN, G. E. KARNIADAKIS, AND C. W. SHU, *The Development of Discontinuous Galerkin Methods*, in Discontinuous Galerkin Methods (Newport, RI, 1999), vol. 11, Springer-Verlag, Berlin, 2000, ch. 1, pp. 3–50.
- [31] B. COCKBURN, M. LUSKIN, C. W. SHU, AND E. SULI, *Post-Processing of Galerkin Methods for Hyperbolic Problems*, in Discontinuous Galerkin Methods (Newport, RI, 1999), Newport, 1999, Springer-Verlag, pp. 291–300.
- [32] B. COCKBURN AND C. W. SHU, *The Local Discontinuous Galerkin Method for Time-Dependent Convection-Diffusion Systems*, SIAM, 35 (1998), pp. 2440–2463.
- [33] R. COURANT, K. FRIEDRICHS, AND H. LEWY, *On the Partial Differnce Equations of Mathematical Physics*, IBM Journal, 11 (1967), pp. 215–234.
- [34] J. CRABILL, F. D. WITHERDEN, AND A. JAMESON, *A Parallel Direct Cut Algorithm for High-Order Overset Methods with Application to a Spinning Golf Ball*, Journal of Computational Physics, 374 (2018), pp. 692–723.
- [35] S. DAVIS, *Simplified Second-order Godunov-type Methods*, SIAM Journal on Scientific and Statistical Computing, 9 (1988), pp. 445–473.
- [36] J. R. DEBONIS, *Solutions of the Taylor-Green Vortex Problem Using High-Resolution Explicit Finite Difference Methods*, 51st AIAA Aerospace Sciences Meeting including the New Horizons Forum and Aerospace Exposition, (2013).
- [37] E. H. DOHA, *On the Coefficients of Differentiated Expansions and Derivative of Jacobi Polynomials*, Journl of Physics A: Mathematical adn General, 35 (2002), pp. 3467–3478.
- [38] J. DOUGALL, *On The Product of Two Legendre Polynomials*, Glasgow Mathematical Journal, 1 (1952), pp. 121–125.
- [39] M. DUBINER, *Spectral methods on triangles and other domains*, Journal of Scientific Computing, 6 (1991), pp. 345–390.
- [40] M. DUMBSER, D. S. BALSARA, E. F. TORO, AND C. D. MUNZ, *A Unified Framework for the Construction of One-Step Finite Volume and Discontinuous Galerkin Schemes on Unstructured Meshes*, Journal of Computational Physics, 227 (2008), pp. 8209–8253.
- [41] J. GAO, *A Block Interface Flux Reconstruction Method for Numerical Simulation with High Order Finite Difference Scheme*, Journal of Computational Physics, 241 (2013), pp. 1–17.



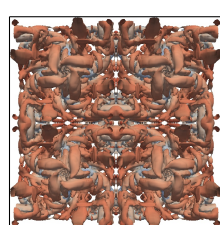
- [42] B. GARFINKEL, *Addition Theorem for a Derivative of a Legendre Polynomial*, The Astronomical Journal, 69 (1964), pp. 567–569.
- [43] W. GAUTSCHI, *Construction of Gauss-Christoffel quadrature formulas*, Mathematics of Computation, 22 (1968), pp. 251–270.
- [44] ——, *A survey of Gauss-Christoffel quadrature formulae*, "E.B. Christoffel - The influence of his work mathemat, (1981), pp. 72–147.
- [45] S. GHOSAL, *An Analysis of Numerical Errors in Large-Eddy Simulations of Turbulence*, Journal of Computational Physics, 125 (1996), pp. 187–206.
- [46] S. K. . GODUNOV, *A Difference Method for Numerical Calculation of Discontinuous Solutions of the Equations of Hydrodynamics*, Mat. Sb., 47(89) (1959), pp. 271–306.
- [47] F. H. HARLOW, *Fluid Dynamics in Group T-3 Los Alamos National Laboratory (with Introduction)*, Journal of Computational Physics, 195 (2004), pp. 413–433.
- [48] A. HARTEN, *High Resolution Schemes for Hyperbolic Conservation Laws*, Journal of Computational Physics, 49 (1983), pp. 357–393.
- [49] A. HARTEN, B. ENGQUIST, S. OSHER, AND S. R. CHAKRAVARTHY, *Uniformly High-Order Accurate Essentially Non-Oscillatory Schemes, III*, Journal of Computational Physics, 71 (1987), pp. 231–303.
- [50] J. S. HESTHAVEN AND R. M. KIRBY, *Filtering in Legendre spectral methods*, Mathematics of Computation, 77 (2008), pp. 1425–1452.
- [51] J. S. HESTHAVEN AND T. WARBURTON, *Nodal Discontinuous Galerkin Methods: Algorithms, Analysis, and Applications*, vol. 54 of Texts in Applied Mathematics, Springer New York, New York, NY, first ed., 2008.
- [52] J. T. HOLDEMAN, *Legendre Polynomial Expansions of Hypergeometric Functions with Applications*, Journal of Mathematical Physics, 11 (1970), pp. 114–117.
- [53] H. HOMANN, J. DREHER, AND R. GRAUER, *Impact of the Floating-Point Precision and Interpolation Scheme on the Results of DNS of Turbulence by Pseudo-Spectral Codes*, Computer Physics Communications, 177 (2007), pp. 560–565.
- [54] F. Q. HU, M. Y. HUSSAINI, AND P. RASETARINERA, *An analysis of the Discontinuous Galerkin method for wave propagation problems*, Journal of Computational Physics, 151 (1999), pp. 921–946.
- [55] H. T. HUYNH, *A Flux Reconstruction Approach to High-Order Schemes Including Discontinuous Galerkin Methods*, in 18th AIAA Computational Fluid Dynamics Conference, vol. 2007-4079, 2007, pp. 1–42.
- [56] ——, *A Flux Reconstruction Approach to High-Order Schemes Including Discontinuous Galerkin for Diffusion*, in 47th AIAA Aerospace Science Meeting, no. January in Fluid Dynamics and Co-located Conferences, American Institute of Aeronautics and Astronautics, jun 2009, pp. 1–34.

- [57] ——, *High-Order Methods Including Discontinuous Galerkin by Reconstructions on Triangular Meshes*, in 49th AIAA Aerospace Sciences Meeting, no. January, 2011, pp. 1–28.
- [58] E. ISAACSON AND H. B. KELLER, *Analysis of Numerical Methods*, John Wiley & Sons Ltd., New York, second ed., 1994.
- [59] M. E. H. ISMAIL, *Classical and Quantum Orthogonal Polynomials in One Variable*, Encyclopedia of Mathematics and its Applications, Cambridge University Press, first ed., 2005.
- [60] A. JAMESON, *Time Dependent Calculations Using Multigrid, with Applications to Unsteady Flows Past Airfoils and Wings*, 1991.
- [61] ——, *Formulation of Kinetic Energy Preserving Conservative Schemes for Gas Dynamics and Direct Numerical Simulation of One-Dimensional Viscous Compressible Flow in a Shock Tube Using Entropy and Kinetic Energy Preserving Schemes*, Journal of Scientific Computing, 34 (2008), pp. 188–208.
- [62] ——, *A Proof of the Stability of the Spectral Difference Method For All Orders of Accuracy*, Journal of Scientific Computing, 45 (2010), pp. 348–358.
- [63] ——, *Advances in Bringing High-order Methods to Practical Applications in Computational Fluid Dynamics*, AIAA Paper, (2011), pp. 1–27.
- [64] A. JAMESON, P. E. VINCENT, AND P. CASTONGUAY, *On The Non-Linear Stability of Flux Reconstruction Schemes*, Journal of Scientific Computing, 50 (2012), pp. 434–445.
- [65] G.-S. JIANG AND C.-W. SHU, *Efficient Implementation of Weighted ENO Schemes*, Journal of Computational Physics, 126 (1995), pp. 202–228.
- [66] G. E. KARNIADAKIS AND S. SHERWIN, *Spectral/hp Element Methods for Computational Fluid Dynamics*, Oxford University Press, Oxford, first ed., 2013.
- [67] C. A. KENNEDY, M. H. CARPENTER, AND R. M. LEWIS, *Low-Storage, Explicit Runge-Kutta Schemes for the Compressible Navier-Stokes Equations*, Applied Numerical Mathematics, 35 (2000), pp. 177–219.
- [68] J. W. KIM AND D. J. LEE, *Characteristic Interface Conditions for Multiblock High-Order Computation on Singular Structured Grid*, AIAA Journal, 41 (2003), pp. 2341–2348.
- [69] D. A. KOPRIVA, *A Conservative Staggered-grid Chebyshev Multidomain Method for Compressible Flows. II. A Semi-Structured Method*, Journal of Computational Physics, 128 (1996), pp. 475–488.
- [70] A. KRAVCHENKO AND P. MOIN, *On the Effect of Numerical Errors in Large Eddy Simulations of Turbulent Flows*, Journal of Computational Physics, 131 (1997), pp. 310–322.
- [71] R. KRESS, *Numerical Analysis*, vol. 181 of Graduate Texts in Mathematics, Springer New York, New York, NY, first ed., 1998.



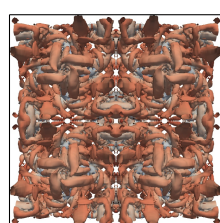
- [72] S. KUJSIN AND A. SHIRIKYAN, *Preliminaries*, in Mathematics of Two-Dimensional Turbulence, Cambridge University Press, Cambridge, first ed., 2012, ch. 1, pp. 1–35.
- [73] R. D. LAUNIUS AND D. R. JENKINS, *Coming Home: Reentry and Recovery from Space*, NASA, first ed., 2012.
- [74] P. D. LAX AND R. D. RICHTMYER, *Survey of the Stability of Linear Finite Difference Equations*, Communications on Pure and Applied Mathematics, IX (1956), pp. 267–293.
- [75] P. D. LAX AND B. WENDROFF, *Systems of Conservation Laws*, Communications in Pure and Applied Mathematics, XIII (1960), pp. 217–237.
- [76] ———, *Difference Schemes for Hyperbolic Equations with High Order of Accuracy*, Comm, XVII (1964), pp. 381–398.
- [77] S. K. LELE, *Compact Finite Difference Schemes With Spectral-Like Resolution*, Journal of Computational Physics, 103 (1992), pp. 16–42.
- [78] G. LEONI, *Part 1: Functions of One Variable*, in A First Course in Sobolev Spaces, American Mathematical Society, Providence, RI, first ed., 2009, ch. 1-7, pp. 3–230.
- [79] M. S. LIOU, *A Sequel to AUSM: AUSM+*, Journal of Computational Physics, 129 (1996), pp. 364–382.
- [80] M. S. LIOU AND C. J. STEFFEN, *A New Flux Splitting Scheme*, Journal of Computational Physics, 107 (1993), pp. 23–39.
- [81] X.-D. LIU, S. OSHER, AND T. CHAN, *Weighted Essentially Non-Oscillatory Schemes*, Journal of Computational Physics, 115 (1994), pp. 200–212.
- [82] Y. LIU, M. VINOKUR, AND Z. J. WANG, *Discontinuous Spectral Difference Method for Conservation Laws on Unstructured Grids*, Computational Fluid Dynamics 2004, Proceedings of the Third International Conference on Computational Fluid Dynamics (ICCFD3), Toronto, 12–16 July 2004, i (2006), pp. 449–454.
- [83] D. P. LOCKARD, K. S. BRENTNER, AND H. L. ATKINS, *High-Accuracy Algorithms for Computational Aeroacoustics*, AIAA Journal, 33 (1995), pp. 247–251.
- [84] A. MASTELLONE, F. CAPUANO, S. BENEDETTO, AND L. CUTRONE, *Problem C3 . 5 Direct Numerical Simulation of the Taylor-Green Vortex at $Re = 1600$* , tech. rep., 2015.
- [85] A. MAZAHERI AND H. NISHIKAWA, *Very Efficient High-Order Hyperbolic Schemes for Time-Dependent Advection-Diffusion Problems: Third-, Fourth-, and Sixth-Order*, Computers and Fluids, 102 (2014), pp. 131–147.
- [86] G. MENGALDO, R. C. MOURA, B. GIRALDA, J. PEIRÓ, AND S. J. SHERWIN, *Spatial Eigensolution Analysis of Discontinuous Galerkin Schemes with Practical Insights for Under-Resolved Computations and Implicit LES*, Computers and Fluids, 169 (2018), pp. 349–364.
- [87] J. MILLER, *Formulas for Integrals of Products of Associated Legendre or Laguerre Functions*, Mathematics of Computation, 17 (1963), pp. 84–84.

- [88] H. NISHIKAWA, *A First-Order System Approach for Diffusion Equation. I: Second-Order Residual-Distribution Schemes*, Journal of Computational Physics, 227 (2007), pp. 315–352.
- [89] H. NISHIKAWA AND P. L. ROE, *Third-Order Active-Flux Scheme for Advection Diffusion: Hyperbolic Diffusion, Boundary Condition, and Newton Solver*, Computers and Fluids, 125 (2016), pp. 71–81.
- [90] NVIDIA, *Nvidai Tesla v100 Gpu Architecture; The Wolrd's Most Advanced Data Center Gpu*, Tech. Rep. August, 2017.
- [91] S. A. ORSZAG AND M. ISRAELI, *Numerical Simulation of Viscous Incompressible Flows*, Annual Review of Fluid Mechanics, 6 (1974), pp. 281–318.
- [92] K. OSSWALD, A. SIEGMUND, P. BIRKEN, V. HANNEMANN, AND A. MEISTER, *$l2$ Roe: A Low Dissipation Version of Roe's Approximate Riemann Solver for Low Mach Numbers*, International Journal for Numerical Methods in Fluids, 81 (2016), pp. 71–86.
- [93] N. PENG AND Y. YANG, *Effects of the Mach Number on the Evolution of Vortex-Surface Fields in Compressible Taylor-Green Flows*, Physical Review Fluids, 3 (2018), pp. 1–21.
- [94] T. PRINGUEY AND R. S. CANT, *High Order Schemes on Three-Dimensional General Polyhedral Meshes - Application to The Level Set Method*, Communications in Computational Physics, 12 (2012), pp. 1–41.
- [95] J. J. QUIRK, *A Contribution to the Great Riemann Solver Debate*, International Journal for Numerical Methods in Fluids, 18 (1992), pp. 555–574.
- [96] P. A. RAVIART AND THOMAS, *A Mixed Finite Element Method for 2nd Order Elliptic Problems*, in Mathematical Aspects of Finite Element Methods, Rome, 1977, Springer Berlin Heidelberg, pp. 292–315.
- [97] W. H. REED AND T. R. HILL, *Triangular Mesh Methods for the Neutron Transport Equation*, Tech. Rep. LA-UR-73-479, 1973.
- [98] K. V. ROBERTS AND N. O. WEISS, *Convective Difference Schemes*, Mathematics of Computation, 20 (1966), pp. 272–299.
- [99] M. RODRIGUES, *Sur l'Attraction des Sphéroïdes*, Correspondence Sur l'École Impériale Polytechnique, 3 (1816), pp. 361–385.
- [100] P. L. ROE, *Approximate Riemann Solvers , Parameter Vectors, and Difference Schemes*, Journal of Computational Physics, 43 (1981), pp. 357–372.
- [101] J. ROMERO, K. ASTHANA, AND A. JAMESON, *A Simplified Formulation of the Flux Reconstruction Method*, Journal of Scientific Computing, 67 (2016), pp. 351–374.
- [102] J. ROMERO, F. D. WITHERDEN, AND A. JAMESON, *A Direct Flux Reconstruction Scheme for Advection–Diffusion Problems on Triangular Grids*, Journal of Scientific Computing, (2017).



- [103] V. RUSANOV, *The Calculation of the Interaction of Non-Stationary Shock Waves with Barriers*, Zh. Vychisl. Mat. Mat. Fiz., 1 (1961), pp. 267–279.
- [104] A. D. SCILLITOE, P. G. TUCKER, AND P. ADAMI, *Numerical Investigation of Three-Dimensional Separation in an Axial Flow Compressor: The Influence of Free-Stream Turbulence Intensity and Endwall Boundary Layer State*, in Volume 2D: Turbomachinery, Seoul, South Korea, jun 2016, ASME, p. V02DT44A025.
- [105] A. SHESHADRI, *An Analysis of Stability of the Flux Reconstruction Formulation With Applications to Shock Capturing*, phd thesis, Stanford University, 2016.
- [106] A. SHESHADRI AND A. JAMESON, *On the Stability of the Flux Reconstruction Schemes on Quadrilateral Elements for the Linear Advection Equation*, Journal of Scientific Computing, 67 (2016), pp. 769–790.
- [107] C.-W. SHU, *High Order Weighted Essentially Nonoscillatory Schemes for Convection Dominated Problems*, SIAM Review, 51 (2009), pp. 82–126.
- [108] C. W. SHU, W. S. DON, D. GOTTLIEB, O. SCHILLING, AND L. JAMESON, *Numerical Convergence Study of Nearly Incompressible, Inviscid Taylor-Green Vortex Flow*, Journal of Scientific Computing, 24 (2005), pp. 569–595.
- [109] J. SLOTNICK, A. KHODADOUST, J. ALONSO, D. DARMOFAL, W. GROPP, E. LURIE, AND D. MAVRIPLIS, *CFD Vision 2030 Study: A Path to Revolutionary Computational Aerosciences*, Tech. Rep. March, 2014.
- [110] A. SODANI, R. GRAMUNT, J. CORBAL, H. KIM, K. VINOD, S. CHINTHAMANI, S. HUSTELL, R. AGARWAL, Y. LIU, AND INTEL, *Knights Landing: Second-Generation Intel Xeon Phi Product*, IEEE Micro, 36 (2016), pp. 34–46.
- [111] J. L. STEGER AND R. F. WARMING, *Flux Vector Splitting of the Inviscid Gasdynamic Equations with Application to Finite-Difference*, Journal of Computational Physics, 40 (1981), pp. 263–293.
- [112] C. K. W. TAM AND J. C. WEBB, *Dispersion-Relation-Preserving Finite Difference Schemes for Computational Acoustics*, Journal of Computational Physics, 107 (1993), pp. 262–281.
- [113] G. I. TAYLOR AND A. E. GREEN, *Mechanism of the Production of Small Eddies from Large Ones*, Proceedings of the Royal Society A: Mathematical, Physical and Engineering Sciences, 158 (1937), pp. 499–521.
- [114] E. F. TORO, *Riemann Solvers and Numerical Methods for Fluid Dynamics - A Practical Introduction*, Springer-Verlag Berlin Heidelberg, Dordrecht Berlin Heidelberg London New York, third ed., 2009.
- [115] L. N. TREFETHEN, *Finite Difference and Spectral Methods for Ordinary and Partial Differential Equations*, Ithaca, New York, first ed., 1994.
- [116] W. TROJAK, *Generalised Lebesgue Stable Flux Reconstruction*, Arxiv, 1805 (2018), pp. 1–15.
- [117] ———, *Generalised Sobolev Stable Flux Reconstruction*, Arxiv, 1804 (2018), pp. 1–19.

- [118] W. TROJAK, R. WATSON, AND P. G. TUCKER, *High Order Flux Reconstruction on Stretched and Warped Meshes*, in AIAA SciTech, 55th AIAA Aerospace Sciences Meeting, Grapevine Texas, 2017, pp. 1–12.
- [119] ——, *Temporal Stabilisation of Flux Reconstruction on Linear Problems*, in 2018 Fluid Dynamics Conference, AIAA AVIATION Forum, Atlanta, jun 2018, American Institute of Aeronautics and Astronautics.
- [120] P. G. TUCKER, *Advanced Computational Fluid and Aerodynamics*, Cambridge Aerospace Series, Cambridge University Press, New York, first ed., 2016.
- [121] P. G. TUCKER, C. L. RUMSEY, P. R. SPALART, R. E. BARTELS, AND R. T. BIEDRON, *Computations of Wall Distances Based on Differential Equations*, AIAA Journal, 43 (2005), pp. 539–549.
- [122] B. VAN LEER, *Towards the Ultimate Conservative Difference Scheme II. Monotonicity and Conservation Combined in a second-Order Scheme*, Journal of Computational Physics, 14 (1974), pp. 361–370.
- [123] ——, *Towards the Ultimate Conservative Difference Scheme III. Upstream-Centered Finite-Difference Schemes for Ideal Compressible Flow*, Journal of Computational Physics, 23 (1977), pp. 263–275.
- [124] B. C. VERMEIRE, S. NADARAJAH, AND P. G. TUCKER, *Implicit Large Eddy Simulation Using the High-Order Correction Procedure via Reconstruction Scheme*, International Journal for Numerical Methods in Fluids, 82 (2016), pp. 231–260.
- [125] B. C. VERMEIRE AND P. E. VINCENT, *On the Properties of Energy Stable Flux Reconstruction Schemes for Implicit Large Eddy Simulation*, Journal of Computational Physics, 327 (2016), pp. 368–388.
- [126] ——, *On the Behaviour of Fully-Discrete Flux Reconstruction Schemes*, Journal of Computational Physics, 315 (2017), pp. 1053–1079.
- [127] P. E. VINCENT, P. CASTONGUAY, AND A. JAMESON, *A New Class of High-Order Energy Stable Flux Reconstruction Schemes*, Journal of Scientific Computing, 47 (2010), pp. 50–72.
- [128] ——, *Insights From von Neumann Analysis of High-Order Flux Reconstruction Schemes*, Journal of Computational Physics, 230 (2011), pp. 8134–8154.
- [129] P. E. VINCENT, A. M. FARRINGTON, F. D. WITHERDEN, AND A. JAMESON, *An Extended Range of Stable-Symmetric-Conservative Flux Reconstruction Correction Functions*, Computer Methods in Applied Mechanics and Engineering, 296 (2015), pp. 248–272.
- [130] P. E. VINCENT, F. D. WITHERDEN, B. C. VERMEIRE, J. S. PARK, AND A. IYER, *Towards Green Aviation with Python at Petascale*, in International Conference for High Performance Computing, Networking, Storage and Analysis, SC, no. November, 2017, pp. 1–11.
- [131] M. A. WAHAB, *A Brief History of the ANSIS Package*, in Mechanics of Adhesives in Composite and Metal Joints: Finite Element Analysis with ANSYS, DEStech Publications, Lancaster, Pa, first ed., 2014, ch. 3, pp. 59–60.



- [132] Z. J. WANG, *Spectral (Finite) Volume Method for Conservation Laws on Unstructured Grids. Basic Formulation: Basic Formulation*, Journal of Computational Physics, 178 (2002), pp. 210–251.
- [133] J. WATKINS, K. ASTHANA, AND A. JAMESON, *A Numerical Analysis of the Nodal Discontinuous Galerkin Scheme Via Flux Reconstruction for the Advection-Diffusion Equation*, Computers and Fluids, 139 (2016), pp. 233–247.
- [134] R. WATSON AND P. G. TUCKER, *Optimising Flux Reconstruction Schemes for Large Eddy Simulation*, in AMMCS-CAIMS, 2015, pp. 1–7.
- [135] A. P. S. WHEELER, R. D. SANDBERG, N. D. SANDHAM, R. PICHLER, AND G. LASKOWSKI, *Direct Numerical Simulations of a High-Pressure Turbine Vane*, Journal of Turbomachinery, 138 (2016), pp. 1–9.
- [136] D. M. WILLIAMS, P. CASTONGUAY, P. E. VINCENT, AND A. JAMESON, *An Extension of Energy Stable Flux Reconstruction to Unsteady, Non-linear, Viscous Problems on Mixed Grids*, Fluid Dynamics, (2011), pp. 1–37.
- [137] D. M. WILLIAMS AND A. JAMESON, *Energy Stable Flux Reconstruction Schemes for Advection-Diffusion Problems on Tetrahedra*, Journal of Scientific Computing, 59 (2014), pp. 721–759.
- [138] F. D. WITHERDEN, A. M. FARRINGTON, AND P. E. VINCENT, *PyFR: An Open Source Framework for Solving Advection-Diffusion Type Problems on Streaming Architectures Using the Flux Reconstruction Approach*, Computer Physics Communications, 185 (2014), pp. 3028–3040.
- [139] F. D. WITHERDEN, J. S. PARK, AND P. E. VINCENT, *An Analysis of Solution Point Coordinates for Flux Reconstruction Schemes on Tetrahedral Elements*, Journal of Scientific Computing, 69 (2016), pp. 1–16.
- [140] V. V. ZHIKOV, *Weighted Sobolev Spaces*, Sbornik: Mathematics, 189 (1998), pp. 1139–1170.

Appendix A

Introductory Theory of Orthogonal Polynomials

In this appendix we will detail some of the theory of orthogonal polynomials. This is by no means exhaustive and some of the results shown in the chapter are also presented throughout the main body of the work, but collected here for the readers convenience. If a more detailed understanding of the theory of orthogonal polynomials is required then the following references are recommended [11, 15, 17, 37, 38, 42–44, 52, 59, 87].

We will begin by introducing the concept of orthogonality when applied to a function, which will lead the way for a defining orthogonal polynomials. If we have a domain such that $\Omega \subset \mathbb{R}$ and $x \in \Omega$. Then, two functions $f(x) : x \rightarrow \mathbb{R}$ and $g(x) : x \rightarrow \mathbb{R}$ are said to be orthogonal iff:

$$\int_{\Omega} f(x)g(x)dx = 0 \quad (\text{A.1})$$

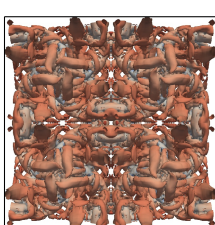
Orthogonality can then be further generalised my defining it with respect to a measure. This measure (or weight function), w is a positive function with infinite support over Ω . Furthermore, moments of the measure must exist:

$$\int_{\Omega} x^n dw(x) \in \mathbb{R} \quad (\text{A.2})$$

for $n \in \mathbb{N}$. With this established, the definition of orthogonality can then be extended to:

$$\int_{\Omega} f(x)g(x)dw(x) = 0 \quad (\text{A.3})$$

The importance of this definition is that we can then establish a set of polynomials, P , where $p_n \in P$ is a polynomial of degree n . By this we mean that the highest order monomial with a non zero coefficient is x^n . To form an orthogonal set we then require



that, again for some weight function, w , that:

$$\int_{\Omega} p_n p_m dw(x) = 0, \quad \forall n \neq m | n, m \in \mathbb{N} \quad (\text{A.4})$$

where $p_n, p_m \in P$. If we state that the polynomials are monic, i.e the coefficient of the largest non-zero monomial is one, this simplifies without loss of generality the analysis. It should then be clear that we can declare the recurrence relation:

$$xp_n = p_{n+1} + \sum_{i=0}^n c_i p_i \quad (\text{A.5})$$

If we then invoke that the polynomial series, P , is orthogonal then we are left with only three terms:

$$xp_n = p_{n+1} + a_n p_n + b_n p_{n-1}, \quad n \leq 0 \quad (\text{A.6})$$

where $p_{-1} = 0$ and $p_0 = 1$. For a full proof see Theorem 2.2 in [59]. An important contribution of Christoffel [44] was the definition of forms for a_n and b_n :

$$a_n = \frac{\langle xp_n | p_n \rangle}{\langle p_n | p_n \rangle} \quad (\text{A.7})$$

$$b_n = \frac{\langle p_n | p_n \rangle}{\langle p_{n-1} | p_{n-1} \rangle} \quad (\text{A.8})$$

where the inner-product is defined as:

$$\langle f | g \rangle = \int_{\Omega} f(x) g(x) dw(x) \quad (\text{A.9})$$

The final result that can be useful, before we present some specific instances, is Rodrigues' formula [99]. If the weight function is such that:

$$\frac{w'}{w} = \frac{A(x)}{B(x)} \quad (\text{A.10})$$

where $A(x)$ is a function with degree at most equal to one and $B(x)$ is a function of degree at most equal to two, then:

$$p_n(x) = \frac{c_n}{w(x)} \frac{d^n}{dx^n} [B(x)^n w(x)] \quad (\text{A.11})$$

where c_n is some constant. Rodrigues' formula represents an important link between orthogonal polynomials, the derivative operator and differential equations.

We will now present some useful results for some specific polynomial families.

A.1 Legendre Polynomials

Legendre polynomials, ψ_n , are a canonical set of orthogonal polynomials as they are defined with the weight function $w(x) = 1$ with $\Omega = [-1, 1]$.

$$\int_{-1}^1 \psi_n(x) \psi_m(x) dx = \frac{2}{2n+1} \delta_{n,m} \quad (\text{A.12})$$

The terms of Rodrigues' formula are then found to be:

$$c_n = \frac{1}{2^n n!} \quad (\text{A.13})$$

$$B(x) = (x^2 - 1) \quad (\text{A.14})$$

and the three recurrence relationship is then:

$$(2n+1)x\psi_n = (n+1)\psi_{n+1} + n\psi_{n-1}. \quad (\text{A.15})$$

Combining these results, the derivative of Legendre polynomials may then be found to be:

$$\frac{d\psi_n}{dx} = (2n-1)\psi_{n-1} + (2n-3)\psi_{n-3} + (2n-5)\psi_{n-5} + \dots \quad (\text{A.16})$$

which can straightforwardly be extended to the end points as:

$$\frac{d^p \psi_n(-1)}{dx^p} = \frac{(-1)^{n-p}(n+p)!}{2^p p!(n-p)!} \quad (\text{A.17})$$

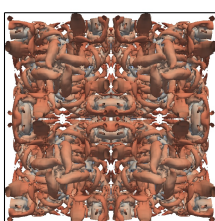
$$\frac{d^p \psi_n(1)}{dx^p} = \frac{(1)^{n-p}(n+p)!}{2^p p!(n-p)!} \quad (\text{A.18})$$

An important result for this work is that of Miller [87] for the integration of Associated Legendre polynomials. First we must introduce the set of functions called Associated Legendre polynomials. These are functions that satisfy:

$$\psi_n^{(m)} = (-1)^m (1-x^2)^{m/2} \frac{d^m \psi_n}{dx^m} \quad (\text{A.19})$$

Millers results was then:

$$\int_{-1}^1 \psi_{n_1}^{(m_1)} \psi_{n_2}^{(m_2)} dx = 2\delta(\text{even}, N) \sum_{q=0}^{(M/2)} \sum_{i=0}^{I(n_1, m_1)} \sum_{j=0}^{I(n_2, m_2)} (-1)^q \binom{M/2}{q} \frac{c_i(n_1, m_1) c_j(n_2, m_2)}{N - M - 2(i + j - q) + 1} \quad (\text{A.20})$$



where $M = \sum_i m_i$, $N = \sum_i n_i$, and c is defined as:

$$c_i(n, m) = \frac{(-1)^i [2(n-i)]!}{2^n (n-m-2i)! (n-i)! i!} \quad (\text{A.21})$$

Here the meaning of $\delta(\text{even}, N)$ is:

$$\delta(\text{even}, N) = \begin{cases} 1, & \text{if } N = \text{even} \\ 0, & \text{if } N = \text{odd} \end{cases} \quad (\text{A.22})$$

Hence by using Eq. (A.19) and recognising that the first summation over q in Eq. (A.20) is due to the $(1-x^2)^{m/2}$ term, we may then write:

$$\int_{-1}^1 \frac{d^{m_1} \psi_{n_1}}{dx^{m_1}} \frac{d^{m_2} \psi_{n_2}}{dx^{m_2}} dx = 2\delta(\text{even}, N) \sum_{i=0}^{\lfloor \frac{n_1-m_1}{2} \rfloor} \sum_{j=0}^{\lfloor \frac{n_2-m_2}{2} \rfloor} \frac{c_i(n_1, m_1) c_j(n_2, m_2)}{N - M - 2(i+j+1)} \quad (\text{A.23})$$

This an incredible powerful result and will come in useful in the generalised analysis of chapter 5.

The final point that should be raised before moving on is the use of Legendre polynomials in polynomial fitting. If we wish to fit a polynomial of order p to the function, f , of order q for $q > p$, while minimising the error, then Legendre polynomial are extremely useful. If we consider the case set out and the error of interest is the L_2 error then we have the problem of finding f_a such that:

$$f_a | \min \sqrt{\int_{-1}^1 (f - f_a)^2 dx} \quad (\text{A.24})$$

If we then say that both f and its approximation f_a are expressed as polynomial series:

$$f = \sum_{i=0}^q \tilde{f}_i L_i \quad \text{and} \quad f_a = \sum_{i=0}^p \tilde{f}_{a,i} L_i \quad (\text{A.25})$$

the integral then becomes:

$$\sqrt{\int_{-1}^1 \left(\sum_{i=0}^q \tilde{f}_i L_i - \sum_{i=0}^p \tilde{f}_{a,i} L_i \right)^2 dx} \quad (\text{A.26})$$

clearly then from the Legendre polynomial orthogonality condition, the minimum is when $\tilde{f}_{a,i} = \tilde{f}_i$ for $i \leq p$. Hence, the Legendre polynomial approximation is optimal with respect to minimum least squares.

A.2 Jacobi Polynomials

Jacobi polynomials are another more general set of orthogonal polynomial sets for $\Omega = [-1, 1]$. Each set of orthogonal polynomials is uniquely defined by two parameters α and β , where $\alpha, \beta \in \{x | x \in \mathbb{R}, x < -1\}$. Jacobi polynomials have proved to be an interesting case of orthogonal polynomial, shown to contain Legendre, Chebyshev and Gegenbauer polynomials. The reason for this is clear when the orthogonality condition is considered:

$$\int_{-1}^1 J_n^{(\alpha, \beta)}(x) J_m^{(\alpha, \beta)}(x) (1-x)^\alpha (1+x)^\beta dx = \frac{2^{\alpha+\beta+1}}{2n+\alpha+\beta+1} \frac{\Gamma(n+\alpha+1)\Gamma(n+\beta+1)}{\Gamma(n+\alpha+\beta+1)n!} \delta_{n,m} \quad (\text{A.27})$$

The terms of Rodrigues' formula are found to be:

$$c_n = \frac{(-1)^n}{2^n n!} \quad (\text{A.28})$$

$$B(x) = (1-x^2) \quad (\text{A.29})$$

and three term recurrence relationship is:

$$(2n+\alpha+\beta+1)(2n+\alpha+\beta+2)(2n+\alpha+\beta)x J_n^{(\alpha, \beta)} = (2n+2)(n+\alpha+\beta+1)(n+\alpha+\beta) J_{n+1}^{(\alpha, \beta)} + \\ (2n+\alpha+\beta+1)(\beta^2 - \alpha^2) J_n^{(\alpha, \beta)} + \\ 2(n+\alpha)(n+\beta)(2n+\alpha+\beta+2) J_{n-1}^{(\alpha, \beta)} \quad (\text{A.30})$$

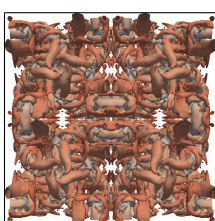
The derivative as a series of lower order Jacobi polynomials was then found by Doha [37] to be:

$$\frac{d^m J_n^{(\alpha, \beta)}}{dx^m}(x) = 2^{-m} (n+\alpha+\beta+1)_m \sum_{i=0}^{n-m} D_{n-m,i}(\alpha+m, \beta+m; \alpha, \beta) J_i^{(\alpha, \beta)}(x) \quad (\text{A.31})$$

where

$$D_{j,i}(\gamma, \delta; \alpha, \beta) = \frac{(j+\gamma+\delta+1)_i (i+\gamma+1)_{j-i} \Gamma(i+\alpha+\beta+1)}{(j-i)! \Gamma(2i+\alpha+\beta+1)} \times \\ {}_3F_2 \left(\begin{matrix} i-j, & j+i+\gamma+\delta+1, & i+\alpha+1 \\ i+\gamma+1, & 2i+\alpha+\beta+2 \end{matrix}; 1 \right) \quad (\text{A.32})$$

We define here that that $(x)_i$ is the rising Pochhammer function and ${}_3F_2(\dots; z)$ is the 3-2 generalised hypergeometric function [11, 15].



A final result that will prove to be very useful is that of Ismail [59] for the changing of the Jacobi polynomial basis:

$$J_n^{(\alpha, \beta)} = \sum_{i=0}^n D_{n,i}(\alpha, \beta; \gamma, \delta) J_i^{(\gamma, \delta)} \quad (\text{A.33})$$

where D is defined in Eq.(A.32).

Appendix B

Extended Range of Energy Stable Flux Reconstruction Correction Functions

After the initial definition of OSFR by Vincent et al. [127] an extension to FR was made that drew on techniques from FE and Spectral Element methods. This extension was presented by Vincent et al. [129] to give what was called Extended Range Stable FR (ESFR). This set of correction functions was far wider than those of OSFR, with more control variables. To introduce this set of corrections functions we will take the gradient of the left correction function to be:

$$\frac{dh_L}{d\xi} = g_L(\xi) = \sum_{i=0}^p \tilde{\mathbf{g}}_{L,i} \psi_i(\xi) \quad (\text{B.1})$$

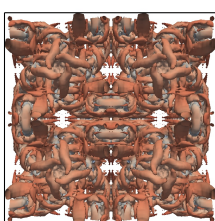
with the right correction similarly defined, and the notation of \bullet generally used for something either in or cast into a Legendrian basis. It followed that the extended range of correction function was defined by the equations:

$$\tilde{\mathbf{g}}_L = -(\tilde{\mathbf{M}} + \tilde{\mathbf{K}})^{-1} \tilde{\mathbf{I}} \quad (\text{B.2})$$

$$\tilde{\mathbf{g}}_R = (\tilde{\mathbf{M}} + \tilde{\mathbf{K}})^{-1} \tilde{\mathbf{r}} \quad (\text{B.3})$$

where $\tilde{\mathbf{I}} = [\psi_0(-1), \dots, \psi_p(-1)]^T$, $\tilde{\mathbf{r}} = [\psi_0(1), \dots, \psi_p(1)]^T$ and

$$\tilde{\mathbf{M}}_{i,j} = \int_{-1}^1 \psi_i \psi_j d\xi = \frac{2}{2j+1} \delta_{i,j}, \quad i, j \in \{0, \dots, p\} \quad (\text{B.4})$$



Here, $\tilde{\mathbf{K}}$ is a matrix dependent on the free variables $\{\kappa_0, \dots, \kappa_n\}$ where $n = \lfloor p/2 \rfloor + 1$, with some constraints imposed upon $\tilde{\mathbf{K}}$. First, it is necessary to define the following matrices:

$$\mathbf{D}_{i,j} = \frac{dl_j(\xi_i)}{d\xi} \quad (\text{B.5})$$

$$\mathbf{V}_{i,j} = \psi_j(\xi_i) \quad (\text{B.6})$$

$$\tilde{\mathbf{D}} = \mathbf{V}^{-1} \mathbf{D} \mathbf{V} \quad (\text{B.7})$$

Hence, $\tilde{\mathbf{K}}$ is a real matrix satisfying the constraints:

$$\tilde{\mathbf{K}} = \tilde{\mathbf{K}}^T \quad (\text{B.8})$$

$$\tilde{\mathbf{K}}\tilde{\mathbf{D}} + (\tilde{\mathbf{K}}\tilde{\mathbf{D}})^T = \mathbf{0} \quad (\text{B.9})$$

$$\tilde{\mathbf{M}} + \tilde{\mathbf{K}} > \mathbf{0} \quad (\text{B.10})$$

together with $h_L(-1) = h_R(1) = 1$ and $h_L(1) = h_R(-1) = 0$ and symmetry conditions, this defined a multi-parameter set of correction functions, with examples for various orders shown by Vincent et al. [129]. Further, it was demonstrated that the single parameter OSFR set of Eq.(5.29 & 5.30) was a subset of ESFR.

To illustrate the ESFR correction function set, consider the case of $p = 3$, then, the Legendre coefficients of the correction function gradient can be found to be:

$$\tilde{\mathbf{g}}_l = - \begin{bmatrix} \frac{1}{2} \\ \frac{3(21\kappa_0+35\kappa_1+6)}{v} \\ \frac{5}{2} \\ \frac{5\kappa_1+2}{21(5\kappa_1+2)} \end{bmatrix} \quad \text{where } v = 175\kappa_1^2 - 42\kappa_0 - 12 \quad (\text{B.11})$$

After having defined the ESFR correction functions using FE methods, the Sobolev stability was investigated and found to hold. We have included ESFR was an appendix here as it is informative to the reader to understand the form that the correction functions take. But, due to there different method of derivation and for clarity, they are not included in the main text.

Appendix C

Correction Function Pseudo Code

Presented in chapter 5 were several families of correction functions. For ease of implementation we will set up the algorithms for generating some of the correction function. Namely Generalised Sobolev and Lebesgue Stable FR. We only include these as Generalised Jacobi correction functions are just a task of precisely implementing Eq.(5.47).

C.1 Generalised Sobolev Stable FR

Of concern when trying to calculate the GSFR correction function is the calculation of the matrix \mathbf{L}_p , hence we will outline the technique for calculating \mathbf{L}_p . The method shown will be valid for the first $p - 2$ rows of \mathbf{L}_p and, as can be seen from Eqs.(5.65,5.67,5.70), the penultimate two rows enforce the boundary conditions of the left correction function. Therefore, we have:

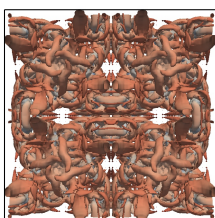
Algorithm 1 Process for calculating the value of $\mathbf{L}_p[m-1][n]$ for a $\mathbf{I}_p = [\iota_0 \dots \iota_p]$. The method of calculating $I_{i,m,n}$ is given in Algorithm 2.

Require: p, m, n, \mathbf{I}_p

```

 $L[m-1][n] \leftarrow 0$ 
for  $0 \leq i \leq p$  do
     $L[m-1][n] \leftarrow L[m-1][n] + \iota_i I_{i,m,n}$ 
end for
for  $1 \leq i \leq p$  do
     $a \leftarrow \frac{(n+i)!(m+i)!}{2^{2i}(i!)^2(n-i)!(m-i)!} (1 - (-1)^{n+m-2i})$ 
     $L[m-1][n] \leftarrow L[m-1][n] - a\iota_i$ 
end for
return  $L[m-1][n]$ 

```



Algorithm 2 Algorithm for calculating the integral of Eq.(5.62) where $b_i(m,n)$ is defined by Eq.(5.63).

Require: m, n, k

```

 $I_{m,n,k} \leftarrow 0$ 
for  $0 \leq i \leq \lfloor \frac{n-m}{2} \rfloor$  do
    for  $0 \leq j \leq \lfloor \frac{k-m-1}{2} \rfloor$  do
         $c \leftarrow \frac{b_i(m,n)b_j(m+1,k)}{n+k-2(m+i+j)} [1 - (-1)^{n+k-2(m+i+j)}]$ 
         $I_{m,n,k} \leftarrow I_{m,n,k} + c$ 
    end for
end for
return  $I_{m,n,k}$ 

```

C.2 Generalised Lebesgue Stable FR

We will now present a short piece of pseudo-code to calculate the left correction functions Legendre polynomial coefficients, $\tilde{\mathbf{h}}_L$. In this example we use $\%$ to mean the modulus or remainder operator, *i.e.* $a\%b = a \bmod b$. Here the input is an array \mathbf{q} with $p-2$ entries that control the shape of h_L .

Algorithm 3 Calculate left GLSFR correction Legendre coefficients

Require: $p, q[p-2]$

```

 $\tilde{h}_L[p-1] \leftarrow 0$ 
 $\tilde{h}_L[p-2] \leftarrow 0$ 
for  $0 \leq i \leq p-3$  do
     $\tilde{h}_L[i] \leftarrow q[i]$ 
     $\tilde{h}_L[p-1] \leftarrow \tilde{h}_L[p-1] - (i + p\%2)q[i]$ 
     $\tilde{h}_L[p-2] \leftarrow \tilde{h}_L[p-2] - (i + p-1\%2)q[i]$ 
end for
 $\tilde{h}_L[p] \leftarrow 0.5(-1)^p$ 
 $\tilde{h}_L[p+1] \leftarrow 0.5(-1)^{p+1}$ 
return  $\tilde{h}_L$ 

```
